

**UNIVERSITA' DEGLI STUDI DI NAPOLI FEDERICO II**



**DOTTORATO DI RICERCA IN INGEGNERIA CHIMICA  
XXIII CICLO**

***Ph.D Thesis***

**Heterogeneous condensation for submicronic particles abatement**

**Scientific Committee**

Prof. Amedeo Lancia  
*DIC University of Naples "Federico II"*

Prof. Andrea D'Anna  
*DIC Università di Napoli "Federico II"*

Dr. Ing. Francesco di Natale  
*DIC Università di Napoli "Federico II"*

Dr. Antonio Salluzzo  
*ENEA*

**Ph.D Student**

Ing. Marco Tammaro

*Amia figlia Giulia*

*“I do not know what I may appear to the world, but to myself I seem to have been only like a boy playing on the sea-shore, and diverting myself in now and then finding a smoother pebble or a prettier shell than ordinary, whilst the great ocean of truth lay all undiscovered before me.”*

Isaac Newton

*“Non so come io appaia al mondo, ma per quel che mi riguarda mi sembra di essere stato solo come un fanciullo sulla spiaggia che si diverte nel trovare qua e là una pietra più liscia delle altre o una conchiglia più graziosa, mentre il grande oceano della verità giace del tutto inesplorato davanti a me”*

Isaac Newton

## **Ringraziamenti**

Vorrei ringraziare innanzitutto il mio tutor, Prof. Amedeo Lancia, per la fiducia che ha riposto in me. Non era facile accettare come dottorando un lavoratore, anche se ricercatore, non più “giovannissimo”, con moglie e figlia, e che aveva da tempo lasciato le aule universitarie. Lo conosco da anni e so che non ha certo accettato per l'amicizia che pure ci lega. Mi auguro di aver ripagato la sua fiducia.

Poi ringrazio tutti gli altri membri del comitato scientifico: il Prof. Andrea D'Anna, il Dott. Antonio Salluzzo e l'Ing. Francesco Di Natale per il loro prezioso aiuto. Con Francesco credo, e spero, che le ore passate insieme, sia da vicino che al telefono, abbiamo anche contribuito ad inaugurare l'inizio di una nuova amicizia. Con Antonio, mio collega ed attuale Responsabile delle mie attività in ENEA, è stata l'occasione di conoscerci meglio reciprocamente e di stimarci ancor di più. Ringrazio il Dott. Patrizio Massoli, del CNR di Napoli, per il prezioso supporto nelle problematiche relative alla diagnostica.

Ringrazio l'ENEA che mi ha consentito di svolgere il dottorato congiuntamente alla mia normale attività lavorativa. Ringrazio tutti i ragazzi del Dipartimento di Ingegneria Chimica di Napoli che non hanno lesinato il loro aiuto quando mi era necessario. Ringrazio quelle persone (amici, parenti, colleghi) che in questi tre anni hanno continuato a ripetermi “ma chi te lo fa fare?”, in quanto, in questo modo, hanno rafforzato la mia convinzione a continuare.

Ringrazio mia moglie Mara per il supporto fornitomi: psicologico, in qualità di moglie; materiale, nelle attività sperimentali e di stesura della tesi, in qualità di collega ENEA. Ma soprattutto la ringrazio per la sua infinita pazienza nel sopportare i miei momenti di particolare impegno e il conseguente stress.

Ringrazio la mia piccola Giulia, nata poco prima dell'inizio del dottorato, la cui presenza, soprattutto nei momenti di sconforto e difficoltà del mio percorso di studio, mi ha ricordato quali sono le cose veramente importanti della vita.

Ringrazio i miei fratelli, Enzo e Roberto, che, nonostante la vita ci abbia portato geograficamente lontano, riesco sempre a sentire vicino. Ringrazio mia madre che, pur non comprendendo bene perché io a quasi quarant'anni stia sempre a studiare, non mi ha mai fatto mancare il suo supporto. Infine, anche se ne fa più parte di questo mondo, ringrazio mio padre il cui ricordo è talmente vivo in me che il suo esempio di serietà e severità sono, da sempre, un riferimento in tutto quello che faccio.

## ABSTRACT

It is now well established that the emission of sub-micrometric particulate matter entrained in flue gases of industry and vehicles exhausts, is one of the most critical treats for human health because of the toxicological effects of ultrafine particles on the respiratory system and their ability to cross alveoli's membranes reaching the circulatory system too.

Albeit this scenario, the traditional particle abatement devices are mainly designed and optimised to treat particles larger than 1  $\mu\text{m}$ , but they are far less effective towards the sub-micrometric particles. In particular, the existing technologies are far less efficient in collecting sub-micrometric particles, especially in the range 0.1 - 1  $\mu\text{m}$ , called *Greenfield gap*.

The aim of this work is the study of the heterogeneous condensation, a promising method that can be used to achieve very high particles removal efficiency with reduced costs: particles undergoing heterogeneous condensation increase their diameter by deposition of a liquid film on the particles surface, generating a liquid-solid aerosol with desired diameter. Therefore, this process can be used as a preconditioning technique to enlarge the particles diameter at micrometric size, allowing the use of conventional separators for gas cleaning. Although largely studied for its effect on atmospheric phenomena and for the application to particle measurement techniques (the CPC units), heterogeneous condensation has never been used at industrial scale as a method for gas cleaning.

In this study, theoretical and experimental analyses on the heterogeneous condensation have been carried out. For this purpose instrumented lab scale equipment has been designed, constructed and tested. Experimental protocols and measurement techniques have been optimized. The core of the equipment is the growth tube, that consists in a glass tube where the particle laden gas flows comes into contact with a supersaturated water vapour environment, generated by a liquid film flowing on the tube internal walls.

Preliminary experimental tests have been carried out to define adequate experimental protocols and to find out the most reliable techniques to measure the size and concentration of the liquid-solid aerosol in the water saturated gas that exists the growth tube. Afterwards, an experimental campaign has been carried out to study the heterogeneous condensation of soot particles produced by a ethylene-air premixed flame at different working conditions. Eventually, the experiments have been interpreted through a simplified theoretical model that allows a good description of observed results.

Experimental and modelling results eventually provide preliminary guidelines for the design of a pilot scale unit to be tested for future experimentation.

## INDEX

Introduction .....	9
Chapter 1 .....	19
<i>State of Art of heterogeneous condensation</i> .....	19
Chapter 2 .....	35
<i>Theoretical framework</i> .....	35
1.    Kelvin's equation .....	35
2.    Nucleation and growth rates .....	39
2.1    Nucleation .....	40
2.1.1    Critical saturation.....	45
2.2.    Growth .....	50
2.2.1    Heat and Mass balance on the single droplet.....	52
2.3.    Supersaturation region.....	62
2.3.1    Heat and mass balance in growth tube .....	63
2.4.    Nucleation and growth rate in the growth tube.....	75
2.5.    Condensational growth of a droplet aerosol.....	81
2.6.    Modification to the model .....	86
Chapter 3 .....	89
<i>Measurement device and experimental apparatus. Preliminary test</i> .....	89
1.    Experimental apparatus.....	89
1.1.    Burner .....	89
1.2.    Sampling system.....	91
1.3.    Cooling system .....	92
1.4.    Growth tube .....	92
1.5.    Sample filter/Measurement device .....	97
2.    Measurement device .....	100
2.1.    Dynamic Light Scattering (DLS).....	100
2.3.2    Brownian motion.....	100
2.3.3    Effect of the ionic strength of the solvent.....	101
2.3.4    Effect of the particle surface structure .....	102
2.3.5    Non-Spherical Particles .....	102
2.3.6    Light Scattering Theories Rayleigh Scattering.....	102
2.3.7    Mie Theory .....	103
2.3.8    How the DLS works .....	104

2.3.9	How a Correlator works .....	106
2.4	Differential Mobility Analyzer (DMA) .....	108
2.5	Laser Aerosol Spectrometer (LAS) model 3340 .....	112
2.3.1	Optical System .....	112
2.3.2	Laser and Associated Components and Optics.....	113
2.3.3	Detection System .....	113
2.3.4	Flow System.....	113
2.3.5	Simulation of measurement with LAS 3340.....	114
3.	Preliminary test.....	116
3.1	Preliminary test with DLS .....	116
3.1.1	Preliminary Test I .....	116
3.1.2	Preliminary Test II .....	121
3.1.3	Blank test for choice of containers.....	122
3.1.4	Blank test for choice of filters.....	123
3.1.5	Test without water in the growth tube.....	126
3.2	Preliminary test with DMA .....	132
Chapter 4	.....	136
	<i>Experimental test</i> .....	136
1.	Blank Test.....	136
2.	Test with flame.....	139
3.	Critical diameter.....	146
4.	Comparison between experimental data and modelling .....	153
Conclusions	.....	164
Appendix	.....	166
Bibliography	.....	170



## Introduction

Particulate matter emitted by flue gas of industrial and vehicles exhausts is one of the major health and environmental concerns. Basically, there are two different classification modes for particles identification: sorting by the size or by the particles formation modes (Whitby, 1978). Figure 1 outlines the terminology used for particles.

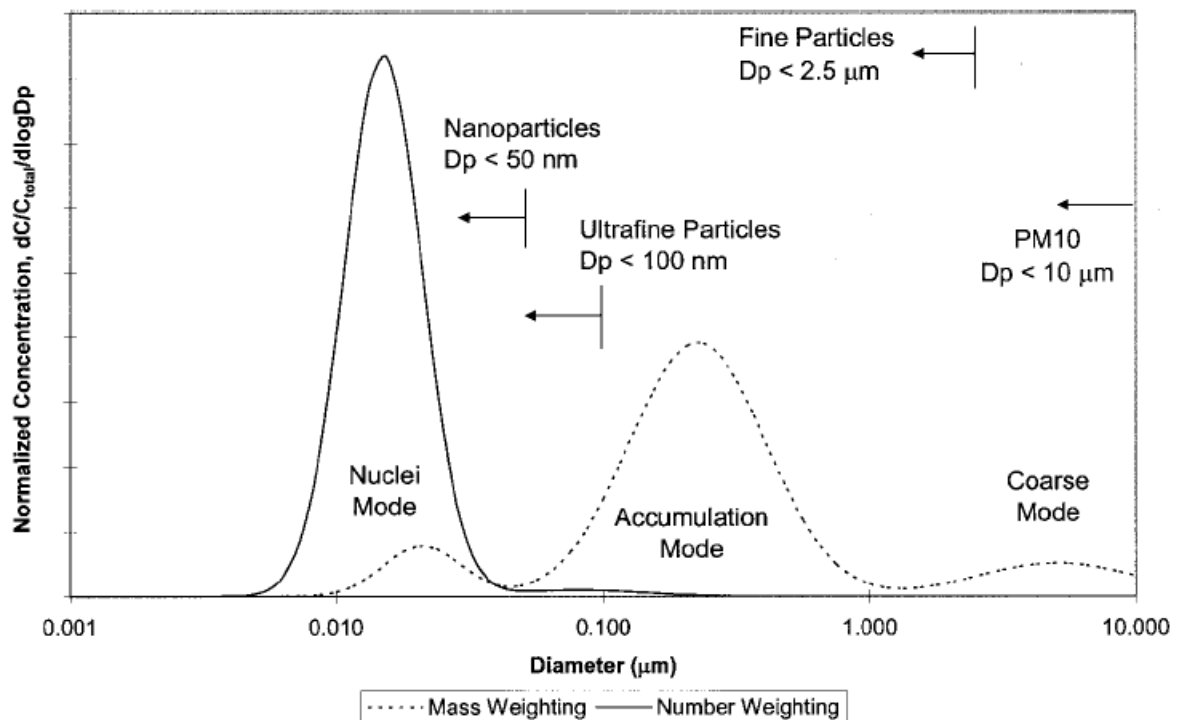


**Figure 1** - Typical engine exhaust size distribution: both in mass and in number (Kittelson, 1998).  $D_p$  is the particle diameter.

The particles formation modes are:

- ✓ Nucleation Mode: Freshly formed particles with diameters below about 10 nm, observed during active nucleation events. The lower limit is currently at about 3 nm;
- ✓ Accumulation Mode: Particles with diameters from about 0.1  $\mu\text{m}$  to just above the minimum in the mass or volume distributions which usually occurs between 1 and 3  $\mu\text{m}$ ;

- ✓ Coarse Mode or Coarse Particles: Particles with diameters mostly greater than the minimum in the particle mass or volume distributions, which generally occurs between 1 and 3  $\mu\text{m}$ .

Among particulate matter, nanoparticles pose a major concern. Nanoscale particles have, by definition, at least one dimension below 50 nm and have properties that may significantly differ from those of non-nanoscale particles of the same chemical composition. They are aggregates of atoms bridging the continuum between small molecular clusters of a few atoms and bulk solids.

Nanoparticles are ubiquitous. They occur as dust in the air, as suspended particles in superficial waters, in soil, in volcanic ashes and in technological applications ranging from ultra tough ceramics to microelectronics. Nanomaterials have a so wide application fields that they can both, pollute the environment and at the same time help keeping it clean. In fact, several applications have been investigated in which nanomaterials are employed for environmental protection and/or remediation. Nanostructured sorbents can capture noxious gases in an exhaust plume (Biswas *et al.*, 1998) or purify drinking water, for example, by removing arsenic (Onyango *et al.*, 2003; Peng *et al.*, 2005) or, some more, can be used as catalysts to reduce mobile source emissions (Lloyd *et al.*, 2005). Have been also reported some applications of nanoparticles to groundwater remediation by injection into subsurface contaminated by plumes (Zhang *et al.*, 1997).

### ***Impact of particles on environment and human health***

Very fine particles pose a concern about their impact on human health and environment in that they can remain suspended in the atmosphere for a long time, travel long distances from the emitting sources and, once inhaled, reach the deepest regions of the lungs and even enter in the circulatory system.

Since the particle size determines the capacity of penetration in the respiratory tract (Figure 2), following a precautionary principle it can be assumed that the lower the particle size, the higher its potential toxicity. Moreover, nanoparticles not only can be harmful by themselves but can also act indirectly as a carrier of hazardous substances.

Toxicologists have already assessed that nanoparticles produce pulmonary inflammation at both epithelial and interstitial sites and that they can enter the bloodstream to reach other target sites, including the cardiovascular system (Nemmar *et al.*, 2002, 2004; Oberdorster, 2001; Oberdorster *et al.*, 2002).

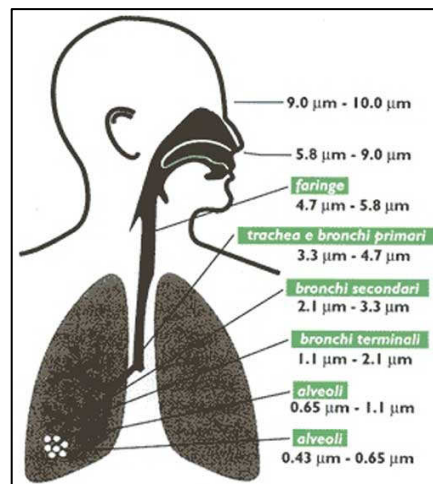


**Figure 2 - Impact on human health**

Toxicological studies also indicate that the ultrafine particles, unlike larger particles, are capable of penetrating the cellular membrane, where they create an inflammatory response by means of oxidative stress and causing damage to the mitochondria (Andre Nel, *et al*/2006).

The growing body of epidemiological studies indicates a clear relationship between the exposure to particulate air pollution in urban areas and acute increase in morbidity and mortality rates, especially for persons with obstructive lung and cardiovascular diseases (Pope *et al.*: 2002). Although it is still not clear, whether it is the mass, the size, the number or the surface area of particles the most determinant parameter determining the health impact, some information from epidemiological studies suggests that ultrafine particles (with a diameter < 100 nm) exert a much stronger physiological effect than the same mass of larger particles (Oberdorster *et al.*, 1992; Donaldson *et al.*, 1998). Well recognized health hazards include heart diseases (strokes, high blood pressure, arteriosclerosis, heart attack) and altered lung functions (asthma, difficult or painful breathing, chronic bronchitis), especially in children and older people. Fine particulate matter associated with diesel engines exhaust is already verified as a carcinogenic substance and is listed as mobile air toxic source.

In the environment, adverse effects of particulate matter are related to reduction of visibility in cities and scenic areas and, most alarming, adverse effects on climate are reported due to its influence on atmospheric radioactive phenomena (Menon *et al.*, 2002). Visibility impairment occurs when particles scatter and absorb light, creating a haze that limits the distance we can see and that degrades the colour, clarity, and contrast of the view (US EPA, 2003; Jung & Kim, 2006). Humidity can also significantly increase visibility impairment by causing some particles to become more efficient at scattering light.

Furthermore, particles can also be deposited, from the atmosphere or through direct release from industrial sites, onto the soil and water bodies and result in secondary contamination or other environmental effects.

### **Sources of particles**

Particulate matter may be generated either by natural processes or, most often, through human activities (Biswas P. *et al.*, 2006). Particles may be primary – when emitted directly into the atmosphere by sources, or secondary – when particles are formed in the atmosphere through the interaction of primary emissions. The Figure 3 provides an overview of the environmental fine particles.

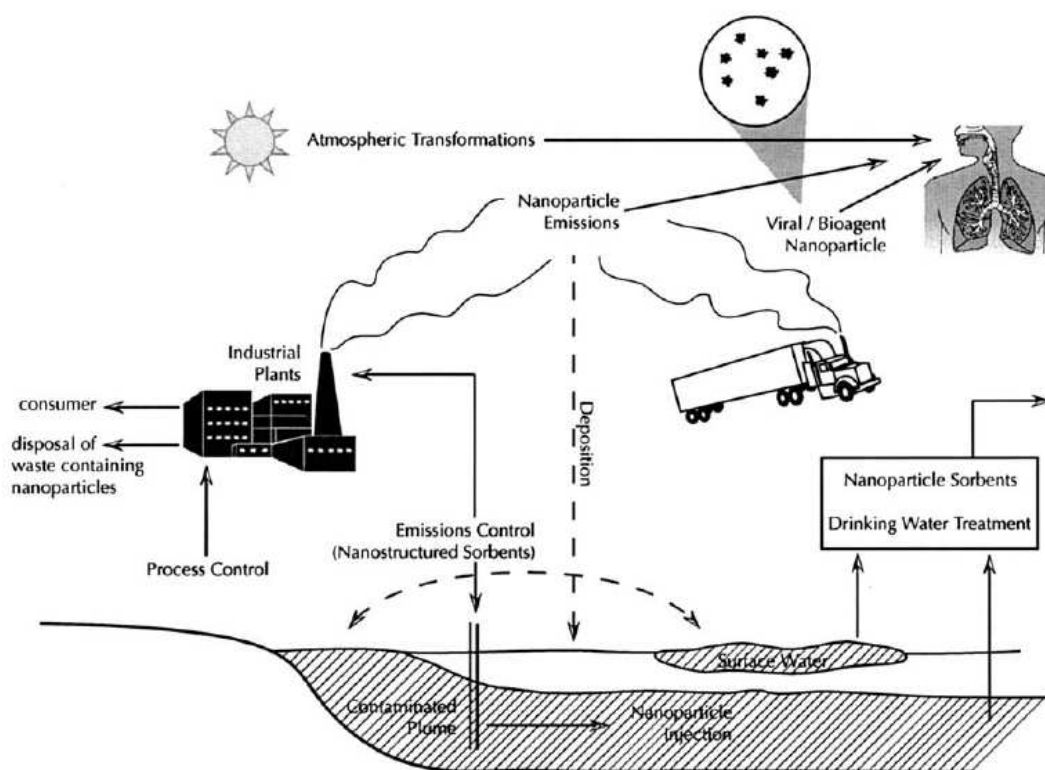


**Figure 3**– Schematic diagram illustrating fine particles in the environment

As can be seen, there are several sources that result in particle formation: stationary industrial sources, such as coal fired combustion systems and incinerators, or occupational environments, such as those where welding processes are prevalent and those where engineered particles are deliberately synthesized (Chang *et al.*, 2004, Vincent *et al.*, 2000); mobile sources such as automobiles and diesel powered vehicles (Kittelson, 1998); and several natural sources of particles of biological origin as well, that also need significant attention (e.g. pollen fragments are potential causes of allergies, and viral

particles can be used as vaccines or can play a significant role in the spread of disease, Hogan *et al.*, 2004).

Secondary particles are formed in the atmosphere by nucleation events following photochemical or radioactive decay processes (McMurry *et al.*, 2000, Kulmana, 2003; Kulmana *et al.*, 2004). Once particles are emitted into the atmosphere, they may undergo chemical and/or physical transformations resulting in alterations of their pristine size and composition. Even these particles are important in the assessment of environmental impact and human exposure (Donaldson *et al.*, 1998).

A summary of some of the important particle source categories is provided in Table 1.

Category		Description
Stationary emissions		✓ Combustion systems by vary fuel types (coal/oil/gas boilers, incinerators, smelters, cooking, residential combustors)
		✓ Indoor sources from combustion
Mobile emissions		✓ Diesel/gasoline/LPG/CNG vehicles
		✓ Metals in catalytic converters/fuel cells
		✓ Noble metal particles may be potentially emitted
Industrial processes		✓ Hot process
		✓ Combustion process
		✓ Bioaerosol
		✓ High energy mechanical process
Engineered nanoparticle production		✓ Manufacturing process, including cleaning
		✓ Waste/wastewater disposal
		✓ Conditioning application

**Table 1** - Sources of particles.

The main source of particulate matter in the environment are the combustion processes arising from both stationary and mobile sources (D'Alessio *et al.*, 1998; D'Anna *et al.*, 2008; D'Anna *et al.*, 2007; De Filippo *et al.*, 2008; Christense *et al.*, 1998).

With the recent advancement of nanotechnology products, nanomaterials are currently intentionally engineered and produced in industrial settings thus constituting novel potential emissions sources in the environment.

Particles are often generated even in exhaust air purification processes, for example aerosols formed by gas-phase reactions, like ammonium chloride (Dahlin *et al.*, 1981), acid fog formed in absorption processes (Schaber, 1995), salt fumes in the flue gas of waste incinerations. Sub-micrometric particles can be also generated as residuals by evaporation of spray droplets in quenchers and scrubbers (Krames *et al.*, 1992).

A summary of the production of particles in many industrial processes is presented in Figure 4, and a typical cumulative frequency distribution is reported for each process. Hildemann and coworkers (1991) have characterized the aerosol size distributions of emissions from combustion processes such as industrial boilers, fireplaces, automobiles, diesel trucks, and meat-cooking operations. The predominant peak in the mass distribution was observed to be at or below  $\sim 0.2 \mu\text{m}$  (Hildemann *et al.*, 1991). On examining the number distribution, many of these sources have their predominant peak much below 100 nm.

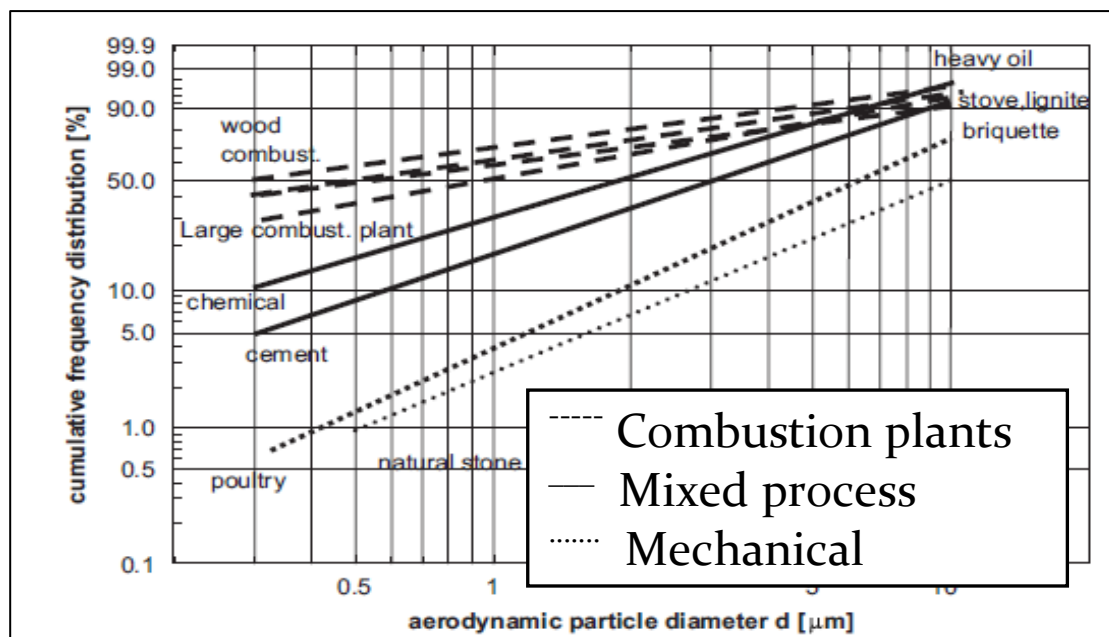


**Figure 4** – Cumulative frequency distribution vs aerodynamic particle diameter for different kind of industrial processes (Ehrlich *et al.*, 2007).

In the past, the measured cumulative frequency distribution was based on gravimetric techniques and showed that typical emitted particulate spans from 0.3 to  $1 \mu\text{m}$ . Gravimetric techniques, however, are ineffective in detecting nanosized particles. Now, new optical techniques allow the analyses of nanometric particles opening new research fields either on the understanding combustion, atmospheric phenomena and the interaction with biological systems.

***Regulations and removal of particles from gas***

The production of ultrafine to nanoparticles in gas-phase requires technical separation processes with high collection efficiency in the sub-micrometric size range to separate and recover the particles from the gas. With the aim of getting clean air streams, sub-micrometric particles removal assume a special significance because they often consist of toxic components and toxic gases or liquids can be adsorbed on them.

The new diagnostic methods for the analysis of particles size and concentration in gas streams have clearly pointed out that the particulate matter emitted by combustion sources is characterized by particle size distributions ranging from few nanometers up to several microns, while the one produced by diesel engines is usually smaller than 0.5  $\mu\text{m}$  (Matti Maricq, 2006; Minutolo *et al.*, 2008; Biswas S. *et al.*, 2009).

As a direct consequence, environmental regulations have gradually reduced the cut-off particle size for industrial flue gas from 10  $\mu\text{m}$  (PM10) to 2.5  $\mu\text{m}$  (PM2.5) until 1  $\mu\text{m}$  (PM1) then generating engineering challenges both for defining very low particulate emission processes and for the implementation of appropriate filtering systems able to pull down the fine particles (Peukert W. *et al.*, 2001; Andronache, 2004; Kuang-Yu Liu *et al.*, 2007; Flagan *et al.*, 1988).

Similarly, restrictive regulations have been applied to diesel engines (e.g. Euro 4 and Euro 5 regulations for cars; USA Tiers 2 standards for diesel locomotives). Also the maritime sector, traditionally refractory to the imposition of environmental regulation, has recently revised its standard (MARPOL VI) to account for the excessive emission of particulate matter, sulphate and nitrate. Albeit this scenario, the traditional particles abatement devices are mainly designed and optimised to treat particles with sizes above or around 1  $\mu\text{m}$ , but they are far less effective towards the sub-micrometric dimensions. Usually, for process industry and combustion units, complex systems including trains of consecutive abatements devices (water scrubber, fabric filters, cyclones, Venturi scrubbers, electrostatic precipitators) are employed (Woodard, 1998). It is possible to verify that all the conventional particulate removal devices are far less efficient in collecting sub-micrometric particles, especially in the range 0.1 - 1  $\mu\text{m}$ , called the *Greenfield gap* (Seinfeld *et al.*, 1998) (see Figure 5). For example, as particle dimensions decrease, the efficiency of common filtering systems is considerably reduced because particles begin to behave as molecules and show a low tendency to remain on the surface of fibres in the filters. In fact, once the particle reaches the fibre surfaces the bounce off effect, due to the

kinetic energy of the particle, could be predominant over the interaction forces between particle and surface (Heim *et al.*, 2005; Wang *et al.*, 1991).

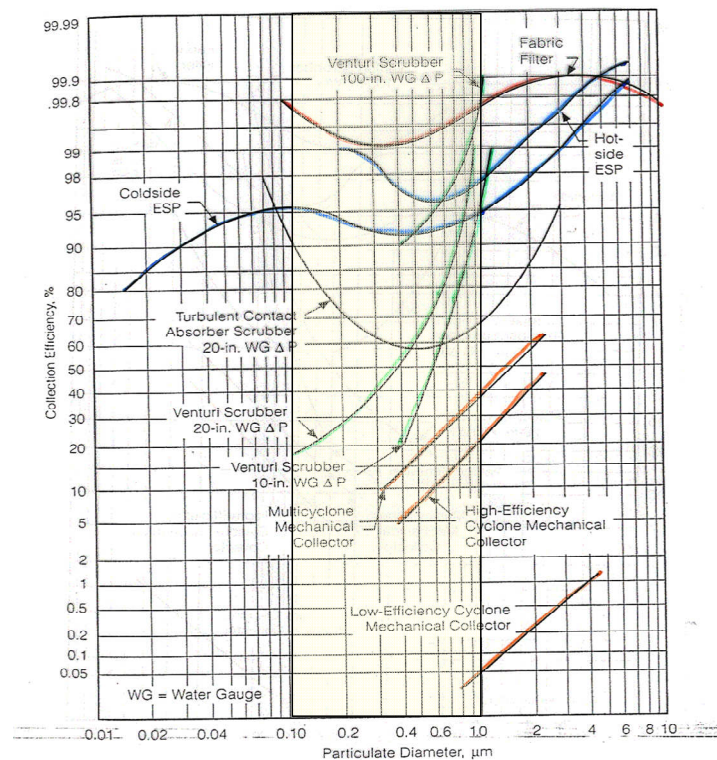


**Figure 5** - Particles with diameters in the range  $0.1 < d_p < 1 \mu\text{m}$  often called "Greenfield gap", appeared to have the lowest efficiency of collection.

As a result of the new awareness on the diffusion and the toxicity of sub-micrometric particles, it appears the necessity of developing new and better techniques and methods for particle abatement devices to remove submicron particulate matter.

The typical example of these new systems is the catalytic DPF (Diesel Particulate Filtration) coupled with EGR (Exhaust Gas Recirculation) developed for car diesel engine. This after-treatment unit allows high removal efficiency for nanometric particles and they are commonly adopted on cars, but the high pressure drops and the catalyst costs reduce their applicability for heavy duty diesel engines as those of trucks, trains or vessels.

The American Lung Association (U.S. Lung Association, 2004) reported that the highest efficiency for sub-micrometric dust removal in indoor ambient environment is achieved by using the two-step-electrostatic separator (ESP). Anyway the efficiency is still lower than the desired quality of standard required preventing health risks (10% of total sub-micrometric particles stills cross the ESP). However, the highly efficient technical separation of submicron particles from gas through the upgrading of conventional technique is difficult and expansive.



**Aim of this thesis**

The separation of submicron particles from gases can be considerably simplified if the particles with size lower than micron are enlarged to a size of some microns by a preconditioning technique, as the heterogeneous condensation. This method allows to a condensable species, like water vapour, to condense on the sub-micrometric particle's surface increasing its size (see Figure 6).

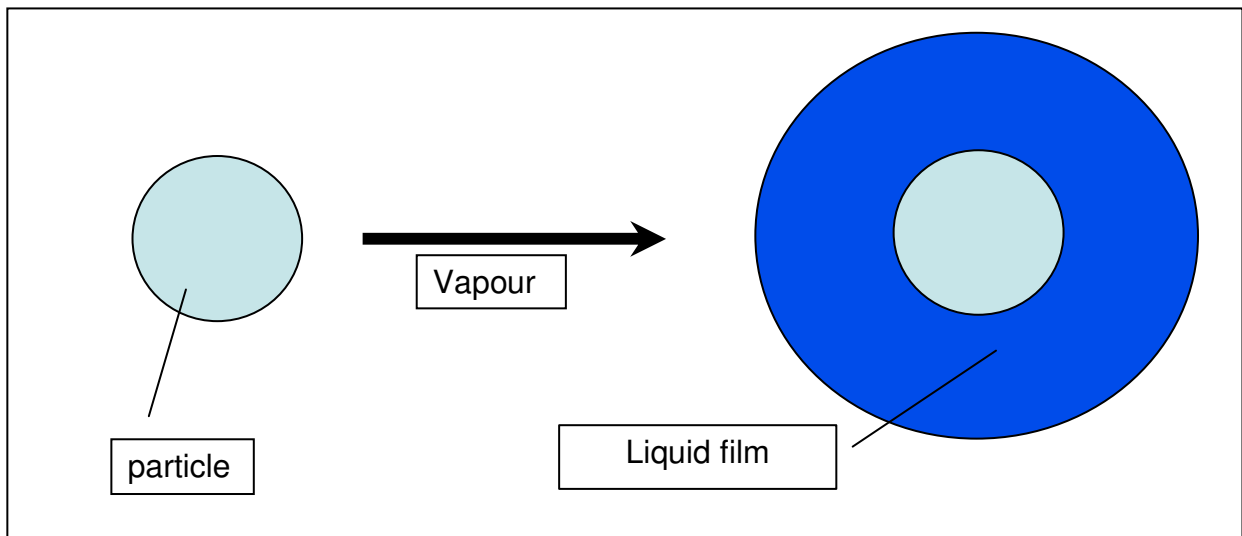


**Figure 6** – Scheme of heterogeneous condensation on the particle

The heterogeneous condensation with water vapour has been exploited as a technique for enlarging particles diameter so to carry out the Greenfield gap prior to conventional separators (Yan Jin-Pei *et al.*, 2008).

The purpose of this thesis is to study the growing of sub-micrometric particles through heterogeneous condensation of water vapour, proposing a simplified way to enlarge the particles, with the use of a purpose-made laboratory system. The geometry of the laboratory system and the approach is similar to techniques used in counters condensation (Hering *et al.*, 2005 (1), (2)) but, unlike CPC, the proposed system is a much simpler and cost-effective plant.

The thesis is structured in four chapters.

In the first chapter of the thesis are reported the state of the art and the pertinent literature on the removal of sub-micrometric particulate from combustion gas by means of heterogeneous condensation. The fundamentals steps of evolution of theory of nucleation and growth are described.

In the second chapter the theoretical framework are illustrated. In this chapter are reported the heat and mass balances required to provide a model for the droplet growth rate.

The third chapter is focused on the analysis systems and laboratory set up developed in this work. Besides a preliminary test are described. In particular the chapter is subdivided in three paragraphs. The first illustrates the instruments (DLS, DMA and LAS 3340) and the experimental protocols used for particles measurement while the second contains the description of the laboratory plant which has been realised for this thesis. The third paragraph reports the results obtained in the preliminary test performed in order to optimise the operating conditions, and to test the experimental set-up.

Chapter four reports the results obtained in the experimental activities and the description of the different conditions performed for the tests. A comparison between experimental results and modelling data is eventually reported. The experimental results have allowed the development of the model that take into account the affective availability of steam.

## Chapter 1

### ***State of Art of heterogeneous condensation***

Heterogeneous condensation of a solid insoluble sub-micrometric particle is an energetically unfavourable process because the liquid free surface increase causes a free energy rising. In order to overcome the energetic barrier, then to activate condensational growth, the vapour must be over saturated: the saturation ratio,  $S$ , defined as the ratio between partial vapour pressure  $P_V$  and equilibrium vapour pressure,  $P^o(T)$ , at the flow temperature,  $T$ , must exceed unity:

$$S = \frac{P_V}{P^o(T)} \quad (1.1)$$

Lord Kelvin (Thomson, 1871) firstly showed that the smaller the particle the higher the supersaturation required to activate condensational growth. This is because the equilibrium vapour pressure over a droplet is higher than over a flat surface as a result of the droplet surface tension. This effect is described by the Kelvin's relation (Thomson, 1871):

$$D_K = \frac{4\sigma M}{\rho R_V T \ln S} \quad (1.2)$$

which associates the equilibrium vapour supersaturation,  $S$ , to the diameter of a droplet with diameter  $D_K$  composed of a condensed vapour, of molecular weight  $M$ , density  $\rho$  and surface tension  $\sigma$ . In equation 1.2  $R_V$  is the universal gas constant and  $T$  is the absolute temperature.

The enlargement of particle size through condensational growth is one of the oldest approaches for aerosol measurement (Podzimek *et al.*, 1985). The study of Aitken (Aitken, 1888) about the enlargement of particles through heterogeneous condensation by means of adiabatic expansion of a saturated air sample, enabling to count the number of dust's particles in the air. The first theoretical description of droplet growth by condensation goes back to Maxwell (Maxwell, 1890).

Indeed the first theory of condensation on completely soluble particles was proposed by Köhler (1936) that form the basis of the understanding of cloud formation.

The process of particle enlargement by heterogeneous condensation can be divided into two stages that can be considered in series. Firstly, the particles have to be activated with formation of a liquid embryo on the particle surface, during a so called *activation* or **nucleation** stage. Then the vapour will condense around the embryo by condensation (**growing** stage).

The saturation of the gas phase is a necessary but not a sufficient condition for the activation of heterogeneous condensation. In fact the saturation ratio  $S$  must exceed a critical value,  $S_{cr}^{hete}$ , defined as the value of  $S$  corresponding the nucleation rate is equal to one embryo per particle per second. However, in order to assure that are the vapour undergoes a heterogeneous condensation it has to avoid any *homogeneous nucleation*, which take place when the nuclei are generated only from the vapour phase where colliding vapour molecules result in the formation of molecule clusters. Molecule clusters which exceed a critical size act as nuclei for the further condensation of the vapour. This condition leads to the assessment of an upper critical value,  $S_{cr}^{hom o}$ , as the value of  $S$  corresponding to nucleation rate equal to one nuclei per second. Homogeneous nucleation requires high degrees of  $S_{cr}^{hom o}$  ( $\approx 2-5$ ). In conclusion we can say that the optimal heterogeneous nucleation occurs for values of  $S$  higher than  $S_{cr}^{hete}$  but lower than  $S_{cr}^{hom o}$  (see Chap. 2).

## 1. Nucleation

Insoluble condensation nuclei were analyzed by Krastanov (1957) when a liquid nucleus completely covers the particle (see Figure 1.2).

Fletcher (1958) verified that the heterogeneous nucleation on an aerosol particle starts from an embryo liquid lens (Figure 1.1). The angle between liquid and solid phase, indicate as  $\theta$  in Figure 1.1, is called *contact angle* and it's defined by Young's equation (see Chap. 2). Fletcher investigated heterogeneous nucleation on homophile aerosol particles when an embryo has finite contact angles ( $\theta > 0^\circ$ ) and is smaller than the particle. The standard scheme for calculation of the nucleation free energy ( $\Delta G^*$ ) is used in the Fletcher's formula

$$J = 4\pi K R_p^2 \exp\left(-\frac{\Delta G^*}{kT}\right) \quad (1.3)$$

that describe the rate of formation of embryo per particle per second (see Chap. 2), is based on the minimization of Gibbs's energy variation respect to the formation of embryo with radius,  $r$  (Figure 1.1). The formula of  $\Delta G^*$  ( $R_p$ ,  $T$ ,  $S$ ,  $\theta$ ,  $\rho$ ,  $M$ ) is illustrated in Chapter 2.

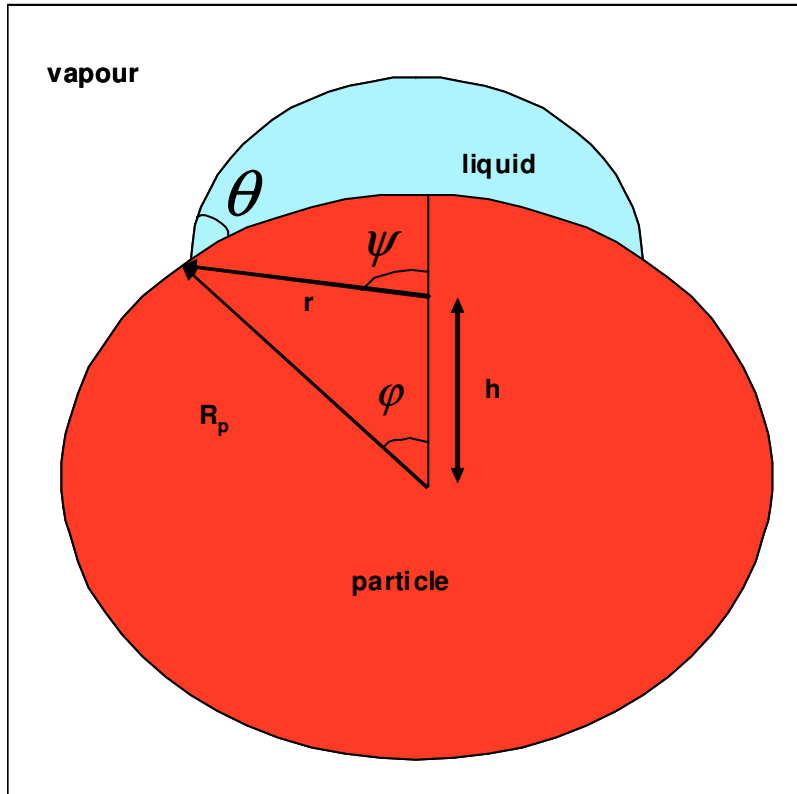


**Figure 1.1** – Model of nucleation by Fletcher with formation of embryo with radius  $r$  on the particle with size  $R_p$

McDonald (1962) applied the condition relating to the minimization of the variation of Gibbs free energy to the study of the formation of condensation nuclei in homogeneous condensation, which is the formation of droplet of pure component from vapour phase. These studies, starting from an initial condition of minimization of Gibbs free energy related to the vapour-liquid passage equilibrium, through a mathematical demonstration arrives to Kelvin's equation, which binds the critical radius, or minimum radius, of the homogeneous nucleus to the equilibrium vapour supersaturation,  $S$ . These studies show that the condensation process is energetically disadvantaged and to overcome this energy barrier  $S$  must be greater than unity. Although MacDonald's work is related to homogeneous condensation, the theoretical results are also applicable to heterogeneous condensation, replacing the concept of minimum radius of the homogeneous nucleus, with

the minimum radius of the solid particle necessary, given  $S$ , to activate the condensation process onto its own surface. The smaller the particle the higher the supersaturation required to activate condensational growth.

Smorodin (Smorodin, 1983; Smorodin *et al.*, 1986) proposed a general model of insoluble particles with “active sites”. This model assumes that on the surface of the insoluble particle there are zones with different chemical and physics characteristics, as the coefficient of wetting. Then from the supersaturated vapour phase different embryos with different radius and contact angle simultaneously may cover the active centres on the particle surface.

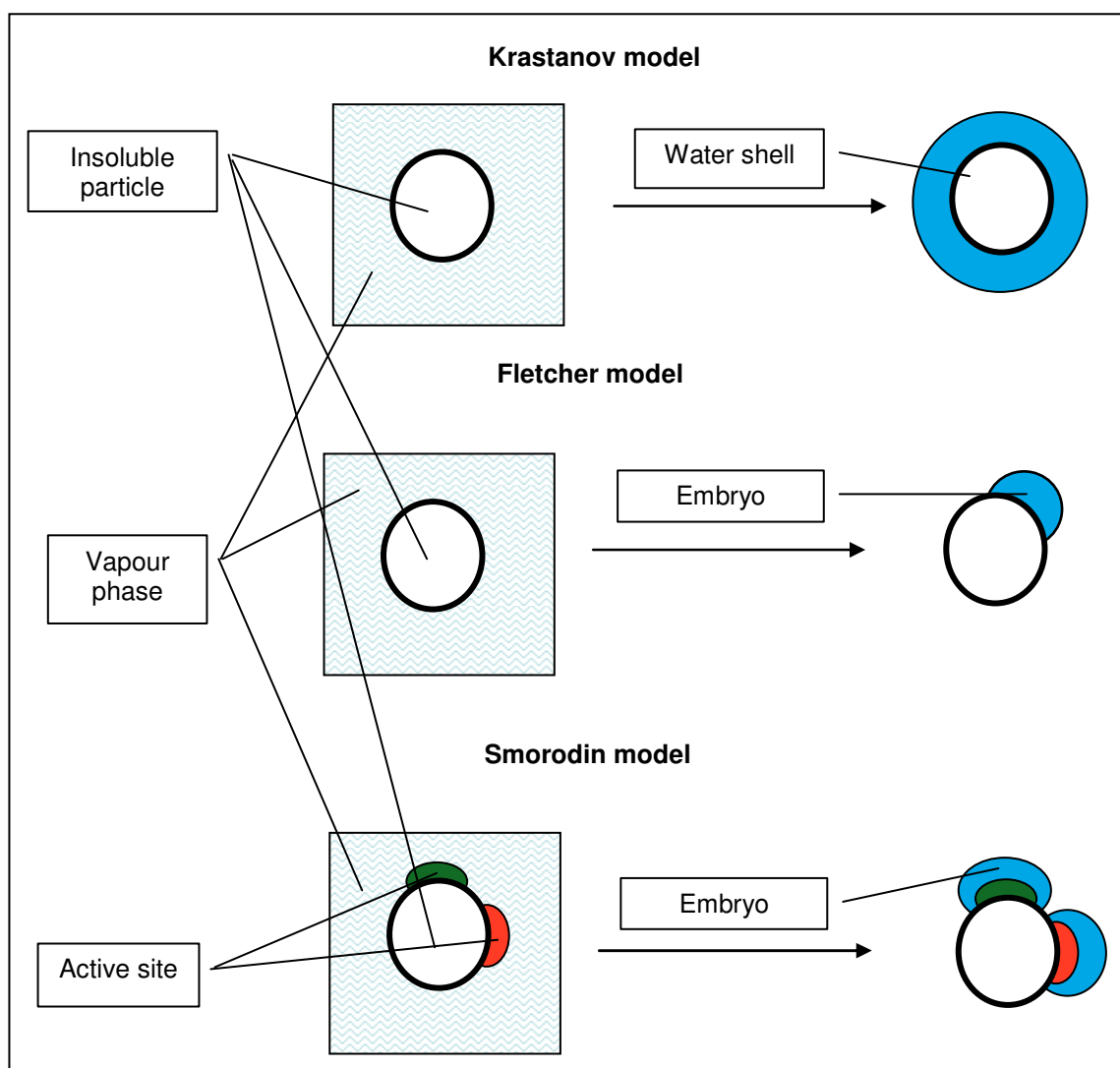


**Figure 1.2** - Schematic diagrams of models for heterogeneous nucleation on insoluble particles.

In the 2004 the same author (Smorodin *et al.* 2004) has presented a study on the possible effects of surface heterophilicity of insoluble aerosol particles on the evolution of their

mean size during heterogeneous condensation, previously measured experimentally by Mavliev *et al.* (2001) and he concluded that the energy and rate of heterogeneous nucleation of polar liquids on heterophilic aerosol particles at a constant supersaturation depends on the particles size. For smaller particles, the rate is smaller; for larger particles the rate is higher due to the role of increased numbers of “active sites”. Therefore, depending on the particle size and supersaturation, heterophilic particles can have different activation behaviours.

Other author (Lee *et al.*, 2003) has examined the connection between molecular properties of the different condensing vapour. The particles are produced by burning natural gas using a Bunsen burner. The experimental data are compared to Fletcher’s heterogeneous nucleation theory. The conclusions cannot explain the gap between the experimental measurements and the Fletcher theory for some working fluid (e.g. octadecane). The author hypothesize that there may be nanoscale interactions that occur between the organic species, the carbon particles and the working vapour, but these speculations do not explain the discrepancy between theory and experiment.

Author	Description	
W. Thompson Lord Kelvin (1871)	$S = \exp \left[ \frac{4\sigma M}{\rho R_v T D_k} \right]$ <p><b>Homogeneous condensation.</b> The particles are pure liquid droplets consisting of the condensed vapour.</p>	
	<b>Heterogeneous condensation</b>	$S = a_w \exp \left[ \frac{4\sigma v_w}{R_v T D_k} \right]$ <p><b>Particles soluble.</b> <math>a_w</math>, <math>v_w</math> and <math>\sigma</math> are the activity of water, the partial molar volume of water and the surface tension of the solution, respectively.</p>
		$S = \exp \left[ \frac{4\sigma M}{\rho R_v T D_k} \right]$ <p><b>Solid insoluble particles.</b> The particle activation depends on their wettability by the liquid. If particles are completely wetted, they behave as pure liquid droplets.</p>
Krastanov (1957)	<b>Shell theory.</b> Heterogeneous condensation starts directly with a liquid shell around the particle	
Fletcher (1958)	<b>Nucleation theory.</b> Heterogeneous nucleation on an aerosol particle starts from an embryo liquid lens. The nucleation rate function of particle wettability Hypothesis: smooth, spherical and homogeneous particles	
Smorodin (1983; 1986; 2004)	<b>Sites theory.</b> This model assumes that on the surface of the insoluble particle there are zones, "active sites", with different chemical and physics characteristics, as the coefficient of wetting. Then different embryos are formed in the course of nucleation phase.	
Lee (2003)	<b>Experimental nucleation.</b> Verification of Fletcher theory with different fluid. There is a gap explained by nanoscale interactions.	

**Table 1.1** - Summary of the main works on the nucleation

## 2. Growth of embryos

Okuyama *et al.* (1984) studied with numerical models the time dependence of the droplet radius during condensational growth of DBP (dibutyl phthalate) under various conditions. They have found that for particles number concentrations higher than  $10^5$  particles/cm<sup>3</sup>, the final droplet radius can be determined by the particle number concentration, besides the vapour content, but at concentration lower than  $10^3$  particles/cm<sup>3</sup> the particle growth can be approximated by the growth of an isolated droplet.

Another approach has been given by two authors Barrett and Fissan (1989) that coupled the equations for the aerosol size distribution and the vapour saturation. In this work the rate of increase in droplet mass can be written as a function of supersaturation ratio, the initial radius of particle and Knudsen number ( $Kn$ ), defined as ratio between free molecular



path and particle diameter and utilized to classify the gas-solid interaction system. This work shows as the condensation on smaller particles is difficult, as explained by the Kelvin effect, and the minimum radius activated, and hence the overall shape of the grown distribution, depends on the vapour source rate, or supersaturation ratio.

Barrett and Clement (1988) analysed the growth rates of the liquid drops in the free molecule ( $Kn \gg 1$ ), continuum ( $Kn \ll 1$ ) and transition regime ( $Kn \approx 1$ ). The basic idea was that droplet growth is controlled by heat and mass transfer.

Williams (1995) proposed a model for liquid droplet growth by condensation for large saturation ratios. Analytical solution and presented in figures in terms of temperature, vapour pressure and saturation ratio at various distances from the droplet surface. Besides, a linear model is proposed for approximation of value of  $S$ , but it's valid in the range 0.6-1.5. In fact the linear approximation is grossly in error for value of  $S$  out of that range.

Kulmala (1993) proposed an analytical solutions for equations for the condensational growth and evaporation of single liquid droplet derived from energy and mass balance in the transition and in continuum regime. The Kelvin effect is considered. The analytical solution is compared with the numerical solution. The closer to the unity the saturation ratio and the smaller the latent heat of vaporization of the vapour, the better is the accuracy of the new expression. The analytical solution gives the condensational growth time (or evaporation time) as a function of initial and final droplet radius. The solution is valid for condensational growth or for evaporation when the droplet radius is more than 5 nm.

Barrett and Baldwin (2000) have proposed an approximate method for estimating the maximum saturation, the nucleation rate and the total number nucleated per second during the laminar flow of a hot vapour-gas mixture along a tube with cold walls is described. The basis of the approach is that the temperature and vapour concentration differences between the wall and a point in the tube are approximately proportional to  $R(r)Z(z)$  and  $R(r)F(Z(z))$ , respectively, where  $r$  and  $z$  are dimensionless radial and axial coordinates and  $R$ ,  $Z$ , and  $F$  are known functions. Key parameters determining the location and magnitude of the maximum saturation are the Lewis number,  $Le$ , and a parameter,  $B$ , which determines the temperature variation of the equilibrium vapour concentration ( $B$  is roughly the latent heat of vaporisation per vapour molecule divided by Boltzmann's constant). For vapour-gas mixtures with  $Le > 1$ , the maximum saturation occurs at the tube axis but for those with  $Le < 1$  it occurs near the tube wall. The magnitude of the maximum saturation

achieved increases rapidly with  $B$ . The approach assumes that condensation on previously nucleated particles is negligible, and a condition on the maximum nucleation rate for this to be so is derived. Predictions are compared with numerical calculations for dibutyl phthalate (DBP) vapour and for water vapour and very good agreement are found.

This approach can be applied to many other two-dimensional systems where simultaneous heat and mass transfer occur provided that the temperature and vapour concentration can be expressed in the forms given above.

Park and Lee (2000) derived an analytical solution when the size distribution changes by condensational growth of polydispersed aerosol, using the growing rate derived by Kulmala (1993). The results show how the size distribution moves to larger diameter.

Condensational droplet growth in the system water vapour-air is investigated in the continuum regime ( $k_n \ll 1$ ) by Heidenreich (1994). A rigorous theoretical consideration based on the complete first-order transport equations for heat and mass is performed. Stefan-flow <sup>(1)</sup>, thermal diffusion and Dufour effect <sup>(2)</sup> thus are included in the consideration. Not only the temperature dependence of the transport coefficients but also their dependence on the composition of the system is taken into account. On the basis of the complete equation for heat transport a temperature profile is derived. With this temperature profile the mass flux caused by thermal diffusion is calculated. For the determination of the unknown droplet temperature an equation can be derived from the heat balance of the droplet. The results show that the temperature of the environment has a significant influence on the droplet growth. The growth rate increases with a higher ambient temperature. This is caused by the fact that the transport coefficients increase with the temperature. The temperature difference between the droplet and the environment also increases. In addition by numerical results showed that for practical calculations a simplified approach can be used. Thermal diffusion and the Dufour effect can be neglected for small value of the thermal diffusion factor ( $\alpha \leq -0.3$ ). The dependence of the thermal conductivity on the composition of the system can also be neglected. It is sufficient to calculate droplet growth in the system water vapour-air with the simplified approach to show that the errors are, mainly:

- about 2% by neglecting the temperature dependence of thermal conductivity and the enthalpy of the vapour molecules;
- about 0.5% by neglecting the Stefan-flow.

---

<sup>1</sup> *Transport phenomena concerning the movement of a chemical species by a flowing fluid that is induced to flow by the production or removal of the species at an interface*

<sup>2</sup> *Energy flux due to a mass gradient occurring as a coupled effect of irreversible processes*

Hering *et al.*, (2005) has presented a new method for the enlargement of particle size through condensation of water vapour in a laminar, thermally diffusive flow. The method involves the introduction of an air flow at temperature  $T_i$  into a wet-walled tube at a wall temperature  $T_w > T_i$ . This approach yields higher supersaturation values than either mixing or cold-walled condensers when operating between the same temperature extremes. Model results for the saturation profiles within the condensing region show that the peak supersaturation are reached along the centreline of the flow, and that the activation efficiency curves are steeper for large temperature differences when the critical diameter is smaller. Experiments conducted with three types of aerosol have confirmed that condensational growth is achieved with this approach, although experimental critical diameter is somewhat higher than predicted for wettable particles.

Based on this method, Hering *et al.* (2005) presented an new condensation particle counter. The particle counter evaluated was marketed as the TSI Model 3785.

Fisenko and Brin (2006) have presented a new mathematical model of laminar flow diffusion chamber, with a cylindrical geometry, which includes mutual influence of homogeneous nucleation and droplets growth on heat and mass transfer processes. In this study the wall temperature is lower than mixture gas-vapour, which is introduced in the chamber. The numerical results applied to experimental results, carried out with helium and argon, shown that the model could be applied only for relatively low nucleation rates. The droplet growth, based on this model, is a function of the radial position, and is maximum along the axial position.

Fisenko *et al.* (2007) have proposed a study about the vapour condensation on nanoparticles in a supersaturated gaseous mixture. The supersaturation was created by mixing two flows with different temperatures in a cylindrical mixer at atmospheric pressure. The conditions for mixing were chosen such that the homogeneous nucleation of vapour did not mask the growth of heterogeneous droplets with nanoparticles inside. A mathematical model of the growth of heterogeneous droplets was developed at one-dimensional description of the mixer. Five parameters that affect the performance of the particles size magnifier were identified: temperature of the saturator and the flow with nanoparticles, the number density and initial radius of the nanoparticles, and the ratio gas and vapour of flow rates. The authors have seen that high number concentration of particles determines low efficiency due to depletion effect and that with high supersaturation the final radius of droplet reaches several microns, but leads the

homogeneous condensation. Besides, the Kelvin effect became important with radii about 10 nm. The results of the simulation are compared with experimental data and they have a good agreement.

Brin and Fisenko (2007) have studied the growth of heterogeneous water droplets containing nanoparticles in two laminar flow diffusion chambers of different designs. It is shown that the efficiency of heterogeneous condensation is, to a substantial extent, governed by the processes of heat and mass transfer inside a chamber condenser. Integral parameter,  $C(R)$ , representing the probability that a nanoparticle with radius  $R$  is covered with a condensate film in a laminar flow chamber, is calculated. It is established that, in air–water vapour mixtures, the radius of heterogeneous water droplets may amount to several micrometers and efficient condensation begins on spherical nanoparticles when their radii exceed 5 nm.

Authors	Description
Barrett and Fissan, (1988; 1989)	The rate of increase in droplet mass as a function of $S$ , the initial radius of particle and $Kn$ . The basic idea was that droplet growth is controlled by heat and mass transfer.
Williams (1995)	Simplified relation for growth rate, but it is valid only $S \in [0.6-1.5]$ .
Kulmala, (1993)	Analytical solutions for equations for the condensational growth of single liquid droplet derived from energy and mass balance. The closer to the unity the $S$ better is the accuracy of the solution.
Barrett and Baldwin (2000)	An approximate method for estimating the $S_{max}$ , the nucleation rate and the total number nucleated per second during the laminar flow of a hot vapour-gas mixture along a tube with cold walls
Heidenreich (1994)	A rigorous theoretical consideration equations for heat and mass. The temperature of the environment has a significant influence on the droplet growth and the growth rate. The results shows that it is sufficient to calculate droplet growth in the system water vapour-air with the simplified approach to show that the errors are $< 1\%$ .
Hering (2005)	New method for the enlargement of particle size through condensation of water vapour in a laminar, thermally diffusive flow. The method involves the introduction of an air flow at temperature $T_i$ into a wet-walled tube at a wall temperature $T_w > T_i$ . This approach yields higher supersaturation values than either mixing or cold-walled condensers when operating between the same temperature extremes.
Fisenko and Brin (2006)	New mathematical model of laminar flow diffusion chamber, with a cylindrical geometry, which includes mutual influence of homogeneous nucleation and droplets growth on heat and mass transfer processes. The wall temperature is lower than mixture gas-vapour, that is introduced in the chamber. The numerical results applied to experimental results, shown that the model could be applied only for relatively low nucleation rates. The droplet growth, based on this model, is a function of the radial position, and is maximum along the axial position.
Fisenko (2007)	The supersaturation was created by mixing two flows with different temperatures in a cylindrical mixer at atmospheric pressure. A mathematical model of the growth of heterogeneous droplets was developed at one-dimensional description of the mixer. The authors have seen that high number concentration of particles determines low efficiency due to depletion effect and that with high supersaturation the final radius of droplet reaches several microns, but leads the

	homogeneous condensation.
Brin and Fisenko (2007)	The efficiency of heterogeneous condensation is governed by the processes of heat and mass transfer. Integral parameter, $C(R)$ , representing the probability that a nanoparticle with radius $R$ is covered with a condensate film in a laminar flow chamber, is calculated. It is established that, in air–water vapour mixtures, the radius of heterogeneous water droplets may amount to several micrometers

**Table 1.2** - Summary of the main works on the growth

### 3. Application of heterogeneous condensation

We have seen that droplet growth by condensation requires a supersaturated vapour phase. A vapour phase is supersaturated if the vapour pressure ( $P_v$ ) in the system is higher than the corresponding saturation vapour pressure ( $P^\circ$ ) which is a function of the temperature of the system.

Generally, supersaturation can be achieved in different ways, for example by mixing saturated gases of different temperature, by cooling, by chemical reactions and by evaporation a liquid surface. In all these cases, supersaturation is caused either by a reduction of the temperature of the system or by an increase in the vapour pressure in the system. The evaporation of a liquid surface is an economically feasible process to achieve supersaturation economically, also on a technical scale.

The heterogeneous condensation of water vapour as a preconditioning technique has been experimentally investigated soon after the Second World War, when there was been the advent of large industrial installations that gave a new impetus and new direction to investigations on cleaning of the flue gases from combustion processes. Initially the approach was purely experimental, with the supersaturation required for heterogeneous condensation obtained by mixing steam with the particle laden gas stream without a specific control about nucleation process (Schauer, 1951). First experimental studies highlighted the contribution of heterogeneous condensation as improved wet scrubber efficiency removal (Lancaster and Strauss, 1971).

Yoshida *et al.*, (1976) produced a mechanism to improve a supersaturated atmosphere by mixing two kinds of saturated air, one of which was humidified by contact with hot water and the other with non-heated water. The degree of supersaturation or the quantity of condensable water vapour was controlled by changing their mixing ratio and the combination of their temperatures. Aerosols were continuously introduced into the supersaturated atmosphere at a constant rate.

The droplet growth can be realized also in trickle bed columns with water as showing investigations of Calvert and Englund (1984) and Johannessen *et al.* (1997) that have shown that fine particles can be separated from saturated warm gas streams in packed trickle beds with cold water. The separation of the fine particles was caused by an enlargement of the particles due to heterogeneous condensation. The main advantage of a trickle bed is that not only supersaturation and correspondingly particle growth by condensation can be achieved but also separation of the droplets takes place simultaneously.

More detailed information about the influence of different parameters, such as supersaturation, mass of condensable water vapour, particle concentration, temperature and initial size distribution on the activation and growth rate of the particles, necessary for the design of an industrial plant, were studied by Heidenreich (1995). In this paper numerical calculations and experimental activities are performed to show the influence of above parameters on the activation and growth rate of sub-micrometric particles. The numerical results are compared with experimental results in which supersaturation was achieved by mixing two water vapour saturated air streams of different temperature. The results described the condensational growth of the droplets from solid nuclei, in the adiabatic and isothermal conditions, as a function of the supersaturation degree, which is the driving force of the process. By an appropriate choice of mixing ratio and temperature of the two air streams, it was possible to adjust the degree of supersaturation, the mass of condensable water vapour and the mixing temperature.

In another work of Heidenreich *et al.*, (2000) in order to demonstrate the degree of supersaturation achieved by simultaneous heat and mass transfer in a packed column some examples of calculated supersaturation profiles are given. The calculations were performed assuming that no particles are present in the system. Thus, the reduction of the supersaturation due to condensational droplet growth is neglected. The degree of supersaturation increases with increasing temperature difference between the gas and the water. Correspondingly, it is possible to enlarge sub-micrometric particles by heterogeneous condensation in packed columns trickled with water which is colder than the gas.

The formation and the behaviour of aerosols formed by heterogeneous nucleation in flue gas cleaning processes have been demonstrated by Gretscher *et al.*, (1999). The experimental work is accompanied by computer simulation with the special software SENECA. These investigations developed a reliable method for the prediction and

characterization of aerosols as well as strategies for the removal of aerosol particles. They are stabilized that the aerosol formation in wet scrubbing processes is present the mechanism of heterogeneous nucleation. The conclusions are that the properties of the particles play a decisive role for the aerosol formation. It is remarkable that such sub-micrometric particles, generated by glowing charcoal and that are not supposed to have a sufficient wettability or any kind of hydrophilicity, serve as condensation nuclei at very low supersaturations of  $S=1.03$ . On the other hand, sub-micrometric environmental particles do not have any effect on the aerosol formation in absorption processes.

More recently (Yan *et al.*, 2008) the heterogeneous condensation has studied to increase the removal efficiency of wet-scrubber of  $PM_{2.5}$  from combustion. In particular an experimental device was set up to investigate the influence of particle initial size distribution, the amount of vapour addition, and the ratio of liquid to gas flow rates on the removal efficiency. The microstructure and major element compositions of fine particles were explored by scanning electron microscopy (SEM) and X-ray photoelectron spectroscopy (XPS). The results show that the physical-chemical properties of fine particles from coal and oil are very different and it has considerable influence on heterogeneous nucleation behaviour. The removal efficiency of  $PM_{2.5}$  of coal combustion is higher than that of oil. Both number and mass removal efficiencies increase with the increase in particle size and additional amount of vapour. The removal efficiency of 81% and 72% can be achieved for coal and oil combustion of fine particles with particle diameters of  $0.4\ \mu m$  at  $0.08\ kg/m^3$  vapour, respectively. Moreover, the collection efficiency can be improved with an appropriate ratio of liquid and gas flow rates. The results show that the heterogeneous condensation as a preconditioning technique can highly promote the removal efficiency in wet-scrubber by 60% and 50% for particles from coal and oil combustion.

A theoretical study of application of heterogeneous condensation derive from a work (Fan *et al.*, 2009) where the vapour nucleation on  $PM_{2.5}$  from MSWI (Municipal Solid Waste Incineration) was modelled combined with the wetting abilities, compositions and surface characteristics of the particles. Nucleation characteristics of the fine particles were numerically studied. In this paper an approach for calculating the characteristics of water vapour nucleation on the  $PM_{2.5}$  from MSWI has been developed. The free energy of embryo formation, the nucleation rate and the critical nucleation saturation under different conditions were calculated, and the corresponding results were obtained. Results show that the free energy barrier of embryo formation is not influenced by the total mass of

soluble salts in the PM<sub>2.5</sub> when the mass fraction of each salt is constant. While the total mass of soluble salts does not change, the free energy barrier changes remarkably with the compositions of the soluble salts in the PM<sub>2.5</sub>. It is also found that the free energy barrier of embryo formation decreases due to the surface roughness of the particle. Simulation results of the nucleation rate and the critical nucleation saturation indicate that both the compositions of the soluble salts and the surface roughness dominate the nucleation capabilities of the PM<sub>2.5</sub> from MSWI. In fact in this study the contact angle is considered a function of roughness and the spatial coordinates (x, y) are introduced

$$\cos \theta(x, y) = \cos[\theta(x, y)_o - \phi(x, y)] \quad (1.4)$$

where  $\theta$  is the local contact angle of the rough surface and  $\Phi$  is the decrease of contact angle due to the surface roughness. For soluble particle, the Kelvin's equation became:

$$S = \frac{P_v}{P^o(T)} = a_w \exp\left[\frac{4\sigma v_w}{R_v T D_k}\right] \quad (1.5)$$

where  $a_w$ ,  $v_w$  and  $\sigma$  are the activity of water, the partial molar volume of water and the surface tension of the solution, respectively. For an exact solution of equation 1.5 it has to be taken into accounts that  $a_w$ ,  $v_w$  and  $\sigma$  are functions of the solute concentration. This study gives the first indications of water vapour nucleation characteristics on the PM<sub>2.5</sub> from MSWI.

Very recently (Yang *et al.*, 2010) a novel process to remove fine particles with high efficiency by heterogeneous condensation in a wet flue gas desulphurisation (WFGD) has been studied. A supersaturated vapour phase, necessary for condensational growth of fine particles, was achieved in the SO<sub>2</sub> absorption zone and at the top of the wet FGD scrubber by adding steam in the gas inlet and above the scrubbing liquid inlet of the scrubber, respectively. The condensational grown droplets were then removed by the scrubbing liquid and a high-efficiency demister. The results show that the effectiveness of the WFGD system for removal of fine particles is related to the SO<sub>2</sub> absorbent adopted. When using CaCO<sub>3</sub> and NH<sub>3</sub>·H<sub>2</sub>O to remove SO<sub>2</sub> from flue gas, the fine particle removal efficiencies are lower than those for Na<sub>2</sub>CO<sub>3</sub> and water, and the morphology and elemental composition of fine particles are changed. This effect can be attributed to the formation of



aerosol particles in the limestone and ammonia-based FGD processes. The performance of the WFGD system for removal of fine particles can be significantly improved for both steam addition cases, for which the removal efficiency increases with increasing amount of added steam.

Authors	Description
Yoshida (1976)	Production of a supersaturated atmosphere by mixing two kinds of saturated air, one of which was humidified by contact with hot water and the other with non-heated water. The degree of supersaturation was controlled by changing their mixing ratio and the combination of their temperatures
Heidenreich (1995)	The influence of supersaturation, mass of condensable water vapour, particle concentration, temperature and initial size distribution on the activation and growth rate of the particles
Heidenreich (2000)	The degree of supersaturation achieved by simultaneous heat and mass transfer in a packed column.
Gretschner (1999).	The formation and the behaviour of aerosols formed by heterogeneous nucleation in flue gas cleaning processes have been demonstrated. These investigations are stabilized that the aerosol formation in wet scrubbing processes is present the mechanism of heterogeneous nucleation.
Fan, 2009	A theoretical study of application of heterogeneous condensation about vapour nucleation on PM <sub>2.5</sub> from MSWI (Municipal Solid Waste Incineration) was modelled combined with the wetting abilities, compositions and surface characteristics of the particles. It is found that the free energy barrier of embryo formation decreases due to the surface roughness of the particle. Simulation results of the nucleation rate and the critical nucleation saturation indicate that both the compositions of the soluble salts and the surface roughness dominate the nucleation capabilities of the PM <sub>2.5</sub> from MSWI.
Yang , 2010	A novel process to remove fine particles with high efficiency by heterogeneous condensation in a wet flue gas desulphurisation (WFGD). The condensational grown droplets were then removed by the scrubbing liquid and a high-efficiency demister. The results show that the effectiveness of the WFGD system for removal of fine particles is related to the SO <sub>2</sub> absorbent adopted. The performance of the WFGD system for removal of fine particles can be significantly improved for both steam addition cases, for which the removal efficiency increases with increasing amount of added steam.

**Table 1.3** - Summary of the main works on the application of heterogeneous condensation

#### 4. Patents

In the following are described the patents which involved the heterogeneous condensation for industrial application in order to remove the particles from gas.

- ✓ Title: Process for cleaning exhaust gases from a combustion engine comprises forming condensation nuclei in the combustion chamber from an additive fed into the chamber, and further processing

Publication date: 09/12/2004

Inventors: Dittler Achim (DE); Kraemer Lutz (DE); Wenninger Guenter (DE)

Abstract: Process for cleaning exhaust gases from a combustion engine comprises forming condensation nuclei in the combustion chamber from an additive fed into the chamber, forming soot particles by heterogeneous condensation of soot and/or soot precursor substances on the condensation nuclei, feeding the soot particles with the exhaust gas to the particle filter, and partially filtering out the soot particles from the exhaust gas

✓ Title: Method and system for purifying a product gas formed from biomass

Publication date: 24/01/2008

Inventors: Van Paasen Sander (NL); Vincent Bern (NL)

Abstract: A method for purifying a combustible gas that is contaminated with contaminants, such as tar and/or dust particle, comprises feeding oil to the contaminated gas. The oil evaporates through contact with the contaminated gas. Said evaporated oil is condensed on a quantity of the contaminants in such a manner that said contaminants grow in size to form particles of increased size in the gas. An electric field between electrodes is applied, by means of which said particles of increased size are electrically charged and removed from the gas. The condensation of the oil takes place at a temperature above the water dew point of the contaminated gas. This water dew point is preferably 50-100 °C, in particular between 50 and 80 °C.

## Chapter 2

### *Theoretical framework*

#### 1. Kelvin's equation

Heterogeneous condensation of a solid insoluble sub-micrometric particle is an energetically unfavourable process because the liquid free surface increase causes a free energy rising (Brin *et al.*, 2007). In order to overcome the energetic barrier and to activate condensational growth, the vapour must be oversaturated. That is, the saturation ratio,  $S$ , defined as a ratio between partial vapour pressure,  $P_v$ , and equilibrium vapour pressure,  $P^o(T)$ , at the flow temperature  $T$ , must exceed unity (Hering *et al.*, 2005 (1); Hering *et al.*, 2005 (2); Fisenko *et al.*, 2007; Fisenko *et al.*, 2006):

$$S = \frac{P_v}{P^o(T)} \quad (2.1)$$

The smaller the particle the higher the supersaturation required to activate condensational growth. This is because the equilibrium vapour pressure over a droplet is higher than over a flat surface as a result of the droplet surface tension (Hering *et al.*, 2005 (1)). This effect is described by the Kelvin's relation (Thompson, 1871; McDonald, 1962), which associates the equilibrium vapour supersaturation to the radius of a droplet composed of that condensed vapour,  $R_C$ , called *critical radius*,

$$R_C = \frac{2\sigma M_w}{\rho_l R_v T \ln S} \quad (2.2)$$

where  $M_w$ ,  $\rho_l$ , and  $\sigma$  are the molecular weight, liquid density, and surface tension of the condensing species, respectively;  $R_v$  is the universal gas constant;  $T$  is the absolute temperature. The radius  $R_C$  is a property of the condensing species and is

equal to the radius of a droplet of the pure condensing species in equilibrium with its vapour at saturation ratio  $S$  and temperature  $T$ .

The above relation describes equilibrium thermodynamically unstable. Growth and evaporation of a droplet of equilibrium size  $r=R_c$  have the same rates. Droplets with a size larger than  $R_c$  will be activated and they grow. The vapour phase is supersaturated for these droplets and thus condensation will take place. Droplets with a size smaller than  $R_c$  will evaporate. The vapour phase is undersaturated for these droplets.

The Kelvin's relation is derived for the case of an ideal condensation of a pure substance to form a single drop of radius  $R_c$  from an energy balance (McDonald, 1962) and its origin is described in the following.

We begin by considering the change of Gibbs free energy ( $G$ ) accompanying the formation of a single drop of pure water of radius  $R_p$  containing  $n$  molecules of the water:

$$\Delta G = G_{droplet} - G_{vapour}$$

Let us assume that the initial total number of molecules of vapour is  $N_t$ ; after condensation the number of vapour molecules remaining is  $N_l = N_t - n$ . Then, if  $g_v$  and  $g_l$  are the Gibbs free energies of a molecule in the vapour and liquid phases, respectively, we have

$$\Delta G = N_l g_v + n g_l + 4\pi R_p^2 \sigma - N_t g_v \quad (2.3)$$

where  $4\pi R_p^2 \sigma$  is the free energy associated with an interface of radius of curvature  $R_p$  and surface tension  $\sigma$ . Because  $n = N_t - N_l$ , we can write

$$\Delta G = n(g_l - g_v) + 4\pi R_p^2 \sigma \quad (2.4)$$

The number of molecules in the drop,  $n$ , and the drop radius,  $R_p$  are related by

$$n = \frac{4\pi R_p^3}{3v_l} \quad (2.5)$$

where  $v_l$  is the volume occupied by a molecule in the liquid phase.

Thus, combining (2.4) and (2.5), we have

$$\Delta G = \frac{4\pi R_p^3}{3v_l} (g_l - g_v) + 4\pi R_p^2 \sigma \quad (2.6)$$

We now need to evaluate the difference in the Gibbs free Energy per molecule of the liquid and vapour phases  $(g_l - g_v)$ .

By definition,  $\Delta G = -SdT + VdP + \sum \mu_i dn_i$ , where  $\mu$  is the chemical potential. Since during condensation of pure gas  $T=\text{const}$ ,  $dn=0$  and  $v_v \gg v_l$ , the free energy variation become

$$dg = -v_v dp \quad (2.7)$$

Assuming that the molecular volume in vapour phase is  $v_v = \frac{RT}{p}$  and integrating we have

$$(g_l - g_v) = -RT \int_{P_A^\circ}^{P_A} \frac{dp}{p} = -RT \ln \frac{P_A}{P_A^\circ} \quad (2.8)$$

where  $P_A^\circ$  is the equilibrium vapour pressure of water over a surface, and  $P_A$  is the partial pressure.

Substituting (2.7) into (2.6) and reminding that  $\frac{P_A}{P_A^\circ} = S$ , we obtain the following expression for the Gibbs free energy variation

$$\Delta G = -\frac{4\pi R_p^3}{3v_l} RT \ln S + 4\pi R_p^2 \sigma \quad (2.9)$$

The radius corresponding to the maximum value of  $\Delta G$  can be calculated by setting

$$\frac{\partial \Delta G}{\partial R_p} = 0 \Rightarrow R_p = R_c \quad (2.10)$$

Solving equation (2.10), we obtain the Kelvin's equation (2.2).

In the case of heterogeneous condensation, the value  $R_c$  represent the minimum size of the solid particle necessary, given  $S$ , to activate the condensation process onto its own surface (i.e. the activation radius). The activation radius and the value of  $R_c$  are equivalent for the specific case of a particle that is readily wetted by the condensing vapour but insoluble in it, but if the particle composed of a material that is unwettable, or for soluble particles, the activation radius is different (Hering *et al.*, 2005 (1)). In fact for particles composed of a material that is not wetted by the condensing vapour, the activation radius will be larger than  $R_c$  by (2.2), dependence on contact angle. For soluble particles, dissolution into the condensate on the particle surface lowers the equilibrium vapour pressure, and the critical radius required for particle growth is smaller, as described by the Köhler curves (1921, 1926). For soluble particle, the Kelvin's equation became:

$$S = \frac{P_v}{P^o(T)} = a_w \exp \left[ \frac{4\sigma v_w}{R_v T D_k} \right] \quad (2.11)$$

where  $a_w$ ,  $v_w$  and  $\sigma$  are the activity of water, the partial molar volume of water and the surface tension of the solution, respectively.

The Figure 2.1 shows as an example the equilibrium vapour pressure at the surface of aqueous sodium chloride droplets as a function of the droplet radius for different solute masses. Such curves were first described by Köhler (1924, 1926). Additionally, the equilibrium curve of a pure water droplet (also called Kelvin curve) is shown in Figure 2.1.

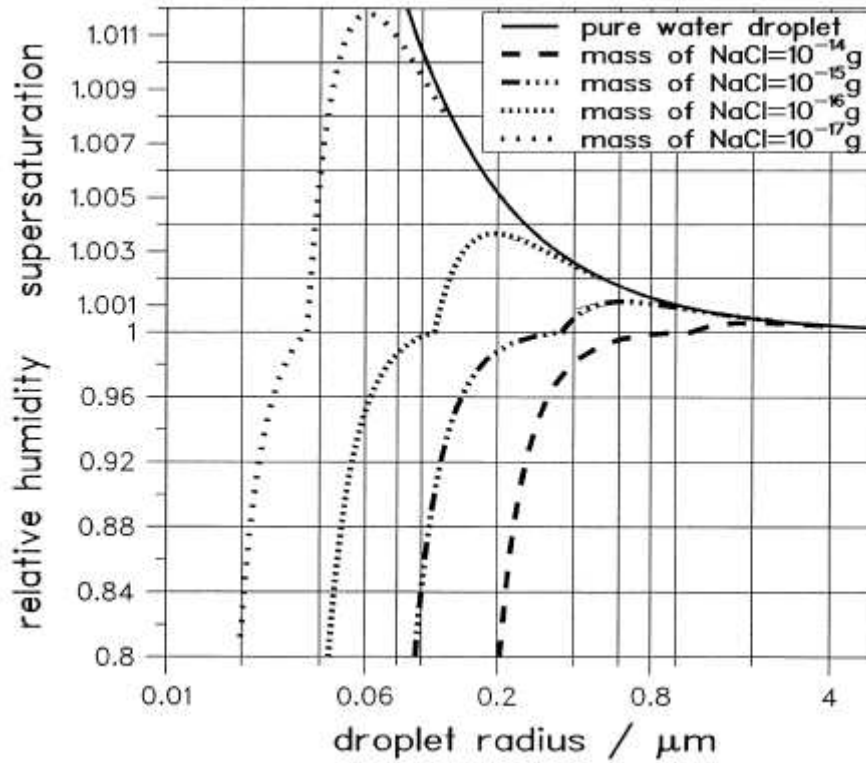


**Figure 2.1** - Equilibrium vapour pressure as a function of droplet size. (Heidenreich *et al.*, 2000)

From (2.2), we can find the critical supersaturation level required for heterogeneous condensation of a solid insoluble particle of radius  $R_c$ .

$$S^* = \exp\left(\frac{2\sigma_s M_W}{\rho_l R_v T R_c}\right) \quad (2.12)$$

The critical value  $S^*$  decreases exponentially with  $R_c$ .

## 2. Nucleation and growth rates

The process of particle enlargement by heterogeneous condensation can be divided into two stages that we can consider in series. Firstly, the particles have to be activated with formation of a liquid embryo on the particle surface, during a so called **nucleation** or *activation* stage (Fletcher, 1958). Then the vapour will condense around the embryo by condensation (**growing** stage) (Smorodin, 2004). This double stage process is illustrated in figure 2.2.

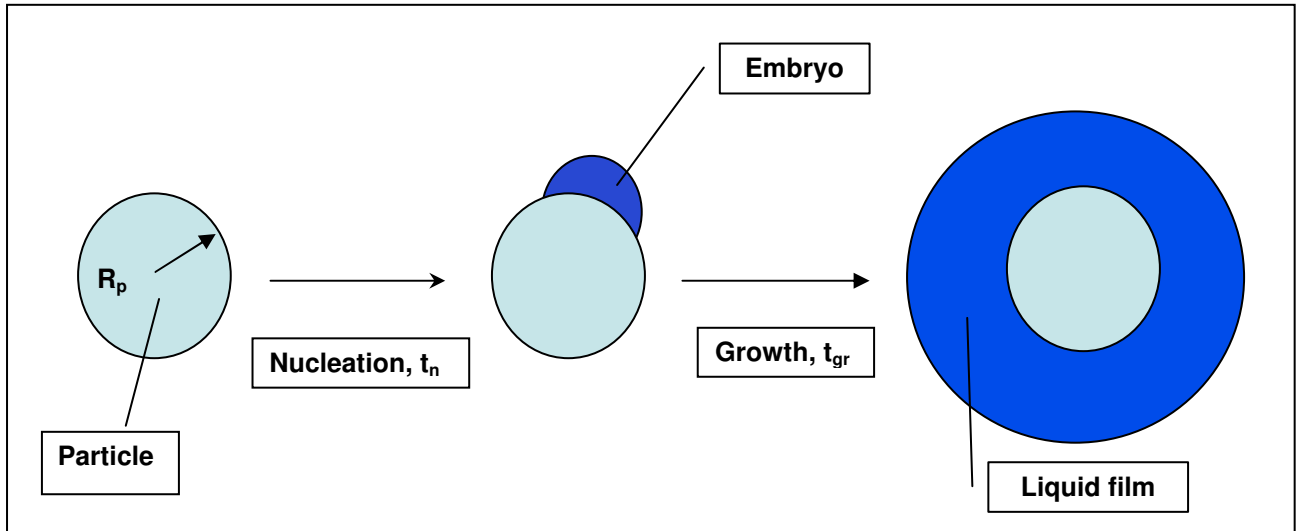


**Figure 2.2** - Scheme of model for nucleation and growth to droplet.  $t_n$  is time of nucleation;  $t_{gr}$  is time of the condensational growth;  $R_p$  is the particles mean radius

In fact the physical and chemical properties of particles (compositions, surface characteristics, and wetting) considerably affect heterogeneous characteristics. For our modelling, we will consider smooth spherical particle of coal.

## 2.1 Nucleation

Nucleation rate represents the number of critical embryos created on a particle surface per second.

Although in the literature many systems have been developed in which the particles are nucleated with water vapour and growth to sizes, complete theoretical models are not yet available. Theoretical models of heterogeneous nucleation for particulates have been limited to spherical particles. Recently there are some studies about interactions between the liquid nucleating embryo and the solid particles that have irregular shapes and complex surfaces (Fan *et al.*, 2009). The model of Fletcher (1958), schematised in Figure 2.3, is the first and more important model for the nucleation rate. More recent models (Lee *et al.*, 2003; Smorodin *et al.*, 2004; Fan *et al.*, 2009) use upgraded version of the Fletcher's model using experimental data to estimated the necessary parameters.

The Fletcher's model, that is with a formation of a stable embryo, called *critical embryo*, from a gas phase on an ideal smooth and homogeneous solid sphere.



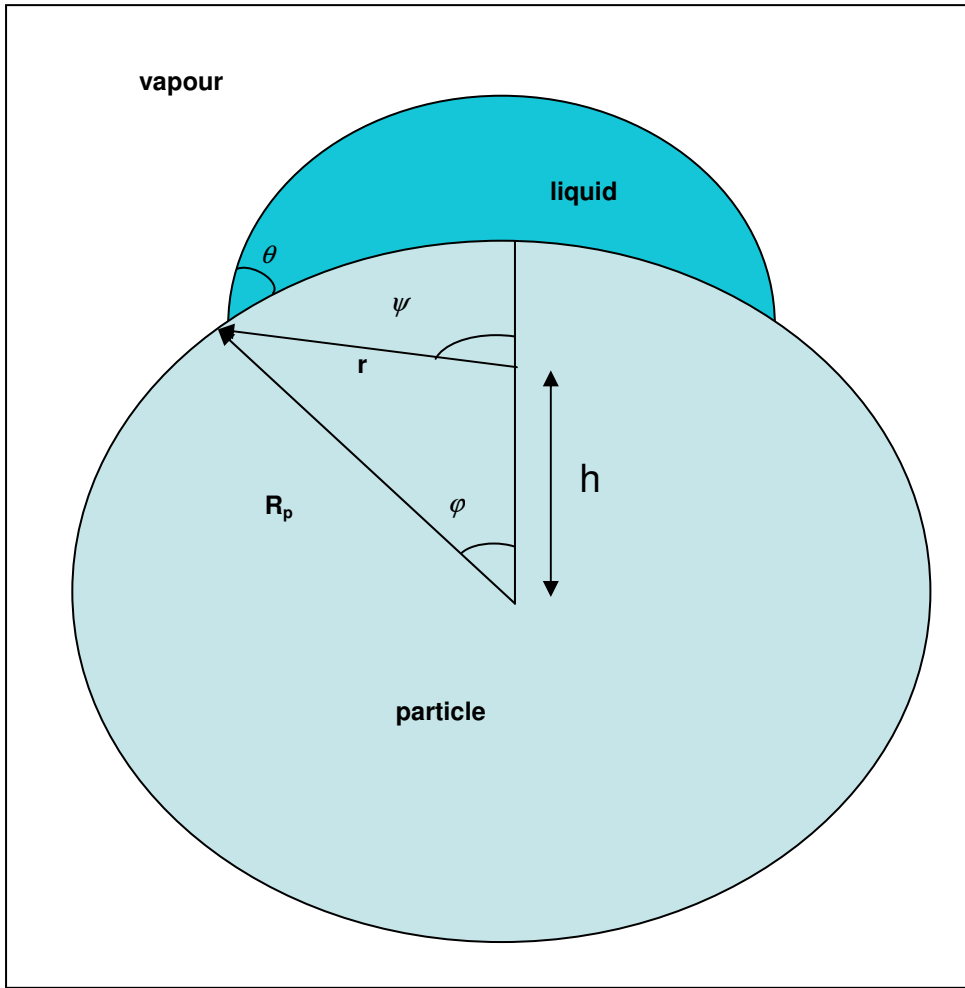


**Figure 2.3** – Schematic representation of a liquid on a spherical particle ( $R_p$ );  $r$ , radius of embryo;  $\theta$ : contact angle

The rate of formation of critical embryo which can then develop into macroscopic droplets is given by the equation (Fletcher, 1958):

$$J = 4\pi K R_p^2 \exp\left(-\frac{\Delta G^*}{k_B T}\right) \quad (2.13)$$

where  $K$  is a kinetic constant and  $\Delta G^*$  is the free energy of formation of a critical embryo. Basically, the nucleation rate increases with supersaturation of the water vapour and size of the particle. The value of  $K$  is somewhat uncertain and depends in detail upon the nucleation situation.

From Fletcher's theory we can say that  $J$  is determined largely by  $\Delta G^*$  then is sufficient to know the value to one or two orders of magnitude of  $K$  (Fletcher, 1958). Fletcher adopts for  $K$  the value of  $10^{25}$  (1/cm<sup>2</sup>sec).

The  $\Delta G^*$  as a result of the critical embryo formation from water vapour under a constant pressure and the temperature can be expressed as

$$\Delta G^* = \frac{8\pi M_w^2 \sigma^3}{3(R_v T \rho_l \ln S)^2} f(m, x) \quad (2.14)$$

where  $M_w$  and  $\rho_l$  are the molar weight and the density of water respectively;  $x$  is a dimensionless factor (defined following) and  $f(m, x)$  is a “geometrical factor” (Fletcher, 1958) which, referring Figure 2.3 , has the following expression:

$$f(m, x) = \left\{ 1 + \left( \frac{1 - mx}{h} \right)^3 + x \left[ 2 - 3 \left( \frac{x - m}{h} \right) + \left( \frac{x - m}{h} \right)^3 \right] + 3mx^2 \left( \frac{x - m}{h} - 1 \right) \right\} \quad (2.15)$$

with

$$h = \sqrt{1 + x^2 - 2mx}$$

and

$$m = \cos \theta = \frac{\sigma_{vs} - \sigma_{ls}}{\sigma_{vl}} \quad (2.16)$$

The (2.16) is the Young's equation (Young, 1805) and is the usual definition of the contact angle  $\theta$  between smooth surface and water, provided  $-1 \leq m \leq 1$  and where:

$\sigma_{vs}$ : surface tension between vapour and solid

$\sigma_{ls}$ : surface tension between liquid and solid

$\sigma_{vl}$ : surface tension between vapour and liquid coinciding with the macroscopic surface tension ( $\sigma$ ) and with surface free energy of the condensing liquid and

In the following figure 2.4 is shown the curve  $f(m, x)$  vs  $x$ , calculated by Fletcher (1958), where  $m$  is shown as a parameter

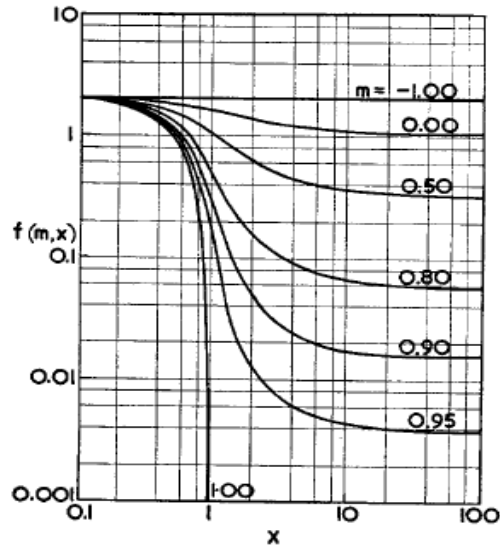


**Figure 2.4** – The geometrical factor  $f(m, x)$  in terms of the ratio  $x = R_p/r^*$ ;  $m$  is shown as a parameter (Fletcher, 1958)

The value of  $m$  depends on the degree of wetting of solid particle. The table 2.1 shown some examples of the degree of wetting based on value of  $\theta$ .

Contact Angle	Degree of Wetting	Strength of:	
		S/L Interactions	L/L Interactions
$\theta = 0^\circ$	perfect wetting	strong	weak
$0^\circ < \theta < 90^\circ$	high wettability	strong	strong
		weak	weak
$90^\circ \leq \theta < 180^\circ$	low wettability	weak	strong
$\theta = 180^\circ$	perfectly non-wetting	weak	strong

**Table 2.1** – Contact angle between water and solid with different wetting degree

In the following the derivation of (2.14) is shown.

Referring to Figure 2.3, the free energy of formation of an embryo of radius  $r$  on a nucleus (particle) of radius  $R_p$  is

$$\Delta G = \Delta G_v V_l + \sigma S_{lg} + m \sigma S_{sl} \quad (2.17)$$

where

- $S_{lg}$  is the surface between phase liquid and gas;
- $S_{sl}$  is the surface between phase solid and liquid;
- $V_l$  is the volume of liquid.

and

$$\Delta G_V = -\frac{k_B T}{v_l} \ln S = -\frac{RT\rho}{M_l} \ln S \quad (2.18)$$

is the free energy difference per unit volume of gas and liquid, and  $k_B$  is the Boltzmann's constant,  $T$  is the temperature and  $v_l$  is the volume occupied by a water molecule in the bulk liquid.

From figure 2.3 we have:

$$S_{lg} = 2\pi r^2 (1 - \cos \psi) \quad (2.19)$$

$$S_{sl} = 2\pi R_p^2 (1 - \cos \varphi) \quad (2.20)$$

$$V_l = \frac{1}{3} \pi r^3 (2 - 3 \cos \psi + \cos^3 \psi) - \frac{1}{3} \pi R_p^3 (2 - 3 \cos \varphi + \cos^3 \varphi) \quad (2.21)$$

and

$$\cos \varphi = \frac{R_p - r \cos \theta}{h} = \frac{R_p - rm}{h} \quad (2.22)$$

$$\cos \psi = \frac{-(r - R_p \cos \theta)}{h} = \frac{-(r - R_p m)}{h}$$

The energy of embryo formation can be identified as the maximum in the curve  $\Delta G$  a function of  $r$  setting:

$$\frac{\partial(\Delta G)}{\partial r} = 0$$

at  $r=r^*$  for fixed  $m=\cos\theta$ , the calculation of the Kelvin's critical radius of the embryo is given by

$$r^* = -\frac{2\sigma}{\Delta G_V} = \frac{2M_l \sigma}{R_V T \rho \ln S} \quad (2.23)$$

Substituting (2.18-2.22) into (2.17) with the (2.23), and

$$x = \frac{R_p}{r^*}$$

we obtain the free energy of formation of the critical embryo (2.14).

In the following Figure 2.5 is shown the curve  $S$  vs  $R_p$ , calculated by Fletcher (1958), where  $m$  is shown as a parameter

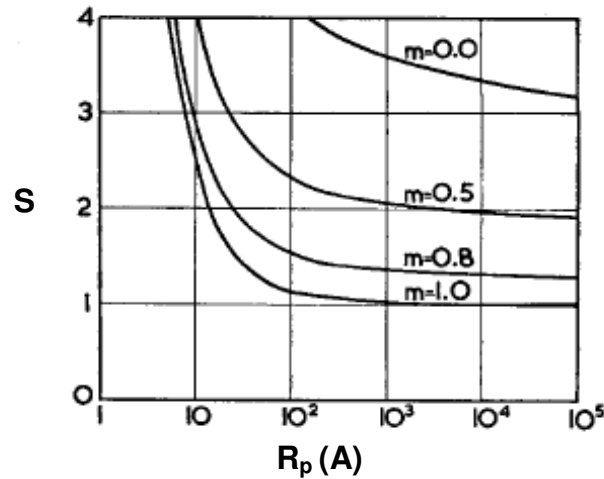


**Figure 2.5** – Supersaturation  $S$  at which condensation occurs on a spherical particle of radius  $R_p$  at temperature 273 K. Parameter is  $m=\cos\theta$  (Fletcher, 1958)

From figure 2.5 it results that for  $m=1$ , the nucleus (particle) is completely wet by water and behaves as a liquid droplet of radius  $R_p$ . For lower values of  $m$ , considerable supersaturation is required for condensation even for quite large particles.

### 2.1.1 Critical saturation

While the Kelvin limit,  $S_{cr}^K$ , represents the minimum value of supersaturation for thermodynamical “existence” of heterogeneous condensation, a *critical saturation* level is required to allow a reliable activation rate. Nucleation rate represents the number of critical embryos created on a particle surface per second. The critical saturation,  $S_{cr}^{hete}$ , is defined as the level of saturation for which the nucleation rate is appreciable, that is the rate (2.13) is one embryo/s. The critical saturation indicates the ambient saturation at which a particle promotes nucleation almost immediately. This it's determined by the particle size, the morphologies, the surfaces of physico-chemical characteristics, and

the vapour property. The creation of a suitable supersaturated vapour is essential to particle enlargement by heterogeneous condensation, and thus the determination of critical saturation is the key step to application of heterogeneous condensation for the removal of the particles.

According to the heterogeneous nucleation theory (Fletcher, 1958; Fan *et al.*, 2009; Lee *et al.*, 2003), the critical supersaturation required to activate an insoluble and spherical particle can be obtained from the equation (2.13), for  $J=1$  (1/s):

$$S_{cr}^{hete} = \exp \left[ \frac{1}{R_v T \rho} \sqrt{\frac{8\pi M_w^2 \sigma^3}{3K_B T \ln(4\pi K R_p^2)}} f(m, x) \right] \quad (2.24)$$

The dependence of the critical nucleation saturation,  $S_{cr}^{hete}$ , on the diameter of the particles are presented from an example in figure 2.8,  $f(m, x)=0.15$  and  $m=0.95$  (high wetting)

We can see that the  $S_{cr}^{hete}$  is strongly affected by the particle size and decreases with the increase with particle size and gas temperature. Thus, steam condensed on the surfaces of bigger particles firstly, and the collection efficiency of fine particles increases with the increase in particle size. Once the particle is activated, water vapour will condensate it immediately and the particle will grow by heterogeneous condensation until supersaturation disappears.

Making a comparison between critical supersaturation (2.24) and supersaturation from Kelvin's equation (2.12), it can be noted that the first provides more severe conditions for the activation of nucleation. How can see from Figure 2.6, to active the nucleation on the same particle size, is necessary a level of supersaturation higher than that described by Kelvin.

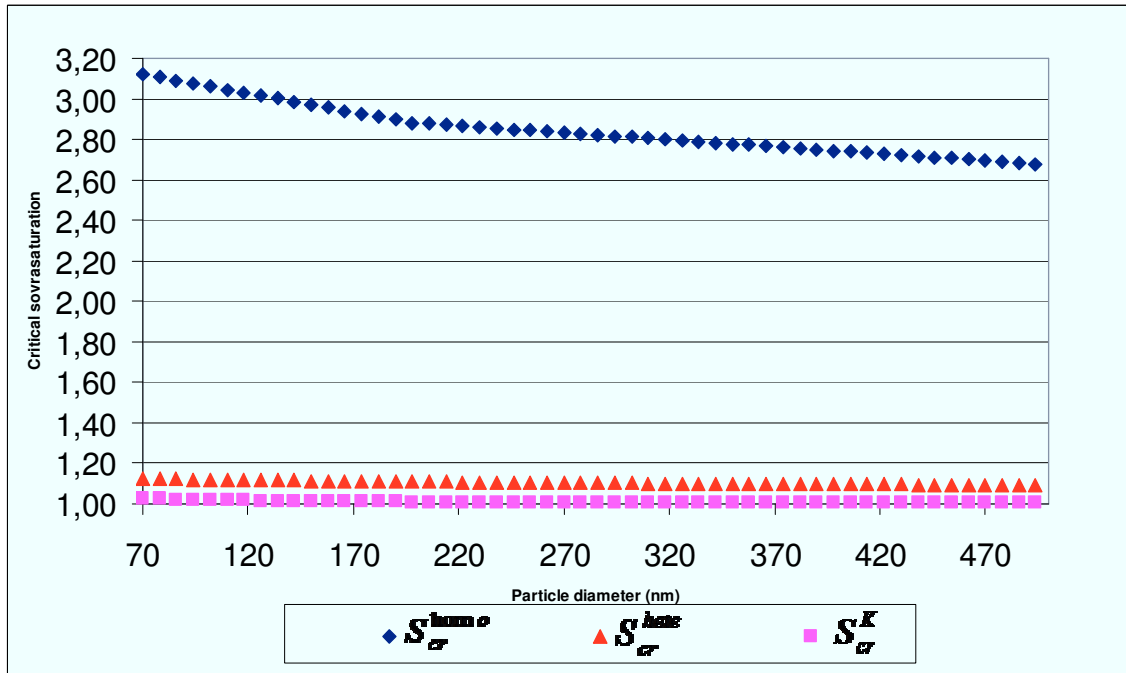


**Figure 2.6** – Comparison between critical supersaturation for homogeneous ( $\diamond S_{cr}^{hom}$ ) and heterogeneous ( $\blacktriangle S_{cr}^{hete}$ ) condensation, and supersaturation by Kelvin's equation ( $\blacksquare S_{cr}^K$ ).

As can be seen the  $S_{cr}^{hete}$  is higher than  $S_{cr}^K$  about 10 %.

We have seen that it's possible to define another mechanism of nucleation, called *homogeneous nucleation*, which take place when the nuclei are generated only of molecules of condensable components. Eventually this leads to a limited use of steam for heterogeneous condensation: the formation of homogeneous drops leads to a decrease of supersaturation and lowers the heterogeneous condensation rate (Figure 2.7).

The critical level of  $S$  for homogeneous condensation represents the highest level of supersaturation for an optimal heterogeneous condensation rate. (Figure 2.6).

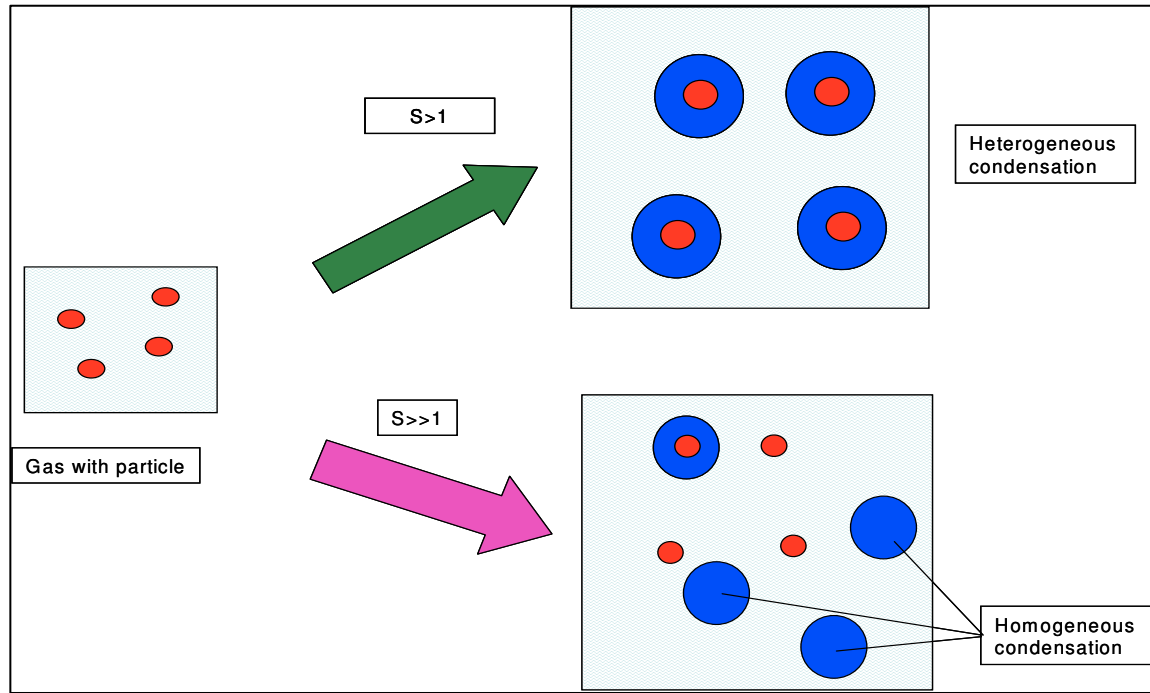


**Figure 2.7** – Comparison between two mechanisms of formation of droplet respect to degree of S

According to classical homogeneous nucleation theory, the rate of new droplets formation per second and cubic meter is given by

$$N = \frac{2}{\rho_l} \sqrt{\frac{m_l \sigma}{2 \pi}} \left( \frac{P^o}{k_B T} \right)^2 \exp \left[ - \frac{\pi \sigma}{3 k T} D^2 \right] \quad (2.25)$$

where

- $k_B$ : Boltzmann's constant
- $m_l$ : the mass of a vapour molecule
- $D$ : nucleus diameter
- $P^o$ : equilibrium pressure of vapour
- $\sigma$ : surface tension of water

A modified expression of nucleation rate, expressed as particle/m<sup>3</sup>\*s, that works relatively well for water condensation has been given by Kashchiev (2006).

$$N = \frac{A_o}{16 B^4} \exp \left( \frac{3 B^{1/3}}{4^{1/3}} \right) (\ln S)^{12m} S \exp \left\{ - \frac{B}{(\ln S)^{2m}} \right\} \quad (2.26)$$

where:



$$A_o = \frac{M}{\rho_l N_A} \left( \frac{2\sigma}{\pi m_o} \right)^{1/2} \left( \frac{P^o}{kT} \right)^2 \quad (2.27)$$

$$B = \frac{16\pi v_l^2 \sigma^3}{3(kT)^3} \quad (2.28)$$

$$v_l(T) = \frac{M}{\rho_l N_A} \quad (2.29)$$

with

- $N_A$ = Avogadro's number
- $m = 1,084$  for water
- $m_o$ = mass of molecule of water
- $P^o$ = equilibrium pressure of vapour
- $v_l$ = volume per molecule of the bulk liquid phase

The Kashchiev's expression highlight the contribution of supersaturation ratio,  $S$ . Then it's possible, in the same way of heterogeneous case, to define a critical value,  $S_{crit}^{hom o}$ , for homogeneous condensation as the value of  $S$  corresponding to nucleation rate (2.22) equal to one nuclei per second. In this way can see that homogeneous nucleation requires high degrees of supersaturation,  $S_{crit}^{hom o} \approx 2-5$  (Heidenreich *et al.*, 1995; Kashchiev, 2006).

The comparison between  $S_{cr}^{hete}$  and  $S_{cr}^{hom o}$ , we plot both curve in the following Figure 2.8.

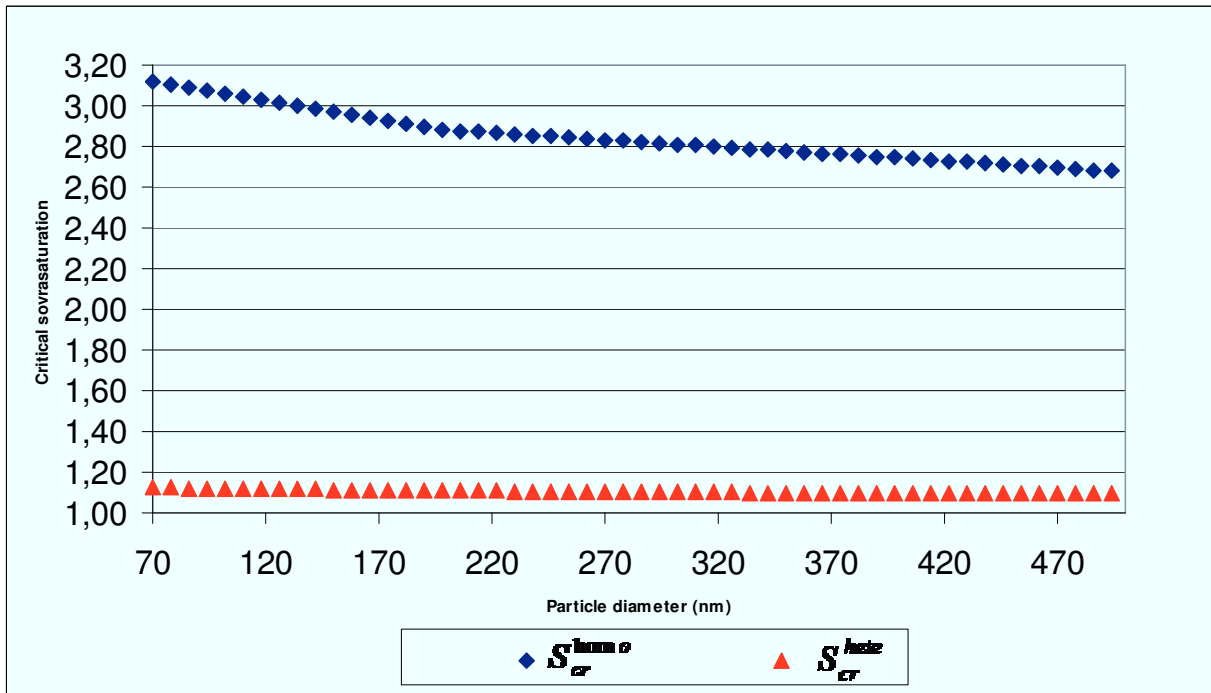


**Figure 2.8** – Comparison between critical supersaturation for homogeneous (♦) and heterogeneous (▲) condensation.

The operating region delimited by the two curves in Figure 2.8 defines the minimum and maximum degree of supersaturation for every particle diameter.

The goal of a good system for heterogeneous condensation of particle of a given diameter  $D_p$  is to operate at supersaturation level as close as possible to  $S_{cr}^{hom}$ .

## 2.2. Growth

After nucleation stage starts the embryo growth by condensation until supersaturation of the gas phase disappears. In this stage is very important the interaction between heat and mass flux between the gas and the droplet. The heat and mass balance on the single particle are performed. Following we'll consider as the particle concentration influences the growth process.

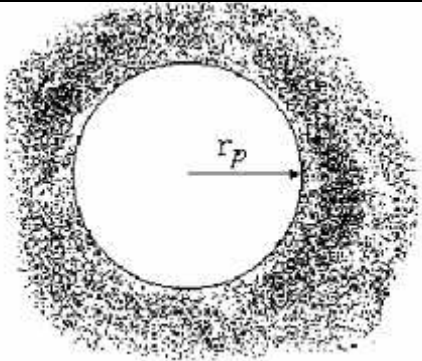
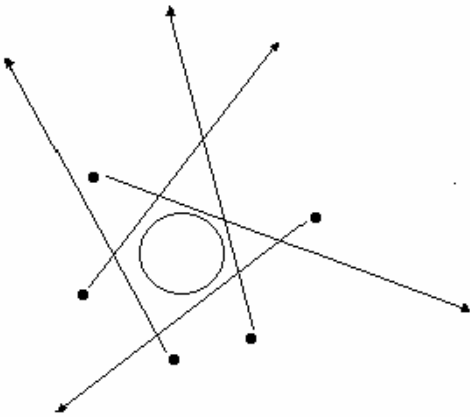
The Knudsen's number is defined as

$$Kn = \frac{l}{d} \quad (2.30)$$

where  $l$  is the free molecular path and  $d$  is the particle diameter.

The mean free path is the average distance a gas molecule travels in a straight line between two consecutive collisions. Based on the value of Knudsen's number, there are two limiting cases and a transition to the type of interaction of particles with the fluid as described in the following and as shown in figure.

- the continuous regime with  $Kn \ll 1$ , where the particle is immersed in a continuous fluid, and everything goes back to the motion of an object in a fluid;
- the transition regime, with  $Kn \sim 1$
- the molecular regime with  $Kn \gg 1$ , where the particle behaves like a molecule of gas and it "sees" an area occupied by molecules of discrete and continuous fluid.

	<b>Continuum regime <math>Kn \ll 1</math></b>
	<b>Molecular regime <math>Kn \gg 1</math></b>

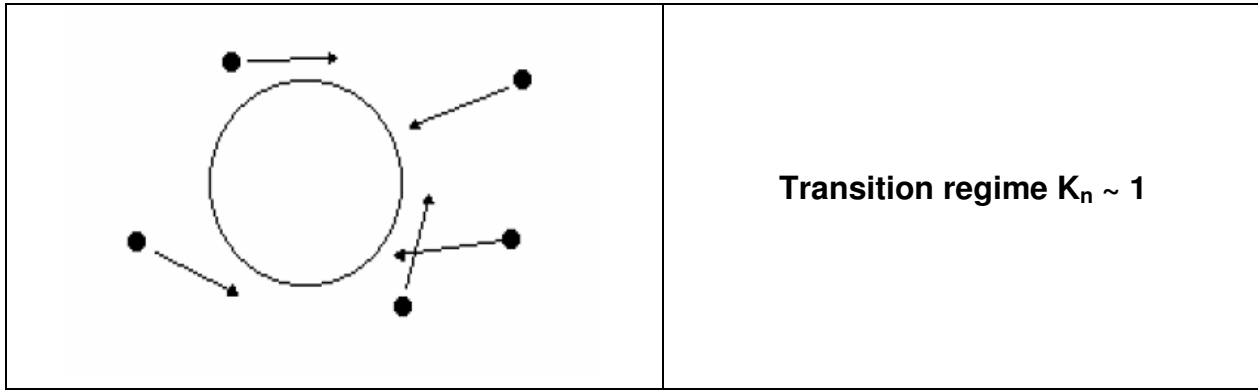


**Figure 2.9** - Scheme of regime with indication of Knudsen number

## 2.2.1 Heat and Mass balance on the single droplet

For our calculation all the properties are considered constant and independent by temperature and composition, and a system air-vapour is considered.

### 2.2.1.1. Heat balance in continuum regime ( $kn \ll 1$ )

For the determination of the droplet temperature an equation can be derived from the heat balance of the droplet. In the following it is assumed that the droplet has a uniform temperature,  $T_d$ , i.e. there is no internal temperature profile in the drops. The heat balance of the droplet is given by:

Change of the amount of droplet heat	=	Heat flux to the droplet	-	Heat flux from the droplet
--------------------------------------	---	--------------------------	---	----------------------------

The heat change of the droplet can be caused by a change of the droplet temperature or a change of the droplet mass. The difference between the heat flux to the droplet and from the droplet is equivalent to the total heat flux to the droplet, which can be defined by the complete heat transport equation. The heat balance written as equation is

$$cm_d \frac{dT_d}{dt} + h_l I_c = Q \quad (2.31)$$

where  $Q$  is the total heat flux and  $I_c$  is the mass flux to the droplet; and  $h_l$ ,  $c$ ,  $m_d$  are the specific enthalpy of the liquid, the specific heat capacity and the mass of the droplet respectively.

Assuming that the heat may be transported by conduction and by diffusion of condensing and that the Dufour effect is neglected, i.e. the diffusion factor has small value ( $\alpha < 0.3$ ) (Heidenreich, 1994).

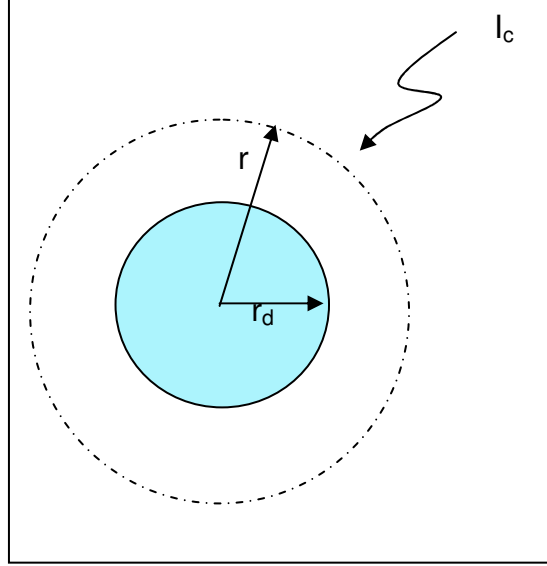


**Figure 2.10** – System for the analysis of mass and heat balance

The heat flux from the gas to the droplet is:

$$q = -\lambda \frac{\partial T}{\partial r} + nhv \quad (2.32)$$

where  $\lambda$  is the thermal conductivity,  $n$  the vapour number of molecules,  $v$  the average velocity of condensing vapour molecules and  $h$  the enthalpy of vapour.

The total mass flux density of the vapour molecules to droplet is given by

$$\dot{j}_v = vnm \quad (2.33)$$

where  $m$  is the mass of a molecule of vapour. Then, from (2.33) we have:

$$vn = \frac{\dot{j}_v}{m} \quad (2.34)$$

The (2.32) can be rewritten as

$$q = -\lambda \frac{\partial T}{\partial r} + j_v \frac{h}{m} = -\lambda \frac{\partial T}{\partial r} + j_v h_v \quad (2.35)$$

The term  $(h/m)$  is the specific enthalpy of vapour,  $h_v$ .

The droplet growth is not a stationary process, but as shown by Fuchs (1959), the growth can be considered as quasi-stationary. Then the (2.31) can be written as that the heat flux is equal to the liquid evaporation from the droplet:

$$h_l I_c = Q \quad (2.36)$$

In a spherically symmetric geometry the heat flux at steady-state is

$$Q = 4\pi r^2 q = \text{const} \quad (2.37)$$

And the mass flux

$$I_c = 4\pi r^2 j_v = \text{const} \quad (2.38)$$

Then the total heat flux to the droplet can be written:

$$h_l I_c = -4\pi r^2 \lambda \frac{dT}{dr} + I_c h_v \quad (2.39)$$

where  $h_l$  is the specific enthalpy of water. From (2.32) we have

$$\frac{dT}{dr} = -\frac{I_c (h_l - h_v)}{4\pi r^2 \lambda} \quad (2.40)$$

With the separation of variables we have:

$$dT = -\frac{I_c (h_l - h_v)}{4\pi r^2 \lambda} dr \quad (2.41)$$

Integrating the first member of (2.34) between  $T_d$  and  $T_\infty$ , temperature at infinite radius,  $r_\infty$ , and between  $r_d$ , the radius of droplet, and  $r_\infty$ , the right member, we have:

$$\int_{T_\infty}^{T_d} dT = \int_{r_\infty}^{r_d} -\frac{I_c (h_l - h_v)}{4\pi r^2 \lambda} dr$$

then

$$(T_d - T_\infty) = -\frac{I_c}{4\pi\lambda} (h_l - h_v) \left[ -\frac{1}{r} \right]_{r_\infty}^{r_d} = \frac{I_c}{4\pi\lambda} (h_l - h_v) \frac{1}{r_d} \quad (2.42)$$

where  $(1/r_\infty)$  is set equal to zero.

The difference  $(h_v - h_l)$  in (2.35) is equal to specific latent heat of condensation,  $L$ .

Then, the (2.35) can be rewritten as:

$$T_d = T_\infty - \frac{I_c L}{4\pi\lambda r_d} \quad (2.43)$$

Which is the solution given by Fuchs (1959). It was shown by numerical analyses (Heidenreich, 1994) that for practical calculations a rigorous consideration is not required, because the influence of neglected terms is smaller than 1%.

The latent heat of condensation released must be transported away since the temperature of the droplet, and accordingly the vapour pressure at the droplet surface, would increase continuously causing condensational droplet growth to stop. The temperature of the droplet, in the condensation conditions, must be greater than temperature of the surrounding atmosphere so that the heat released can be carried off (Figure 2.11).

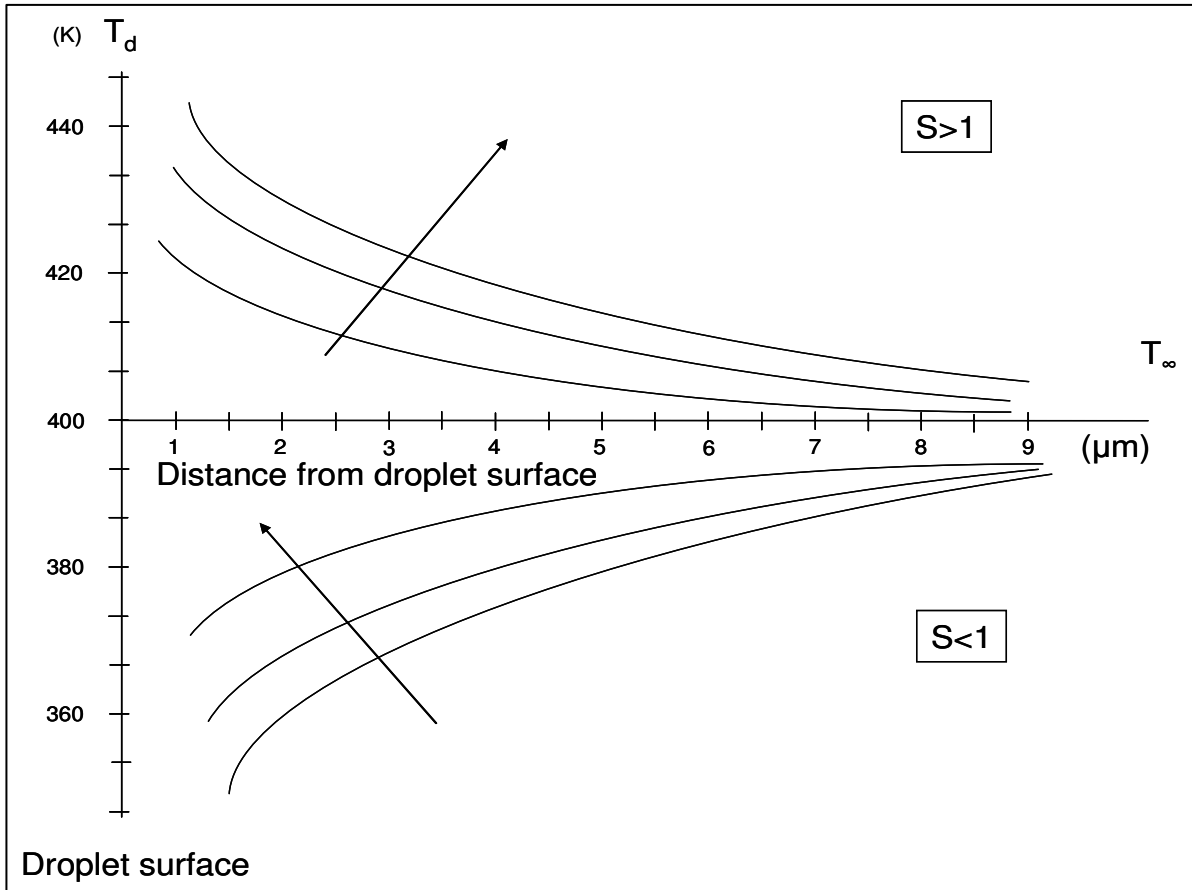


**Figure 2.11** – Temperature profile surround droplet depending on the S value (Williams, 1995)

### 2.2.1.2. Mass balance in continuum regime ( $kn \ll 1$ )

The mass balance between a gas and a single droplet for in a binary mixture and in the continuum regime ( $kn \ll 1$ ) only takes in account the diffusion mass flux. The Stefan-flow is neglected because is shown that the influence of the Stefan-flow on the droplet growth is about 0.5% (Heidenreich, 1994). The flux caused by temperature gradient (Soret effect) is also neglected because is shown that for value of the thermal diffusion factor,  $\alpha$ , close to zero ( $\alpha < -0.3$ ) the influence of thermal diffusivity on the droplet growth is smaller than 1%. Finally the gas velocity surrounding droplet is neglected (Heidenreich, 1994).

The mass flux at steady-state is given by equation (2.31). With the above hypothesis it results:

$$J_v = -D \frac{\partial \rho}{\partial r} \quad (2.44)$$



where  $D$  is the diffusion coefficient and  $p$  the vapour density.

Considering a perfect gas phase, it results

$$J_v = -D \frac{\partial \rho}{\partial r} = -\frac{DM}{RT} \frac{\partial P_v}{\partial r} \quad (2.45)$$

Then the mass flux to the droplet is given by:

$$I_c = -4\pi r^2 J_v = 4\pi r^2 \frac{DM}{RT} \frac{\partial P_v}{\partial r} \quad (2.46)$$

After separation of variables and integrating from infinite to droplet surface:

$$I_c \int_{r_\infty}^{r_d} \frac{1}{r^2} dr = -4\pi \frac{DM}{RT} \int_{P_{v,\infty}}^{P_{v,a}} dP_v \quad (2.47)$$

Thus

$$I_c \left[ -\frac{1}{r_d} \right]_{r_\infty}^{r_d} = -4\pi \frac{DM}{RT} (P_{v,a} - P_{v,\infty}) \quad (2.48)$$

setting  $(1/r_\infty)$  equal to zero, we have:

$$I_c = \frac{4\pi r_d MD}{RT} (P_{v,a} - P_{v,\infty}) \quad (2.49)$$

which is the equation yields by Maxwell (Fuchs, 1959). During condensation  $P_{v,\infty} > P_{v,a}$  then  $I_c$  results negative; for this some authors (Heidenreich, 1994, 1995) put a minus sign on the right-hand side of equation (2.49).

From the definition of  $I_c$  as:

$$I_c = -\frac{dm}{dt} = -4\pi \rho_l r_d^2 \frac{dr_d}{dt} \quad (2.50)$$

where  $dm/dt$  is the change of the droplet mass and  $\rho_l$  is the density of the liquid.

From (2.49) and (2.50) we have:

$$-4\pi\rho_l r_d^2 \frac{dr_d}{dt} = \frac{4\pi r_d MD}{RT} (P_{v,a} - P_{v,\infty}) \quad (2.51)$$

After separation of variables and integrating from initial radius,  $r_{d,o}$ , to final radius,  $r_{d,f}$ , of droplet and from initial time  $t_0=0$  to final time  $t_f=t$ :

$$\int_{r_{d,o}}^{r_{d,f}} r_d dr_d = -\frac{MD}{\rho_l RT} (P_{v,a} - P_{v,\infty}) \int_{t_0}^{t_f} dt \quad (2.52)$$

thus

$$\frac{1}{2} [r_d^2]_{r_{d,o}}^{r_{d,f}} = -\frac{MD}{\rho_l RT} (p_{v,a} - p_{v,\infty}) [t]_0^t \quad (2.53)$$

Then can rewritten as:

$$r_{d,f} = \sqrt{r_{d,o}^2 - \frac{2MD}{\rho_l RT} (P_{v,a} - P_{v,\infty}) t} \quad (2.54)$$

In the continuum regime the vapour pressure at the droplet surface,  $p_{v,a}$ , is assumed to be in equilibrium with the vapour phase. In the case of a pure water droplet (homogeneous condensation) or a droplet with an insoluble nucleus (heterogeneous condensation), the vapour pressure at the droplet surface is given by the Kelvin equation:

$$p_{v,a} = p^\circ(T_d) \exp\left(\frac{2\sigma M}{RT_d \rho_l r_d}\right) \quad (2.55)$$

Substituting (2.55) into (2.54), the final droplet radius is:

$$r_{d,f} = \sqrt{r_{d,o}^2 + \frac{2MD}{\rho_l RT} \left( P_v - P^o(T_d) \exp\left( \frac{2\sigma M}{RT_d \rho_l r_{d,o}} \right) \right) t} \quad (2.56)$$

The value of  $r_{d,f}$  depends on temperature, vapour partial pressure and time.

In terms of diameter we have:

$$D_{d,f} = \sqrt{D_{d,o}^2 + \frac{8MD}{\rho_l RT} \left( P_v - P^o(T_d) \exp\left( \frac{4\sigma M}{RT_d \rho_l D_{d,o}} \right) \right) t} \quad (2.57)$$

The dependence of the growth rate and the final diameter on the temperature is shown in following figure.

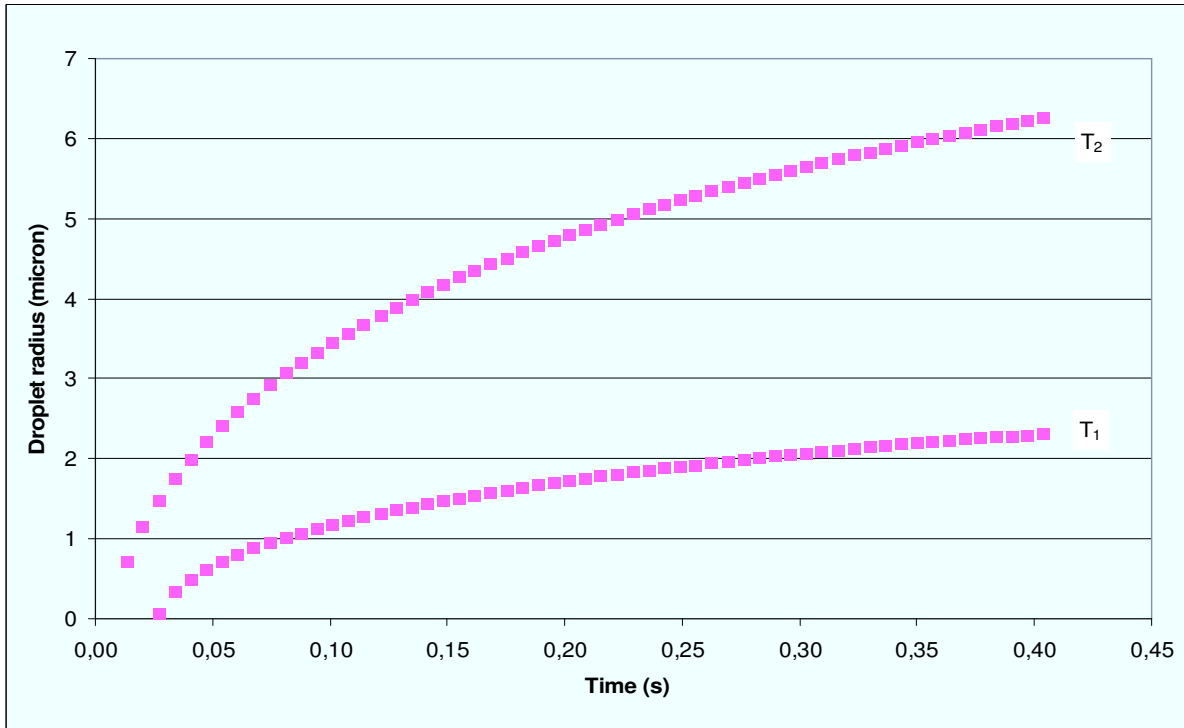


**Figure 2.12** – Influence of temperature on the final droplet radius, with  $T_2 = 323$  K and  $T_1 = 313$  K

As can be seen from Figure 2.12, the droplets grow after a short time. The rate of droplet growth depends on the droplet size. Smaller droplets have a higher growth rate than larger droplets. Thus, theoretically, the droplet aerosol should grow to a system containing nearly monodisperse droplets (Heidenreich, 1994; 1995).

The droplet growth is also influenced by initial supersaturation. As the supersaturation increases, both the growth rate and final diameter increase. With adiabatic growth, the differences between the final diameters are smaller than in the case of isothermal

growth. In the case of adiabatic growth, the dependence on the temperature is smaller and usually negligible (Heidenreich, 1995).

### 2.2.1.3. Rigorous consideration on the mass balance in continuum regime

On the basis of the general diffusion equation for a binary mixture a rigorous for mass flux expression, was given by (Heidenreich, 1994):

$$I_c = -4\pi r^2 \frac{MD}{RT \left(1 - \frac{p_v}{P}\right)} \left[ \frac{\partial p_v}{\partial r} + \frac{\alpha p_v p_g}{p} \frac{\partial \ln T}{\partial r} \right] \quad (2.58)$$

Where  $p$  is the total pressure,  $p_g$  is the partial pressure of air,  $T$  is the gas temperature,  $\alpha$  is the thermal diffusion factor.

The equation (2.58) takes in account for the mass flux caused by concentration and temperature gradient (Soret effect) and for the Stefan-flow. Under the assumptions of the standard solution method, a temperature profile derived from Fourier's law of heat conduction and a vapour pressure profile derived from Fick's law of diffusion were combined. Thus an expression for the relation between the gradient  $\frac{\partial T}{\partial r}$  and  $\frac{\partial p_v}{\partial r}$  can

be found as:

$$\frac{\partial T}{\partial r} = \frac{T_d - T_\infty}{p_{v,a} - p_{v,\infty}} \left( \frac{\partial p_v}{\partial r} \right) \quad (2.59)$$

Where  $p_{v,a}$  is the partial pressure of vapour at the droplet surface, and  $p_{v,\infty}$  the partial pressure of vapour far from droplet surface.

Combination of (2.58) and (2.59) yields

$$I_c = -\frac{4\pi r^2 MD}{RT \left(1 - \frac{p_v}{p}\right)} \left[ 1 + \frac{\alpha p_v (p - p_v)}{pT} \frac{T_d - T_\infty}{p_{v,a} - p_{v,\infty}} \right] \frac{\partial p_v}{\partial r} \quad (2.60)$$

After separation of variable and integration from infinity to the droplet surface at steady-state, the mass flux to the droplet is:

$$I_c = -\frac{4\pi r_d MDp}{RT} \left[ \ln \frac{1 - \frac{p_{v,a}}{p}}{1 - \frac{p_{v,\infty}}{p}} - \frac{\alpha}{2} \frac{T_d - T_\infty}{T} \frac{p_{v,a} + p_{v,\infty}}{p} \right] \quad (2.61)$$

This equation reports the rigorous expression for the droplet mass balance, but Heidenreich (1994; 1995) showed that if  $\alpha$  is assumed to be zero and the Stefan and Soret flows should be reliably neglected, coming back to the equation (2.49)

#### 2.2.1.4. Heat and mass balance in the transition regime ( $Kn \sim 1$ )

In the transition regime ( $Kn \sim 1$ ), where the size of the droplet is of the order of the mean free path of the surrounding medium, a jump in vapour pressure and also in temperature occurs at the droplet surface. This requires the introduction of correction factor function of  $Kn$ ,  $f(Kn)$ , to describe both the fluid dynamic and the transport phenomena between the gas and the particle. Commonly, the Fuchs-Sutugin (1971) formula is used:

$$f(K_n) = \frac{1 + K_n}{1 + 1.71K_n + 1.33K_n^2} \quad (2.62)$$

Then the mass flux, from (2.49) became the classical approach (Fuchs and Sutugin, 1971) propose to include the factor  $f(Kn)$  directly in the equations for the mass (2.49) and temperature (2.43) evolution:

$$I = I_c f(K_n) = \frac{4\pi r_d MD}{RT} (p_{v,a} - p_{v,\infty}) f(K_n) \quad (2.63)$$

$$T_d = T_\infty - \frac{I_c L}{4\pi \lambda r_d f(K_n)} \quad (2.64)$$

### 2.3. Supersaturation region

We have seen that droplet growth by condensation requires a supersaturated vapour phase. A vapour phase is supersaturated if the vapour pressure in the system is higher than the corresponding saturation vapour pressure, which is a function of the temperature of the system. In the following table a scheme of conditions for nucleation and growth is presented.

Supersaturation	Nucleation	Growth
$S = \frac{P_v}{P_v^o(T)} > 1$ <p> <math>P_v</math>: partial pressure  <math>P_v^o</math>: equilibrium partial pressure         </p>	<p>For appreciable nucleation</p> $S > S_{crit}$ <p>where <math>S_{crit}</math>: critical saturation depending on nucleation mechanism</p> <p>Homogeneous nucleation:</p> $S_{crit} \approx 2 - 5$ <p>Heterogeneous nucleation:</p> $S_{crit} \approx 1 - 1.8$	<p>Differences between adiabatic and isothermal conditions.</p> <p>Final diameter depending on temperature and supersaturation,</p> <p>Growth rate depending on droplet size, temperature and supersaturation</p>

**Table 2.2** – Scheme of conditions for nucleation and growth

Generally, supersaturation can be achieved in different ways, for example by mixing saturated gases of different temperature, by cooling, by chemical reactions and by simultaneous heat and mass transfer at a liquid surface. In all these cases, supersaturation is caused either by a reduction of the temperature of the system or by an increase in the vapour pressure in the system. The simultaneous heat and mass transfer at a liquid surface is a process to achieve supersaturation economically, also on a technical scale.

In this study a cylindrical reactor with an evaporation liquid film is considered. This system is known as growth tube and is similar to condensation particle counters. The elevated temperature of the wetted walls produces a high concentration of water vapour, while the “cooling” arises from the entering sample gas flow. In this scenario

the diffusion of water vapour from the walls to the centreline is faster than the warming of the flow.

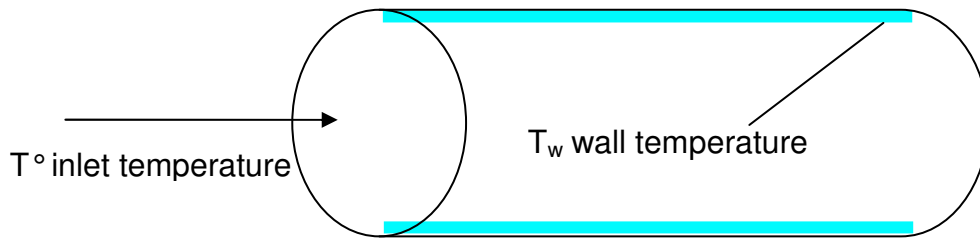


**Figure 2.13** – Scheme of growth tube

### 2.3.1 Heat and mass balance in growth tube

The gas temperature and the vapour partial pressure profiles in the gas and, then, the supersaturation at any point in a growth tube are described by a energy and mass balances (Hering, 2005 (1 - 2)).

In all the following we assume that:

- ✓ the gas phase is very diluted with air, then the presence of particles not influence the heat and mass balance;
- ✓ the properties of the fluid, evaluated at a mean temperature, are considered constants and assimilated to the air;
- ✓ the axial thermal diffusion and other second-order effects are neglected;
- ✓ a plug flow with fully developed parabolic flow profile;
- ✓ uniformity of entering temperature and partial pressure of vapour profile;
- ✓ uniformity of the temperature of the water film inside tube wall.

Besides the temperature and the vapour partial pressure profiles throughout the condensing region are modelled considering the axial symmetry of the growth tube and by using a two-dimensional model for convective and diffusive heat and mass transfer. These problems take the form of the classic Graetz problem (1883).

The equations for temperature, vapour partial pressure and supersaturation are reported in the following.

### 2.3.1.1 Temperature profile

For the cylindrical geometry, the values of the gas temperature,  $T$ , throughout the growth tube are obtained by solving the energy balance throughout the tube:

$$2U \left[ 1 - \left( \frac{r}{R} \right)^2 \right] \frac{\partial T}{\partial z} = \alpha_t \frac{1}{r} \frac{\partial}{\partial r} \left( r \frac{\partial T}{\partial r} \right) \quad (2.65)$$

Where  $r$  and  $z$  are radial and axial coordinates respectively;  $R$  is tube radius;  $U$  is average flow velocity; and  $\alpha_t$  is thermal diffusivity of the flowing gas.

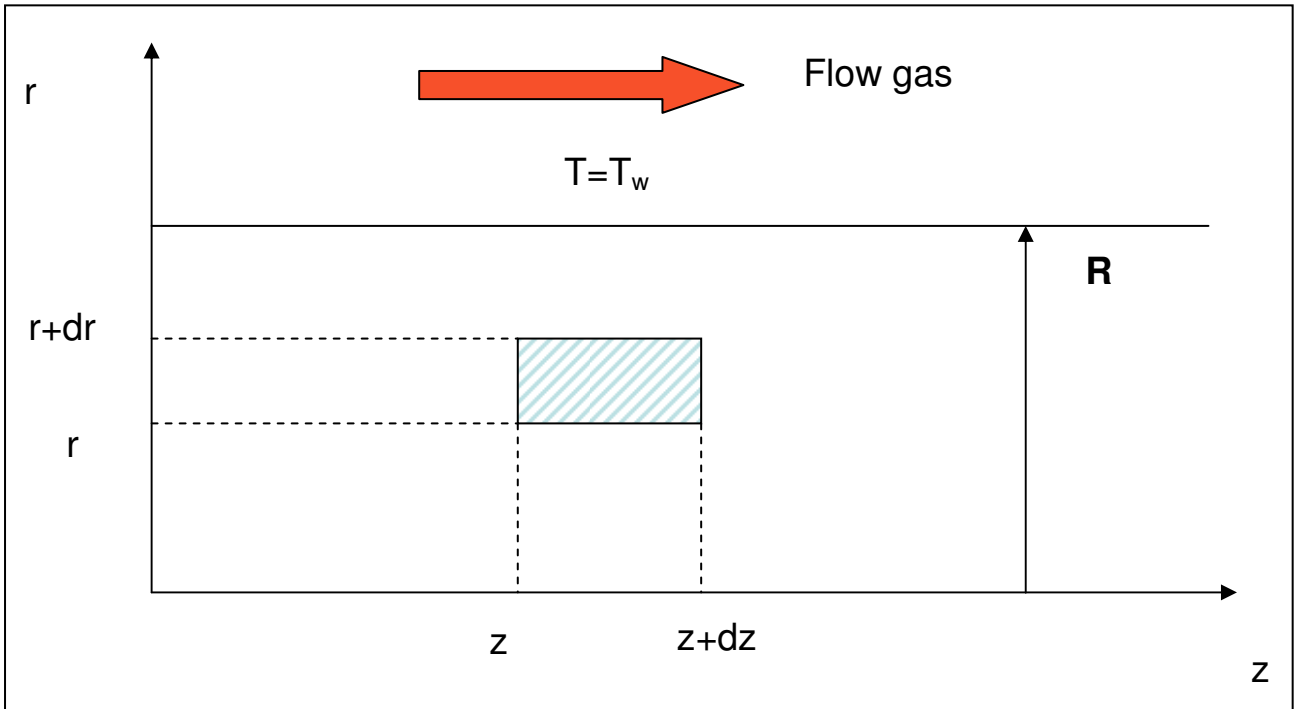


**Figure 2.14** - Ring-shaped control volume for the derivation of the energy equation for laminar flow through a tube;  $R$  is tube radius,  $r$  and  $z$  are the cylindrical coordinate

The temperature profile is obtained from an energy balance on a ring-shaped control volume, as sketched in Figure 2.14

$$u(r)\rho C_P (T_z - T_{z+dz}) 2\pi r dr + [(r + dr)q_{r+dr} - rq_r] 2\pi dz = 0 \quad (2.66)$$

where

$$q = -k \frac{\partial T}{\partial r} \text{ is the thermal flux by conduction, with } k \text{ the thermal conductivity;}$$



$\alpha_t = \frac{k}{\rho C_p}$  is the thermal diffusivity, with  $\rho$  the density and  $C_p$  the specific heat.

A fully developed parabolic flow profile and uniform entering temperature ( $T_o$ ) and wall temperature ( $T_w$ ) are assumed. Fluid properties are evaluated at a mean temperature and considered constants over the domain. Axial thermal diffusion (conduction) and radial thermal convection are ignored.

The parabolic velocity profile for the velocity field gas:

$$u(r) = 2U \left[ 1 - \left( \frac{r}{R} \right)^2 \right] \quad (2.67)$$

The equation (2.66) can be rewritten as:

$$u(r) \rho C_p \frac{(T_z - T_{z+dz}) 2\pi r dr}{2\pi r dr dz} + k \frac{\frac{\partial T}{\partial r} 2\pi r dz \Big|_r - \frac{\partial T}{\partial r} 2\pi (r+dr) dz \Big|_{r+dr}}{2\pi r dr dz} = 0$$

If we put  $r + dr \cong r$  then we have the (2.65).

Introducing dimensionless coordinates  $\mathbf{x}=\mathbf{r}/\mathbf{R}$  and  $\mathbf{y}=\mathbf{z}/\mathbf{R}$ , and defining the parameter  $f_t$  as ,

$$f_T = \frac{T - T_w}{T_o - T_w} \quad (2.68)$$

with some rearrangement we have

$$2U [1 - x^2] \frac{\partial f_T}{\partial y} = \alpha_t \frac{1}{xR} \frac{\partial}{\partial x} \left( x \frac{\partial f_T}{\partial x} \right) \quad (2.69)$$

with the boundary conditions

$$\begin{cases} z=0 & y=0 & f_T=1 \\ r=0 & x=0 & \frac{\partial f_T}{\partial r}=0 \\ r=R & x=1 & f_T=0 \end{cases} \quad (2.70)$$

The (2.69) is solved by separation of variables (Eckert *et al.*, 1972), then we put a function for the temperature T like the product of a function of x and y:

$$f_T = \phi(x)\varphi(y)$$

Introducing this expression into equation (2.69) we have:

$$2UR [1 - x^2] \frac{\partial \phi(x)\varphi(y)}{\partial y} = \alpha_t \frac{1}{xR} \frac{\partial}{\partial x} \left( x \frac{\partial \phi(x)\varphi(y)}{\partial x} \right) \quad (2.71)$$

After separation of functions we have

$$\frac{2UR}{\alpha_t} \frac{1}{\varphi(y)} \frac{d\varphi(y)}{dy} = \frac{1}{x(1-x^2)\phi(x)} \frac{d}{dx} \left( x \frac{d\phi(x)}{dx} \right) \quad (2.72)$$

Equation (2.72) be satisfied only when both sides of the equation are equal to a constant. Denoting this constant by  $(-\beta_i^2)$ , the equation can now be separated into two total differential equations:

$$\frac{2UR}{\alpha_t} \frac{1}{\varphi(y)} \frac{d\varphi(y)}{dy} = -\beta_i^2 \quad (2.73)$$

$$\frac{1}{x} \frac{d}{dx} \left( x \frac{d\phi(x)}{dx} \right) + \beta_i^2 (1-x^2)\phi(x) = 0 \quad (2.74)$$

Integration of equation (2.73) results in

$$\varphi = C_i \exp \left( -\beta_i^2 \frac{\alpha_t}{2UR} y \right) \quad (2.75)$$

This expression describes the variation of the variables field in the  $z$  direction, and for physical meaning obviously it requires the exponent to be negative.

The (2.74) was integrated numerically by Nusselt (1910), with the boundary conditions

at  $x=0$   $\frac{d\phi(x)}{dx} = 0$  and  $\phi = 1$ .

The general solution, expressed in the form of the standard series solution, is

$$f_T = \sum C_i \exp\left(-\beta_i^2 \frac{\alpha_t}{2UR} \frac{z}{R}\right) \phi_i \frac{r}{R} \quad (2.76)$$

In figure 2.15 are shown the first three functions  $\phi_i$  (Eckert *et al.*, 1972).

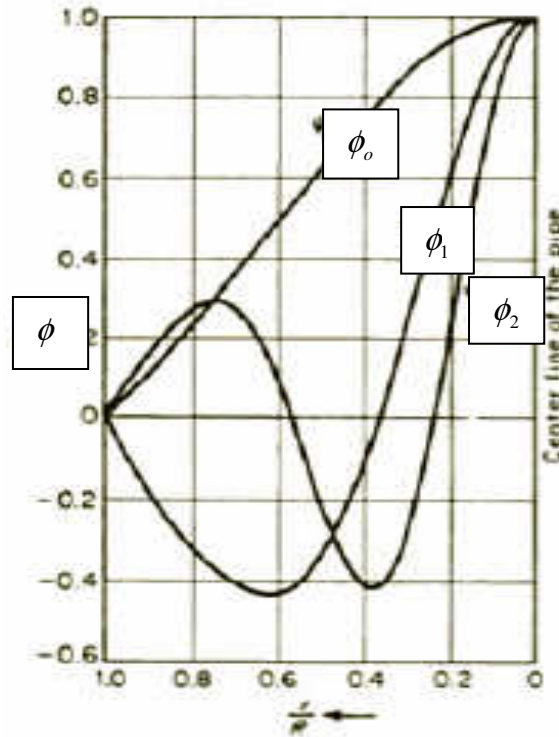


**Figure 2.15** – Function  $\phi$  for the calculation of the temperature field in the thermally developing region of laminar flow through a tube. (Nusselt, 1910)

The constant  $C_i$  can now be found through the boundary condition (2.70) at  $z=0$  through the equation

$$1 = \sum C_i \phi_i \frac{r}{R}$$

The solution of equation (2.69), along the centreline, is represented by the first three terms in the series solution (2.76) with boundary conditions (2.70) as follows (Hering, 2005 (1)):

$$f_T = 1.47\exp(-3.657\mu) - 0.806\exp(-22.3\mu) + 0.589\exp(-57\mu) \quad (2.77)$$

The temperature is obtained from (2.77), through equation (2.68) by setting:

$$\mu = \mu_T = \frac{\alpha_T z}{R^2 U}$$

In the following Figures 2.16 and 2.17 are shown the temperature profiles for three different radial position and for two values of wall temperatures (see Fig. 2.13), with following conditions:  $U = 0.74$  m/s,  $T_{in} = 298$  K;  $R = 0.0075$  m.

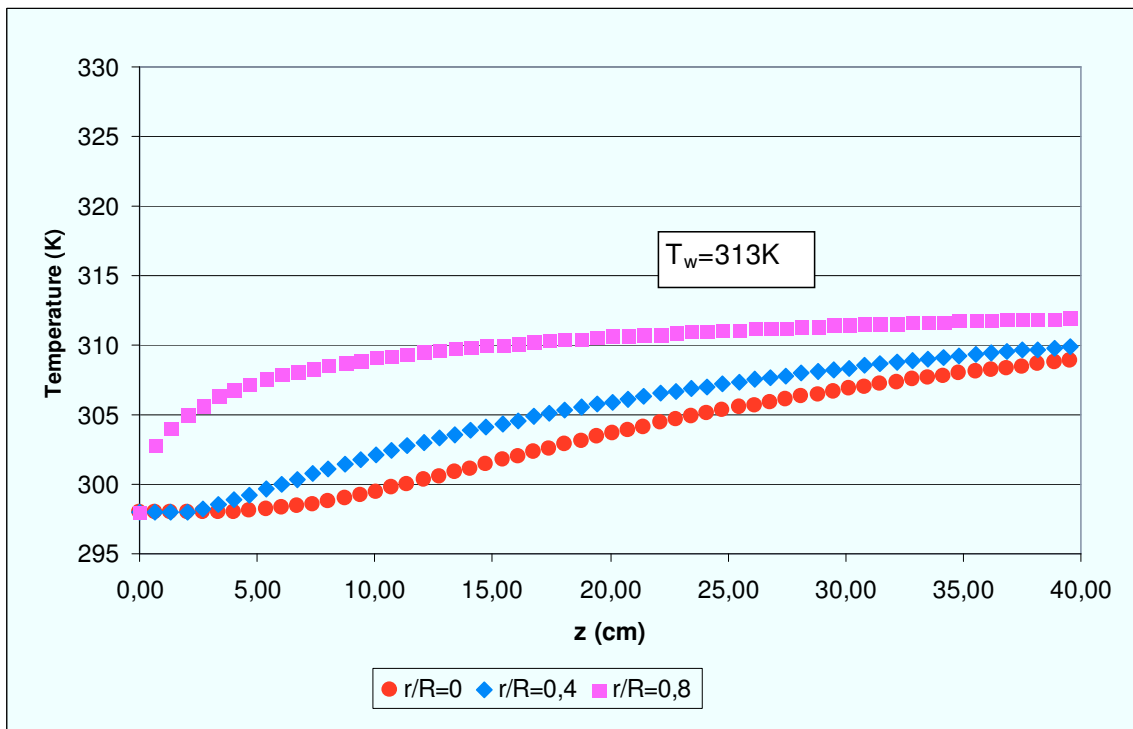


**Figure 2.16** – Temperature profile for three different value of  $(r/R)$  and for  $T_w = 313$  K

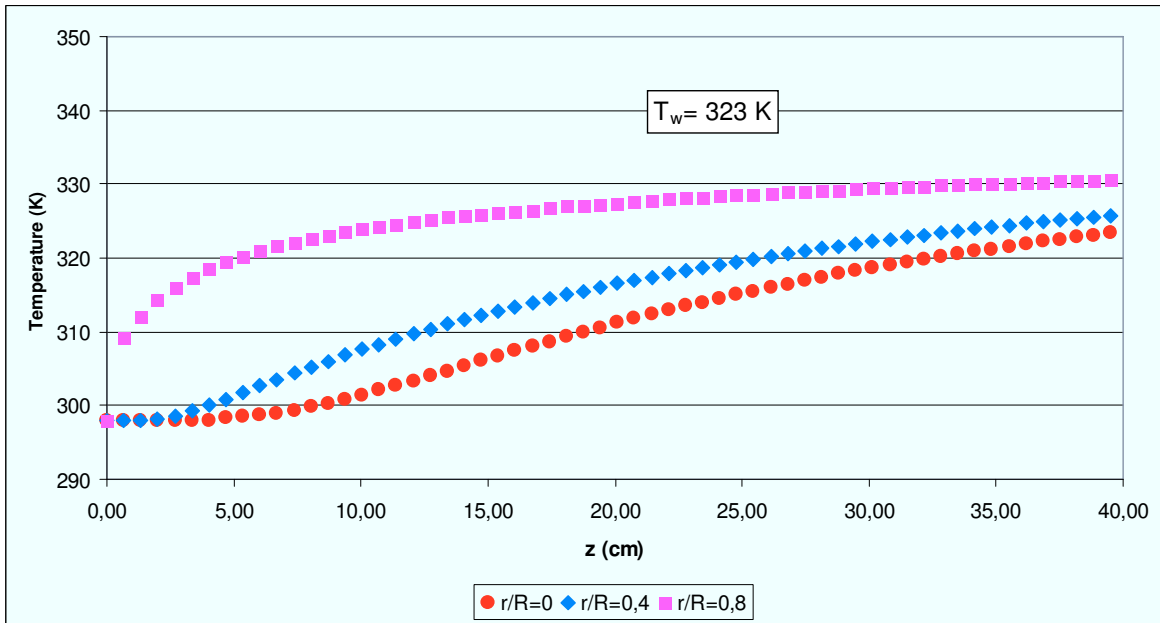


**Figure 2.17** – Temperature profile for three different value of  $(r/R)$  and for  $T_w = 323$  K

### 2.3.1.2 Water mass balance and pressure profile

For the cylindrical geometry, the values of the partial pressure of vapour,  $P_v$ , throughout the growth tube are obtained by solving the mass balance throughout the tube:

$$2U \left[ 1 - \left( \frac{r}{R} \right)^2 \right] \frac{\partial P_v}{\partial z} = \alpha_v \frac{1}{r} \frac{\partial}{\partial r} \left( r \frac{\partial P_v}{\partial r} \right) \quad (2.78)$$

where  $\alpha_v$  is the vapour diffusivity

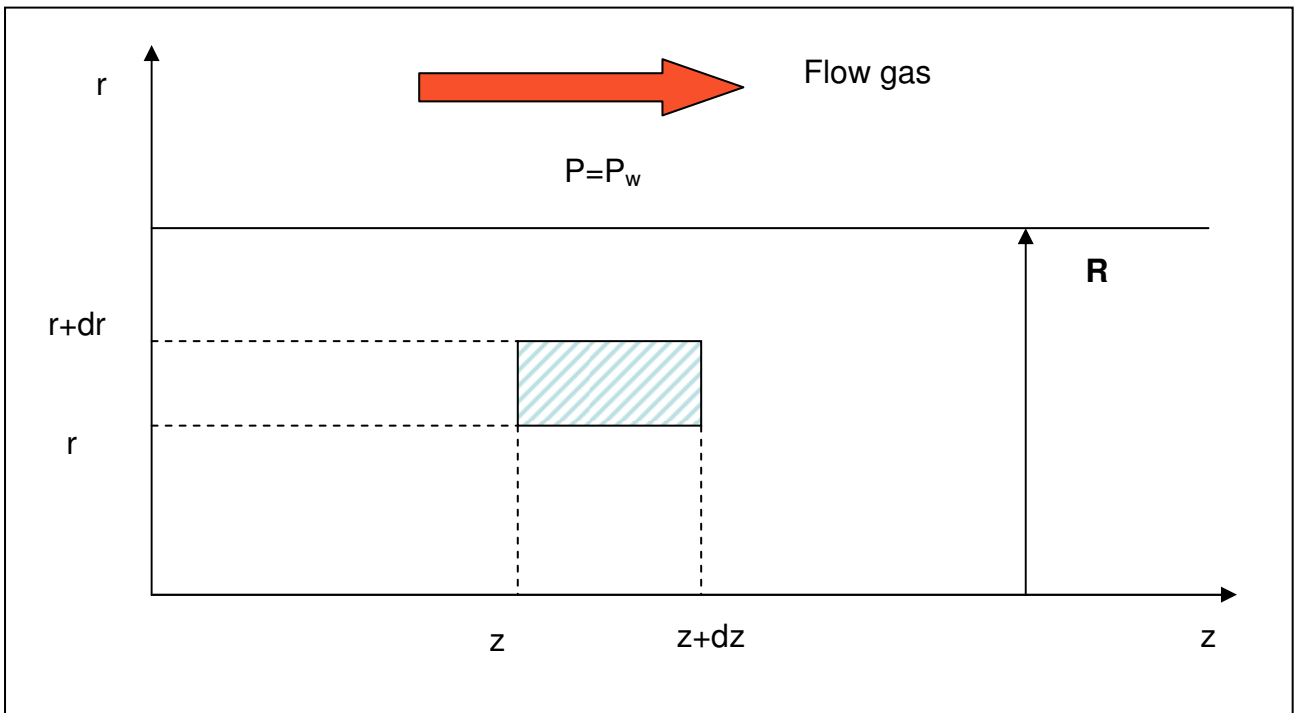


**Figure 2.18** - Ring-shaped control volume for the derivation of the mass equation for laminar flow through a tube; R is tube radius, r and z are the cylindrical coordinate

The partial pressure vapour field is obtained from a mass balance on a ring-shaped control volume, as sketched in Figure 2.18.

$$u(r) \rho (Y_v|_z - Y_v|_{z+dz}) 2\pi r dr + \rho [(r+dr) J_d|_{r+dr} - r J_d|_r] 2\pi dz = 0 \quad (2.79)$$

where  $Y_v$  is the fraction mass of vapour, defined as ratio between partial pressure vapour and total pressure, which assumed constant along growth tube:

$$Y_v = \frac{P_v}{P} \quad (2.80)$$

and  $J_d$  is the diffusion flux in dimensions of (kg/m<sup>2</sup>s) which measures the amount of substance that will flow through a small area during a small time interval, and is defined by Fick's law, for one (spatial) dimension as:

$$J_d = -\rho\alpha_v \frac{\partial Y_v}{\partial r} \quad (2.81)$$

where  $\alpha_v$  is the diffusion coefficient or diffusivity in dimensions of m<sup>2</sup>/s.

The Fick's law relates the diffusive flux to the concentration field, by postulating that the flux goes from regions of high concentration to regions of low concentration, with a magnitude that is proportional to the concentration gradient (spatial derivative).

A fully developed parabolic flow profile is assumed with uniform entering partial pressure profile,  $P_{in}$ , and uniform wall partial pressure in equilibrium with film water at  $T_w$  defined by Raoult's law:

$$P_w = P^\circ(T_w)$$

Thus, equation (2.79) can be rewritten as

$$u(r)\rho \frac{(Y_v|_z - Y_v|_{z+dz})2\pi r dr}{2\pi r dr dz} + \rho\alpha_v \frac{\left[ -\frac{\partial Y_v}{\partial r} \Big|_{r+dr} (r+dr) + \frac{\partial Y_v}{\partial r} \Big|_r r \right]}{2\pi r dr dz} 2\pi dz = 0$$

If we put  $r + dr \cong r$  then we have:

$$u(r)\rho \frac{\partial Y_v}{\partial z} - \rho\alpha_v \frac{1}{r} \left[ \frac{\partial}{\partial r} \left( r \frac{\partial Y_v}{\partial r} \right) \right] = 0$$

Substituting the (2.80) and (2.67), in above equation, we have the (2.78).

Introducing dimensionless coordinates  $\mathbf{x}=\mathbf{r}/\mathbf{R}$  and  $\mathbf{y}=\mathbf{z}/\mathbf{R}$  in (2.78) and defining the parameter  $f_v$  as

$$f_v = \frac{(P_v - P_w)}{(P_{in} - P_w)} \quad (2.82)$$

after some rearrangement, we have:

$$2U[1-x^2]\frac{\partial f_v}{\partial y} = \alpha_t \frac{1}{xR} \frac{\partial}{\partial x} \left( x \frac{\partial f_v}{\partial x} \right) \quad (2.83)$$

with the boundary conditions:

$$\begin{cases} z = 0 \rightarrow y = 0 \rightarrow f_v = 1 \\ r = 0 \rightarrow x = 0 \rightarrow \frac{\partial f_v}{\partial r} = 0 \\ r = R \rightarrow x = 1 \rightarrow f_v = 0 \end{cases} \quad (2.84)$$

The equation (2.83) is solved by separation of variables (Eckert *et al.*, 1972); then we put a function for  $f_v$  like the product of a function of  $x$  and  $y$ :

$$f_v = \phi(x)\phi(y) \quad (2.85)$$

The procedure to solving the (2.85) is the same followed in the steps (2.71-2.75). In the end we have the following expression

$$f_v = \sum C_i \exp\left(-\beta_i^2 \frac{\alpha_v}{2UR} \frac{z}{R}\right) \phi_i \frac{r}{R} \quad (2.86)$$

The constant  $C_i$  can be found through the boundary condition (2.84) at  $z=0$ :

$$1 = \sum C_i \phi_i \frac{r}{R}$$

The solution, along the centreline, of equation (2.83) is represented by first three terms in the series solution (2.86) with boundary conditions (2.84) as follows (Hering, 2005 (1)):

$$f_v = 1.47 \exp(-3.657\mu) - 0.806 \exp(-22.3\mu) + 0.589 \exp(-57\mu) \quad (2.87)$$



The partial pressure is obtained from equation (2.87) through equation (2.82) by setting

$$\mu = \mu_v = \frac{\alpha_v z}{R^2 U}$$

In the following Figures 2.19 and 2.20 are shown the partial pressure vapour profile for three different radial position and for two values of wall temperature (see Figure 2.13), with following conditions:  $U = 0.74$  m/s,  $P_{in} = 3160$  (N/m<sup>2</sup>),  $R = 0.0075$  m and  $P_v^w = P^o(T_w)$ .

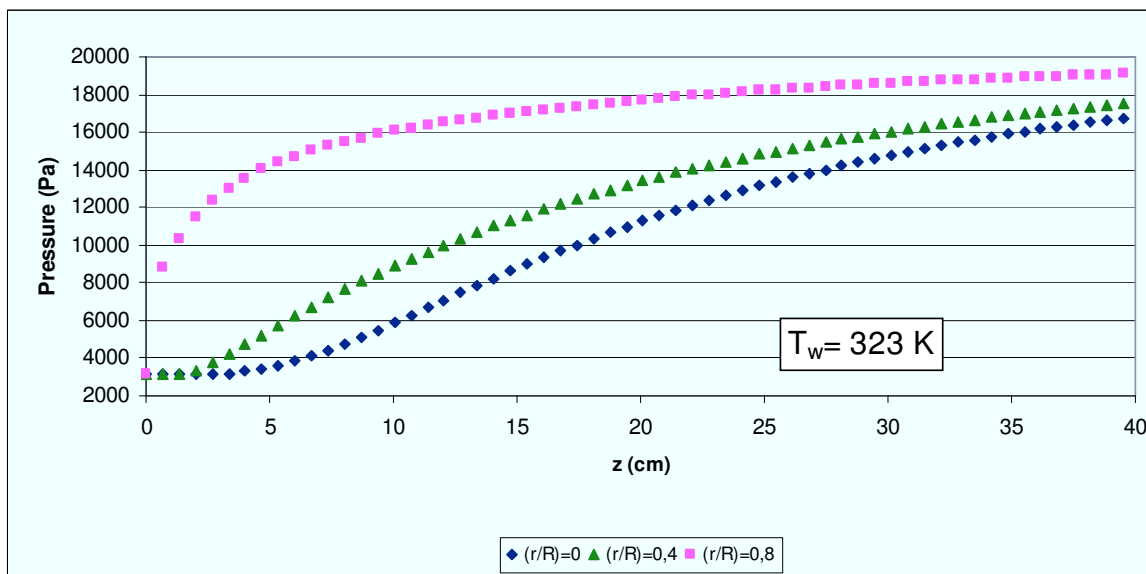


**Figure 2.19** - Partial pressure vapour profile for three different value of  $(r/R)$  and for  $T_w = 323$  K

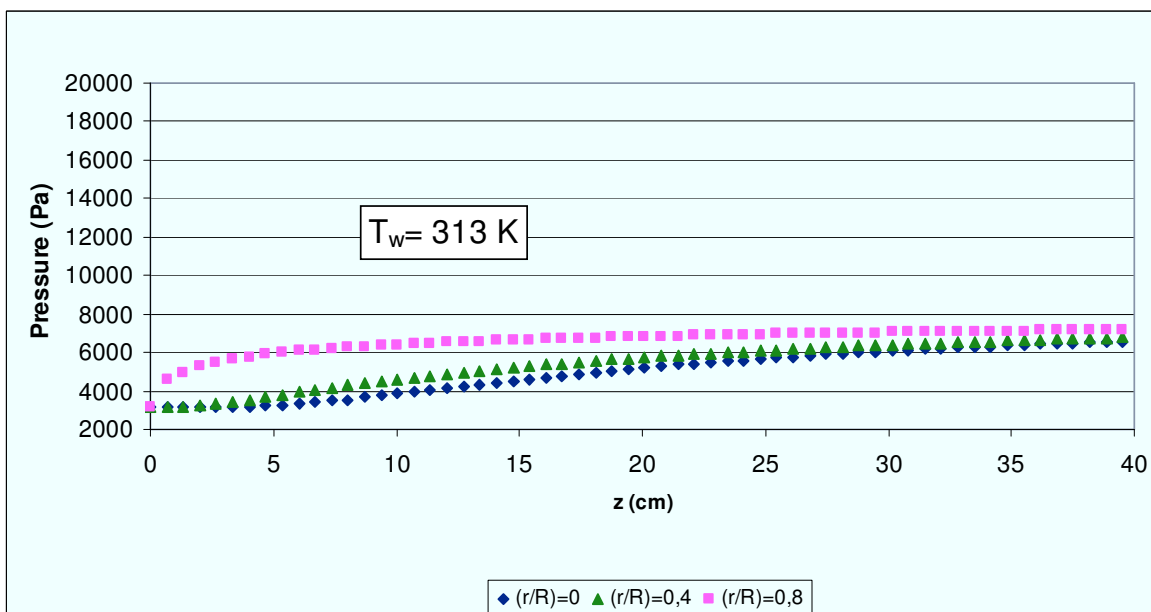


**Figure 2.20** - Partial pressure vapour profile for three different value of  $(r/R)$  and for  $T_w = 313$  K

### 2.3.1.3 Supersaturation ratio profile

The profile of  $S$  is obtained by equation (2.1), where the local value of the equilibrium partial pressure  $P^\circ(T)$  is obtained by Antoine's formula:

$$\log(P^\circ) = \left[ A - \left( \frac{B}{C + T} \right) \right] \quad (2.88)$$

with

$$A = 8.07131$$

$$B = 1730.63$$

$$C = 233.426$$

and

$$P^\circ [=] \text{ mmHg}$$

$$T [=] ^\circ\text{C}$$

In the following figure is shown the supersaturation profile in the growth tube for different  $(r/R)$  value.

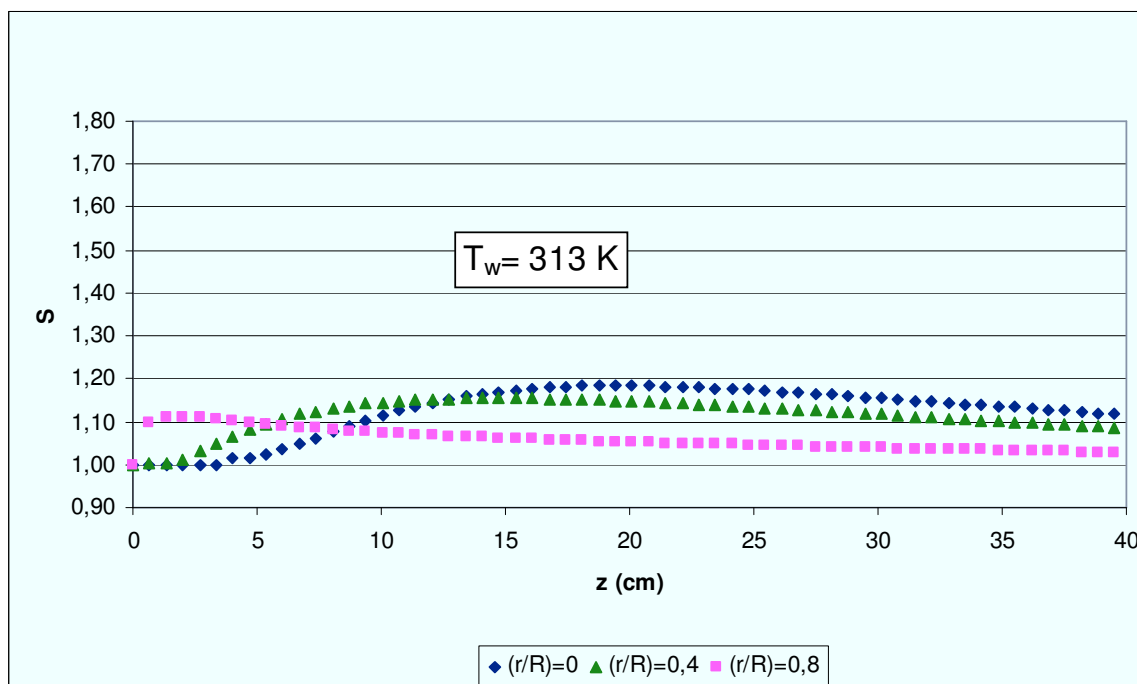


**Figure 2.21** - Supersaturation profile for three different values of  $(r/R)$  and for  $T_w = 313 \text{ K}$

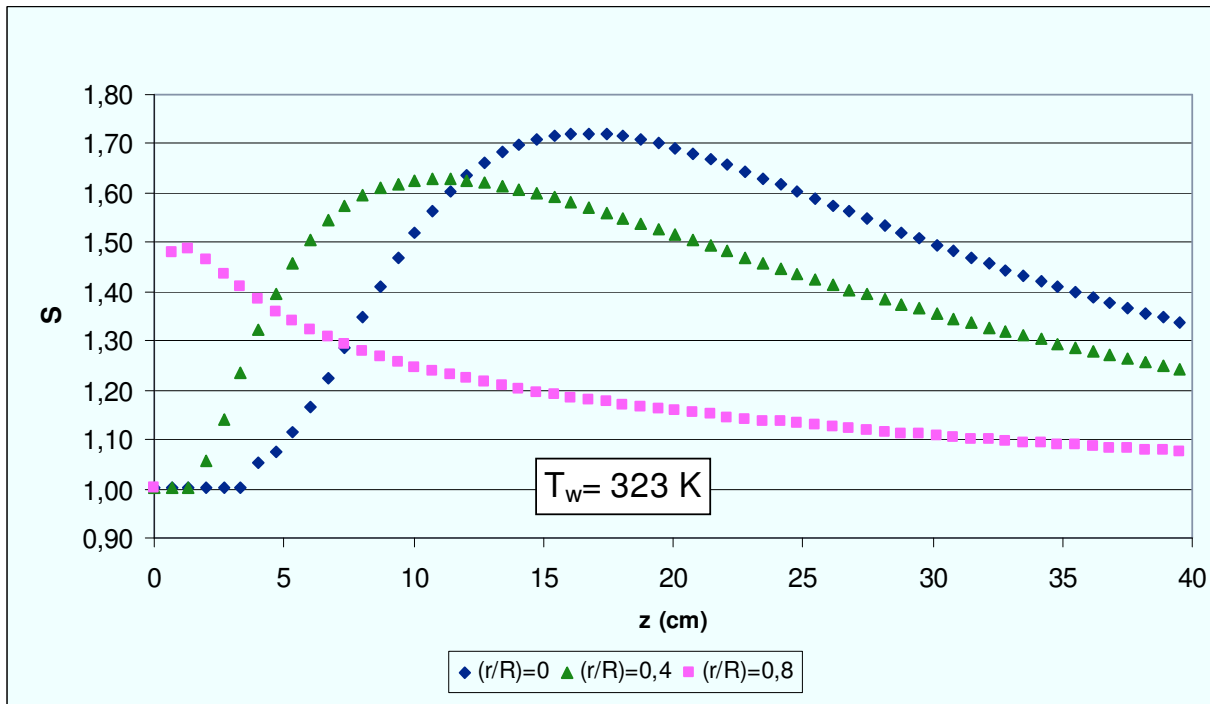


**Figure 2.22** - Supersaturation profile for three different values of  $(r/R)$  and for  $T_w = 323$  K

As can be seen the peak of the supersaturation is reached along the centreline ( $r/R=0$ ), with the supersaturation near the wall rapidly decaying to 1. From comparison between the above graphs, it is clear the influence of the wall temperature on the supersaturation degree.

#### 2.4. Nucleation and growth rate in the growth tube

In the following figure is shown the scheme of the processes of nucleation and condensation growth in the growth tube. With our modelling we have hypothesised that the two processes are in series.

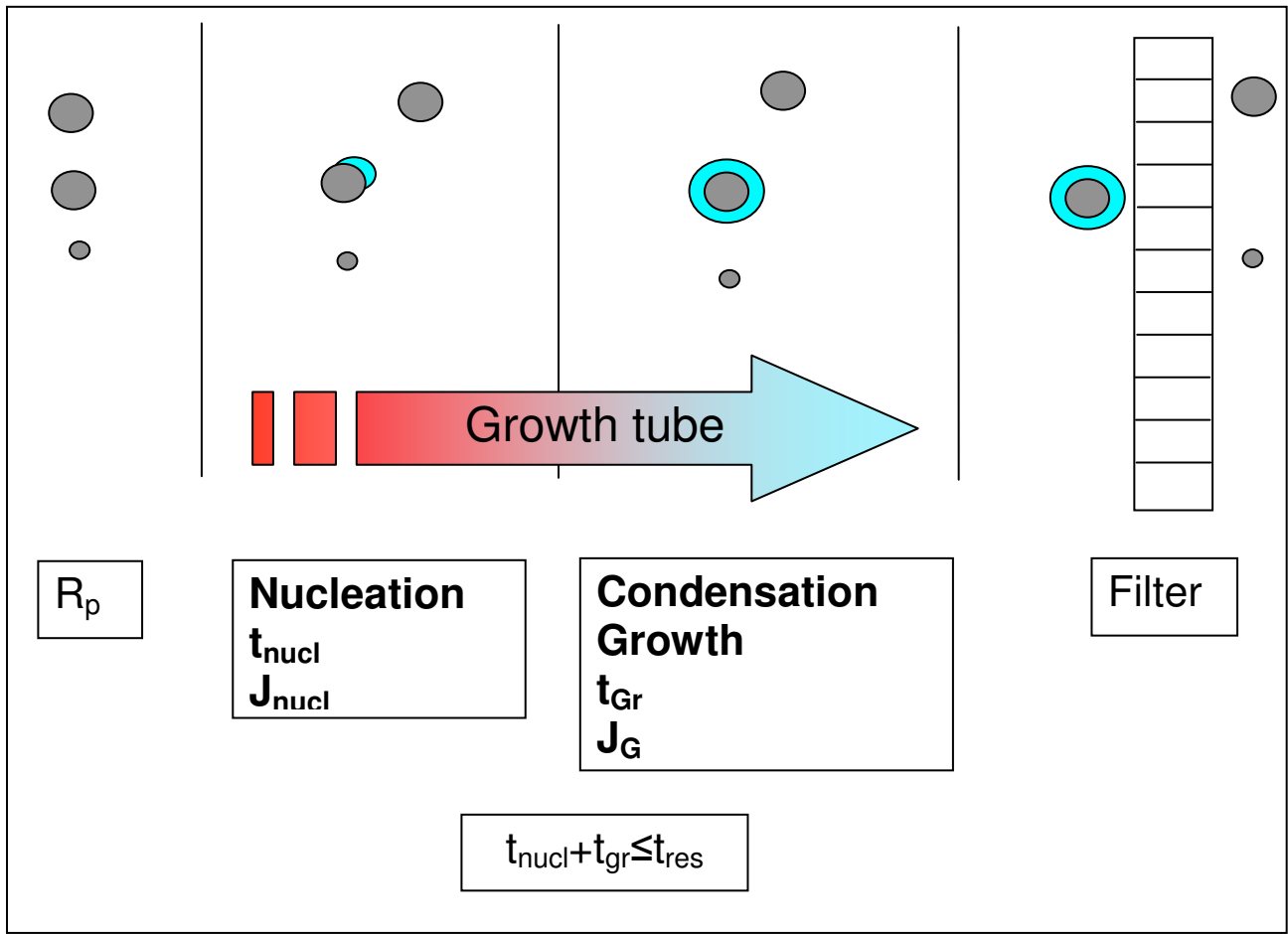


**Figure 2.23** – Scheme of model for nucleation and growth

Every stage is characterised by a rate and time; of course the sum of characterised times must be lower or equal to residence time ( $t_{res}$ ) in the growth tube.

It's possible, from pressure, temperature and supersaturation profile in the growth tube, to plot, in the same conditions, also an example of nucleation and growth rate, as can be seen from following figures 2.24-25 and 2.26-27 respectively.

The dashed line in figure 2.24 and 2.25 corresponds to the condition  $J=1$  (embryo/s), or the same  $S=S_{cr}$ , necessary for activation of nucleation process. The nucleation process is active when the corresponding curve is above the dashed line; indeed when it's below the nucleation doesn't take place.

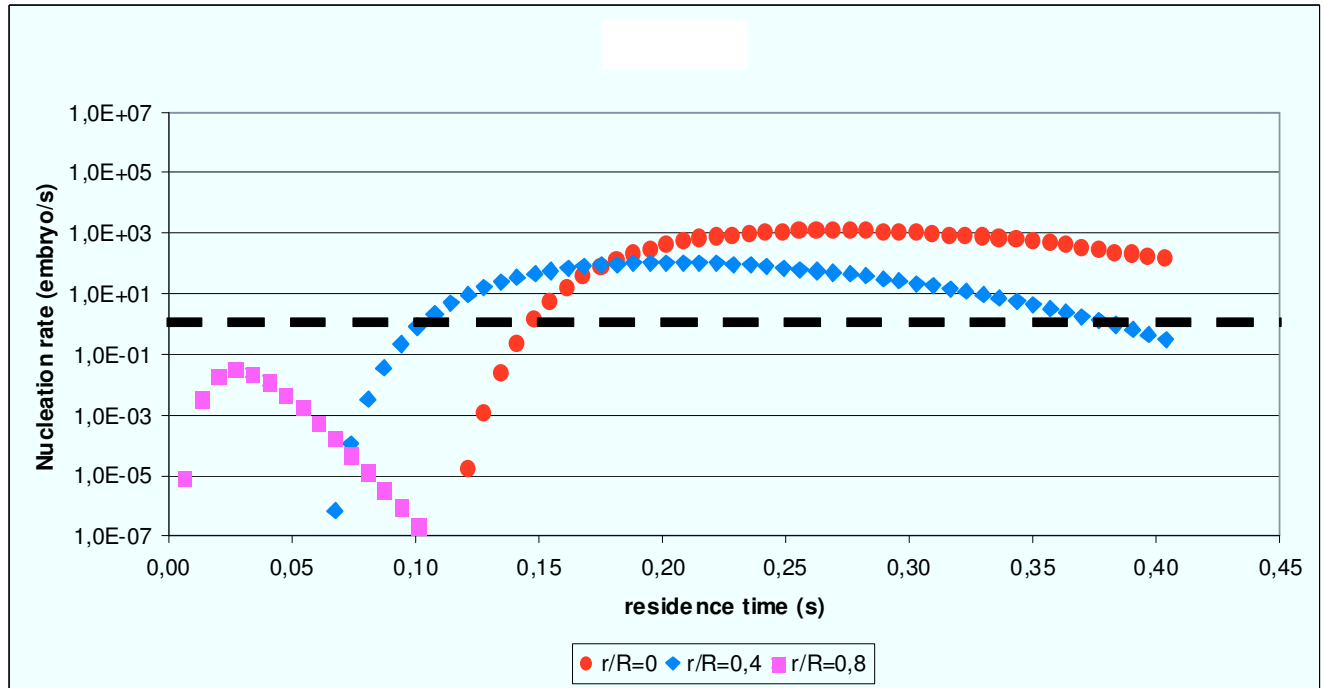


**Figure 2.24** – Nucleation rate vs residence time for three different radial position and with  $T_w = 313$  K. The dashed line indicates the condition  $J=1$  (embryo/s), corresponding to critical supersaturation

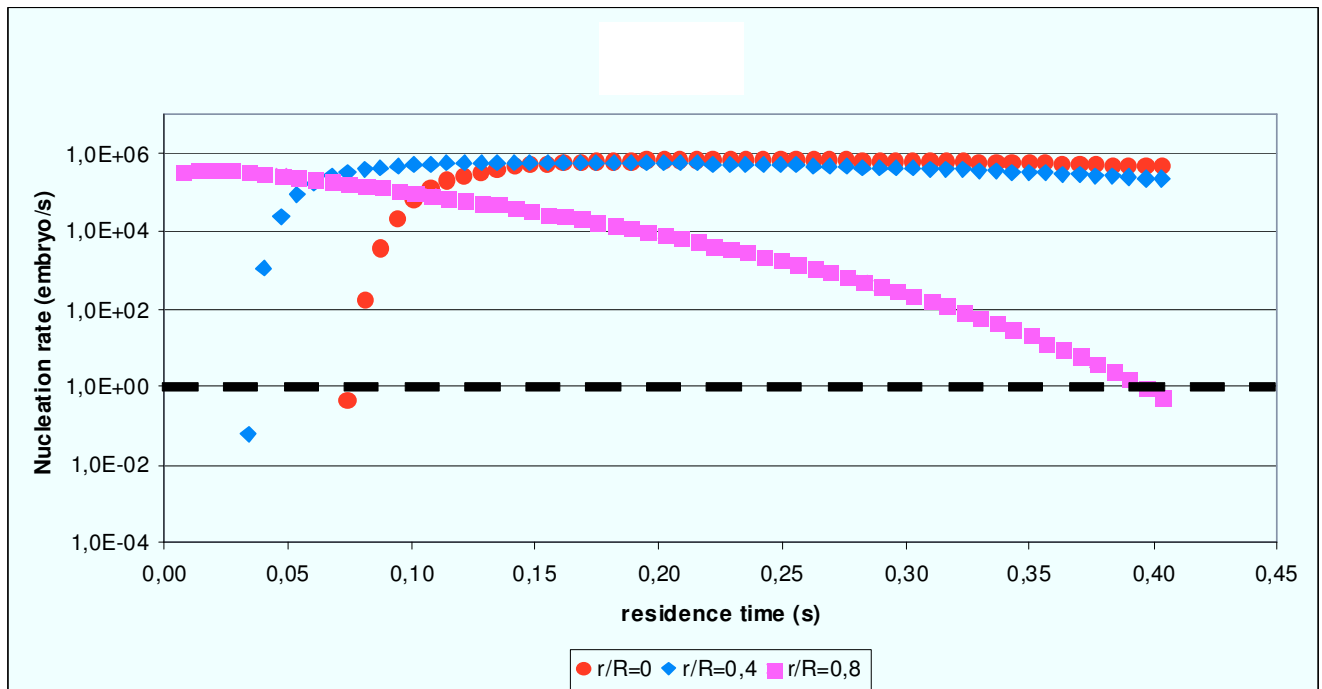


**Figure 2.25** - Nucleation rate vs residence time for three different radial position and with  $T_w = 323$  K. The dashed line indicates the condition  $J=1$  (embryo/s), corresponding to critical supersaturation

From comparison between the curves of the figures 2.24 and 2.25 we can see that the nucleation rate is strongly affected by wall temperature. Besides, it can be seen that the heterogeneous condensation occurs at different extent in function of the radial position.

Then, when the nucleation is not active (below dashed line), the corresponding growth doesn't take place, how can see from following figures.

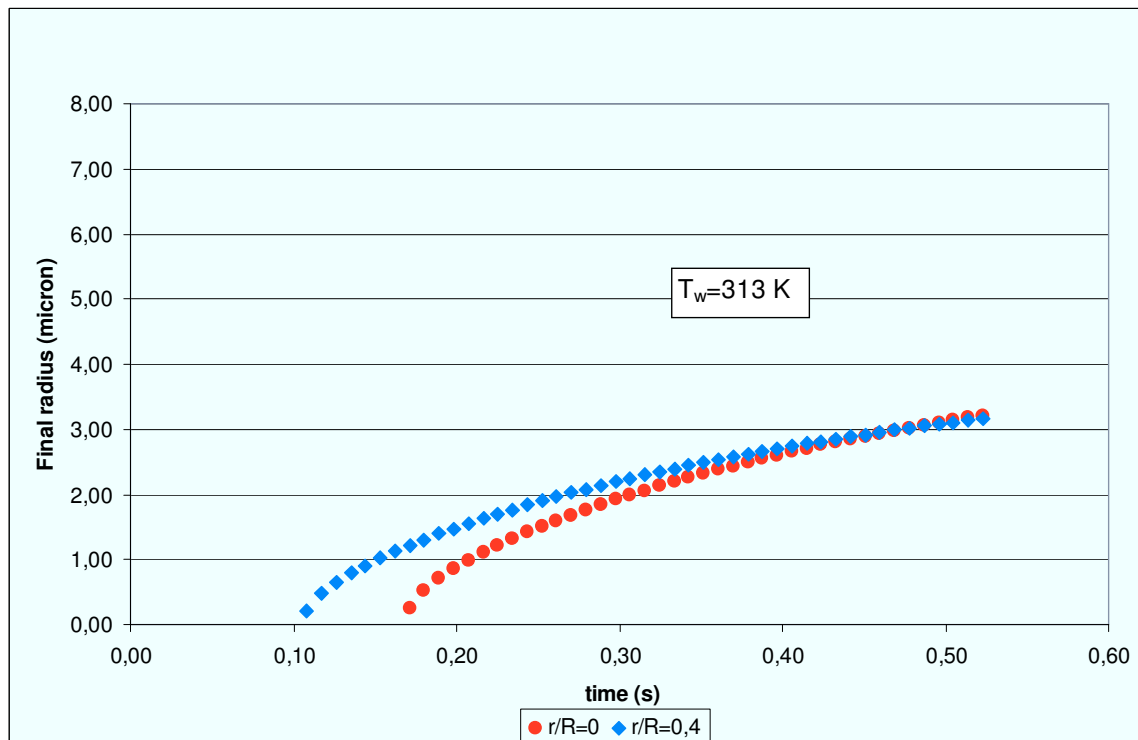


**Figure 2.26** - – Final droplet radius vs residence time for different radial position and  $T_w = 313 \text{ K}$

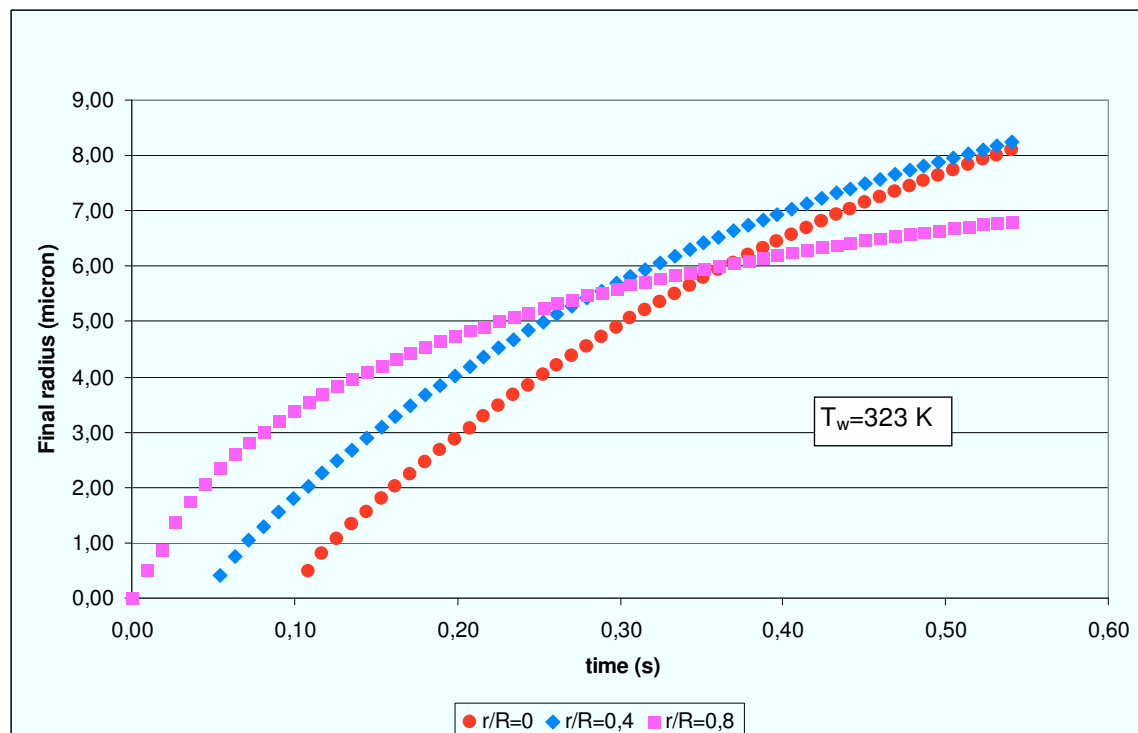


**Figure 2.27** - Final droplet radius vs residence time for three different radial position and  $T_w = 323 \text{ K}$

From Figure 2.26 we can see that in the group of curve corresponding to  $T_w = 313$  K there isn't the radial position ( $r/R=0.8$ ), because, in that radial position is not reached the condition  $J=1$  (embryo/s), in fact the nucleation curve of radial position ( $r/R=0.8$ ) is above the dashed line (see Figure 2.24).

The curves of figures 2.26 and 2.27 start at different times, because the droplet growth starts when the condition  $J=1$  (embryo/s) is reached, and this condition is reached at different times, how can see from figures 2.24 and 2.25, or the same when the condition  $S=S_{cr}$  is realised, as can be seen from following figures 2.28 and 2.29.

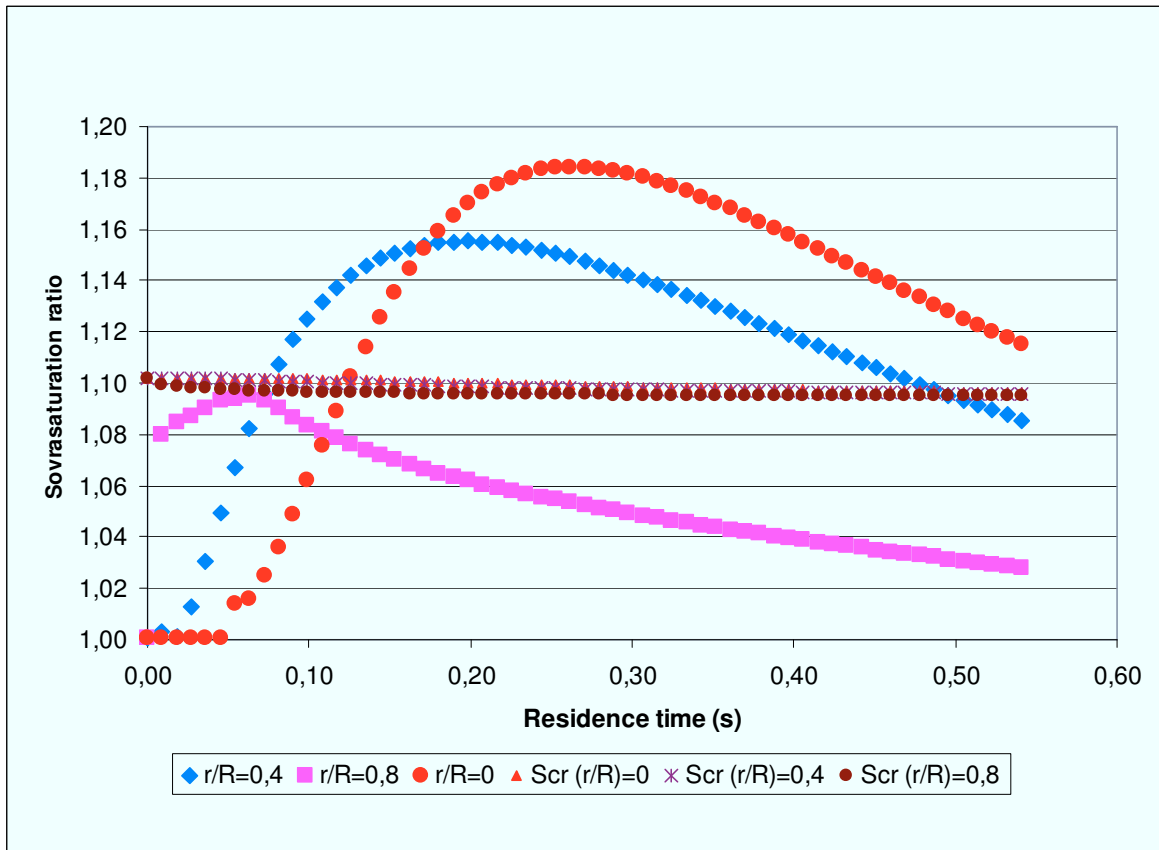


**Figure 2.28** - Comparison between supersaturation profile e  $S_{cr}$  vs residence time in the growth tube for three different radial position, for  $T_w = 313$  K

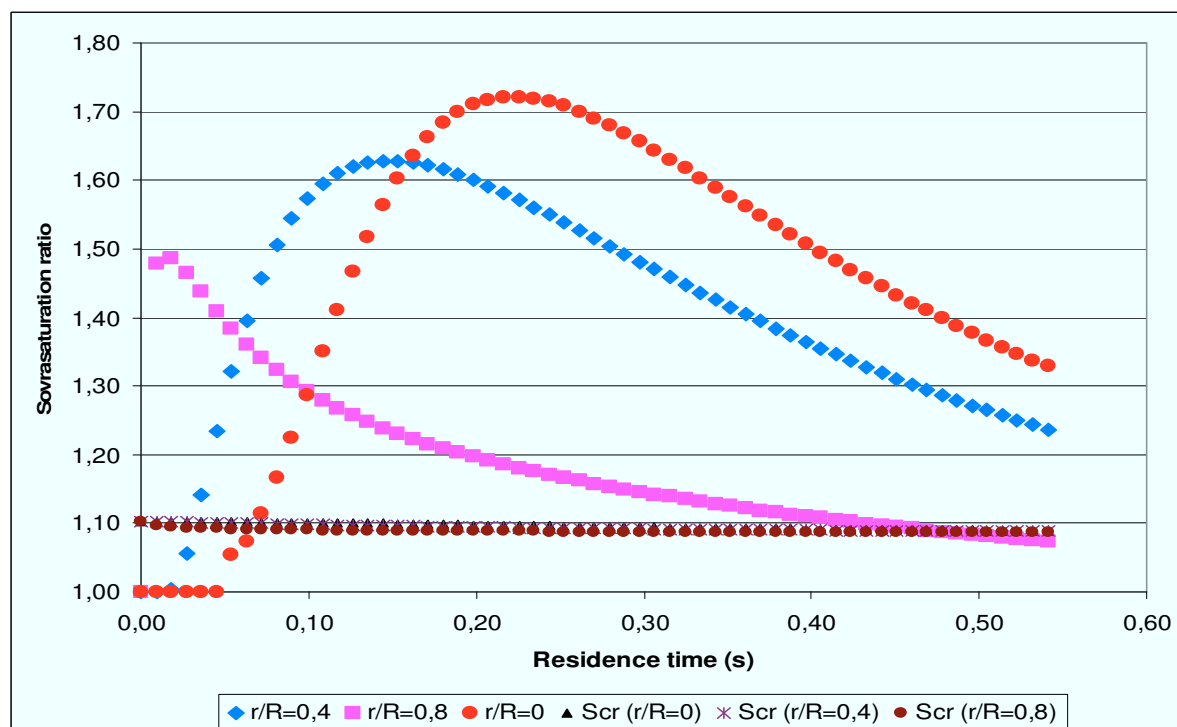


**Figure 2.29** - Comparison between supersaturation profile e  $S_{cr}$  vs residence time in the growth tube for three different radial position, for  $T_w = 323$  K

As can be seen from Figure 2.28, in this example for radial position ( $r/R=0.8$ ) the condition  $S=S_{cr}$  is not realised.

Finally in the following figure is shown the comparison between critical supersaturation for three radial positions at two wall temperatures.

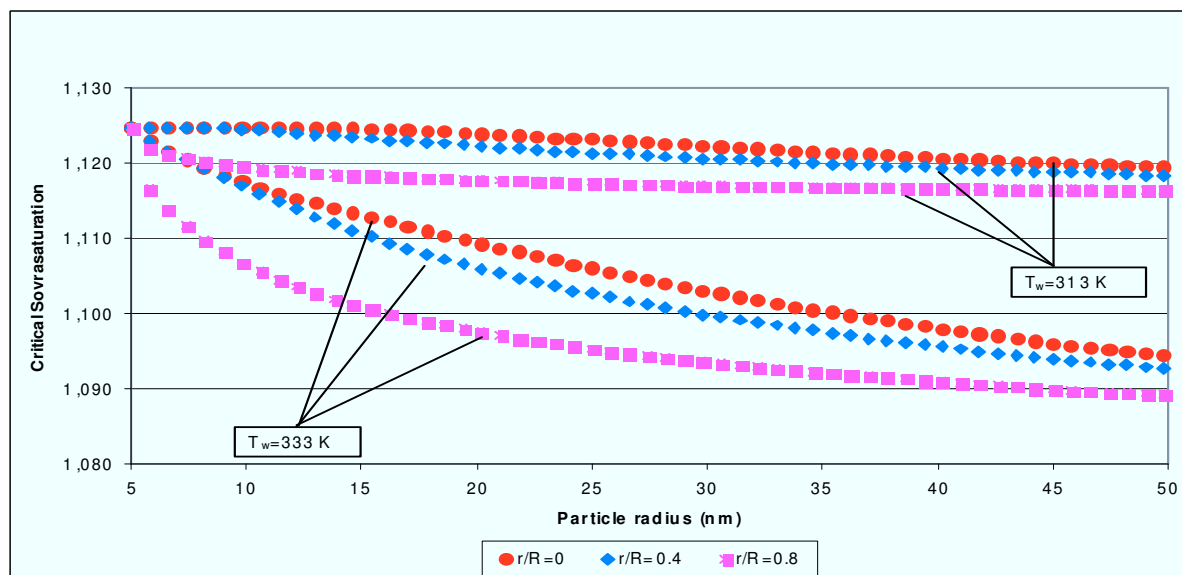


**Figure 2.30** - Critical supersaturation vs particle radius for three radial positions at  $T_w = 313$  K and 323 K

As can be seen the critical supersaturation is strongly dependence on temperature.



## 2.5. Condensational growth of aerosol

In order to describe the growth of a polydisperse droplet aerosol by condensation, the interaction of the droplets and their coupling with the surrounding continuous phase must be taken into account. This is only possible by means of models which simplify the process.

One model is the so-called cellular model in which each droplet is surrounded by a cell of a defined volume. This volume is given by unity divided by the number concentration of droplets. The boundary of each cell is considered as impermeable. Thus, no interaction occurs between cells. The growth laws of a single droplet are applied to each droplet thus solving the given boundary conditions and the conservation of vapour mass and energy for each cell.

Another model is characterized by time-dependent bulk conditions. It is assumed that the distance between the droplets is large compared to the droplet size and thus the vapour concentration and the temperature profiles between the droplets are horizontal. Only in the neighbourhood of the droplet surface are high vapour concentrations and temperature gradients exhibited. Thus, average bulk conditions for the vapour pressure and the temperature of the surrounding continuous phase can be calculated by solving the equations for the conservation of vapour mass and energy. Droplet growth is determined by means of the growth laws for a single droplet and interactions between the droplets are not considered. As shown by Carstens *et al.*, (1970) who have solved the vapour concentration and temperature profiles for two neighbouring droplets: the influence of the neighbouring droplets on the vapour concentration and the temperature profile only occurs if the distance between the droplets is of the order of the droplet radius. For example, assuming a concentration of  $10^6$  particle  $\text{cm}^{-3}$  and equidistant droplets, the distance between the droplets is 100  $\mu\text{m}$ . For submicron particles growing to 5  $\mu\text{m}$ , the probability of an interaction between the droplets remains small. But, in reality, the droplets are not equidistant and the probability of droplet interaction exists. Thus, interaction between the droplets cannot be excluded completely. In our modelling, we have calculated the growth of a droplet aerosol by using the time-dependent bulk condition model. The bulk conditions have been calculated on the basis of vapour mass and energy conservation in a unit volume of

the system. The aerosol is discretely subdivided into  $N$  size ranges with a number concentration  $C_i$  per unit volume in the  $i$ -th size range with an average radius  $r_i$ .

In the following the change in the vapour pressure from the mass balance for a unit volume of the system is calculate. The growth condensation of droplets surrounding the particles determines depletion in the amount of condensable vapour, then decreasing the vapour partial pressure.

Under the hypothesis of ideal gas we have:

$$P_v = \frac{RT}{M} C \quad (2.89)$$

where  $C$  is the mass vapour concentration. The time derivative of both sides gives

$$\frac{dP_v}{dt} = \frac{RT}{M} \frac{dC}{dt} \quad (2.90)$$

The variation of concentration,  $dC$ , can be written as:

$$dC = \sum_{i=1}^N C_i dm_i \quad (2.91)$$

where

$C_i$  : number of droplet with radius  $i$  per unit volume

$dm_i$  : variation of single droplet mass with radius  $i$

From definition of mass flux (2.43) we can write

$$dm_i = -I_i dt \quad (2.92)$$

where  $I_i$  is the flux of mass to droplet with radius  $r_i$ .

From combination of (2.91) and (2.92), the (2.90) can be rewritten as:

$$\frac{dP_v}{dt} = -\frac{RT}{M} \sum_{i=1}^N C_i I_i \quad (2.93)$$

After separation of variables and integrating the (2.93), we have:

$$P'_v = P_v^o - \frac{RT}{M} \sum_{i=1}^N C_i I_i (t' - t_o) \quad (2.94)$$

where  $P'_v$  is the partial pressure vapour at time  $t=t'$  and  $P_v^o$  that at  $t=t_o$ .

In the following, the steps for calculation of change in the temperature profile are reported.

The latent heat of condensation released causes an increase in the temperature of the surrounding continuous phase if droplet growth is considered to be an adiabatic process. The energy balance for unit volume of the system is

$$V(C_{pg} C_g + C_{pv} C_v) \frac{dT}{dt} = LV \sum_{i=1}^N I_i C_i \quad (2.95)$$

where  $C_{pg}$  and  $C_{pv}$  are the heat specific of gas and vapour respectively,  $L$  is the heat latent,  $V$  is the volume,  $C_g$  is the gas concentration and is given by

$$C_g = (P - P_v) \frac{M_g}{RT} \quad (2.96)$$

where  $M_g$  and  $P$  are the mass molecular of gas and the total pressure respectively; the  $C_v$  is the vapour concentration and is given by equation (2.89).

Substituting (2.96) and (2.89) in the (2.95), we have:

$$\frac{dT}{dt} = \frac{RTL}{(P - P_v)C_{pg}M_g + P_vC_{pv}M_v} \sum_{i=1}^N I_i C_i \quad (2.97)$$

After separation of variables and integration of the (2.97), the change in temperature of the gas phase around the droplet is given by:

$$T' = T_0 e^{\alpha(t'-t_o)} \quad (2.98)$$

where  $\alpha$  is given by

$$\alpha = \frac{RL}{(P - P_v)C_{pg}M_g + P_v C_{pv}M_v} \sum_{i=1}^N I_i C_i$$

Then the (2.57) became:

$$D_{d,f} = \sqrt{D_{d,o}^2 + \frac{8MD}{\rho_l RT'} \left( P'_v - P^o(T_d) \exp\left( \frac{4\sigma M}{RT_d \rho_l D_{d,o}} \right) \right) t} \quad (2.99)$$

In order to demonstrate the influence of particle's concentration on the process of particle enlargement by condensation, in following Figure 2.31 is shown as an example some calculated droplet growth curves. The curves were calculated for different particle number concentrations. In the example given here, the initial supersaturation was 1.5 and the initial temperature of the gas/vapour mixture was 308 K. The calculated growth curves indicate that droplets grow by condensation very fast. Particles with a size down to a few nanometers can be enlarged to droplets of a size of 1.5  $\mu\text{m}$  within 5 ms. For concentrations higher than  $2 \times 10^5$  particles per  $\text{cm}^3$ , the growth is complete in less than 50 ms. The higher the particle concentration is, the faster the growth is complete. The final droplet diameter depends on the particle concentration. With an increase in the particle concentration the vapour condenses on more particles and thus the amount of vapour which condenses on each particle decreases. Correspondingly, the final droplet diameter decreases with increasing particle concentration (Heidenreich *et al.*, 2000; Wagner, 1982).

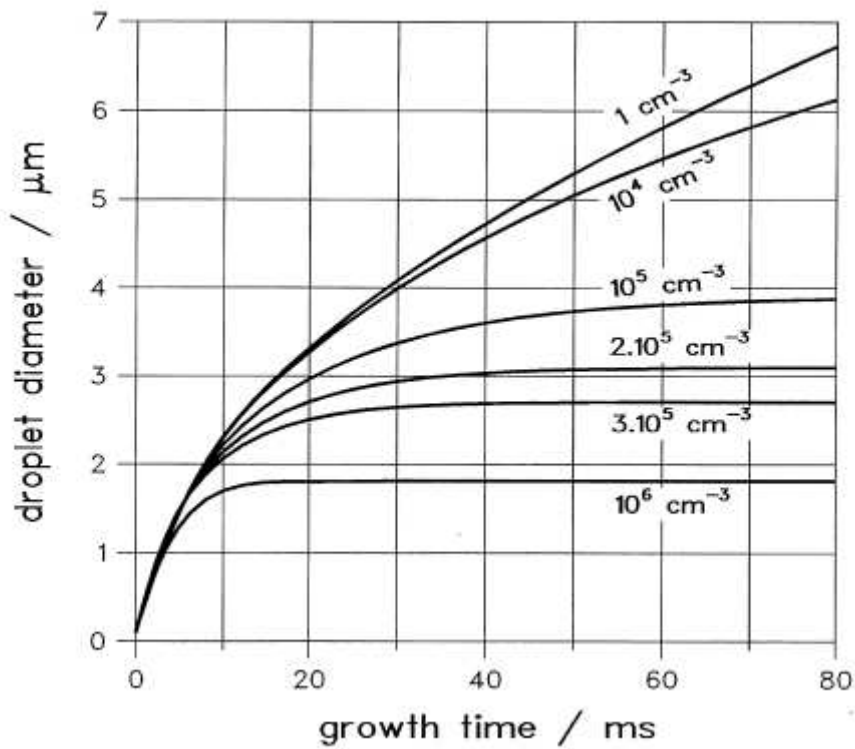


**Figure 2.31** - Droplet growth curves for different particle number concentrations. Initial properties of the gas/vapour mixture:  $T=308$  K and  $S=1.5$ . (Heidenreich *et al.*, 2000)

As can be observed for concentrations lower than  $10^5$  particles per  $\text{cm}^3$  ca, the amount of latent heat of condensation released and the depletion in mass of vapour is negligible and then the final diameter is independence from particle's concentration (Heidenreich *et al.*, 1995). In fact as can be seen from Figure 2.31 the two curves relative to concentration 1 and  $10^4 \text{ cm}^{-3}$  have almost the same trend.

## 2.6. Modification to the model

The model equations reported so far and summarized by the (2.99) are based on the fundamental assumption that the water vapour is always available without any limitation in the growth tube. In practice, however, the vapour concentration in the growth tube may be limited by the effective mass flux from the evaporating liquid film.

In order to take in account the effective vapour mass presents in the system, a modification to the model is presented. At this purpose lets make a comparison between the effective evaporation rate from the liquid film on the wall of the growth tube (Figure 2.13), and the ideal evaporation rate which provides the mass of vapour required for the growing of droplets according to the model (2.99).

To this aim, the formula for determination of evaporation rate from film liquid has been considered.

$$E = K_c (\rho_s - \rho_b) \quad (2.100)$$

expressed as (kg/sm<sup>2</sup>) and where

- ✓  $K_c$  is the mass transport coefficient
- ✓  $\rho_s$  is the surface film liquid vapour density
- ✓  $\rho_b$  is the bulk vapour density

The density, with hypothesis of ideal gas, is calculated by

$$\rho = \frac{PM}{RT} \quad (2.101)$$

For calculation of  $\rho_s$ , the temperature and the pressure to put in (2.101) are the film liquid temperature ( $T_w$ ) and the corresponding equilibrium pressure ( $P_w = P_w(T_w)$ ) respectively. Then the (2.100) can rewritten as:

$$E = K_c \frac{M}{R} \left( \frac{P_w}{T_w} - \frac{P_b}{T_b} \right) \quad (2.102)$$

where  $P_b$  and  $T_b$  are the vapour partial pressure and temperature in the gas phase derived from mass and heat balance respectively.

The coefficient  $K_c$  is obtained from Sherwood number that, for wetted-wall column with falling film (Perry *et al.*, 1984), is given by

$$Sh = \frac{LK_c}{D} = \left( \frac{P}{P_v} \right) 0.023 Re^{0.83} Sc^{0.44} \quad (2.103)$$

where

- ✓ L: geometrical factor (for our system is the diameter of the growth tube)
- ✓ D: mass diffusivity
- ✓ P: total pressure
- ✓  $P_v$ : vapour partial pressure
- ✓  $Re = \frac{\rho v L}{\mu}$ : Reynolds number (where  $\mu$  is the viscosity and  $v$  is the gas velocity)
- ✓  $Sc = \frac{\mu}{\rho D}$ : Schmidt number

It's possible to calculate the effective partial pressure vapour ( $P_b^{eff}$ ) as the sum of two contributes: the amount of vapour derivate from evaporation of film liquid and the vapour present in the gas phase at inlet growth tube. Then the effective evaporation rate can write as:

$$E_{eff} = K_c \frac{M}{R} \left( \frac{P_w}{T_w} - \frac{P_b^{eff}}{T_b} \right) \quad (2.104)$$

The ratio between effective and ideal evaporation rate, called M, can write as

$$M = \frac{E_{eff}}{E} = \frac{\frac{P_w}{T_w} - \frac{P_b^{eff}}{T_b}}{\frac{P_w}{T_w} - \frac{P_b}{T_b}} \quad (2.105)$$

Now if we call B the ratio between the effective droplet diameter measured in the experimental test,  $D_{exp}$ , and the droplet diameter corresponding to model (2.99),  $D_{mod}$ ,

$$B = \frac{D_{\text{exp}}}{D_{\text{mod}}} \quad (2.106)$$

and writing a relation between factors M and B in the form:

$$B = a * M^n \quad (2.107)$$

we can found the two factors,  $a$  and  $n$ , through a data experimental analysis (see chapter 4).

Thus we can define a modified model that takes in account the effective mass of vapour through the enhancement factor,  $(a*M^n)$ , and which has the following expression:

$$D'_{d,f} = (aM^n) \sqrt{D_{d,o}^2 + \frac{8MD}{\rho_l RT'} \left( P'_v - P^o(T_d) \exp\left(\frac{4\sigma M}{RT_d \rho_l D_{d,o}}\right) \right)} t \quad (2.108)$$



## Chapter 3

### ***Measurement device and experimental apparatus. Preliminary test***

#### **1. Experimental apparatus**

In Figure 3.1 the experimental flow chart is shown. It is composed by following principal parts:

- ✓ Burner
- ✓ Sampling system
- ✓ Cooling system
- ✓ Growth tube
- ✓ Sample filter/Measurement device

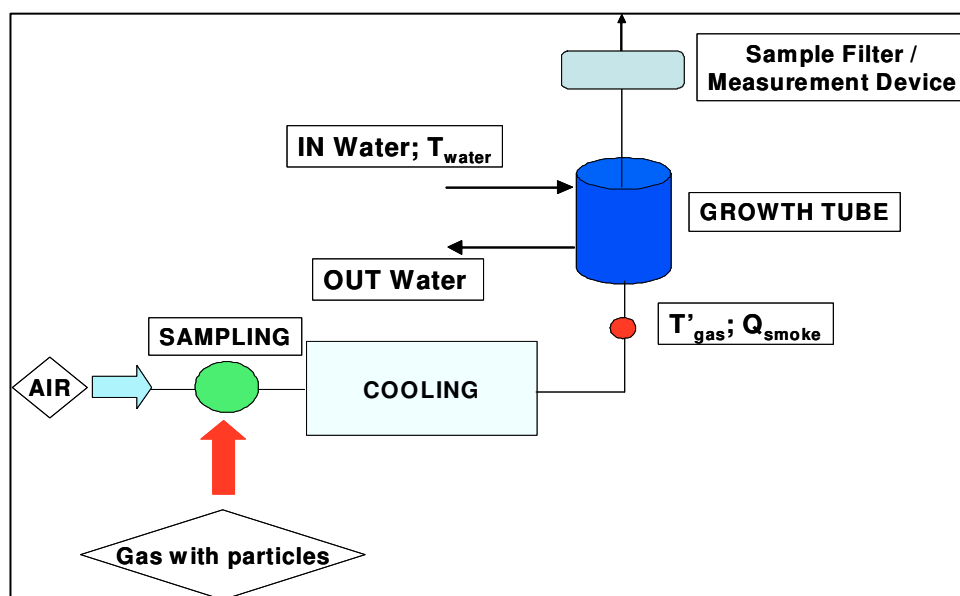


**Figure 3.1** – Flow chart of experimental apparatus

Every part is connected with others through a PTFE flexible tube with internal diameter of 6 mm.

#### **1.1. Burner**

The particles are produced by premixed ethylene ( $C_2H_4$ ) - air one-dimensional flame generated at atmospheric pressure. Nevertheless some tests have been carried out with a Bunsen burner fed with  $CH_4$ . The burner consists of two concentric stainless steel tubes. The inner tube has an internal diameter of 9 mm and a height of 140 mm. At the upper end of tube there is a 40 mm thickness layer of mullite honeycomb (400 cpsi zirconia mullite, produced by Ceramique Technique Industrielles CTI) that allows to obtain the laminar flow

of gas and the stable flame. The tube is inserted into a Teflon bushing with three entrances to 120° from each other. The outer tube produces an annulus of inner diameter of 23.5 mm and 32 mm outside. It has the function of thermal insulation. The flame is then obtained from a mixture of air and ethylene and each gas flow rates are regulated by float flowmeter. In following Figure 3.2 are shown the flame velocities versus composition of different fuels mixtures in air. As can be seen, the ethylene has got the highest velocity flame. Therefore it is important to regulate the cold gasses in order to have a velocity about 10 cm/s and a percentage of ethylene lower than 4 % or higher than 10 %, by this way it is possible to have flame velocity equal to the cold gas velocity

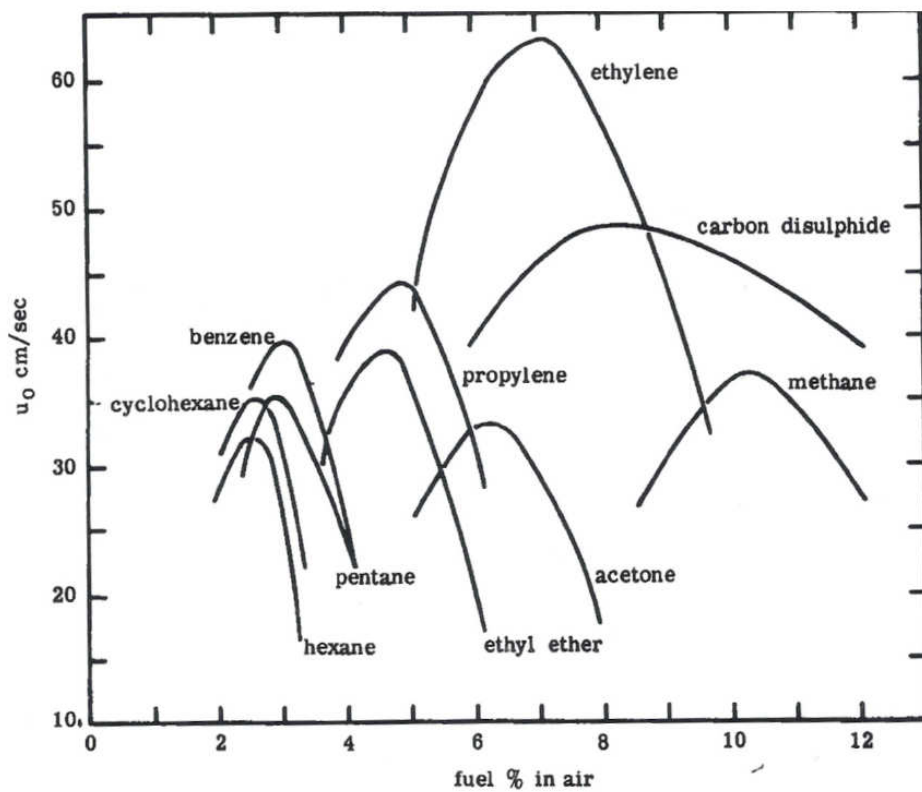


**Figure 3.2** - Flame velocities versus composition of different fuels mixtures in air.

The equivalent ratio ( $\Phi$ ) is adjusted through the control of the ethylene and air flows to the burner. The equivalence ratio of a system is defined as the ratio of the fuel-to-oxidizer ratio to the stoichiometric fuel-to-oxidizer ratio:

$$\phi = \frac{m_{fuel}/m_{ox}}{(m_{fuel}/m_{ox})_{st}} = \frac{n_{fuel}/n_{ox}}{(n_{fuel}/n_{ox})_{st}} \quad (3.1)$$

where,  $m$  represents the mass,  $n$  represents number of moles, suffix  $st$  stands for stoichiometric conditions. The advantage of using equivalence ratio is that it does not depend on the units of measure. Another advantage of using the equivalence ratio is that ratios greater than one always represent excess fuel in the fuel-oxidizer mixture than would be required for complete combustion (stoichiometric reaction) irrespective of the fuel and oxidizer being used, while ratios less than one represent a deficiency of fuel or equivalently excess oxidizer in the mixture.

Traditionally laboratory premixed one-dimensional flames involving ethylene as the fuel represent simpler system to study the mechanisms of fuel decomposition and particles formation in flames. In recent years different studies have been performed to characterize the premixed ethylene/air flame in different burning conditions in order to reveal some important properties of these particles (D'Anna *et al.*, 2007, 2009). In particular it was found that in ethylene/air premixed flame, the volume fraction of particles, expressed as ppm (part per million) increases with ratio (carbon/Oxygen), at least until  $C/O = 0.77$  (D'Anna, 2009). Besides it has been found that the diameter of particles, produced with  $C/O = 0.69$ , increases with HAB (Height Above Burner), until diameter of 90 nm corresponding to  $HAB = 15$  mm and that the max flame temperature measured is about 1700K (Echavarria *et al.*, 2010). In addition, the particles so produced seem to experience a size-dependent coagulation rate at high temperature (D'Alessio *et al.*, 2005).

The study of formation mechanism and of the physico-chemical properties of particles formed in the premixed ethylene/air flame is not the purpose of this thesis. In fact, for the study of heterogeneous condensation, with simplified hypothesis of smooth, spherical and homogeneous particles, it is important to quantify the growth of the droplet, through the measurement of initial diameter of particles and the final diameter of droplet, for different fluidodynamic conditions. Therefore for this purpose, the measurement of particles size in absence of water in the growth tube, i.e. when the heterogeneous condensation is not activated, represents the initial diameter. Then the droplet size measured at outlet of growth tube, when the heterogeneous condensation is activated, represents the final diameter.

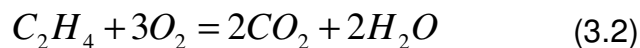
## **1.2. Sampling system**

The sampling of smokes from the burner is performed by means of a hood connected to a pump. The hood is made of steel and it is collocated on the burner to capture the total gas

flow of the burned. The hood aspires also the ambient air, whose flow is calculated as the difference between the measured total flow and the burned gas flow. The burned gas flow is calculated as illustrated in the following paragraph. The relative humidity and temperature of indoor air, measured, are 30% and 25 °C respectively; they are constant because the laboratory ambient is controlled.

### 1.3. Cooling system

The sampled gas then passes through a cooling system where the temperature drop ( $\Delta T = T_g - T'_g$ ) is sufficient to reach the water vapour saturation conditions in the gas phase ( $S=1$ ) at the inlet of growth tube. This condition is necessary to optimised the supersaturation region. The cooling is realized by heat exchange with water in two shell and tube glass exchangers of which temperature and flow are controlled through a thermostatic bath. The control of the total flow, composed by smokes produced by combustion and the air, aspirated from the indoor ambient is controlled through a flowmeter. By knowing the abovementioned flows (Ethylene, air and total smoke), the indoor air relative humidity, and from the stoichiometry of the reaction between oxygen and ethylene,



it is possible to calculate the amount of vapour present in the burned gas phase and in the total flow smoke, and then the vapour partial pressure,  $P_v$ , at the inlet of the growth tube. Therefore, in order to have a gas saturated by water vapour, through the relation (2.1) it is possible to calculate the corresponding gas temperature  $T'_g$ . Then the saturated gas is introduced into the growth tube.

### 1.4. Growth tube

The most important part of the experimental plant, called the *growth tube*, is where the supersaturation condition is created and the size amplification of particles through heterogeneous condensation takes place.

A vapour phase is supersaturated if the vapour pressure in the system is higher than the corresponding saturation vapour pressure of the gas which is a function of the temperature of the system (see table 2.2, chap. 2). Generally, supersaturation can be achieved in

different ways, for example by mixing saturated gases of different temperature, by cooling, by chemical reactions and by simultaneous heat and mass transfer at a liquid surface. In all these cases, supersaturation is caused either by a reduction of the temperature of the gas or by an increase in the vapour pressure in the system. The simultaneous heat and mass transfer at a liquid surface is a process to achieve supersaturation economically, also on a technical scale. For our studies the water vapour supersaturation is achieved by introducing air flow into the growth tube, with temperature lower than that of the tube walls, as illustrated in Figure 3.3. The walls are wetted to maintain a partial pressure of water vapour at the walls near the equilibrium vapour pressure at the wall temperature. Then, the particle laden gases flows and the water film along the wall produce the necessary vapour. In fact, the elevated temperature of the wetted walls produces a high concentration of water vapour, while the cooling arises from the entering sample gas flow. In this scenario the diffusion of water vapour from the walls to the centreline is faster than the warming of the flow. The condensation of vapour on the particle surface is active while the temperature of gas-particles is lower than that of vapour. This must be achieved along the growth tube because in our operating conditions the diffusion of water vapour from the walls to the centreline, is faster than the increase in temperature of the particle air stream (Hering *et al.*, 2005 (1); Brin *et al.*, 2007). In fact, in our working temperature range (300 - 323) K, the values of the vapour diffusivities in air and thermal diffusivity of air are  $0.265 \text{ cm}^2/\text{s}$  and  $0.215 \text{ cm}^2/\text{s}$  respectively (Perry *et al.*, 1984).

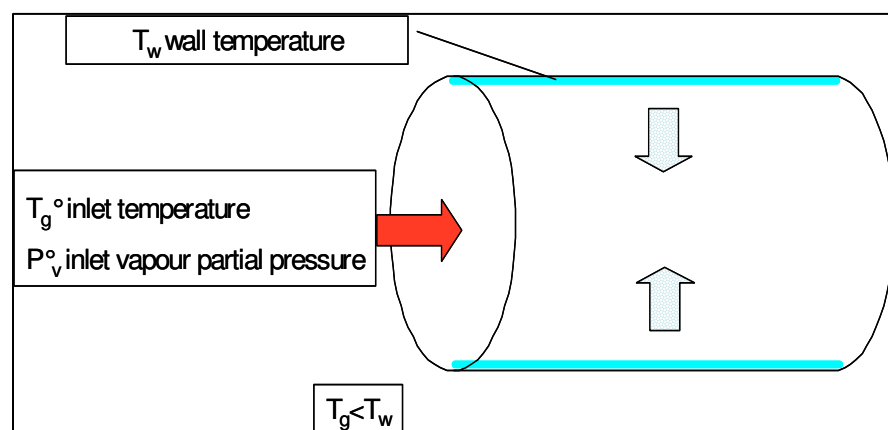


**Figure 3.3** – Scheme of growth tube

The growth tube utilised for the experimental activities was designed and constructive on purpose for this thesis (see Figure 3.4). It is made by a glass pipe with length  $L = 40 \text{ cm}$  and diameter  $D = 1,5 \text{ cm}$ , placed vertically. The tube has an inlet and outlet section for the

gas (d), that flows upward, and an inlet and outlet for section the water (d'=0.5 cm), that flows downward. The inlet and outlet gas section are build through two glass cylinders, with diameter d= 1 cm and length l=6 cm, which are concentric with the growth tube. The function of this connection is to eliminate the interference between gas and water at the inlet and outlet sections. In order to ensure a residence time ( $t_{res}$ ) of the gas stream equal or higher than necessary for nucleation and for a condensational growth of droplet,  $\tau$  (see chapter 2), in our gas flow rate range (2 - 4) l/min.

In the following are described the steps for the design of the growth tube.

From Figures 2.26 and 2.27 it is possible to evaluate the total time  $\tau$  in growth tube. For our calculation, we choose the worst operating conditions, i.e. those relating to the centreline ( $r/R=0$ ) of the growth tube at  $T_w= 313$  K (Figure 2.26) and as final threshold of the growth, the formation of a droplet with diameter of 1  $\mu\text{m}$ . This diameter represents the upper limit of Greenfield gap (see Introduction), that is the minimum diameter of droplet to reach in order to remove the droplet, with inclusions, through a conventional method. As can be seen from Figure 2.26, the  $\tau$  is equal to sum of two terms: the nucleation time, corresponding to intercept with x-axis of curve ( $r/R=0$ ) at  $T_w= 313$  K, i.e.,  $t_{nucl}= 0.2$  s ca, and the proper growth time, that starts from the nucleation time and stops to the time corresponding to droplet diameter equal to 1  $\mu\text{m}$ , i.e.  $t_{gr} = 0.5$  s ca.. Then the sum is equal to 0.25 s ca; but for our conservative calculation we considered  $\tau=0.3$  s. Similar residence times are reported in literature (Smorodin *et al.*, 2004; Fengxian *et al.*, 2009).

The vapour has to diffuse from wall to centreline in a time,  $t_{diff}$ , with a diffusivity equal to  $0.265 \text{ cm}^2/\text{s}$ . From theory of phenomena transport (Bird *et al.*, ed. 2002) we have that the boundary layer thickness,  $\delta$ , in laminar flow ( $Re<2000$ ) is given approximately by:

$$\delta = 4\sqrt{Dt_{diff}} \quad (3.3)$$

where  $D=0.265 \text{ cm}^2/\text{s}$  is the vapour diffusivities in air.

The *boundary layer* is defined as the region where there is a velocity profile in the flow due to the shear stress at the wall. When the flow is considered to be fully developed, at first approximation the time required for vapour diffusion from the wall to the centreline can be estimated, by posing  $\delta = R$ , as:

$$t_{diff} = \frac{R^2}{16D} \quad (3.4)$$

For our calculation, considering the heterogeneous condensation the main process in the growth tube, we put the following conservative conditions:

$$t_{res} \geq 3\tau \quad (3.5)$$

$$t_{diff} \leq \left(\frac{1}{8}\right)t_{res} \quad (3.6)$$

These conditions were chosen in order to ensure that the residence time is sufficient high to have the nucleation and growth of droplet and that the time of diffusion of vapour from wall to centreline is most lower.

From (3.6) through the (3.4) we have that:

$$R = 4\sqrt{\frac{D\tau}{2}} \quad (3.7)$$

From definition of residence time we have that:

$$t_{res} = \frac{volume}{flow} = \frac{\pi R^2 L}{Q} \quad (3.8)$$

where L is the tube length and Q is the flow capacity of gas.

Substituting the (3.7) in (3.8) and with condition (3.5), we have:

$$L = \frac{Q}{2\pi D} \quad (3.9)$$

Using the values of  $\tau = 0.3$  s and  $Q = 4$  (l/min), the higher flow, in the (3.7) and (3.9) respectively, we have

$$\begin{aligned} L &= 40.06 \text{ cm} \\ R &= 0.69 \text{ cm} \end{aligned} \quad (3.10)$$

The real radius of growth tube is been fixed to 0.75 cm for reason construction. These dimensions of the growth tube are consistent with other works present in literature (Hering *et al.*, 2005 (1 and 2)).

The liquid film on internal walls has been obtained with a tangential inlet of the water; also the outlet is tangential. The water flow is supplied in closed loop by a thermostatic bath

that contains the purified water at controlled temperature,  $T_w$ . The thickness of liquid film,  $d_w$ , is fixed to 1 mm and then the water flow,  $Q_w$ , is given by:

$$Q_w = v_w S_w = v_w (2R - d_w) d_w \pi \quad (3.11)$$

where  $v_w$  is water velocity (10 cm/s ca) and  $S_w$  is the liquid film section area. The water used is MilliQ, with final filter at 200 nm.

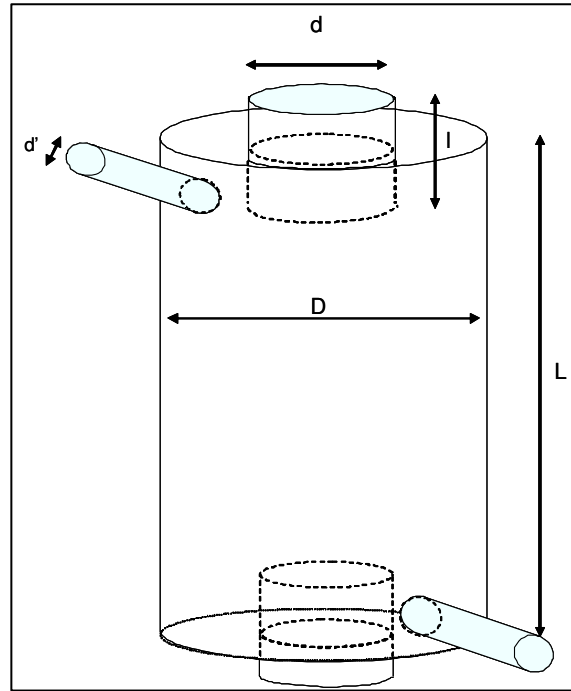


**Figure 3.4** - Scheme of the growth tube.  $L = 40$  cm;  $D = 1,5$  cm;  $d = 1$  cm;  $l = 6$  cm;  $d' = 0,5$  cm

In the following figure is shown the scheme of functioning of growth tube, with indication of formation of droplets surround particles contained in the gas.



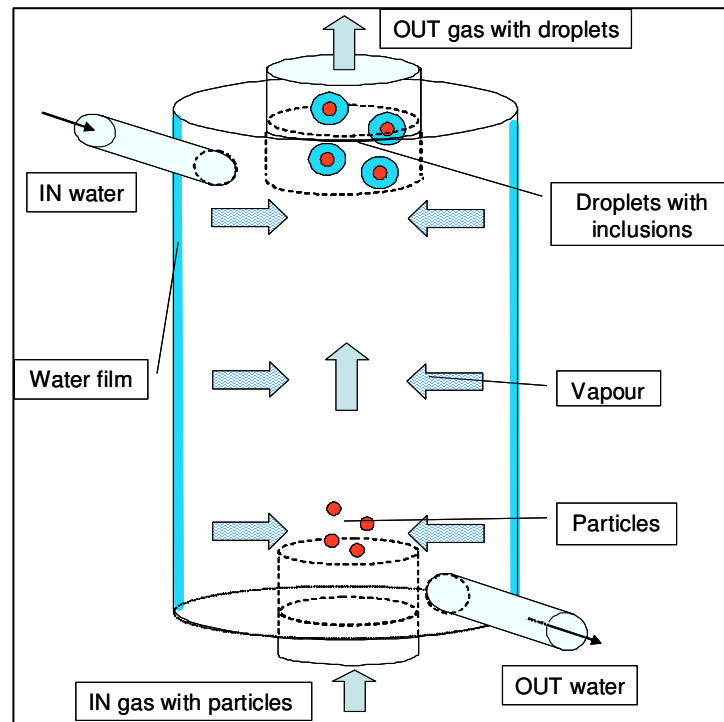


**Figure 3.5** – Scheme of functioning of the growth tube

The growth tube can be assimilated to a adiabatic system, since, the liquid film along the walls, acts as a thermal guard that isolates the system from outside.

### 1.5. Sample filter/Measurement device

At the end of the growth tube are placed either a filter or the measurement device, according on the performed test.

The filter collects the fraction of particles enclosed in the droplets of larger size and then the filtrate can be analysed with a DLS to obtain information on the collected particles size. The filter have different mesh, from 0.2 to 3  $\mu\text{m}$ , used individually or in series. They are made in PTFE (produced by Sartorius) and allocated in a metallic filter-holder. Before the filter are placed a drechsel, i.e. trap, that has the function to capture the biggest droplet of water, to assure that the filtered water do not clog the filter pores. Same drechsel are also placed along the pipeline to capture the bigger droplets, to protect the device or to prevent connecting tube obstruction. In following Figure 3.6 an example of experimental set up with filter allocated at end of growth tube is shown. The filters are collocated with decreasing mesh size. At end of the pipeline is placed a pump for the smoke aspiration, from hood to filters.

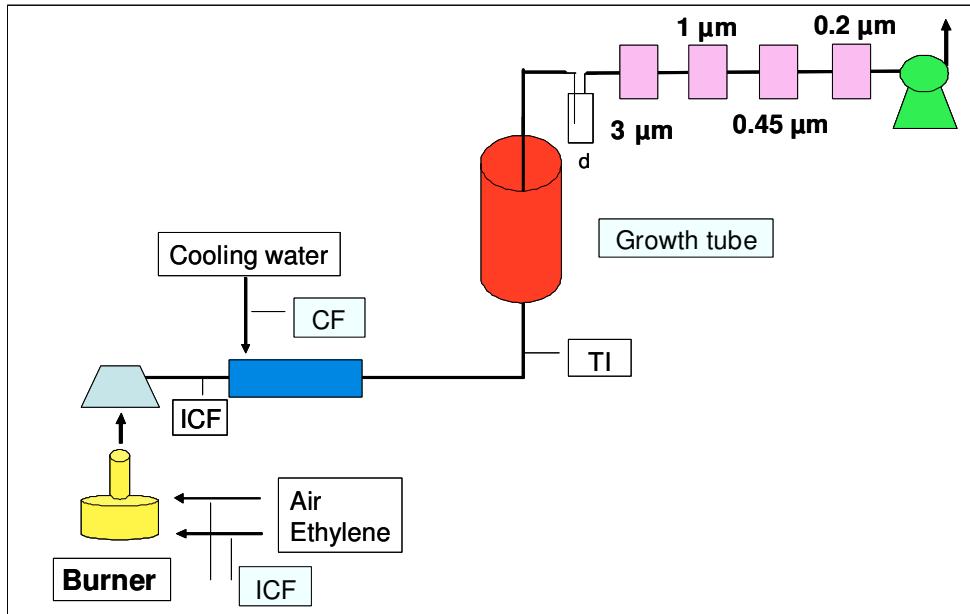


**Figure 3.6** - Experimental set up with use of filter. ICF: Indicator Controller Flow; TI: Temperature Indicator; CF: Controller Flow; d: drechsel

The measurement devices used for on line analysis of particles concentration are DMA and LAS 3340.

For the tests with the DMA, the gas leaving the growth tube is totally deviated to the device. The particles are produced by a Bunsen burner fed with methane. Before the DMA are placed three drechsels, to prevent damage to the instrument due to the excessive presence of water. In the Figure 3.7 is shown the corresponding experimental set up. The smoke aspiration is performed by the pump of the same DMA.

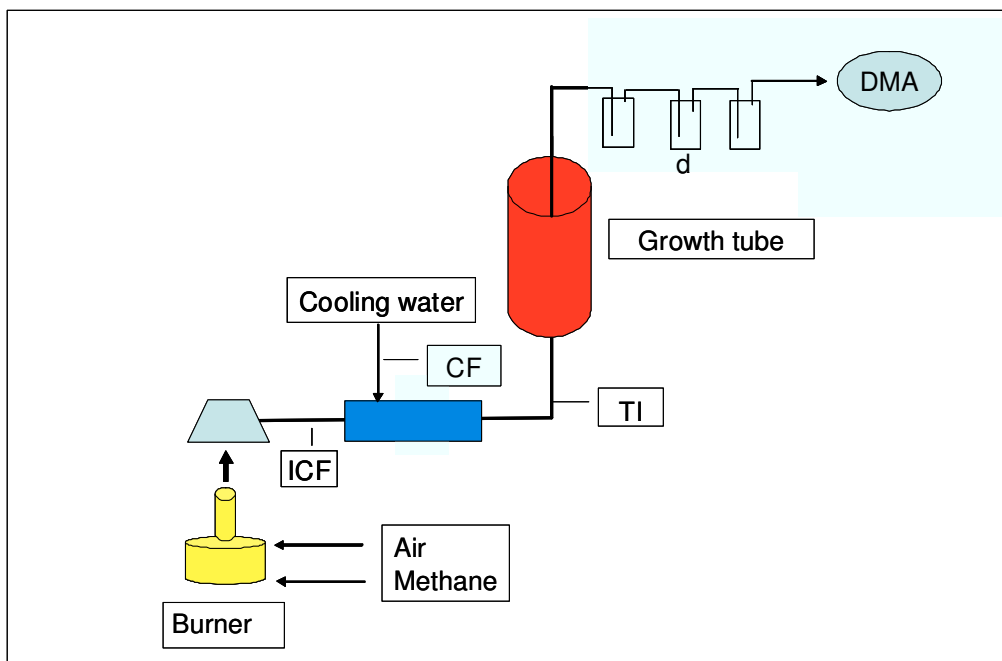


**Figure 3.7** - Experimental set up with use of DMA as on line measurement device. TI: Temperature Indicator; CF: Controller Flow; d: drechsel

For the tests with the LAS 3340 (Figure 3.8), a pump is collocated immediately after the hood to allow the aspiration of smoke from the burner and to send gas in the pipeline. The drechsel was placed immediately after the hood in order to prevent damage to the pump due to the excessive presence of water.

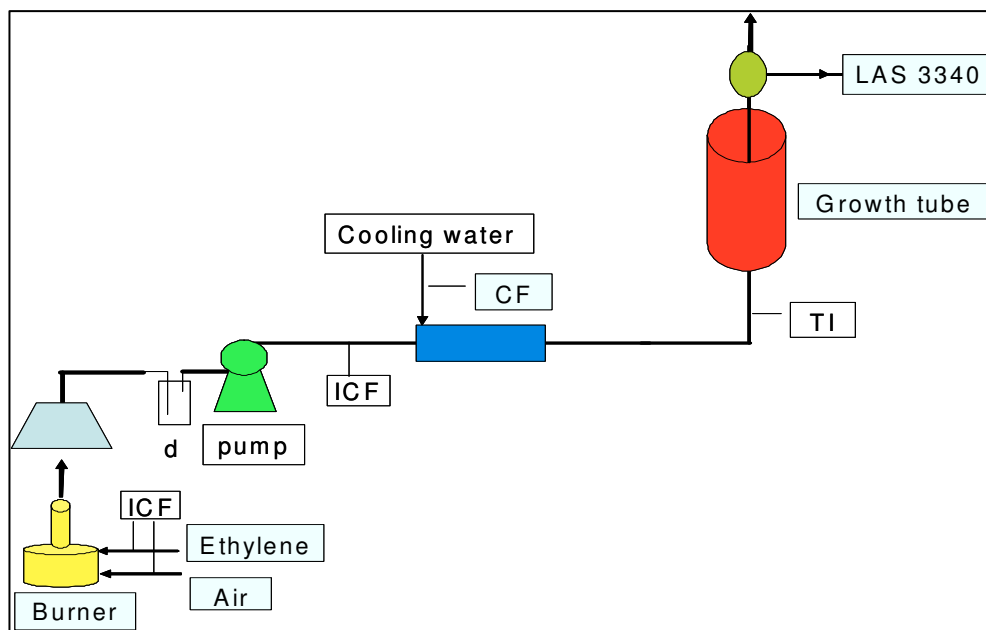


**Figure 3.8** - Experimental apparatus with use of LAS 3340. ICF: Indicator Controller Flow; TI: Temperature Indicator; CF: Controller Flow; d: drechsel

The gas leaving growth tube is sampled from main flow (Figure 3.9), through a steel probe inserted in a flexible tube made in PTFE and coaxial with growth tube. The probe has a hook shape, with the opening facing against the flow of gas and was designed to allow an isokinetic sampling. The probe is connected to LAS 3340 through a PTFE flexible tube.

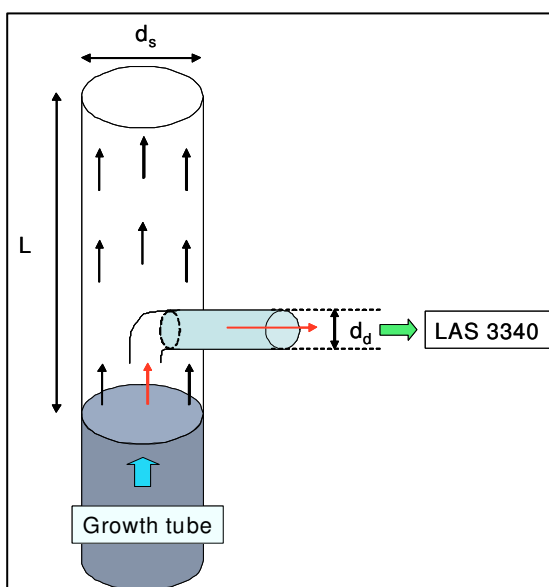


**Figure 3.9** – Isokinetic probe for the sampling system at outlet of growth tube for analysis with LAS 3340.  $L = 10$  cm;  $d_s = 1$  cm;  $d_d = 0.4$  cm

## 2. Measurement device

One of the most relevant problems in the experimental activities regards the detection and the analysis of particulate concentration and size distribution in a gas flow rich of water. For this reason, different analytical techniques have been utilised in order to obtain the best result for our experimental activities. In the following, the techniques adopted in this thesis are illustrated, in details.

### 2.1. Dynamic Light Scattering (DLS)

**Dynamic Light Scattering** (sometimes referred to as **Photon Correlation Spectroscopy** or **Quasi-Elastic Light Scattering**) is a technique for measuring the size of particles typically in the sub micron region. Light scattering methodologies allow for both real-time and on line monitoring of aerosols. The intensity of the elastically scattered light varies as the sixth power of diameter for nanoparticles. Because of this, the scattered light signals from nanoparticles are very small and cannot be detected reliably. Nonelastic light scattering methodologies, such as dynamic light scattering, have been used for measuring nanoparticles. Dynamic light scattering, also called photon correlation spectroscopy, is the spectral broadening of the signal because of Brownian motion of the particles. In this method, the diffusion coefficient of the particles is determined by interpretation of the dynamically scattered light signal, and with knowledge of the temperature, an estimate of the particle size can be obtained. Clearly, this poses challenges several because of the difficulties in an accurate determination of temperature, for example, in combustion systems. Moreover, the optics are rather complicated, and, hence, the technique is not extensively used for *in situ* monitoring. However, there are several commercial instruments that are used offline to determine the fractional size distributions of particles in the nanometer-size regime

#### 2.3.2 Brownian motion

DLS measures Brownian motion and relates this to the size of the particles. Brownian motion is the random movement of particles due to the collision with by the solvent molecules that surround them. Normally DLS is concerned with measurement of particles suspended within a liquid. The larger the particle, the slower the Brownian motion will be.

Smaller particles are “kicked” further by the solvent molecules and move more rapidly. An accurate measure of temperature is necessary for DLS since knowledge of the viscosity is required. The temperature also needs to be stable, otherwise convection currents in the sample will cause non-random movements that will ruin the correct interpretation of size. The velocity of the Brownian motion is defined by a property known as *translational diffusion coefficient* (usually given the symbol,  $D$ ).

The size of a particle is the hydrodynamic diameter and is calculated from the translational diffusion coefficient by using the Stokes-Einstein (Eq. 1 Appendix). The diameter that is measured in a DLS is considered the hydrodynamic diameter. The diameter that is obtained by this technique is the diameter of a sphere that has the same translational diffusion coefficient as the particle. The translational diffusion coefficient will depend not only on the size of the particle “core”, but also on any surface structure, as well as the concentration and type of ions in the solvent. The factors that affect the diffusion speed of particles are the strength of the solvent; the particle surface structure and the particle sphericity.

### 2.3.3 Effect of the ionic strength of the solvent

The ions in the solvent and the total ionic concentration can affect the particle diffusion speed by changing the thickness of the electric double layer, which is named *Debye length*. Thus a low conductivity solvent will produce an extended double layer of ions around the particle, reducing the diffusion speed and resulting in a larger, apparent hydrodynamic diameter. Conversely, higher conductivity media will suppress the electrical double layer and reduces the measured hydrodynamic diameter.

The performance of a DLS instrument is normally verified by measurement of a suitable polystyrene latex standard. If the standard needs to be diluted prior to measurement, then dilution in an appropriate solvent is important. The International Standard on DLS (ISO13321 Part 8 1996) says that dilution of any polystyrene standard should be made in 10mM NaCl. This concentration of salt will suppress the electrical double layer and ensure that the hydrodynamic diameter reported will be the same as the hydrodynamic diameter on the certificate or the expected diameter.

### 2.3.4 Effect of the particle surface structure

Any change to the surface of a particle that affects the diffusion speed will correspondingly change the apparent size of the particle. An adsorbed polymer layer projecting out into the solvent will reduce the diffusion speed more than if the polymer is lying flat on the surface. The nature of the surface and the polymer, as well as the ionic concentration of the solvent can affect the polymer conformation, which in turn can change the apparent size by several nanometres.

### 2.3.5 Non-Spherical Particles

All particle-sizing techniques have an inherent problem in describing the size of non-spherical particles. The sphere is the only object whose size can be unambiguously described by a single figure. Different techniques are sensitive to different properties of the particle, e.g. projected area, density, scattering intensity, and in general will produce different mean sizes and size distributions for any given sample. Even the size in a microscope image will depend on parameters set, such as edge contrast etc. It is important to understand that none of these results are inherently “correct”.

The hydrodynamic diameter of a nonspherical particle is the diameter of a sphere that has the same translational diffusion speed as the particle. If the shape of a particle changes in a way that affects the diffusion speed, then the hydrodynamic size will change. For example, small changes in the length of a rod-shaped particle will directly affect the size, whereas changes in the rod’s diameter, which will hardly affect the diffusion speed, will be difficult to detect. The conformation of proteins and macromolecules are usually dependent on the exact nature of the dispersing solvent. As conformational changes will usually affect the diffusion speed, DLS is a very sensitive technique for detecting these changes.

### 2.3.6 Light Scattering Theories Rayleigh Scattering

If the particles are small compared to the wavelength of the laser used (typically less than  $d = \lambda/10$  or around 60nm for a He-Ne laser), then the scattering from a particle illuminated by a vertically polarised laser will be essentially isotropic, i.e. equal in all directions.

The Rayleigh approximation tells us that ( $I \propto d^6$ ) and also that ( $I \propto 1/\lambda^4$ ), where

- $I$  = intensity of light scattered,
- $d$  = particle diameter
- $\lambda$  = laser wavelength.

The  $d^6$  term tells us that a 50nm particle will scatter  $10^6$  or one million times as much light as a 5nm particle. Hence there is a danger that the light from the larger particles will swamp the scattered light from the smaller ones. This  $d^6$  factor also means it is difficult with DLS to measure, for example, a mixture of 1000 nm and 10 nm particles because the contribution to the total light scattered by the small particles will be extremely small. The inverse relationship to  $\lambda^4$  means that a higher scattering intensity is obtained as the wavelength of the laser used decreases.

### **2.3.7 Mie Theory**

When the size of the particles becomes roughly equivalent to the wavelength of the illuminating light, then a complex function of maxima and minima with respect to the scattering angle is observed. Figure 3.10 shows the theoretical plot of the log arithmetic of the relative scattering intensity versus the particle size at angles of  $173^\circ$  (the detection angle of the Zetasizer Nano S and Nano ZS in aqueous media) and  $90^\circ$  (the detection angle of the Nano S90 and Nano ZS90) assuming a laser wavelength of 633nm, real refractive index of 1.59 and an imaginary refractive index of 0.001. Mie theory is the only theory that explains correctly the maxima and minima in the plot of intensity with angle and will give the correct answer over all wavelengths, sizes and angles. Mie theory is used in the Nano software for conversion of the intensity distribution into volume.

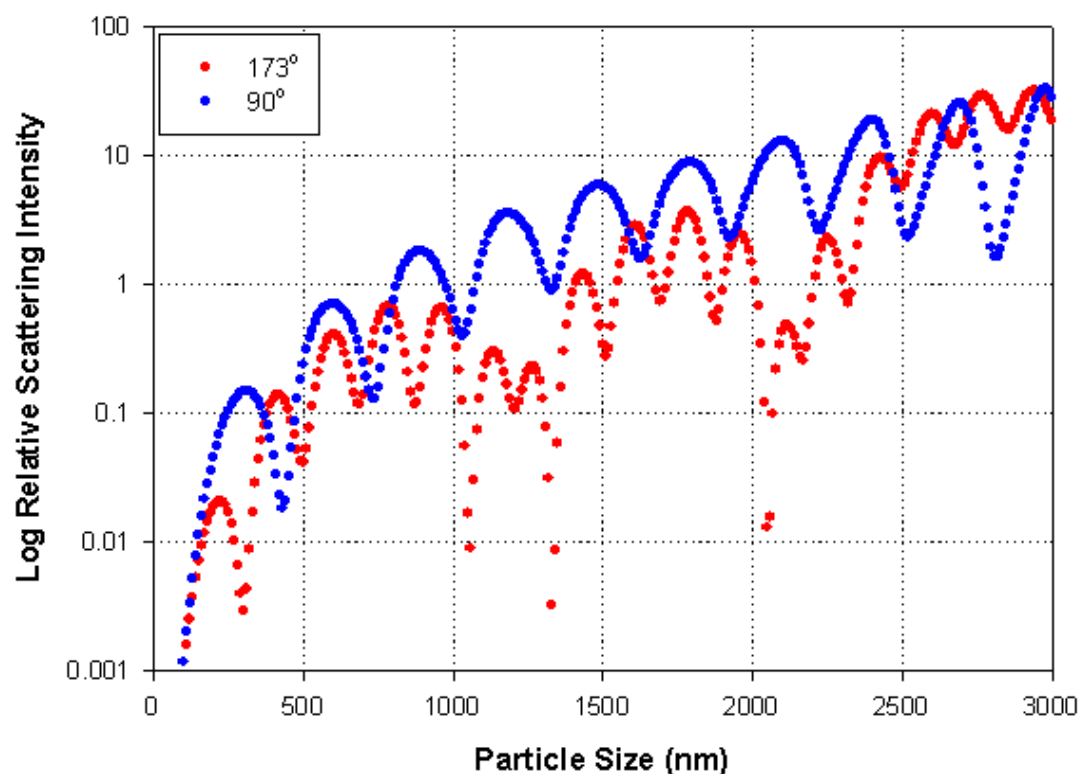


**Figure 3.10** - Theoretical plot of the log of the relative intensity of scattering versus particle size at angles of  $173^\circ$  (the detection angle of the Nano S, and Nano ZS in aqueous media) and  $90^\circ$  (the detection angle of the Nano S90 and Nano ZS90) assuming a laser beam at a wavelength of 633nm, real refractive index of 1.59 and an imaginary refractive index of 0.001

### 2.3.8 How the DLS works

In dynamic light scattering, the speed at which the particles are diffusing due to Brownian motion is measured. This is done by measuring the rate at which the intensity of the scattered light fluctuates when detected using a suitable optical arrangement. When a liquid sample that contains stationary particles is illuminated by a laser and a frosted glass screen to view the sample cell is used, a classical speckle pattern would be seen (Figure 3.11).



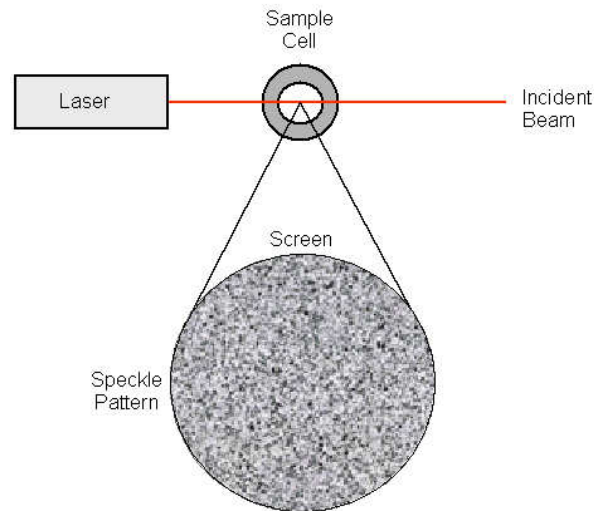


**Figure 3.11** - Schematic representation of a speckle pattern

The speckle pattern will be stationary both in speckles size and position, because the whole system is stationary. The dark spaces are where the phase additions of the scattered light are mutually destructive and cancel each other out (Figure 3.12A). The bright “blobs” of light in the speckle pattern are where the light scattered from the particles arrives with the same phase and interfere constructively to form a bright patch (Figure 3.12B).

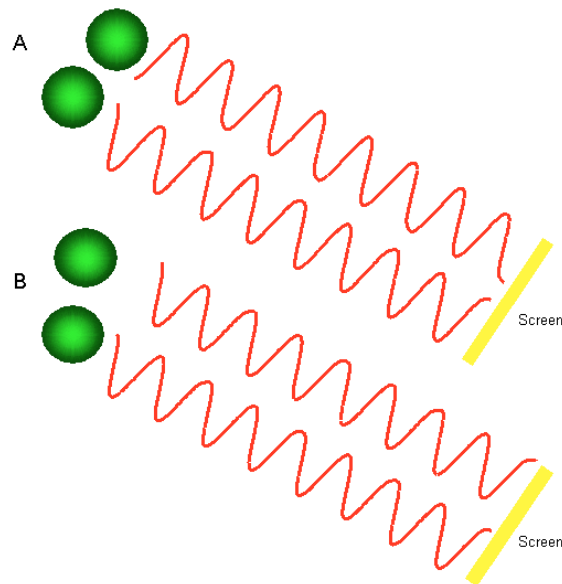


**Figure 3.12** - The observed signal depends on the phase addition of the scattered light falling on the detector. In example A, two beams interfere and ‘cancel each other out’ resulting in a decreased intensity detected. In example B, two beams interfere and ‘enhance each other’ resulting in an increased intensity detected.

For a system of particles undergoing Brownian motion, a speckle pattern is observed when the position of each speckle is seen to be in constant motion. This is because the phase

addition from the moving particles is constantly evolving and forming new patterns. The rate at which these intensity fluctuations occur will depend on the size of the particles. Figure 3.13 schematically illustrates typical intensity fluctuations arising from a dispersion of large particles and a dispersion of small particles. The small particles cause the intensity to fluctuate more rapidly than the large ones.

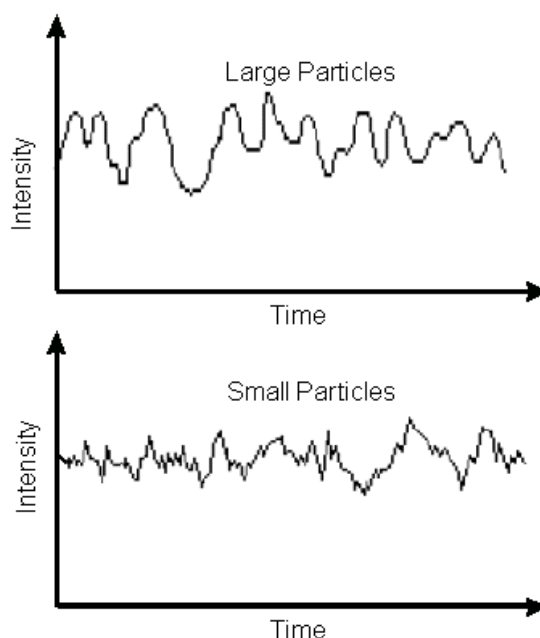


**Figure 3.13** - Typical intensity fluctuations for large and small particles

### 2.3.9 How a Correlator works

A correlator is basically a signal comparator. It is designed to measure the degree of similarity between two signals, or one signal with itself at varying time intervals. If the intensity of a signal is compared with itself at a particular point in time and a time much later, then for a randomly fluctuating signal it is obvious that the intensities are not going to be related in any way, i.e. there will be no correlation between the two signals (Figure 3.14). Knowledge of the initial signal intensity will not allow the signal intensity at time  $t = \text{infinity}$  to be predicted. This will be true for any random process such as diffusion. However, if the intensity of signal at time  $t$  is compared to the intensity a very small time later ( $t + \delta t$ ), there will be a strong relationship or correlation between the intensities of two signals. The two signals are strongly or well correlated. If the signal, derived from a random process such as Brownian motion at  $t$ , is compared to the signal at  $(t + 2\delta t)$ , there will still be a reasonable comparison or correlation between the two signals, but it will not be as good as the comparison at  $t$  and  $(t + \delta t)$ . The correlation efficiency is reducing with time. The period of time  $\delta t$  is usually very small, maybe nanoseconds or microseconds and

is called the sample time of the correlator. If the signal intensity at  $t$  is compared with itself there is perfect correlation as the signals are identical. Perfect correlation is indicated by unity (1.00) and no correlation is indicated by zero (0.00). If the signals at  $t+2\delta t$ ,  $t+3\delta t$ ,  $t+4\delta t$  etc. are compared with the signal at  $t$ , the correlation of a signal arriving from a random source will decrease with time until at some time, effectively  $t = \infty$ , there will be no correlation. If the particles are large, the signal will be changing slowly and the correlation will persist for a long time (Figure 3.15). If the particles are small and moving rapidly, then correlation will reduce more quickly (Figure 3.16).

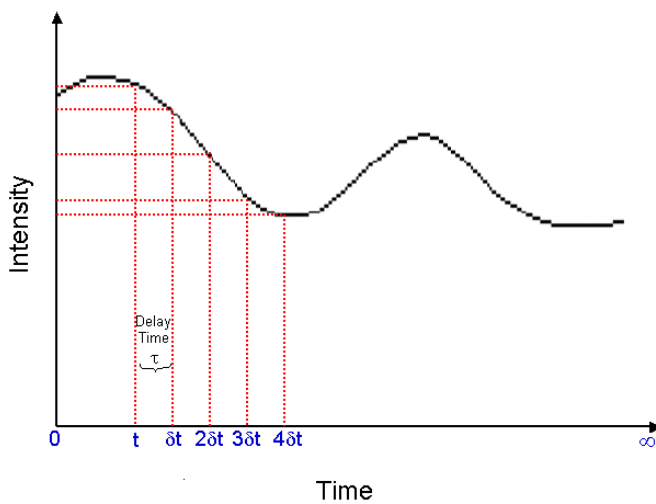


**Figure 3.14** - Schematic showing the fluctuation in the intensity of scattered light as a function of time

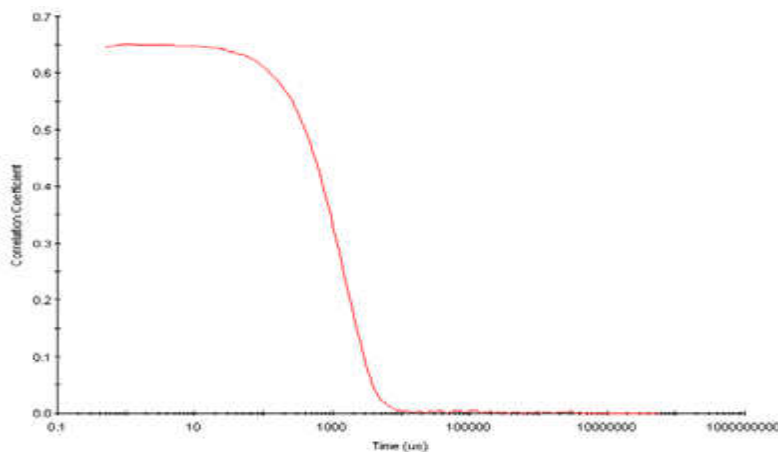


**Figure 3.15** - Typical correlogram from a sample containing large particles in which the correlation of the signal takes a long time to decay

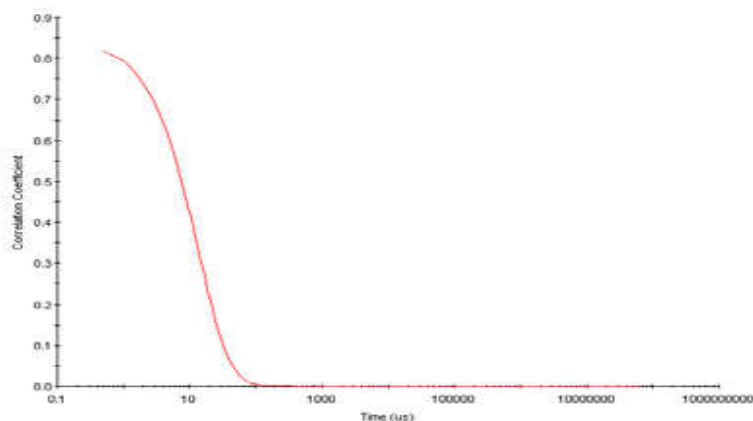


**Figure 3.16** - Typical correlogram from a sample containing small particles in which the correlation of the signal decays more rapidly

## 2.4 Differential Mobility Analyzer (DMA)

Scanning Mobility Particle Sizes (SMPS) is useful experimental tool for the study of the emissions of carbonaceous ultrafine and fine particles since, in principle, it furnishes the measure of the size distribution of aerosols in size ranges from 1 to 1000 nm.

The Model 3936 SMPS, used in this thesis, measures the number size distribution of particles using an electrical mobility detection technique. The SMPS uses a bipolar charger in the Electrostatic Classifier to charge the particles to a known charge level distribution. The particles are then classified according to their ability to traverse an electrical field, and counted.

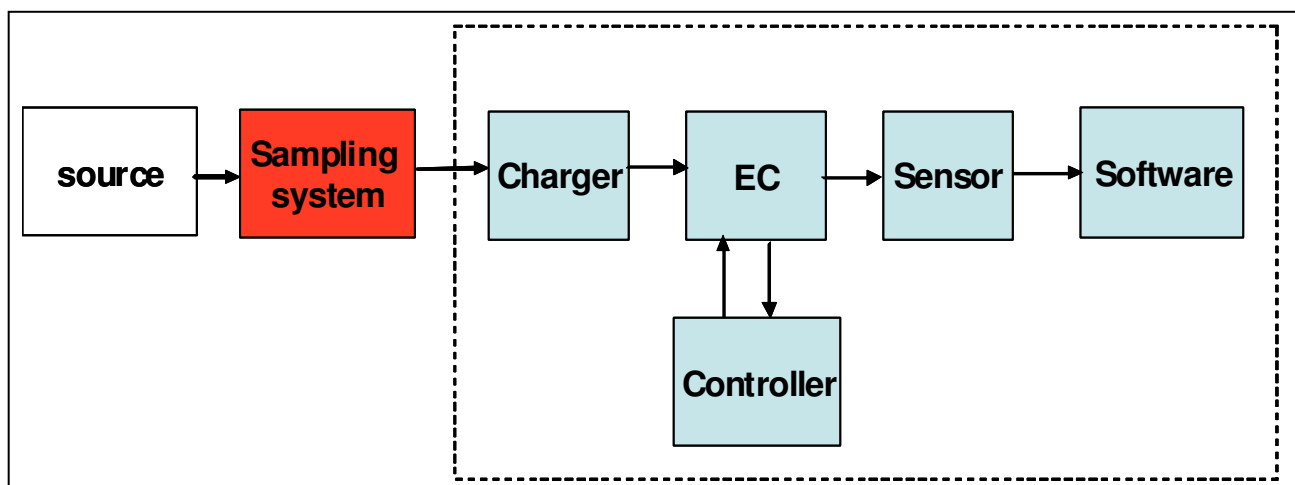


**Figure 3.17** – General sketch of the measurement with SMPS

As schematically displayed in Figure 3.17, the sampling systems are generally made of five main components: a charger which brings the polydisperse aerosol sample to a well defined “steady-state” (size dependent) charge distribution (Adachi *et al.*, 1983; Wiedensohler *et al.*, 1986; Wiedensohler, 1988), a controller to determine flows and high-voltage, an electrostatic classifier (EC), a sensor which measure the particle concentration and a customized software to control individual instruments, collect and store sample data. Specifically, polydisperse aerosol, entering the charger, receive either a unipolar charge in the case of unipolar charger (ionizer) or positive, negative or zero charge in the case of a radioactive bipolar charger (neutralizer). Then, particles enter the electrostatic classifier (EC) where they are separated by their ability to transverse an electric field, namely by their electrical mobility. Thus a DMA classifies particles according to their electrical mobility.

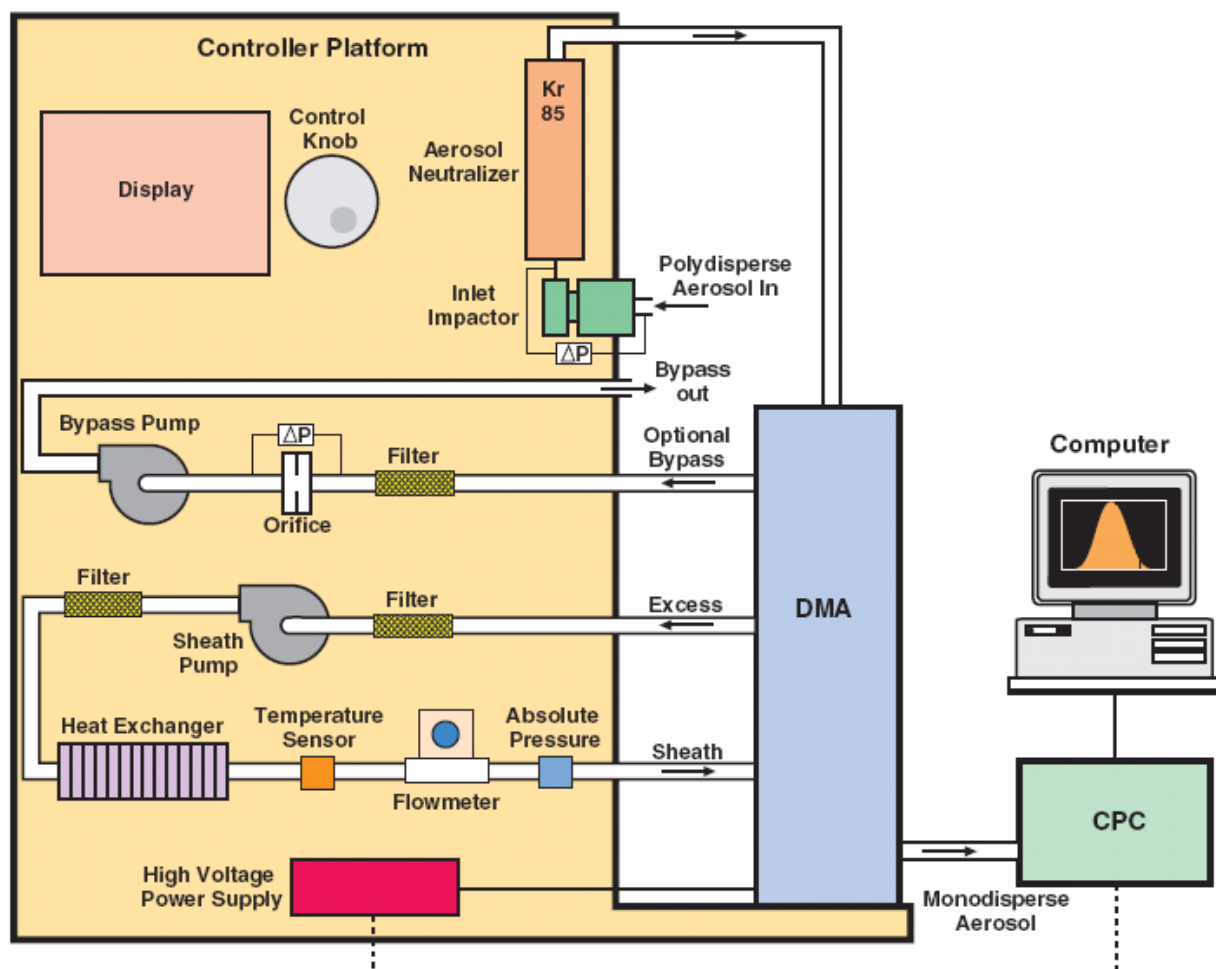


**Figure 3.18** – Scheme of DMA (series 3936)

The DMA (Figure 3.18) employs a cylindrically symmetric electric field applied to the electrostatic classifier to separate the charged aerosol particles. A stainless steel cylinder

constitutes the outer electrode with a metal rod, lined along its axis, working as the inner electrode of the electrostatic classifier (EC) where the particles are separated by their ability to transverse an electric field, namely by their electrical mobility. The sample charged aerosol enters the outer periphery of the classifier and mixes with a larger laminar sheath of particle free air,  $Q_{sh}$ , which flows through the annular cavity between the two electrodes, with inner radius  $R_1$  and outer radius  $R_2$ . The electric field applied across the central rod and the outer cylinder attracts the opposite charged particles toward the rod. Particles with a narrow range of electrical mobility  $\Delta Z$  have the proper trajectory to travel from the aerosol inlet to the exit aperture (distance of the travel,  $L$ ) and enter the sensor for the subsequent detection. Thus, the size distribution is calculated from the distribution of  $Z$  (V), as function of the applied voltage or the electric field in the classifier, in terms of mobility diameter,  $dm^2$ , by the Millikan-Fuchs's equation, which is valid for spherical particles:

$$Z = \frac{Q_{sh}}{2\pi VL} \ln \left( \frac{R_2}{R_1} \right) = \frac{qeC_c}{3\pi\mu d_m} \quad (3.12)$$

where  $q$  is the number of charges on the particles,  $e$  is the unit charge, and  $\mu$  is the viscosity of the carrier gas. The Cunningham correction factor,  $C_c$ , is a function of the Knudsen number (Hinds, 1999),

$$C_c = 1 + K_n \left[ \alpha + \beta \exp \left( -\frac{\gamma}{K_n} \right) \right]^3 \quad (3.13)$$

Where

$$\alpha = 1.142$$

$$\beta = 0.558$$

$$\gamma = 0.999$$

(Allen *et al.*, 1985)

With the Electrometer, the current delivered by charged particles is measured by a Faraday Cup (Flagan, 1998). The particle concentration,  $N_{ae}$ , is obtained from the aerosol electrometer current,  $I$ , using the following relationship:

$$N_{ae} = \frac{I}{Qe} \quad (3.14)$$

where Q is the volumetric flow rate through the electrometer, e is the charge per electron. The advantage of the Electrometer is to provide an independent measurement that does not rely on condensation and on the particle size.

After exiting the DMA, the classified particles are counted by a CPC, which accurately measures the particle concentration. By ramping the voltage of the inner electrode exponentially over a user-selected period of time, the entire particle size distribution and number concentration are measured to a high degree of accuracy. The flow rates in the Series 3080 Electrostatic Classifiers are temperature and pressure corrected. The principle of the Model 3080 Electrostatic Classifier, used in this thesis, is based on the monotonic relationship between electrical mobility and particle size charged with one electron only. To ensure a fixed percentage of particles carrying one unit of charge, the particles are introduced to a bipolar charge where they undergo frequent collisions with bipolar ions. This process is known as bipolar charging or “neutralization.” As a result, an equilibrium state is obtained, with known percentages of particles carrying no charge, a single charge, or multiple charges of both positive and negative polarity. These aerosol particles are then measured with the differential mobility analyzer. The mobility distribution, and hence size distribution, can be determined from the measurement.

The Aerosol Instrument Manager software controls the counting process, as well as data collection, calculation, and storage. It also corrects for multiple-charge effects and CPC detection efficiency.

## **2.5 Laser Aerosol Spectrometer (LAS) model 3340**

The Model 3340 by TSI (TSI Incorporated), is a laser aerosol spectrometer that measures the size of particles as a function of the amount of light scattered by the particle as it passes through an intense laser beam.

In the instrument, particles are confined to the centerline of the laser beam by sheath air. Side-scattered light is collected by dual Mangin mirror pairs that focus the collected light onto two solid-state photodetectors. The electronics convert the light pulses into electrical pulses, the amplitude of which are then measured to determine the diameter for each individual particle. Transit times are also measured and minimum and maximum transit thresholds may be set for each detector gain stage.

The TSI Model 3340 is able to sizing particles in the range from 90 nm to 7.5  $\mu\text{m}$  in diameter. It uses fully user-specified size binning of up to 100 channels anywhere within its size range.

The spectrometer instrument consists of five general subsystems:

- ✓ The main optical subsystem responsible for generating the laser light, detecting the scattering from the particles and providing a mechanical enclosure for the optical system and for delivery of the sample aerosol.
- ✓ The flow system for bringing the sample aerosol through the optical interaction region, including flow control and measurement.
- ✓ The analog electronics system for amplifying and processing the particle signals.
- ✓ The digital electronics system for analyzing particle signals, binning signals according to user-specified bin mappings and generating a histogram of number of particles in the specified bins, and for communicating with the PC and system monitor/control functions.
- ✓ An onboard PC running Windows and a specialized application GUI for instrument control, setup and data reporting and collection.

### **2.3.1 Optical System**

The Optical system consists of

- The laser and associated components and optics.
- The detection system, including collection optics and photodetectors and reference monitoring.
- Mechanical housing for above.



### 2.3.2 Laser and Associated Components and Optics

The laser is a Helium-Neon gas laser. It operates in the fundamental spatial mode on the 633 nm laser line with an intracavity power  $\sim 1$  to 10 W. The laser mode has a  $1/e^2$  intensity diameter of  $\sim 400$   $\mu\text{m}$  at the interaction region. The standing wave laser mode is perpendicular to the flow of particles. Particle scatter is collected in a direction perpendicular to both the particle flow and the laser standing-wave. As particles traverse the laser mode, they scatter light into the detection system. The amount of light scattered is a strong function of the particle size.

### 2.3.3 Detection System

The detection system consists of two pairs of Mangin collection optics capable of collecting light over a large solid angle. The Mangins image the volume of space at which the flow intersects the laser mode onto a photodiode. There are two pairs of collecting optics: one pair images onto an Avalanche Photo Diode (APD) for detecting the smallest particles (the primary scattering detection system). The other pair (located on the opposite side of the block) images onto a low-gain PIN photodiode for detection of the upper size range of the instrument (the secondary scattering detection system). Each detector is amplified in a current-to-voltage stage which feeds the analog electronics system. The system can detect particles as small as 90 nm ( $\geq 50\%$  efficiency,  $< 0.1$  count/ 5 minute dark count rate). The system size sensitivity is limited by several noise sources: a baseline noise process from the photon shot noise on the detected molecular scatter from background gas, a baseline noise process from the Johnson noise in the photodiode transimpedance feedback resistor and from technical noise of various sources.

### 2.3.4 Flow System

The mechanical laser mount forms a sealed block around the laser and the input/output jets. A pump draws on an exhaust jet pulling flow through the inlet jet and across the laser mode. The input jet is an aerodynamically focused assembly with a sample nozzle of 500- $\mu\text{m}$  diameter and a sheath nozzle of 760- $\mu\text{m}$  diameter. The tip of the sheath jet sits close to the edge of the laser mode. Sample flows are between 5 and 100  $\text{Ncm}^3/\text{min}$  and the sheath flow is typically 650  $\text{Ncm}^3/\text{min}$ . Particle velocity depends on sheath flow rate, but is on the order of 50 to 100 m/s. The particles are confined to a region of space whose extent

is limited to a fraction of the laser mode size. This yields a sizing resolution of approximately 5% of the particle size.

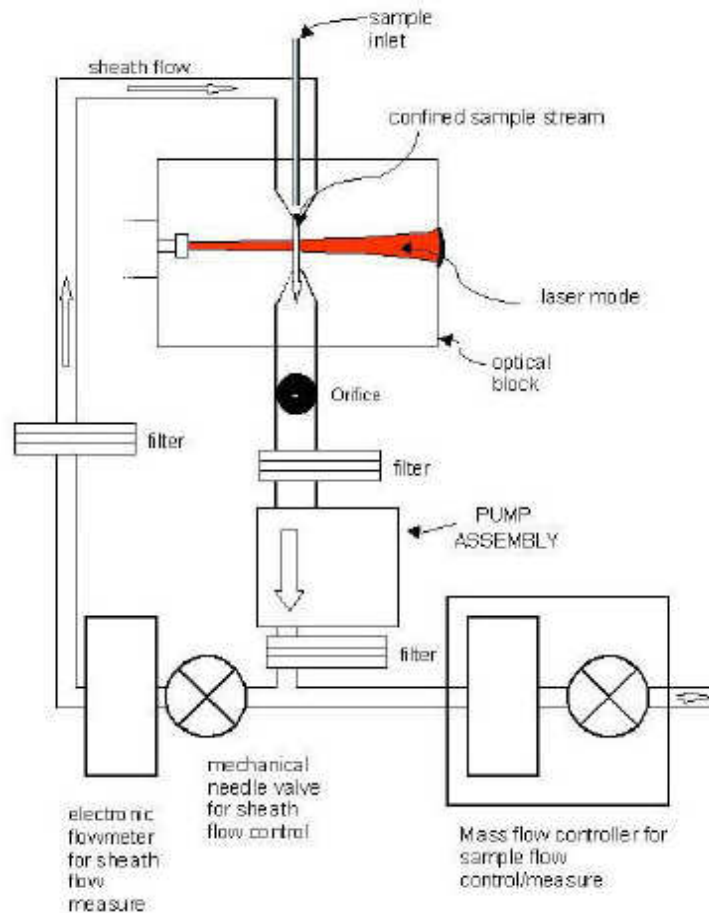


**Figure 3.19 - Schematic Diagram of Flow System**

### 2.3.5 Simulation of measurement with LAS 3340

At the exit of the growth tube, the suspended aerosol phase is made by the solid particles and by the condensed water droplets, part of which including the solid nuclei. Therefore, the aerosol is made by a mixture of different materials, characterized by a different refractive index. This leads to possible incorrect size detection by laser scattering based devices. For this reason, in collaboration with Institute of Research on Combustion of Naples, a simulation of measurement of droplets with inclusions by LAS 3340 is been performed, as can be seen from following figure, in order to evaluate the error by considering the droplet with inclusions as a pure component droplet.

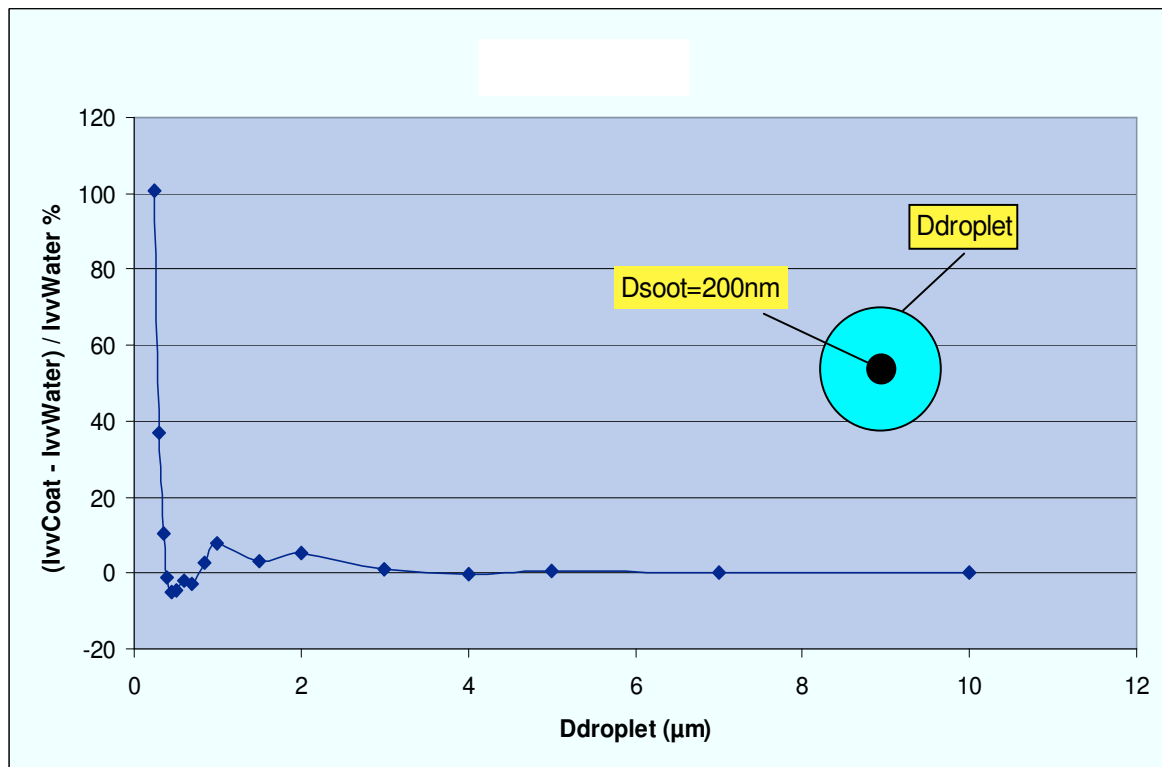


**Figure 3.20** – Error of measurement considering the droplets with inclusions as composed by pure component, vs diameter

The case study consists in the analysis of the scattering signal for a particle with diameter of 200nm included in a drop of water. On the axis x of Figure 3.20 is reported the outer diameter of the drop. Then the computation was held fixed the core of soot while the thickness of the layer of water was varied. For example, 1 micron mean  $D_{\text{droplet}} = 200 \text{ nm (core)} + 400 \text{ nm (thickness of the water)}$ .

Two tests have been considered: a homogeneous drop of water and a 200 nm soot particle surrounded by a water layer having the same diameter of the homogeneous drop. For each diameter, the LAS 3340 provides two intensity of light scattering between  $35^\circ$ - $120^\circ$ ,  $I_{\text{vvcoat}}$  for heterogeneous case and  $I_{\text{vvwater}}$  for the homogeneous case.

As can be seen from Figure 3.20, from the simulation appears that for  $D_{\text{droplet}} > 2\mu\text{m}$  the presence of core soot has weakly influence. In fact the variation is less than 5%.

### 3. Preliminary test

We have seen that the growth tube utilised is been designed and realised especially for this thesis. In order to verify the functionality, some preliminary tests are been performed. We will divide the tests in two groups, depending on the measurement device used. The experimental set up is also different for each group.

#### 3.1 Preliminary test with DLS

The following tests have been performed with use of DLS as device for analysis of particles size. These tests are divided in two subgroup, called I and II.

##### 3.1.1 Preliminary Test I

Preliminary tests have been performed on the experimental system in Figure 3.21.

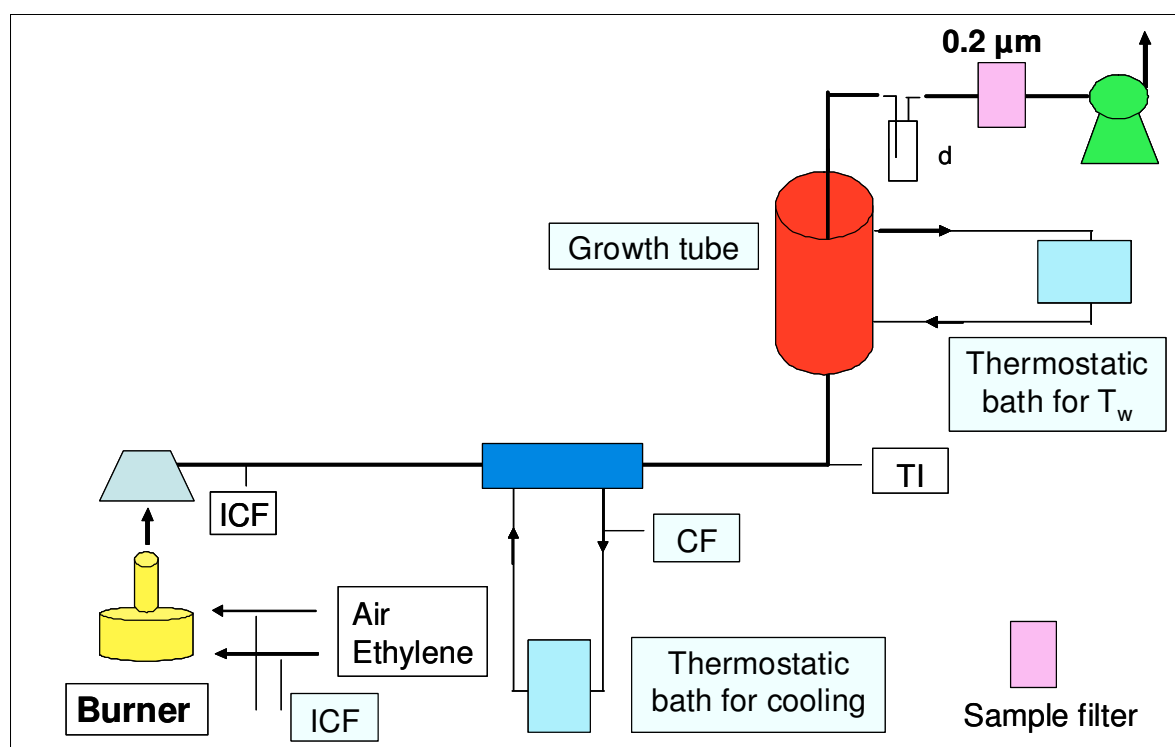


**Figure 3.21** – Experimental plant for preliminary test I

The particles were produced by burning natural gas using a Bunsen burner.

In the following table (table 3.1) are shown the operating conditions of the tests. Can be seen that two kind of tests are performed. The first is the blank test, without any flame (Test 1 and 2); the second is the tests with flame (Test 3 and 4). The mesh of the sample

filter was 200 nm. The total flow of gas, composed by burned gas and indoor air, is 1 l/min, corresponding to residence time equal to 4.2 s. The duration of each test is 15 minutes.

Without flame	
Test 1	Test 2
$T_w = 293 \text{ K (20 } ^\circ\text{C)}$	$T_w = 333 \text{ K (60 } ^\circ\text{C)}$
$T_{\text{gas}} = 293 \text{ K (20 } ^\circ\text{C)}$	$T_{\text{gas}} = 293 \text{ K (20 } ^\circ\text{C)}$
With flame	
Test 3	Test 4
$T_w = 293 \text{ K (20 } ^\circ\text{C)}$	$T_w = 333 \text{ K (60 } ^\circ\text{C)}$
$T_{\text{gas}} = 293 \text{ K (20 } ^\circ\text{C)}$	$T_{\text{gas}} = 293 \text{ K (20 } ^\circ\text{C)}$

**Table 3.1** – Preliminary tests operating conditions (I).  $T_{\text{gas}}$ : temperature gas Inlet to growth tube;  $Q_{\text{smoke}} = 1$  l/min: total flow gas in the growth tube;  $T_w$ : temperature wall; duration each test: 15 min; residence time (tres)= 4.2 s

At the end of testing the filtrate was recovered from the filter by injection with purified water.

In Figure 3.22 the correlation coefficients recorded in the experimental trials are reported. The correlation coefficients have an exponential decay whose rate depends upon the diffusion of the particles being measured, that is their hydrodynamic radius by means of Stokes-Einstein equation. The scattering intensity is proportional to the sample concentration so that the higher is the intercept the higher is the particles concentration. DLS measurements of the four samples clearly show that in tests 1 and 2 (without the flame) no detectable trace amount of particles have been found; whereas tests 3 and 4 (with flame) produced very similar particle sizes distribution.

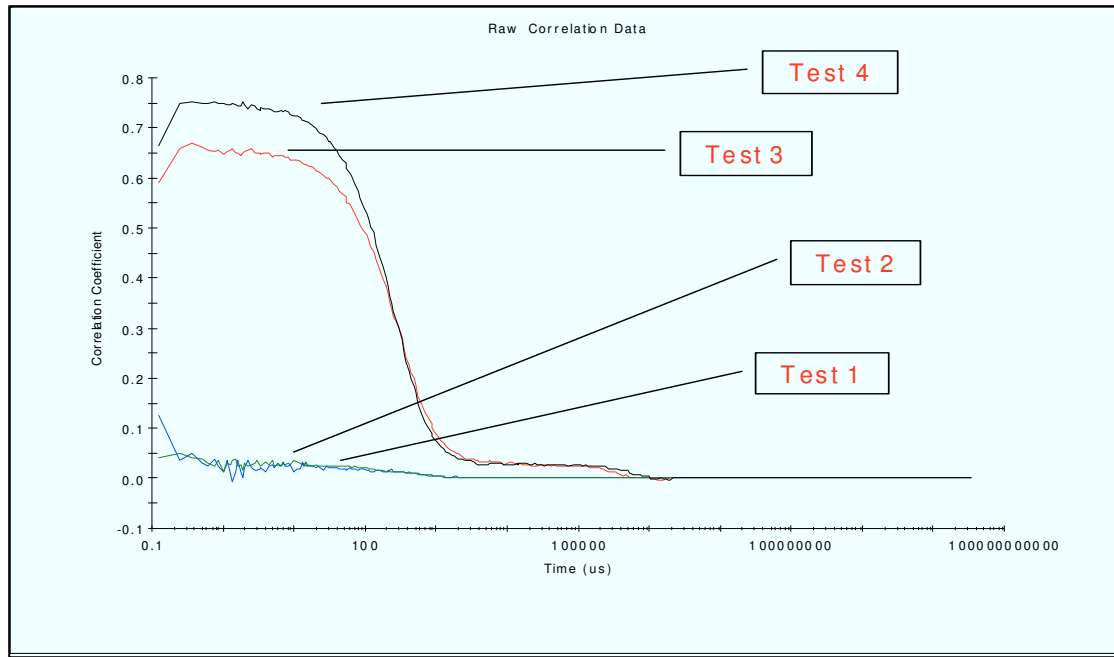


Figure 3.22 – Correlation data curve

The Table 3.2 shows the intensity recorded for samples coming from Test 3 ( $T_w = 293$  K) and Test 4 ( $T_w = 333$  K). As can be seen, in the same particle size range the sample of Test 4 shows a narrower distribution leading to higher intensity percentage.

TEST 3											
Size	Mean % Intensity	Std Dev % Intensity	Size	Mean % Intensity	Std Dev % Intensity	Size	Mean % Intensity	Std Dev % Intensity	Size	Mean % Intensity	Std Dev % Intensity
0,4	0		5,615	0		78,82	1,2		1106	0,7333	
0,4632	0		6,503	0		91,28	2,298		1281	0,3024	
0,5365	0		7,531	0		105,7	3,568		1484	0,07228	
0,6213	0		8,721	0		122,4	4,841		1718	0	
0,7195	0		10,1	0		141,8	5,979		1990	0	
0,8332	0		11,7	0		164,2	6,888		2305	0,09343	
0,9649	0		13,54	0		190,1	7,525		2669	0,2987	
1,117	0		15,69	0		220,2	7,878		3091	0,5993	
1,294	0		18,17	0		255	7,96		3580	0,951	
1,499	0		21,04	0		295,3	7,788		4145	1,292	
1,736	0		24,36	0		342	7,386		4801	1,553	
2,01	0		28,21	0		396,1	6,779		5560	1,67	
2,328	0		32,67	0		458,7	6,001		6439	0	
2,696	0		37,84	0		531,2	5,093		7456	0	
3,122	0		43,82	0		615,1	4,11		8635	0	
3,615	0		50,75	0		712,4	3,116		1e+004	0	
4,187	0		58,77	0,05047		825	2,18				
4,849	0		68,06	0,426		955,4	1,369				
TEST 4											
Size	Mean % Intensity	Std Dev % Intensity	Size	Mean % Intensity	Std Dev % Intensity	Size	Mean % Intensity	Std Dev % Intensity	Size	Mean % Intensity	Std Dev % Intensity
0,4	0		5,615	0		78,82	1,568		1106	0	
0,4632	0		6,503	0		91,28	5,116		1281	0	
0,5365	0		7,531	0		105,7	9,543		1484	0	
0,6213	0		8,721	0		122,4	13,4		1718	0	
0,7195	0		10,1	0		141,8	15,54		1990	0	
0,8332	0		11,7	0		164,2	15,47		2305	0	
0,9649	0		13,54	0		190,1	13,35		2669	0	
1,117	0		15,69	0		220,2	9,873		3091	0,031	
1,294	0		18,17	0		255	6,007		3580	0,407	
1,499	0		21,04	0		295,3	2,722		4145	1,161	
1,736	0		24,36	0		342	0,6847		4801	2,122	
2,01	0		28,21	0		396,1	0		5560	3,005	
2,328	0		32,67	0		458,7	0		6439	0	
2,696	0		37,84	0		531,2	0		7456	0	
3,122	0		43,82	0		615,1	0		8635	0	
3,615	0		50,75	0		712,4	0		1e+004	0	
4,187	0		58,77	0		825	0				
4,849	0		68,06	0		955,4	0				

Table 3.2 – Mean intensity in Test 3 and 4.

In Figure 3.23 the intensity particle size distribution of samples 3 and 4 are reported. Test 3 produced a wide distribution centred around 255 nm whereas Test 4 produced a narrow distribution with its peak at 142 nm. These results suggest that the catching mechanism of nanoparticles is different in the two cases, because the filter mesh (200 nm) is the same in both cases.

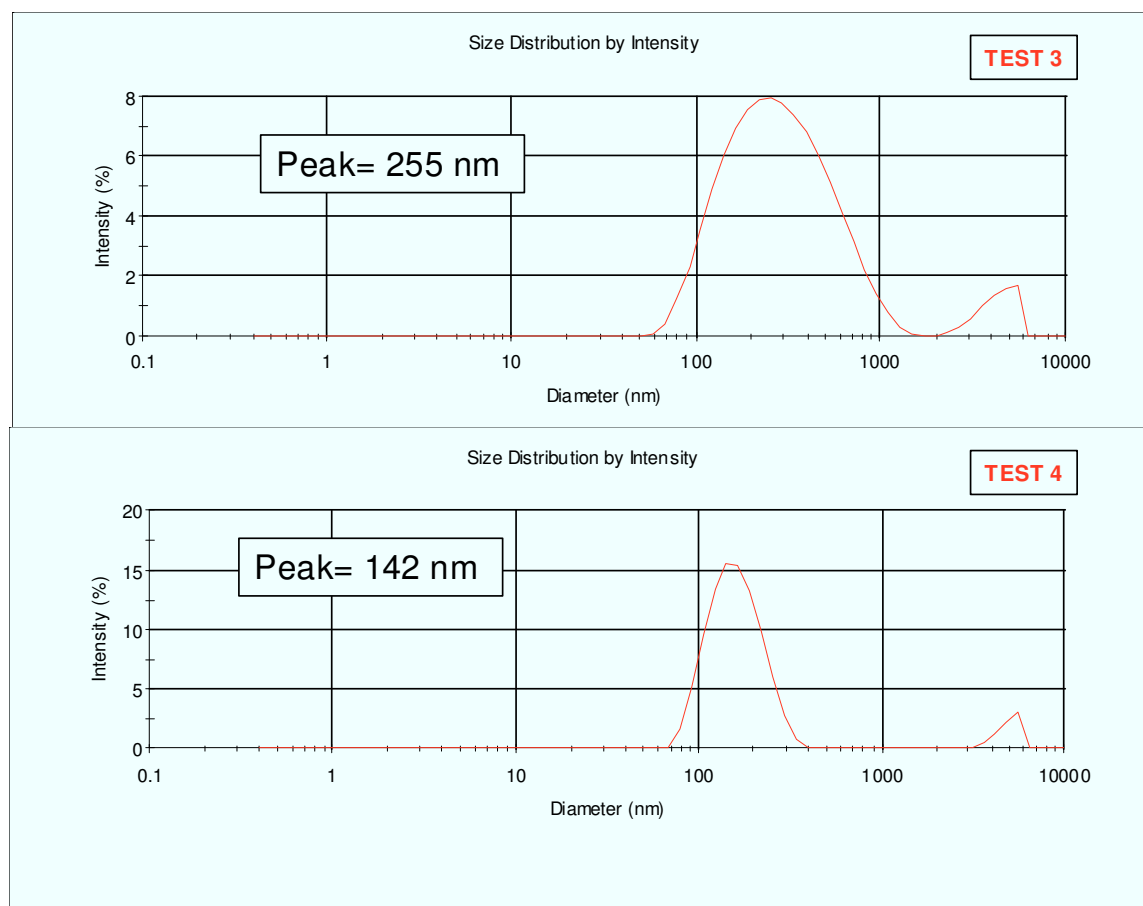


**Figure 3.23** – Curve of mean intensity test 3 and 4

By comparison of the tests results we can notice that when the water temperature is set to 333 K and gas temperature is set to 293 K (Test 4), the relative percentages of collected particles is slightly higher than when gas and water are at the same temperature (293 K, Test 3). Moreover, in test 4 the mean size of the collected particles is lower.

Therefore, we can conclude that in Test 4 the heterogeneous condensation was active giving larger particle removal efficiency. In fact, small particles (i.e.  $D_c < d_p < 200$  nm) have grown forming a complex structure 'particle + water film' (Figure 3.24) whose total dimension exceed the 200 nm of the sample filter, as the mean size of the measured particles proves.

In the other case (Test 3), the only mechanism for collecting particles is the filtration as the mean of the particle size distribution is well above 200 nm.

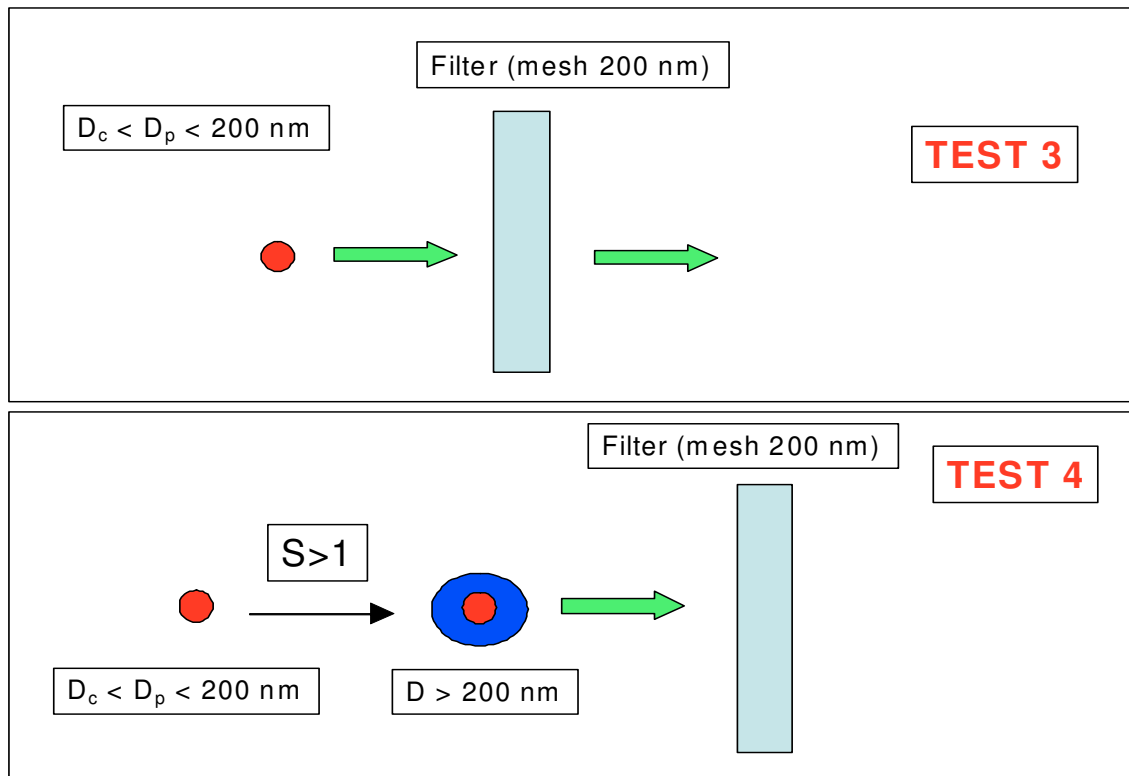


**Figure 3.24** – Scheme of Test 3 and 4 (preliminary test I)



### 3.1.2 Preliminary Test II

The second group of preliminary tests with DLS is been performed in order to found the better operating conditions and experimental set up to study the droplet growth trough heterogeneous condensation. For this purpose the set up in the following figure was adopted.

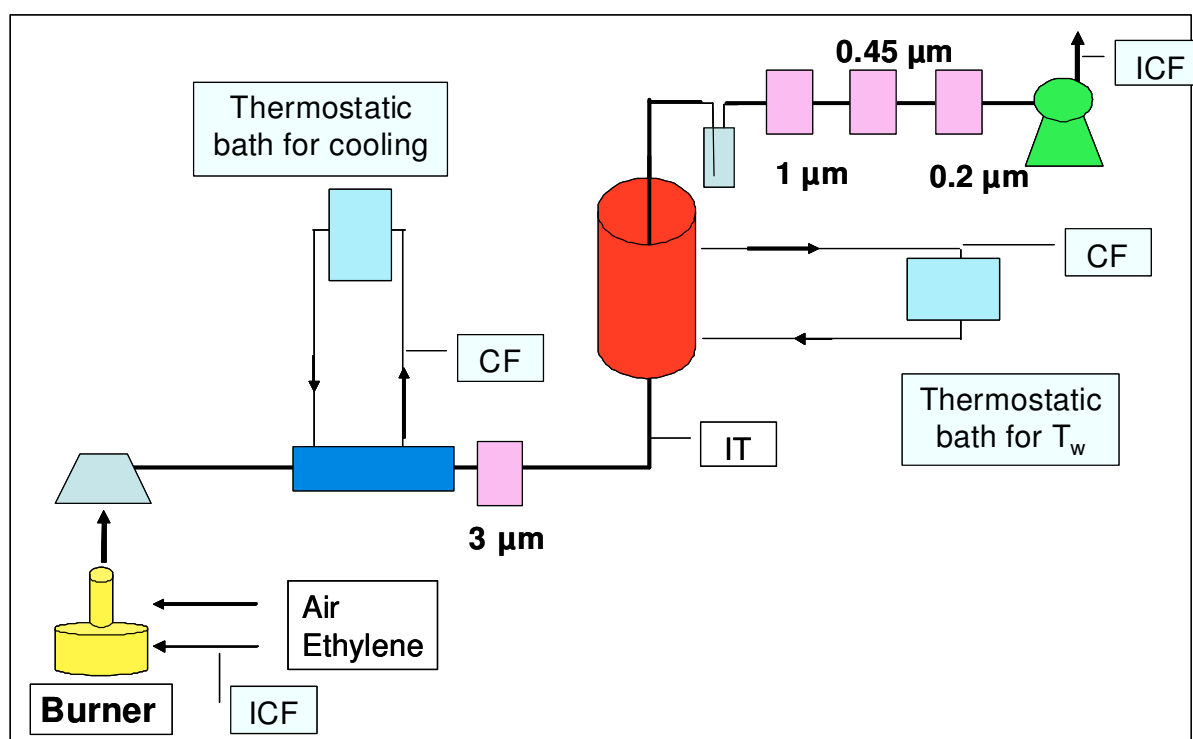


**Figure 3.25** – Experimental set up for preliminary test II with DLS

During these tests, a procedure to optimize the use of DLS for our system was also studied. The measurement of particle size was conducted using the following steps:

1. The filters are allocated in steel holder-filter placed along the gas line in order of decreasing mesh
2. At the end of the test, filters are recovered from holder-filter with tweezers, in order to avoid contamination
3. The filtrate is recovered and transferred it into a purified aqueous matrix
4. The sample liquid is analysed with the DLS

For the analyse the water used with the DLS is MilliQ, with final filter at 200 nm. In the following paragraph are described the procedures adopted to optimize the

abovementioned steps. As can be seen, this procedure is cumbersome and may be subject to external pollution or to operator errors.

Sonication was used for recovery of the filtrate. The procedure:

1. The filter is immersed in about 5 cc of purified water in a container;
2. The container is immersed in the sonication bath;
3. Sonication is executed for a given time;
4. At the end of sonication a water sample is poured directly into the cuvette used for DLS

Defined this four points procedure, several experiments were carried to optimize each point in order to minimize external contamination. In fact the manipulation is done by placing filters tweezers and at end of each test the filters are positioned in special plastic and aseptic "filter holder".

### 3.1.3 Blank test for choice of containers

Tests to highlight the emission of particles from containers used for sonication were performed. For this purpose two containers, made glass and PFTE, which contain the same water volume (5 cc), are tested with 30 minutes in a sonication bath. In Figure 3.26 the results of measurement on the water contained in the abovementioned containers are shown.

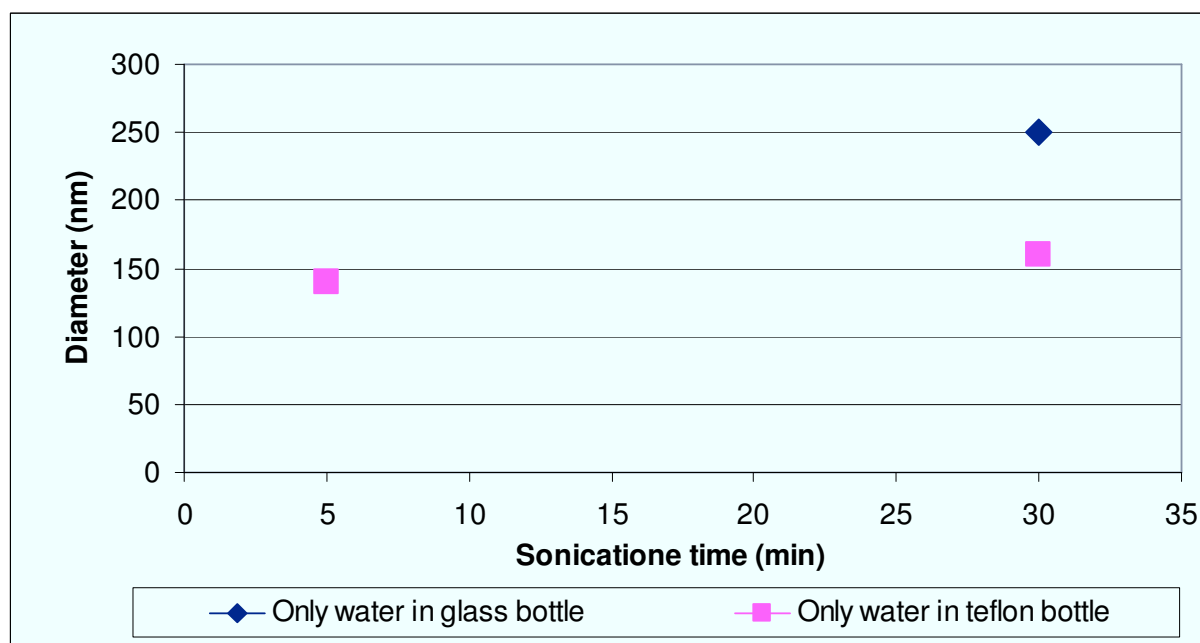


**Figure 3.26** – Particles detected, with DLS, in water contained in two containers, glass and PTFE, after 30 minutes of sonication

The results show clearly that the PTFE container, compared to glass, may minimize the pollution of the sample. The presence of particles, though smaller than 200 nm, is due to aqueous matrix, or to the process used to produce water. As mentioned, the MilliQ distiller used present a final filter with mesh of 200 nm, and therefore smaller particles should still be present.

### 3.1.4 Blank test for choice of filters

The choice of filter, was carried out sonicating for 30 minutes the filters composed by different materials such as nylon, fiberglass and PTFE, immersed in purified water, in the abovementioned PTFE container. The results are shown in Figure 3.27.

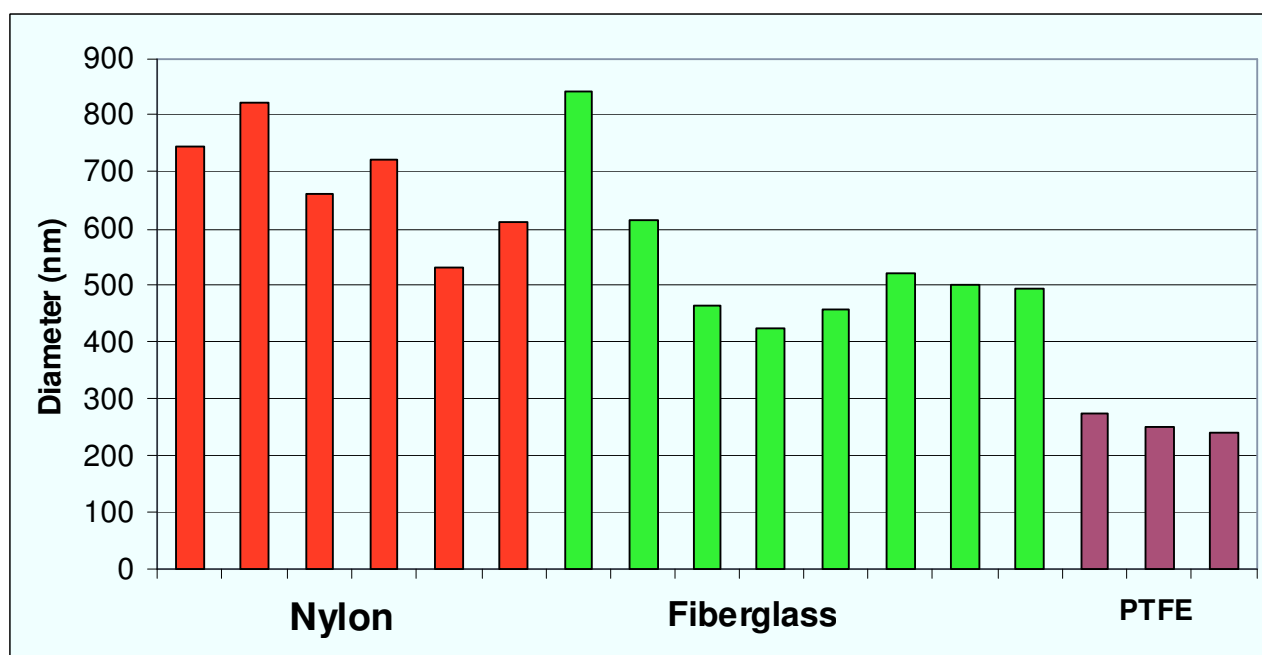


**Figure 3.27** – Particles detected in water after 30 minutes of sonication in a volume of liquid in which it was immersed the corresponding filter

As can be seen the PTFE filters are those that emit smaller particles.

Then it was carried out the assess the emission of particles from PTFE filters with different mesh as 3, 1, 0.45 and 0.2 microns, in order to have a "blank" for the tests with the particles produced by burner. Therefore we proceeded with sonication of these filters with the procedure described above. The results of the analysis performed with the DLS were shown in Figures 3.28 and table 3.3.

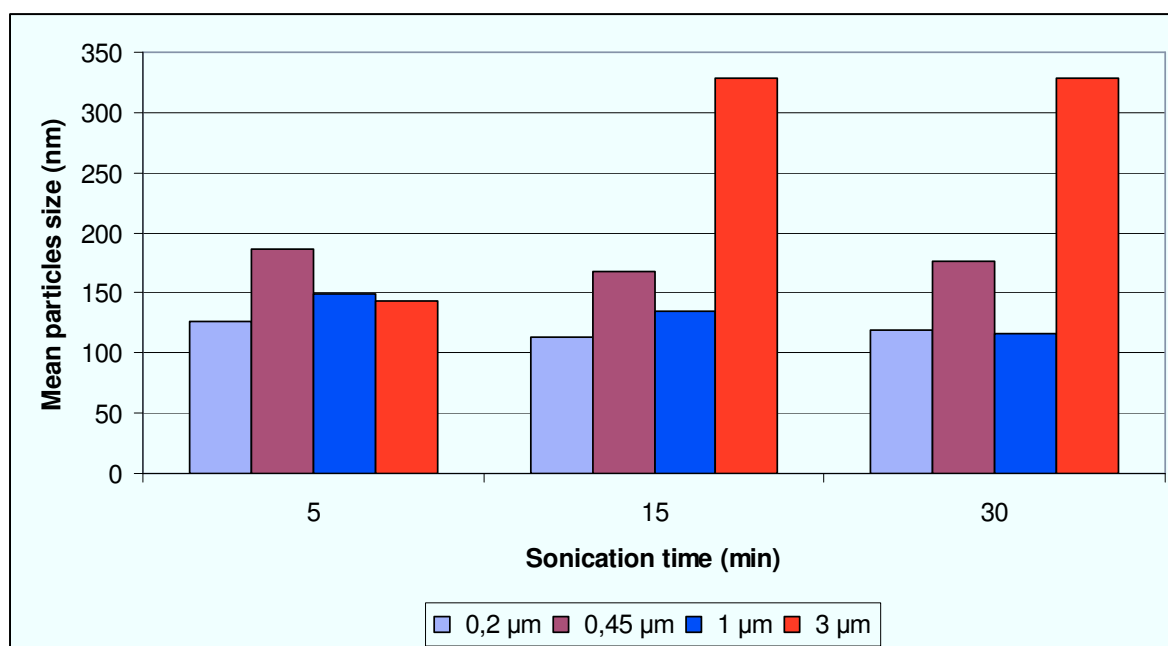


**Figure 3.28** – Mean particle size from test with filter in water vs sonication time

The figure 3.28 shows the values of the mean particles size. As can be seen the average particles size is lower than 200 nm, for all the filters, only when the sonication is 5 minutes. Therefore, based on graphs of Figure 3.28 we choose to set at 5 minutes the time to recover the filtrate in order to avoid contamination from the letter material.

The Table 3.3 report the data sheet from DLS. As can be seen, for every measured size, five runs are performed. The final data (yellow background) is the arithmetic mean of five data from each run performed by the device. The number of run is indicated in brackets in column called “filter mesh (µm)”.

The cell with green background indicates the quality report provided by DLS.

Sonication time (min)	Filter mesh (µm)	Mean Count Rate (kpcs)	Z-Ave (nm)	Pk 1 Mean Int (nm)	Pk 2 Mean Int (nm)	Pk 1 Area Int (%)	Pk 2 Area Int (%)	Intercept Correlation	Quality report
30	filter 3 (1)	186,7	620	4440	140	60,8	39,2	0,8	ok
	filter 3 (2)	261,3	224	233	4300	86,2	13,8		
	filter 3 (3)	148,6	231	239	4220	85,6	14,4		
	filter 3 (4)	226,8	312	269	4530	80,9	19,1		
	filter 3 (5)	310,8	254	250	4330	81,6	18,4		
		226,84	328,20	1086,20	3504,00	79,02	20,98	0,75	ok
	filter 1 (1)	71,2	110	131	0	100	0		
	filter 1 (2)	77,3	117	125	4550	94,8	5,2		
	filter 1 (3)	76,3	113	138	0	100	0		
	filter 1 (4)	81,4	117	137	5000	98,4	1,6		
	filter 1 (5)	86,9	127	131	4500	94,7	5,3		
		78,62	116,80	132,40	2810,00	97,58	2,42	0,65	ok
	filter 0,45 (1)	71,7	172	213	4720	95,3	4,7		
	filter 0,45 (2)	73,1	187	183	0	100	0		
	filter 0,45 (3)	83,3	181	244	4520	95,5	4,5		
	filter 0,45 (4)	78,4	171	193	4790	94,1	5,9		
	filter 0,45 (5)	78,6	172	232	4790	98,1	1,9		
		77,02	176,60	213,00	3764,00	96,60	3,40	0,7	ok
	filter 0,2 (1)	165,4	118	132	0	100	0		
	filter 0,2 (2)	177,5	118	147	0	100	0		
	filter 0,2 (3)	177,1	116	130	5040	98,8	1,2		
	filter 0,2 (4)	167,2	118	152	0	100	0		
	filter 0,2 (5)	180,8	123	152	3820	97,4	2,6		
		173,60	118,60	142,60	1772,00	99,24	0,76	0,7	ok
	filter 3 (1)	188,3	169	171	0	100	0		
	filter 3 (2)	167,1	144	168	0	100	0		
	filter 3 (3)	158,7	138	195	0	100	0		
	filter 3 (4)	154	129	180	0	100	0		
15	filter 3 (5)	158,2	138	170	4820	95,3	4,7	0,6	ok
		165,26	143,60	176,80	964,00	99,06	0,94		
	filter 1 (1)	75,3	118	143	5030	98,2	1,8		
	filter 1 (2)	83,2	138	158	3560	92	8		
	filter 1 (3)	89,2	146	154	0	100	0		
	filter 1 (4)	85,7	134	138	0	100	0	0,65	ok
	filter 1 (5)	81,7	135	131	0	100	0		
		83,02	134,20	144,80	1718,00	98,04	1,96		
	filter 0,45 (1)	77,4	247	101	0	100	0		
	filter 0,45 (2)	77	148	130	0	100	0		
	filter 0,45 (3)	74,8	137	128	0	100	0	0,7	ok
	filter 0,45 (4)	75,3	140	155	0	100	0		
	filter 0,45 (5)	77	147	131	0	10	0		
		76,30	163,80	129,00	0,00	82,00	0,00		
	filter 0,2 (1)	144,1	117	120	0	100	0	0,75	ok
	filter 0,2 (2)	144,6	115	130	5310	98,9	1,1		
	filter 0,2 (3)	148,5	113	133	4510	98,8	1,2		
	filter 0,2 (4)	145,1	113	125	5040	98,7	1,3		
	filter 0,2 (5)	154,2	112	123	4770	97,8	2,2		
		147,30	114,00	126,20	3926,00	98,84	1,16	0,7	ok
	filter 3 (1)	167,6	119	165	3680	95,8	4,2		
	filter 3 (2)	189,7	131	94,8	371	50,7	49,3		
	filter 3 (3)	198,4	138	130	596	69,8	30,2		
	filter 3 (4)	188,3	133	175	4460	96,3	3,7		
5	filter 3 (5)	190,8	129	148	4350	93,1	6,2	0,7	ok
		186,96	130,00	142,56	2691,40	81,14	18,72		
	filter 1 (1)	63,7	145	133	0	100	0		
	filter 1 (2)	64,4	147	131	0	100	0		
	filter 1 (3)	70,1	151	145	0	100	0	0,6-0,7	ok
	filter 1 (4)	73,1	153	155	0	100	0		
	filter 1 (5)	65	148	140	0	10	0		
		67,26	148,80	140,80	0,00	82,00	0,00		
	filter 0,45 (1)	87,7	170	152	0	100	0	0,75	ok
	filter 0,45 (2)	92,1	190	195	0	100	0		
	filter 0,45 (3)	95,7	189	195	0	100	0		
	filter 0,45 (4)	96,9	201	194	0	100	0		
	filter 0,45 (5)	92,1	183	216	46,4	96	4		
		92,90	186,60	190,40	9,28	99,20	0,80	0,75	ok
	filter 0,2 (1)	145	123	133	4700	95,3	4,7		
	filter 0,2 (2)	151,9	123	139	4680	96,4	3,6		
	filter 0,2 (3)	145,5	122	149	31,4	96,3	2,4		
	filter 0,2 (4)	156,2	125	162	0	100	0		
	filter 0,2 (5)	166,3	139	143	5220	96,6	3,4		
		152,98	126,40	145,20	2926,28	96,92	2,82		

Table 3.3 – Data sheet report from DLS analysis in blank tests

### 3.1.5 Test without water in the growth tube

The following tests were performed with particles produced by premixed ethylene ( $C_2H_4$ ) - air flame generated at atmospheric pressure with three different values of equivalent ratio, 2.36, 3.27 and 6.33, but in the absence of water in the tube growth. The aim was to make a comparison between the particles emitted by filter (blank test) and particles captured by filter after flow of gas particle-laden. The filters are placed as indicated in Figure 3.25. The filter with mesh  $3\text{ }\mu\text{m}$  is placed before the growth tube in order to remove from flow gas all the bigger particles. After the growth tube are placed three filters with decreasing mesh, from 1 to  $0.2\text{ }\mu\text{m}$ . The procedure to recovery the filtrate from filter is the same described (paragraph 3.2). The results are shown in the following figures. The sonication time is 5 minutes for all tests.

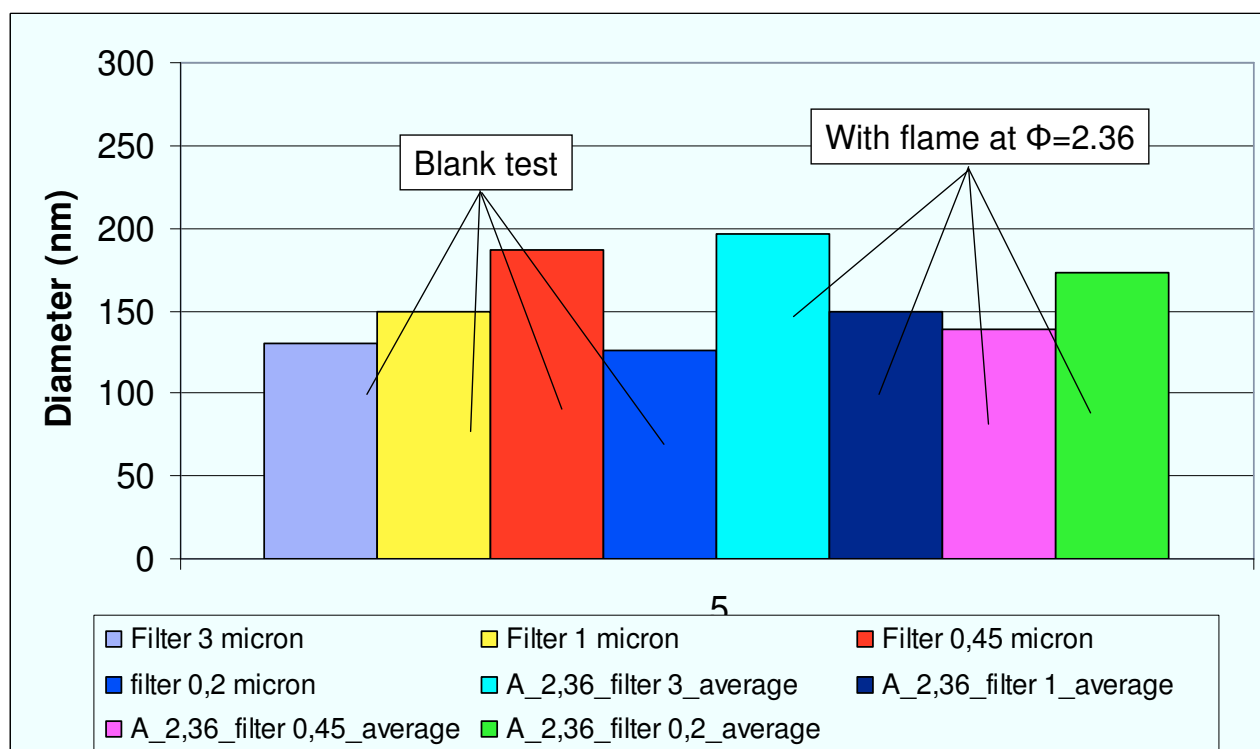


**Figure 3.29** – Comparison between mean particles size captured by filter from flow gas with equivalent ratio,  $\Phi=2.36$ , and those emitted by filter, at equal sonication time of 5 minutes.

The figure 3.29 shows the comparison between the mean particles size captured by filters from gas produced by premixed ethylene-air flame with equivalent ratio  $\Phi=2.36$ , and the particles emitted by the same filters in blank test.

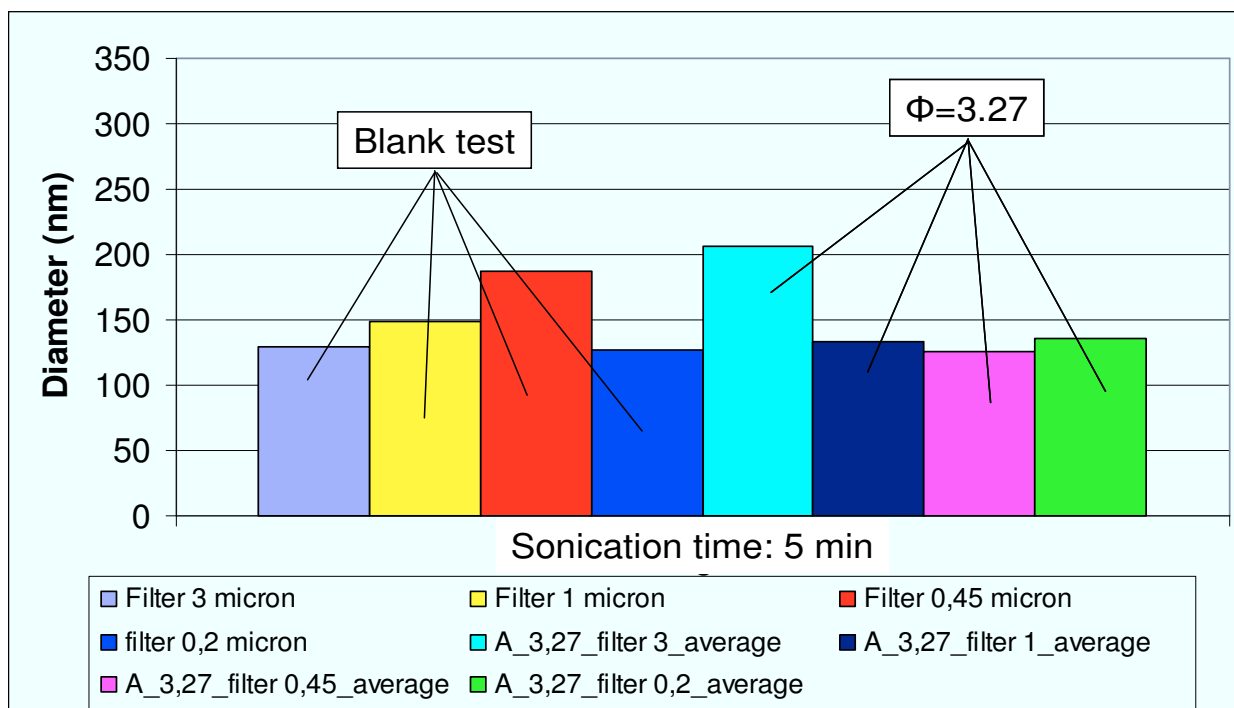


**Figure 3.30** - Comparison between mean particles size captured by filter from flow gas with equivalent ratio,  $\Phi=3.27$ , and those emitted by filter, at equal sonication time of 5 minutes.

The figure 3.30 shows the comparison between the mean particles size captured by filters from gas produced by premixed ethylene-air flame with equivalent ratio  $\Phi=3.27$ , and the particles emitted by same filters in blank test.

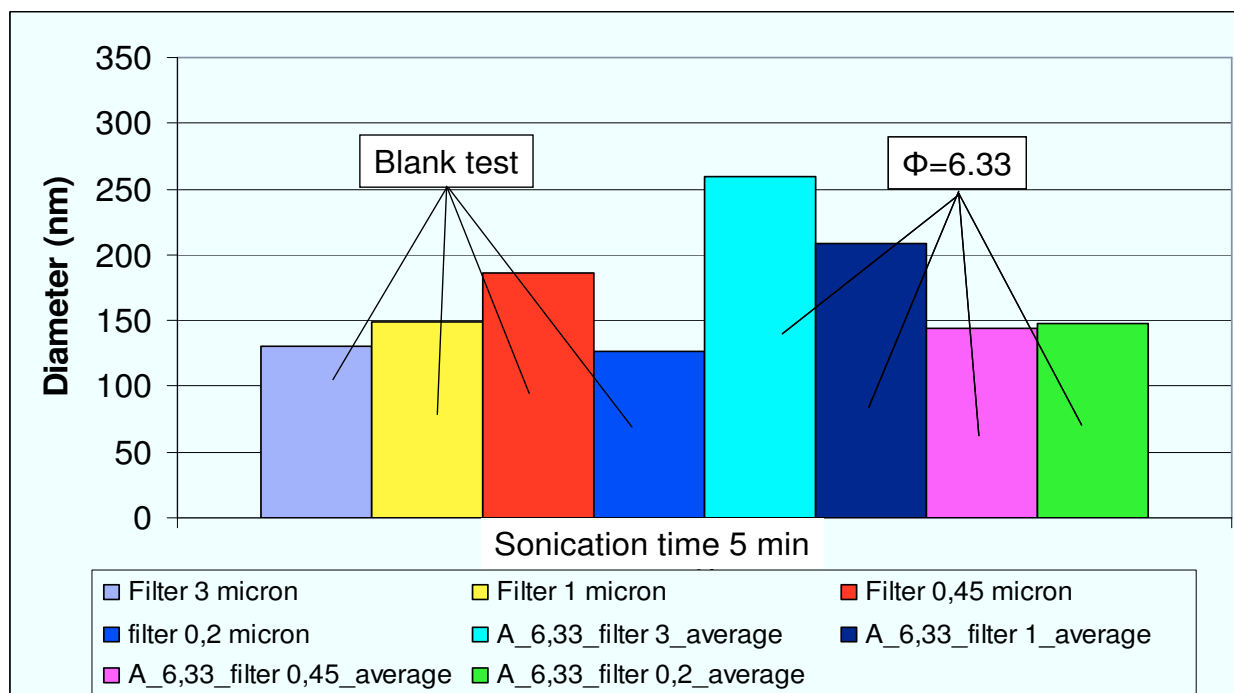


**Figure 3.31** - Comparison between mean particles size captured by filter from flow gas with equivalent ratio,  $\Phi=6.33$ , and those emitted by filter, at equal sonication time of 5 minutes.

The figure 3.31 shows the comparison between the mean particles size captured by filters from gas produced by premixed ethylene-air flame with equivalent ratio  $\Phi=6.33$ , and the particles emitted by the same filters in blank test. The following Tables 3.4-7 show, for each filter, a comparison between the curves of Correlation data, size distribution by volume and size distribution by number.

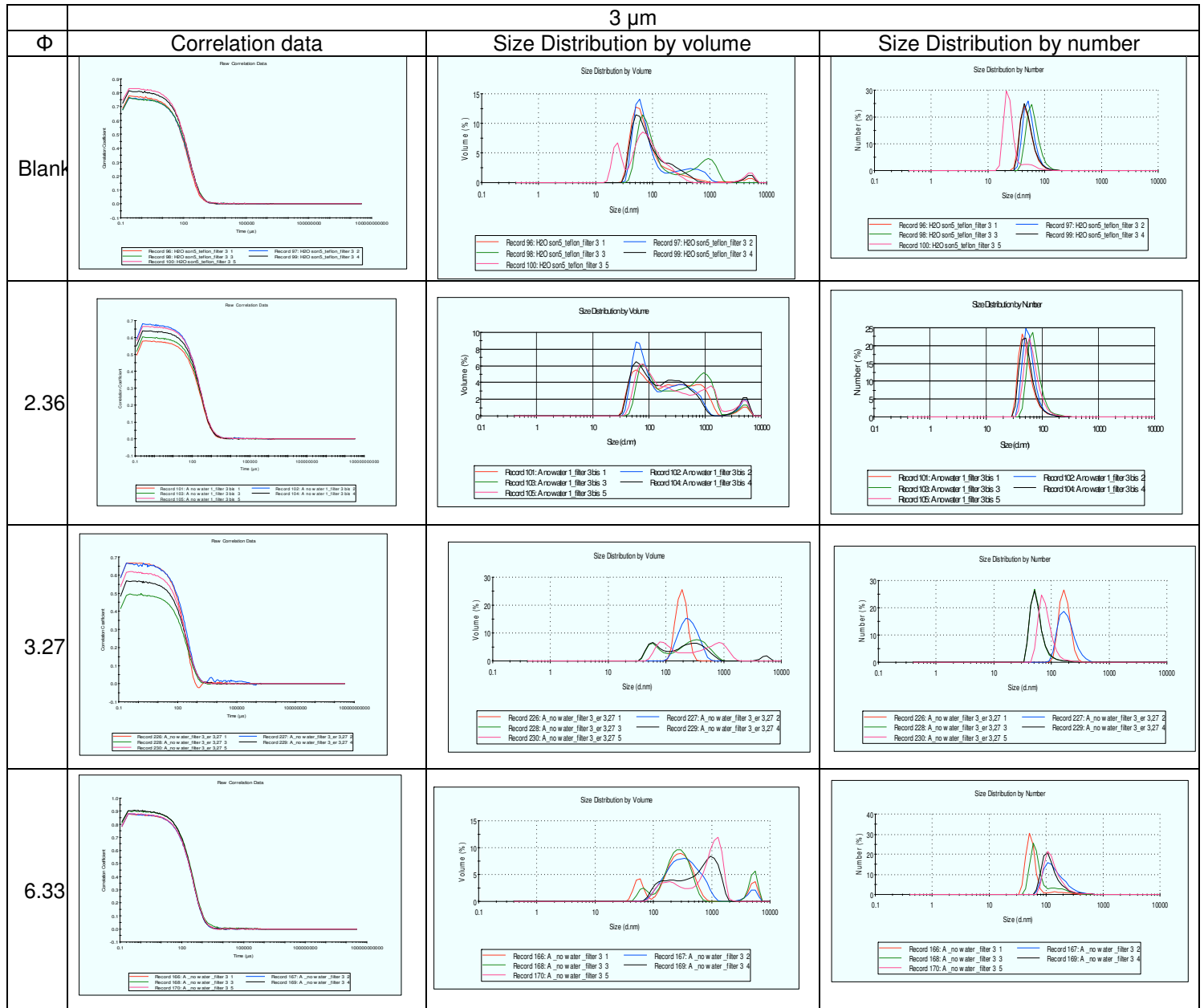


**Table 3.4** - Comparison between the curves of Correlation data, Size distribution by volume and Size distribution by number at different equivalent ratio and those in blank test, for filter 3  $\mu\text{m}$ .



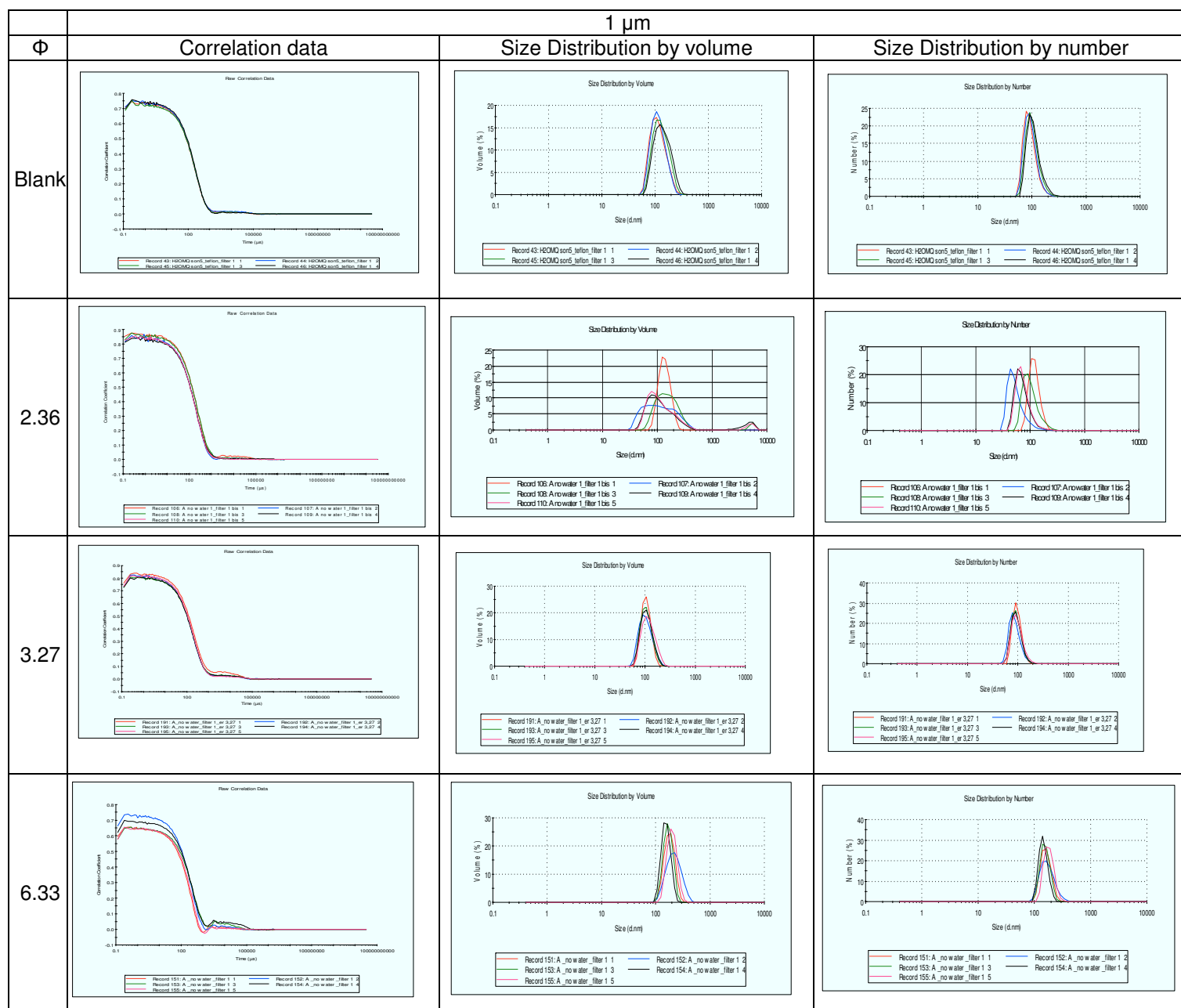


**Table 3.5** - Comparison between the curves of Correlation data, Size distribution by volume and Size distribution by number at different equivalent ratio and those in blank test, for filter 1  $\mu\text{m}$ .

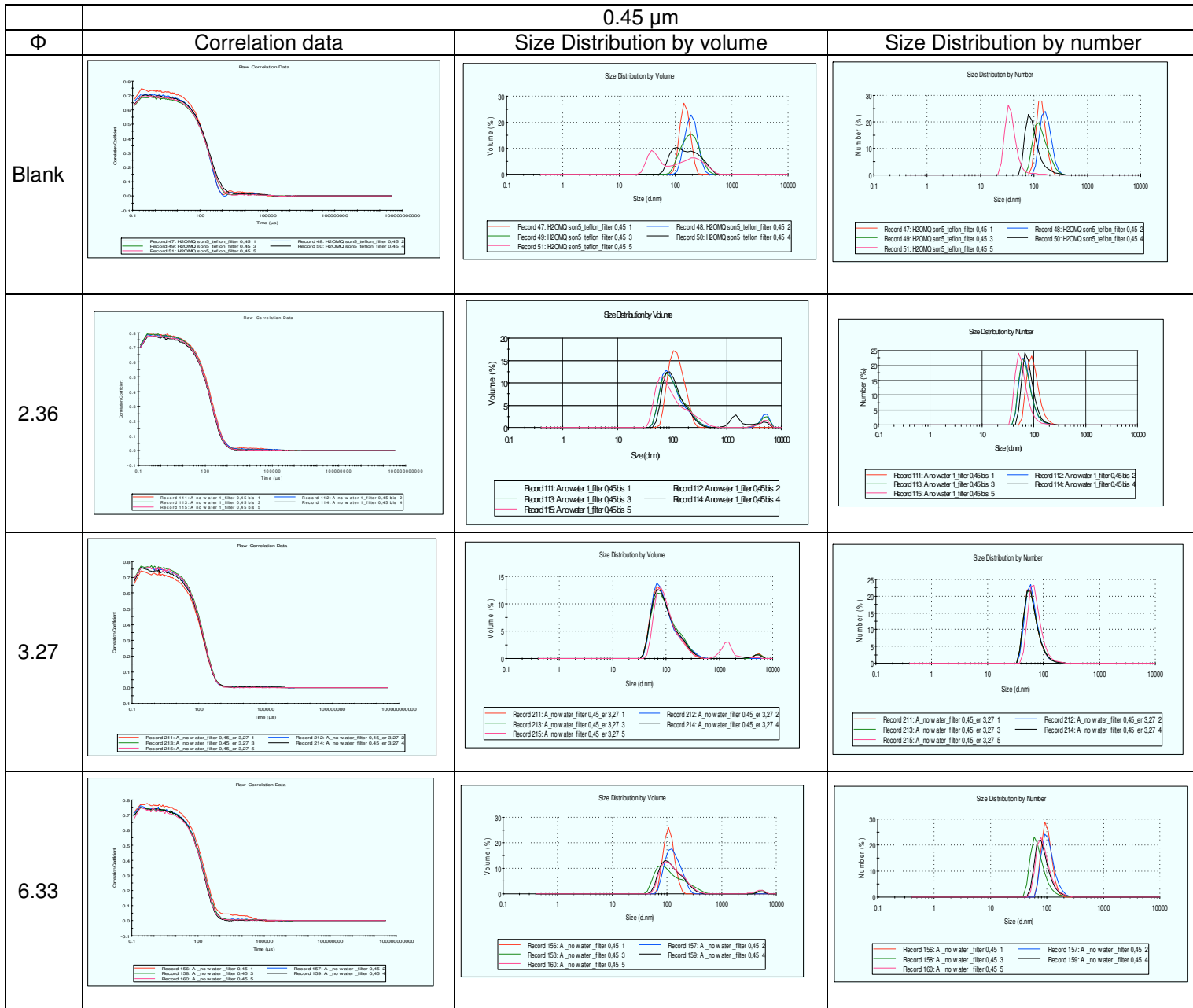


**Table 3.6** - Comparison between the curves of Correlation data, Size distribution by volume and Size distribution by number at different equivalent ratio and those in blank test, for filter 0.45  $\mu\text{m}$ .

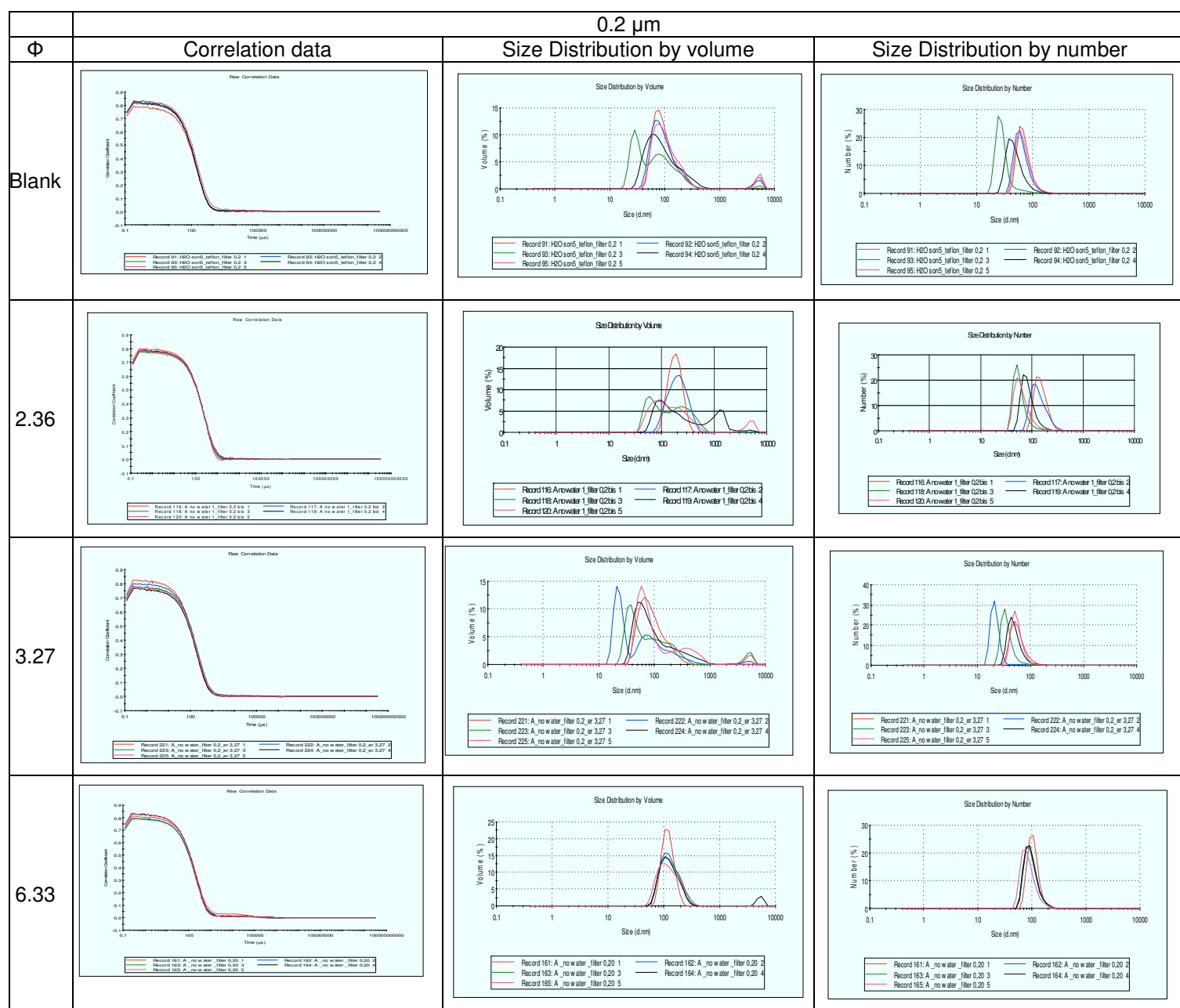


**Table 3.7** - Comparison between the curves of Correlation data, Size distribution by volume and Size distribution by number at different equivalent ratio and those in blank test, for filter 0.2  $\mu\text{m}$ .

As can be seen from Figures 3.29-31 and Tables 3.4-7, there is not a remarkable difference between the results of blank test and the experimental test with different equivalent ratio, both in terms of particles size and concentration.

Therefore the DLS is not very suitable for these experimental activities. The blank tests show that the particles emitted by filter during the sonication treatment, necessary to recovery the filtrate, are not negligible, both in size and in concentration. Therefore it is necessary to adopt another kind of measurement device. However, the DLS has been used successfully for the first information about the functioning of the growth tube.

### 3.2 Preliminary test with DMA

The last group of preliminary test, with DMA, is been performed in order to found the better operating conditions and experimental set up for study of the droplet growth trough heterogeneous condensation. For this purpose an experimental tests are performed with set up shows in following figure.

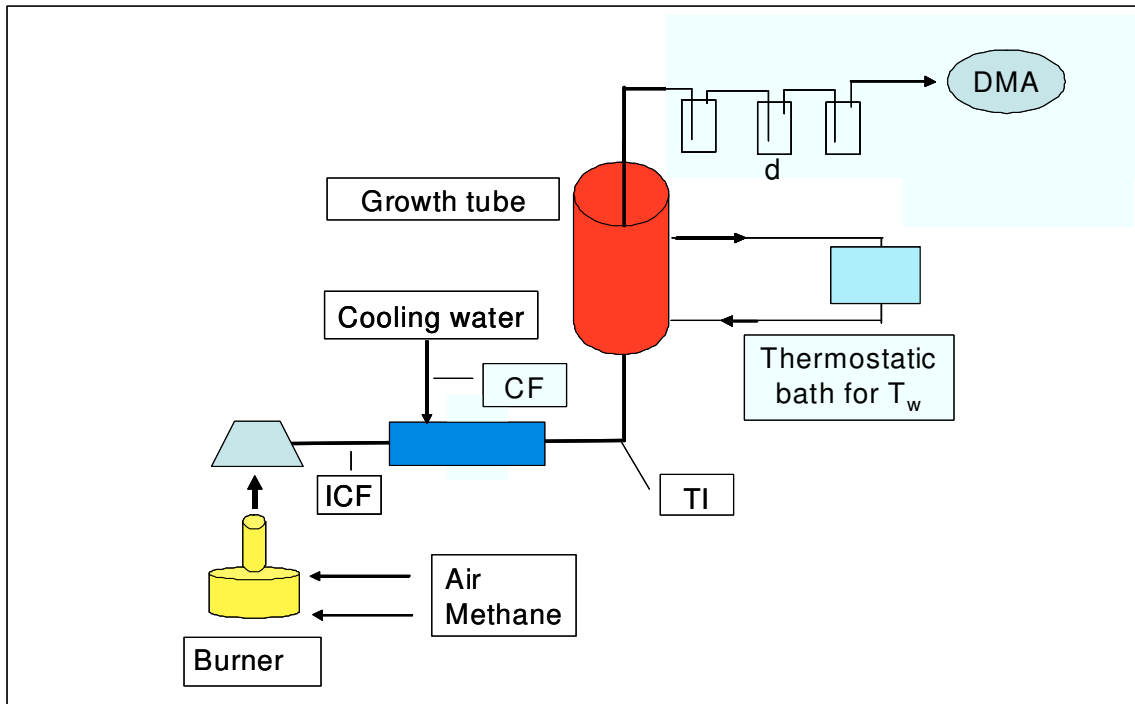


**Figure 3.32** - Experimental plant for preliminary test with DMA

In this case the filter, usually placed at the end of the growth tube, is substituted by three drechsel in order to capture the bigger water droplets, with or without inclusions (particle). The DMA is placed after the drechsel. The aspiration of gas flow to analyse is guaranteed by the same pump of the device. The particles were produced by burning natural gas using a Bunsen burner.

The following table shows the operating conditions of tests.

Test	Operating conditions
1	Only air
2	Flame without water in the growth tube
3	Flame with growth tube at a 313 K
4	Flame with growth tube at 323 K

**Table 3.8** - Preliminary tests operating conditions .

The Test 1 is performed without flame but only with indoor air. The aim was to make a comparison between the particles emitted by flame and the particles present in indoor air. The Test 2 is performed with flame, but without water in the growth tube. The purpose is to have a characteristic size distribution of the flame to compare with the size distribution in outlet of growth tube when the heterogeneous condensation is active. The Tests 3 and 4 are performed with liquid film in the growth tube at temperature  $T_w$  equal to 313 K and 333 K respectively.

The following figures 3.33 show the result of Test 1.

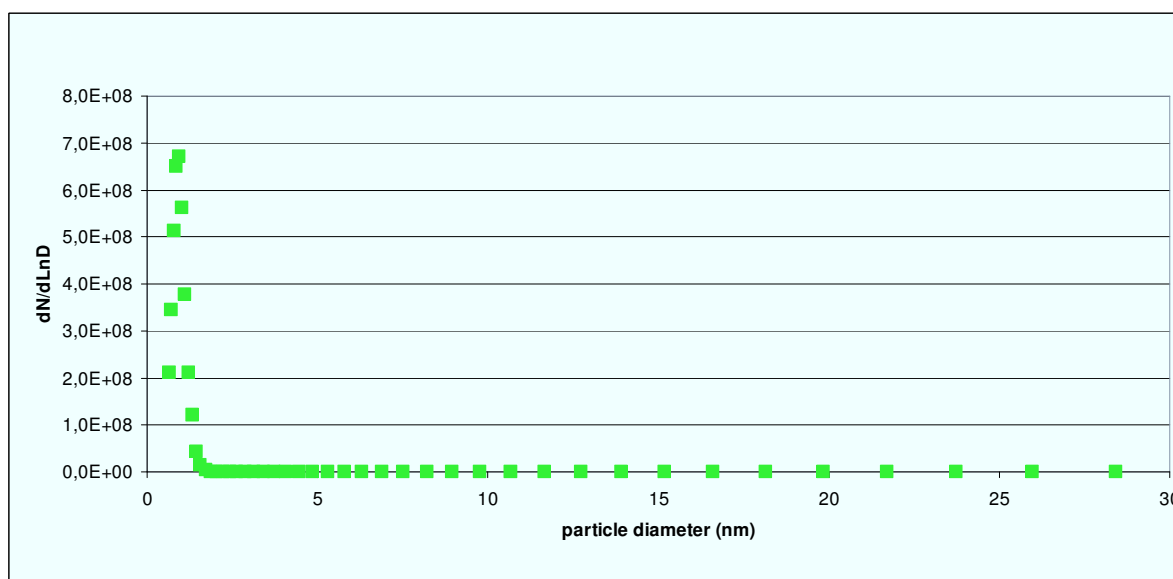


**Figure 3.33** – The particle size distribution from Test 1

The following figure shows the results of Test 2, 3 and 4.

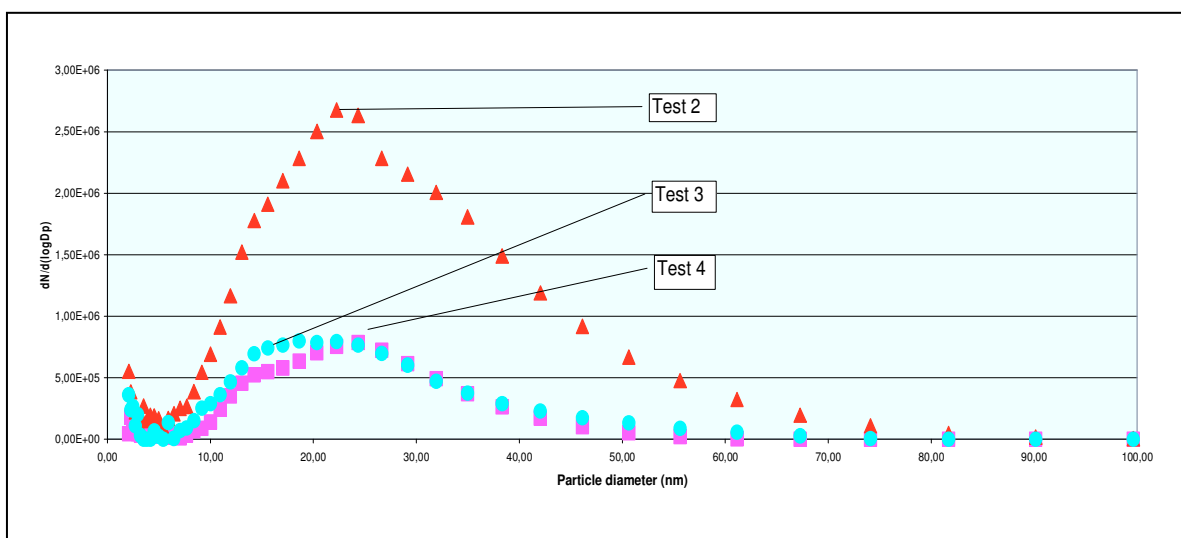


**Figure 3.34** – Particle size distributions for Test 2, 3 and 4

In Figure 3.33 is showed the size distribution when just air flow is introduced into the growth tube, without water. The purpose is to verify the absence of particle in the air.

In Figure 3.34 the results of all the experiments conducted in the presence of flame are shown. It is worth noting that as the wall temperature rises, the particle size distribution curves move to larger size, because the activation's process in growth tube became more efficient. We can conclude that in Tests 3 and 4 the processes of nucleation and growth have been efficiently working.

Besides, if we consider the three drechsel before the DMA and at outlet of growth tube as a system to removal the droplet with particles inclusions from flow gas by inertial forces, then it is possible to define a removal efficiency as:

$$\eta = \frac{C^{\circ} - C^f}{C^{\circ}} \times 100 \quad (3.15)$$

where  $C^{\circ}$  is the initial size distribution, given by Test 2, and  $C^f$  is the size distribution when the heterogeneous condensation is actives with liquid film a  $T_w = 313$  K and 323 K, given by Test 3 and 4 respectively. The results are show in following Figure 3.35.

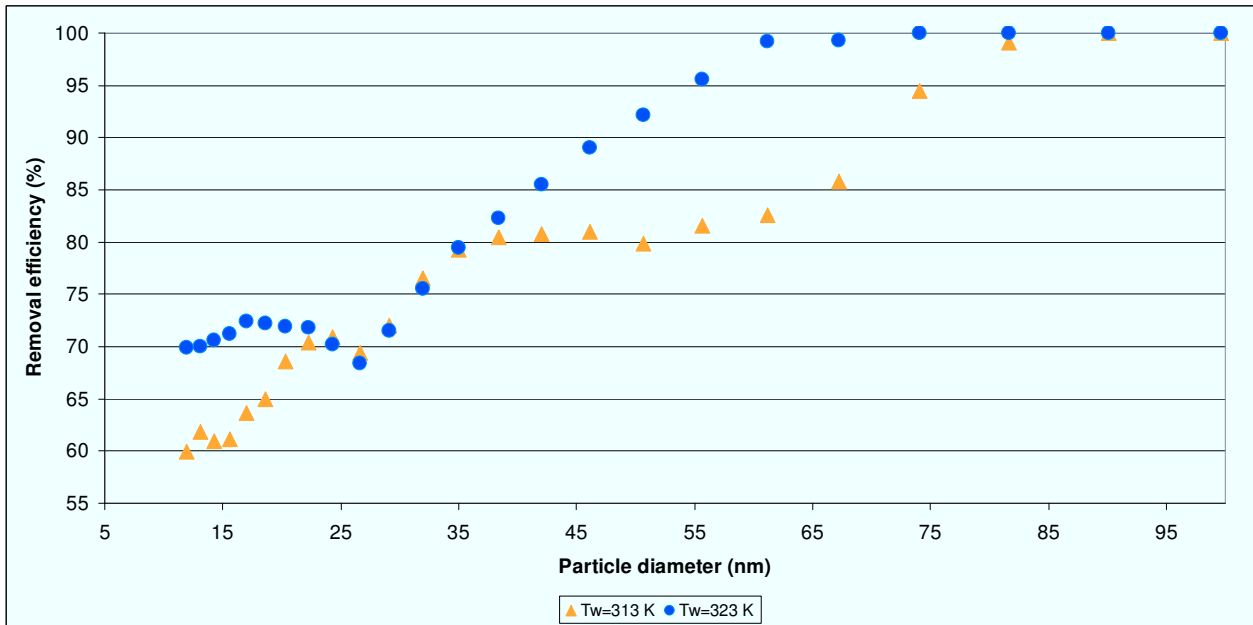


**Figure 3.35** – Removal efficiency vs particle diameter for two wall temperature,  $T_w$

Figure 3.35 shows the removal efficiency of particles. It can be seen that the removal efficiency increase with diameter and with temperature. This behaviour can be explained as follows: the condition for the formation and the growth of droplets by condensation is that the degree of supersaturation is greater than the critical supersaturation,  $S_{cr}$  (the supersaturation corresponding to nucleation rate equal to 1), which decreases by the

increasing the particle size, then, vapour condensed on the surfaces of bigger particles firstly, and the collection efficiency of particles increases with the increase in particle size. This effect is amplified by increasing the temperature. The influence of temperature on the removal efficiency is small when increasing the particle size, because in an adiabatic system, as the growth tube may be assimilated, the influence of temperature on the droplet growth rate and the final droplet diameter is small.

## Chapter 4

### Experimental test

With preliminary tests we have verified the functionality of the growth tube. The last part of this thesis is on the experimental tests and modelling in order to study the nucleation and growth of the droplet surrounding the particles. The tests are performed with the measurement device LAS 3340 by TSI and with experimental set up illustrated in following figure and previously described in Chapter 3.

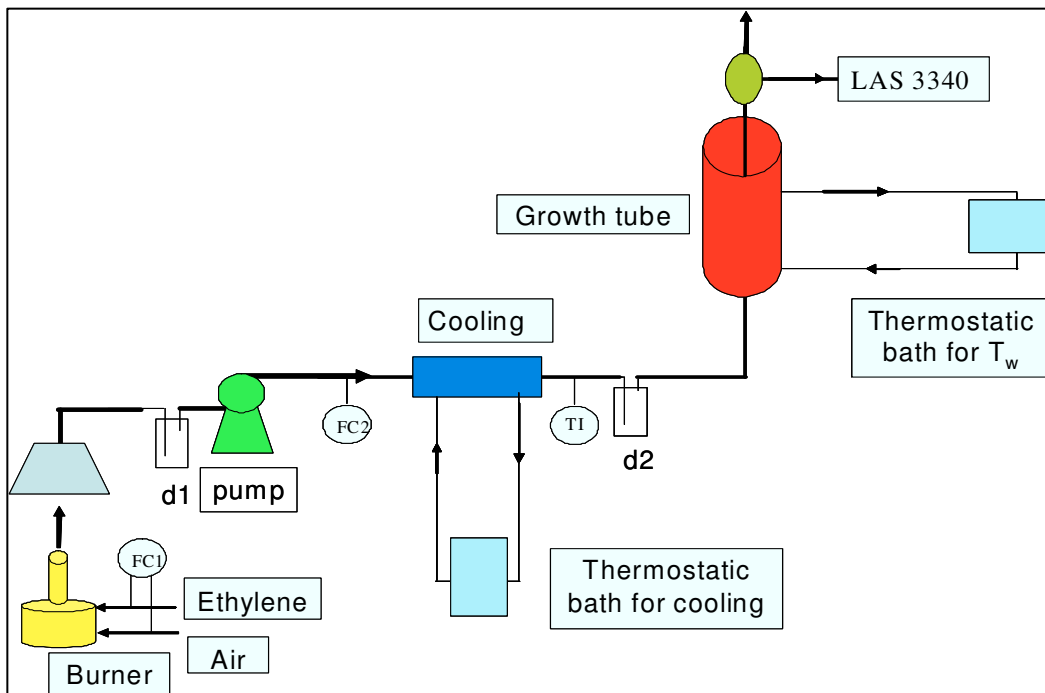


**Figure 4.1** – Experimental set up

#### 1. Blank Test

The first tests are performed only with air (i.e. without flame) in order to have a method blank. The experimental planning is described in the following table.



Test	$T_w$ (K)	$t_{res}$ (s)	Q (l/min)	U (m/s)	$T_{in\ GT}$ (K)
<b>B1</b>	<b>no water</b>				
B2	313	1,06	4,00	0,38	292
B3	323				
<b>B4</b>	<b>no water</b>				
B5	313	0,94	4,50	0,42	291
B6	323				
<b>B7</b>	<b>no water</b>				
B8	313	1,21	3,50	0,33	293
B9	323				
<b>B10</b>	<b>no water</b>				
B11	313	1,41	3,00	0,28	295
B12	323				
<b>B13</b>	<b>no water</b>				
B14	313	1,70	2,50	0,24	297
B15	323				
<b>B16</b>	<b>no water</b>				
B17	313	2,12	2,00	0,19	299
B18	323				

**Table 4.1** – Planning for blank test with only air

Tests are divided in six groups, corresponding to six different air flows and to as many residence times. Each group is composed by three tests, one without water in the growth tube and two with liquid film in the growth tube at 313 K and 323 K, respectively. The  $T_{in\ GT}$  is the temperature to reach in order to have saturated gas at inlet growth tube (Chapter 3); Q is the total air flow aspirated;  $t_{res}$  is the residence time;  $T_w$  is the liquid film temperature; U is the mean gas velocity in the growth tube.

In the following, the graphs that illustrate the results of blank tests are shown. Every data are derived by an arithmetic mean from 20 samplings and corresponding measurement performed by LAS 3340.

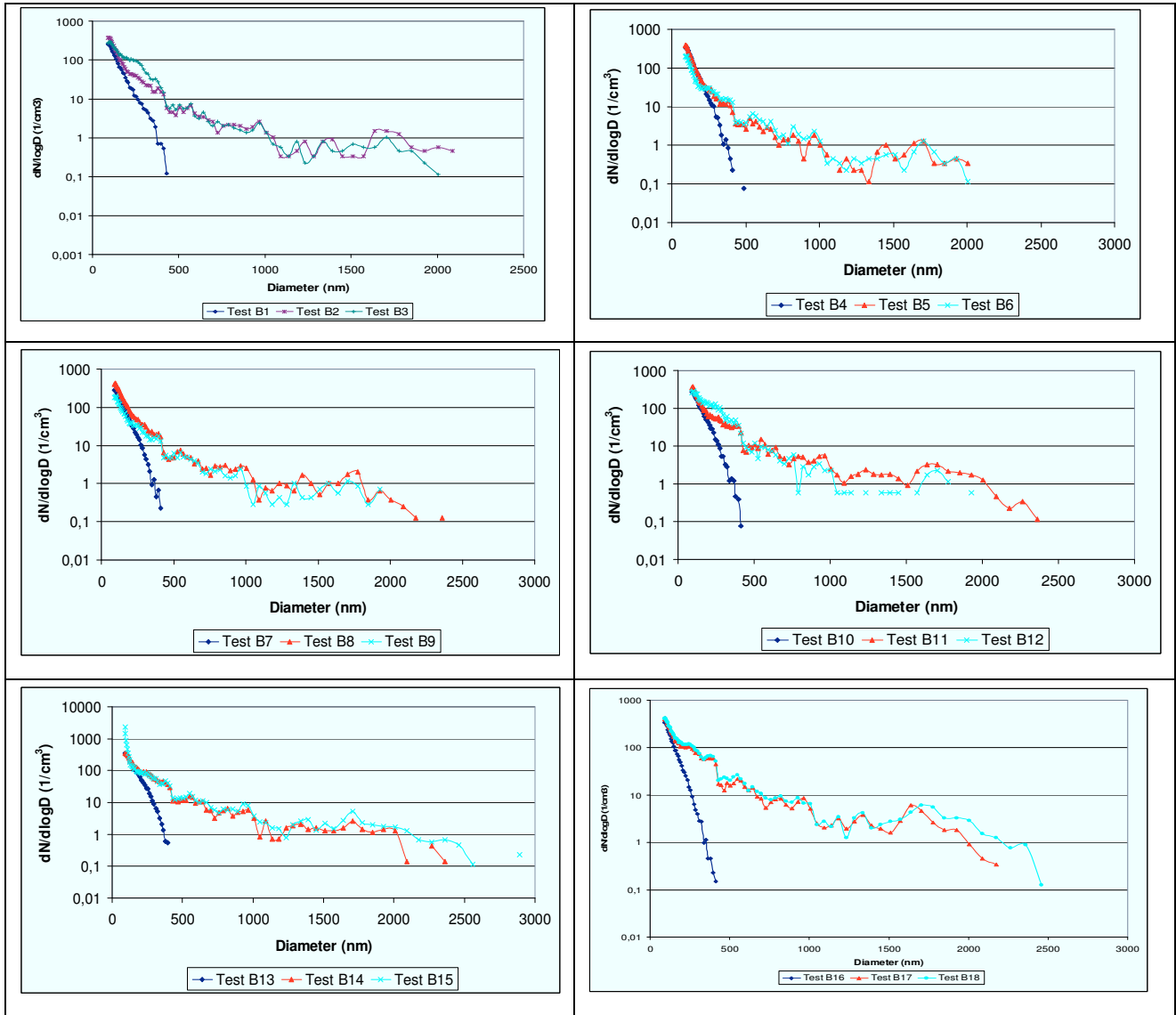


**Figure 4.2** – Results of blank test, described in Table 4.1, as Size distribution vs particle diameter. The tests B1, B4, B7, B10, B13 and B16 are performed without liquid film in the growth tube.

As expected, the concentration of particles is very low (see Figure 4.2). The curves corresponding to tests without the liquid film (B1, B4, B7, B10, B13 and B16) show the size distribution of particle in the indoor air. The other curves, corresponding to tests with liquid film at two wall temperature, ( $T_w=313$  K and 323 K), show the size distribution of particle when the heterogeneous condensation is active. In fact as can be seen, the size distribution moves toward larger diameters. We have already seen (Chapter 3) that the growth tube can be assimilated to an adiabatic system. In the adiabatic case, the dependence of growth rate and final droplet diameter on the temperature that increases with it is small (Heidenreich *et al.*, 1995). As can be seen in Figure 4.2 from behaviour of the two curves corresponding to the two  $T_w$ , there is not remarkable difference between the two curves.

## 2. Test with flame

In the following Table 4.2 is described the planning for the tests with particles produced by a premixed ethylene ( $C_2H_4$ )-air one-dimensional flame generated at atmospheric pressure. The tests are divided in two groups, corresponding to as many equivalent ratios and to as many pairs of ethylene and air-to-burner flows. Each group is composed by six subgroups, corresponding to different dilution ratio and residence time and to six different gas flows, composed by smoke and indoor air. Each subgroup is composed by three tests, one without water in the growth tube and two with liquid film at 313 K and 323 K respectively.

The  $T_{in\ GT}$  has the same meaning as described above;  $Q$  is total aspirated flow composed by air and smoke (produced by the burner);  $Dr$  is the dilution ratio given by the ratio between air and smoke flows;  $t_{res}$  is the residence time;  $Q_{air}$  is the air flow to the burner as combustive agent;  $T_w$  is the liquid film temperature;  $U$  is the mean gas velocity in the growth tube.

Test	$T_w$ (K)	$t_{res}$	$Dr$	$T_{in\ GT}$ (K)	$Q$ (l/min)	$U$ (m/s)	$Q_{C_2H_4}$ (ml/min)	$Q_{air}$ (ml/min)	$\Phi$
<b>1</b>	<b>no water</b>								
2	313	1,06	8,65	292	4,00	0,38			
3	323								
<b>4</b>	<b>no water</b>								
5	313	0,94	9,86	291	4,50	0,42			
6	323								
<b>7</b>	<b>no water</b>								
8	313	1,21	7,45	293	3,50	0,33			
9	323								
<b>10</b>	<b>no water</b>						59,20	355,20	2,38
11	313	1,41	6,24	295	3,00	0,28			
12	323								
<b>13</b>	<b>no water</b>								
14	313	1,70	5,03	297	2,50	0,24			
15	323								
<b>16</b>	<b>no water</b>								
17	313	2,12	3,83	299	2,00	0,19			
18	323								
<b>19</b>	<b>no water</b>						81,80	354,20	3,30
20	313	1,06	8,17	292	4,00	0,38			
21	323								
<b>22</b>	<b>no water</b>								
23	313	0,94	9,32	291	4,50	0,42			
24	323								
<b>25</b>	<b>no water</b>								
26	313	1,21	7,03	293	3,50	0,33			
27	323								
<b>28</b>	<b>no water</b>								
29	313	1,41	5,88	295	3,00	0,28			

30	323					
<b>31</b>	<b>no water</b>					
32	313	1,70	4,73	297	2,50	0,24
33	323					
<b>34</b>	<b>no water</b>					
35	313	2,12	3,59	299	2,00	0,19
36	323					

**Table 4.2** – Planning for tests with flame

In the following figures the tests with  $\Phi=2.38$  are shown. Every data are derived by an arithmetic mean from 20 samplings and corresponding measurement performed by LAS 3340.

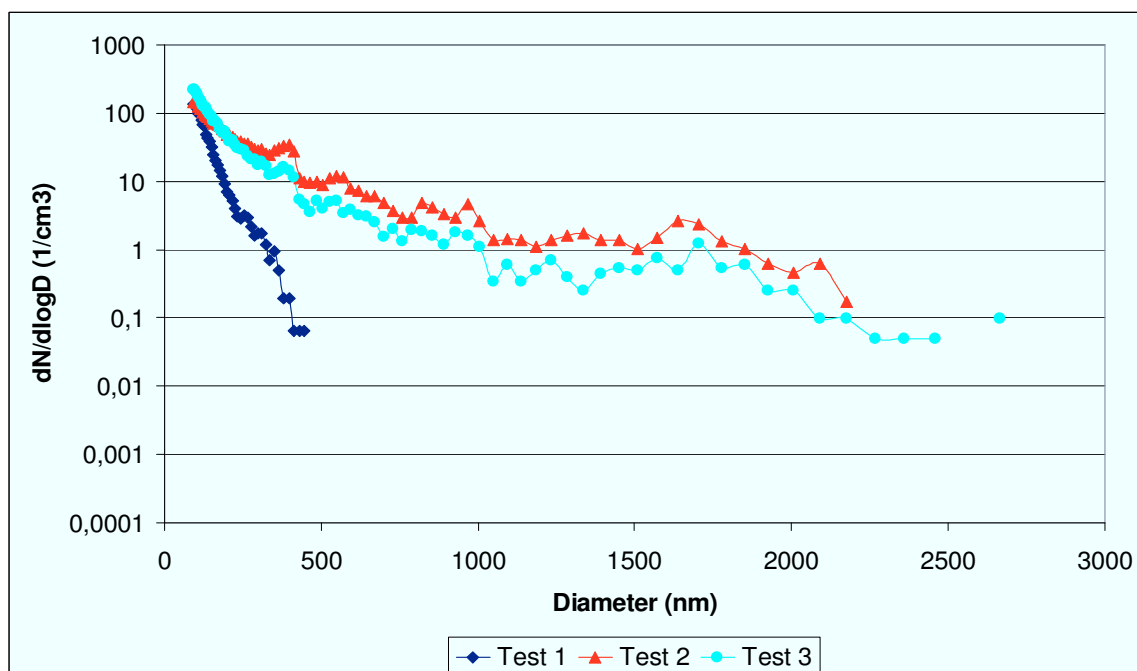


**Figure 4.3** – Size distribution vs diameter in Test 1 - 2 - 3, with  $\Phi=2.38$ . The test 1 is performed without liquid film in the growth tube.

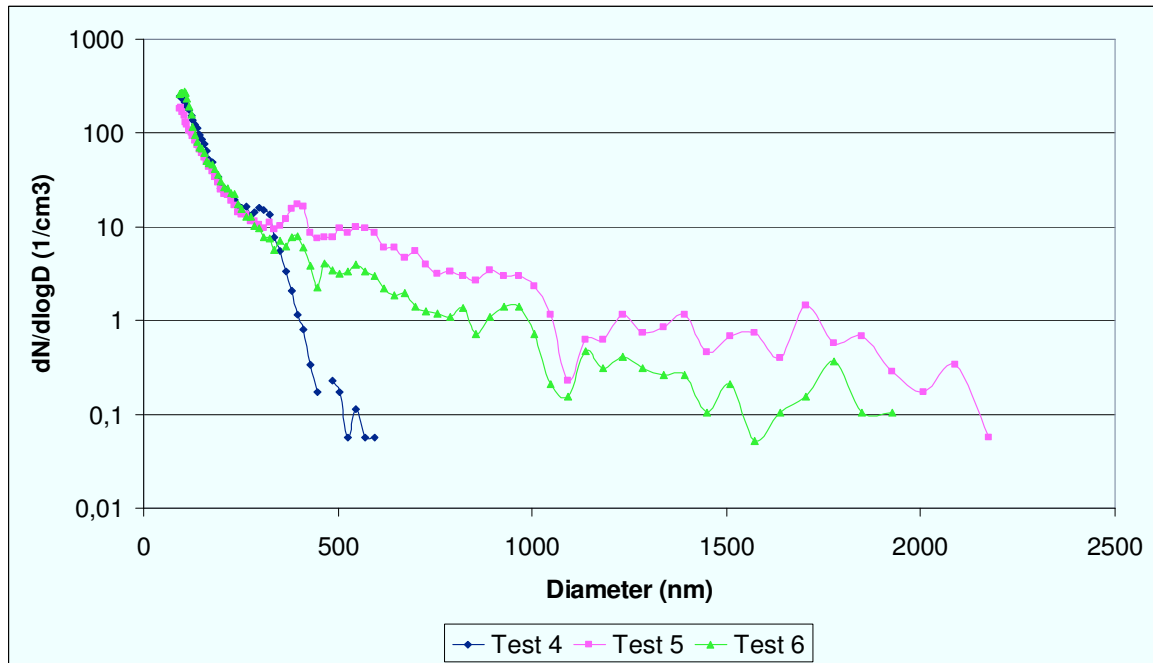


**Figure 4.4** – Size distribution vs diameter in Test 4 - 5 - 6, with  $\Phi=2.38$ . The test 4 is performed without liquid film in the growth tube.

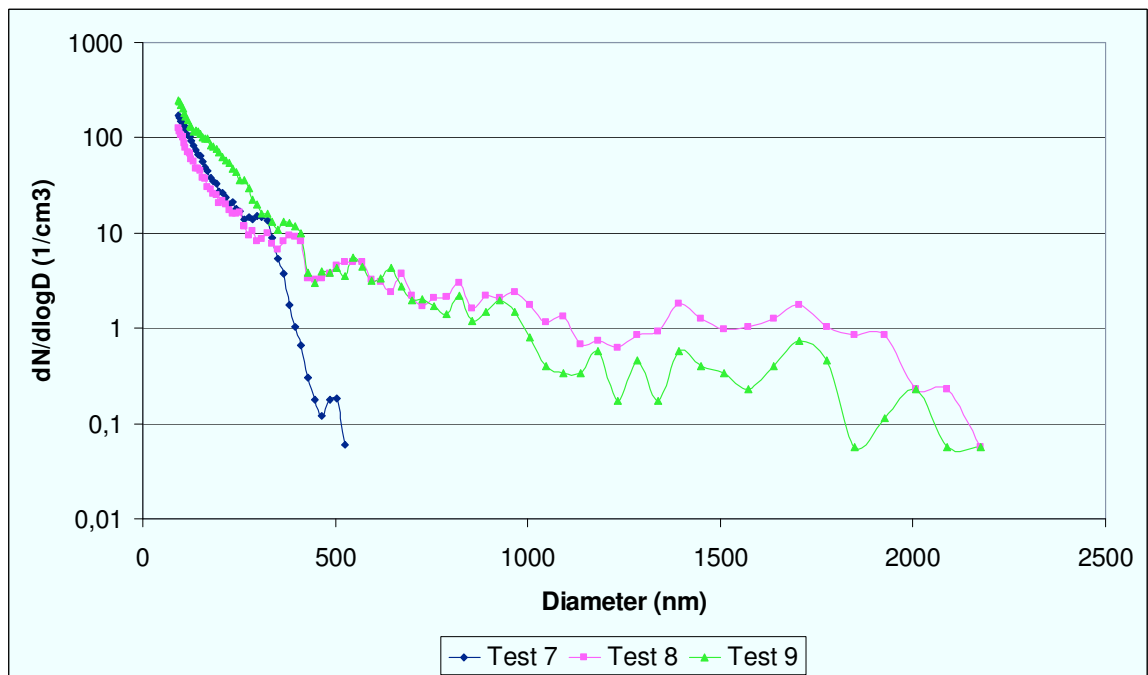


**Figure 4.5** – Size distribution vs diameter in Test 7 - 8 - 9, with  $\Phi=2.38$ . The test 7 is performed without liquid film in the growth tube.

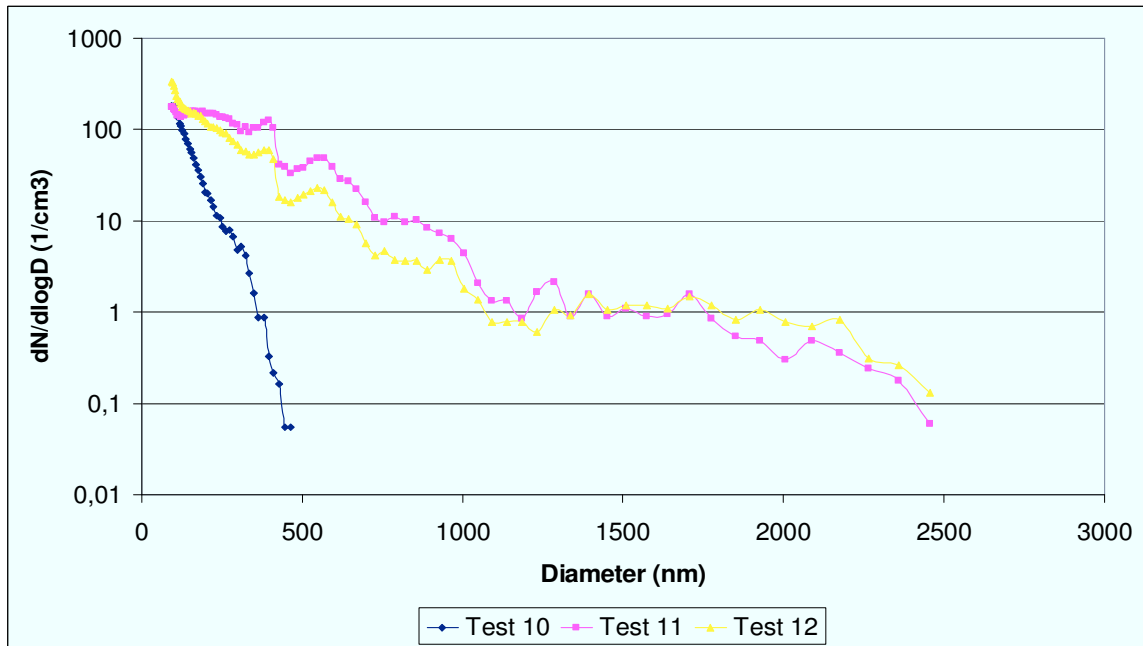


**Figure 4.6** – Size distribution vs diameter in Test 10 - 11 - 12, with  $\Phi=2.38$ . The test 10 is performed without liquid film in the growth tube.

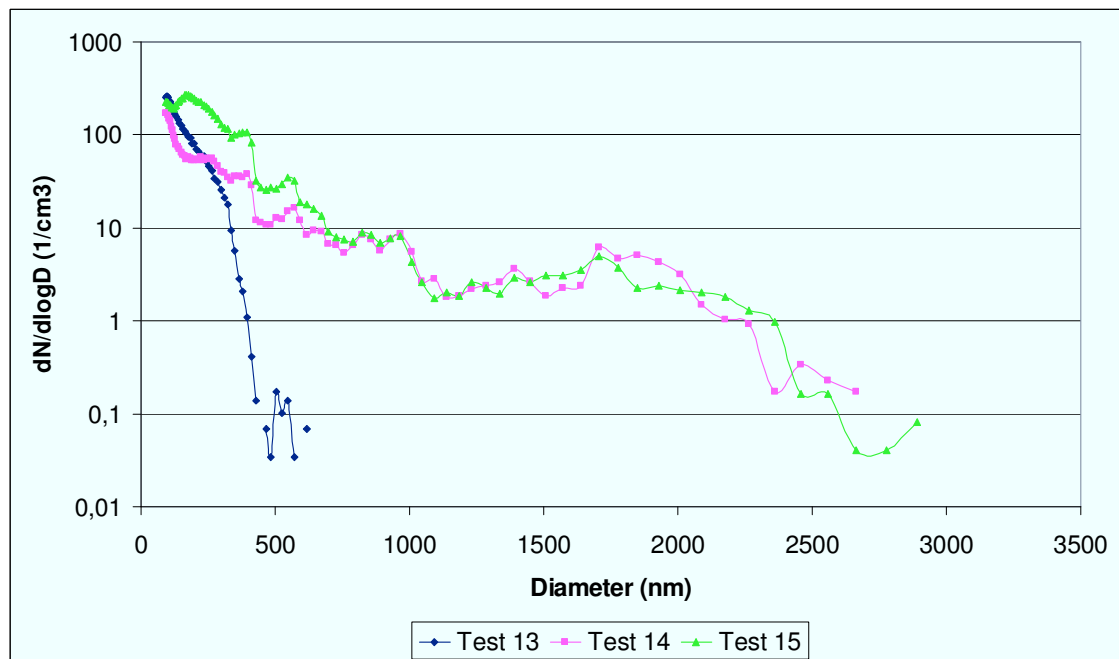


**Figure 4.7** – Size distribution vs diameter in Test 13 - 14 - 15, with  $\Phi=2.38$ . The test 13 is performed without liquid film in the growth tube.

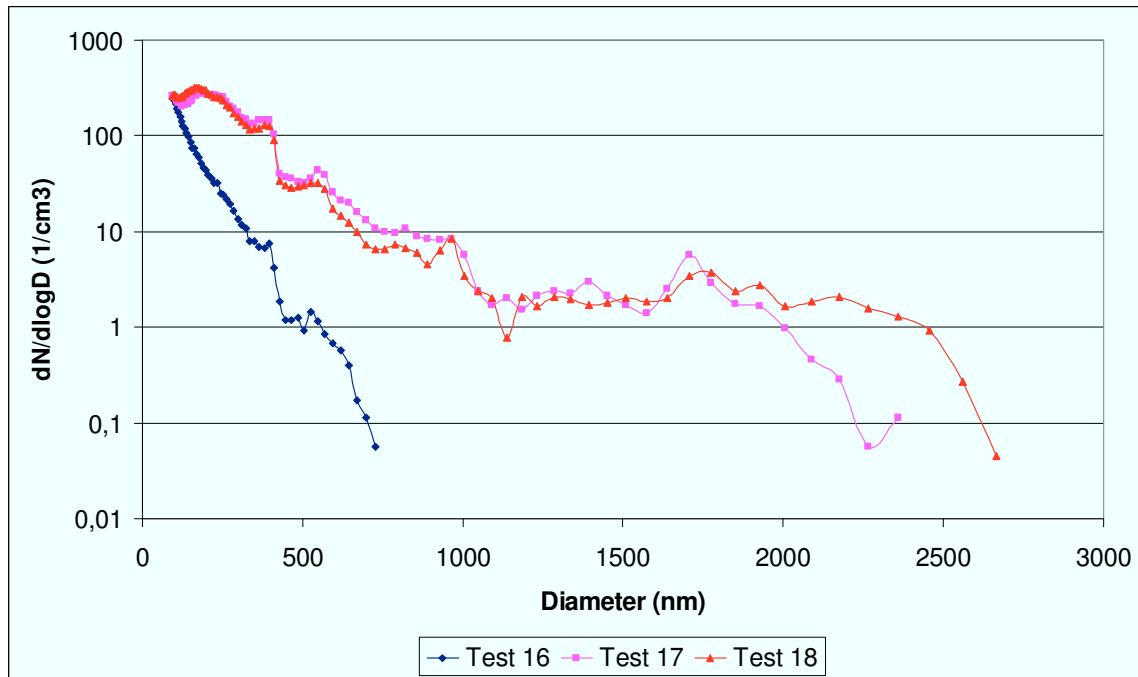


**Figure 4.8** – Size distribution vs diameter in Test 16 - 17 - 18, with  $\Phi=2.38$ . The test 16 is performed without liquid film in the growth tube.

In the following figures the tests with  $\Phi=3.30$  are shown. Every data are derived by an arithmetic mean from 20 samplings and corresponding measurement performed by LAS 3340.

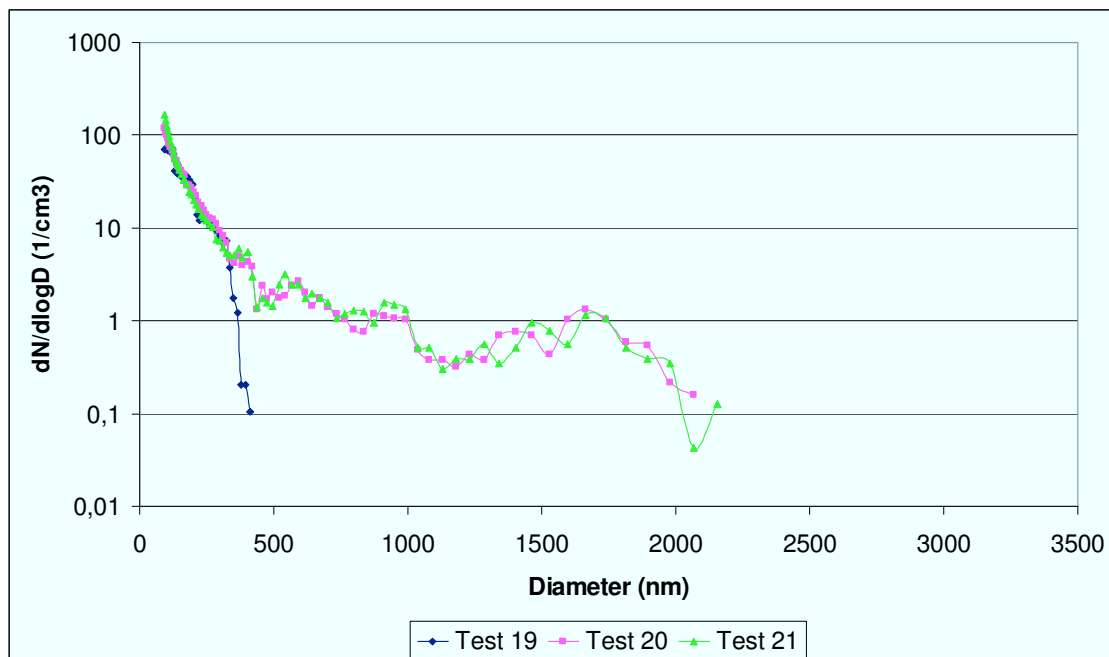


**Figure 4.9** – Size distribution vs diameter in Test 19 - 20 - 21, with  $\Phi=3.30$ . The test 19 is performed without liquid film in the growth tube.

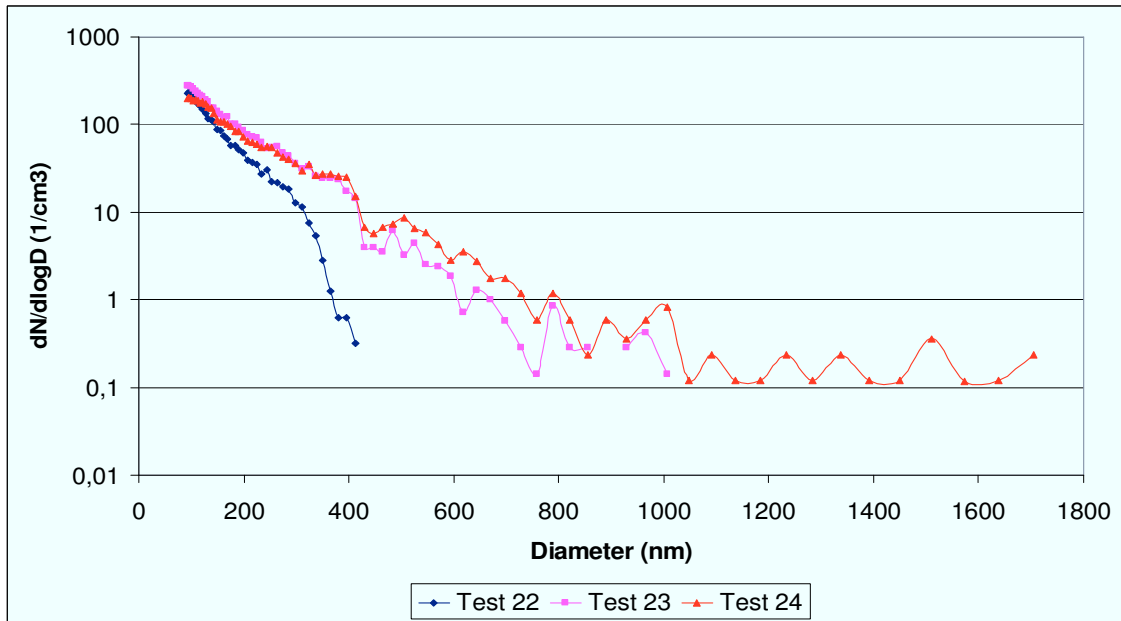


**Figure 4.10** – Size distribution vs diameter in Test 22 - 23 - 24, with  $\Phi=3.30$ . The test 22 is performed without liquid film in the growth tube.

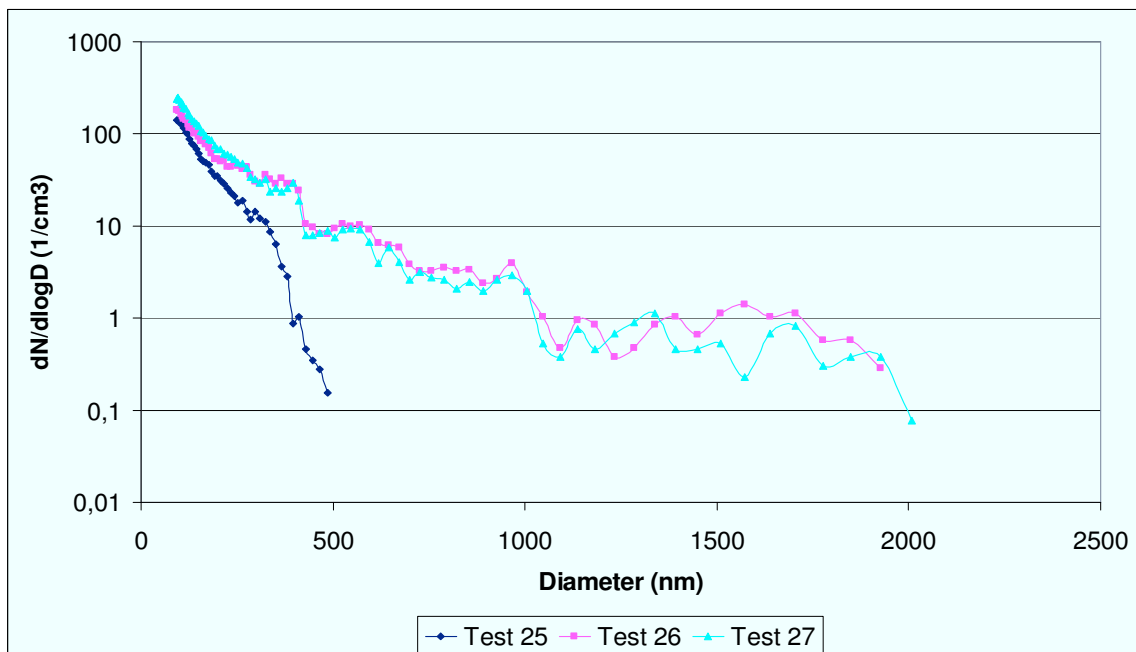


**Figure 4.11** – Size distribution vs diameter in Test 25 - 26 - 27, with  $\Phi=3.30$ . The test 25 is performed without liquid film in the growth tube.



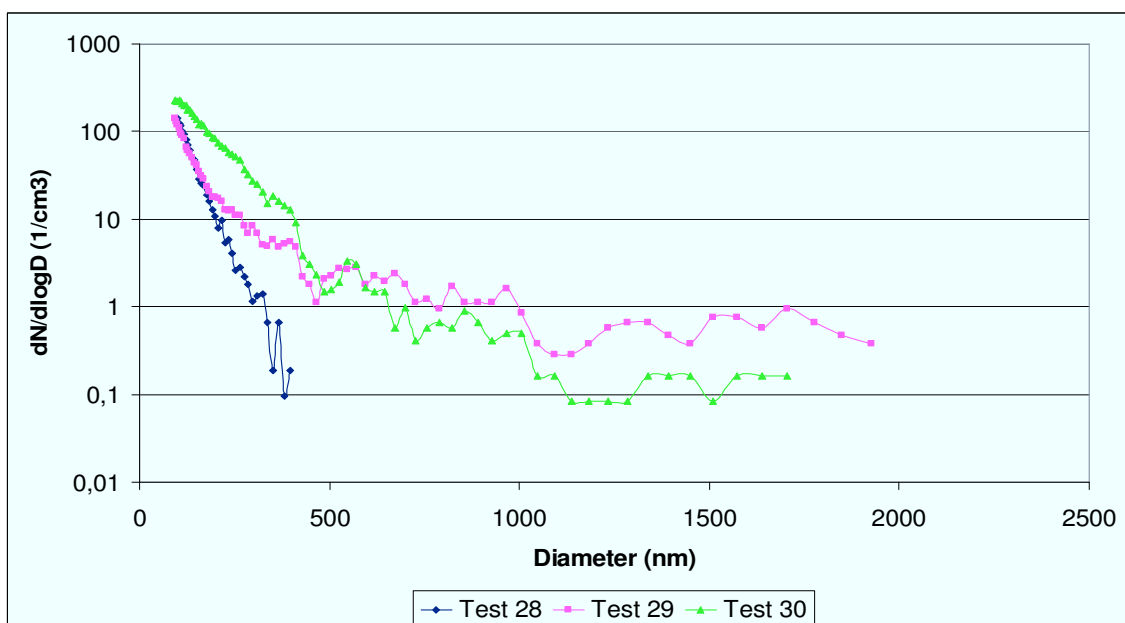


**Figure 4.12** – Size distribution vs diameter in Test 28 - 29 - 30, with  $\Phi=3.30$ . The test 28 is performed without liquid film in the growth tube.

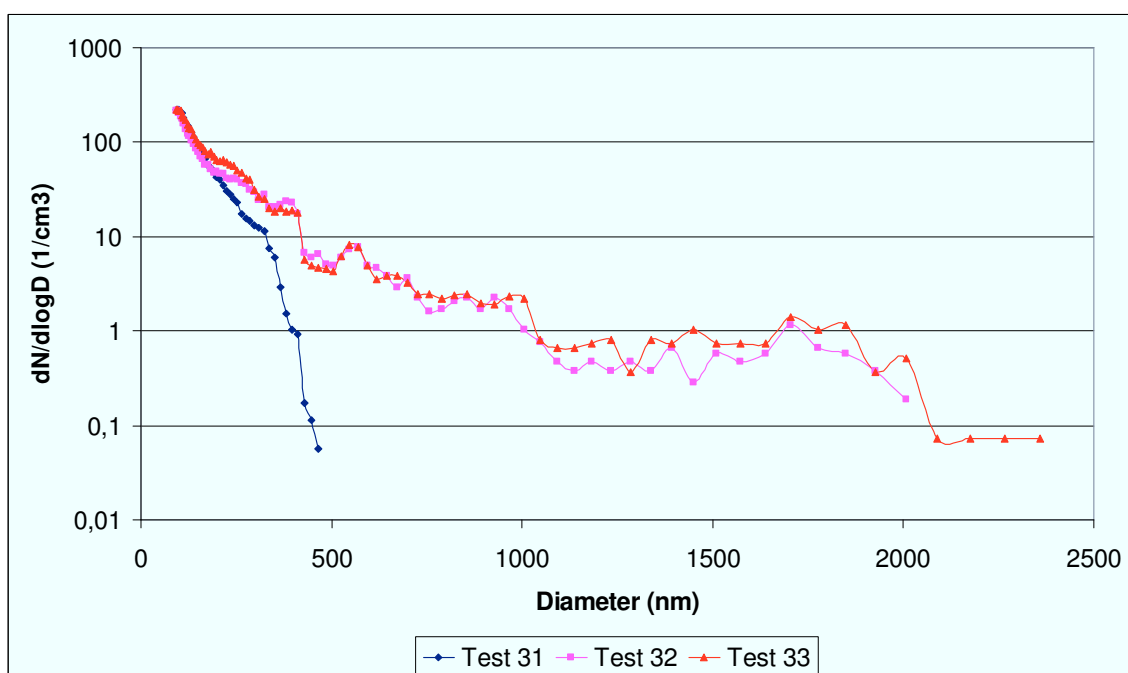


**Figure 4.13** – Size distribution vs diameter in Test 31 - 32 - 33, with  $\Phi=3.30$ . The test 31 is performed without liquid film in the growth tube.

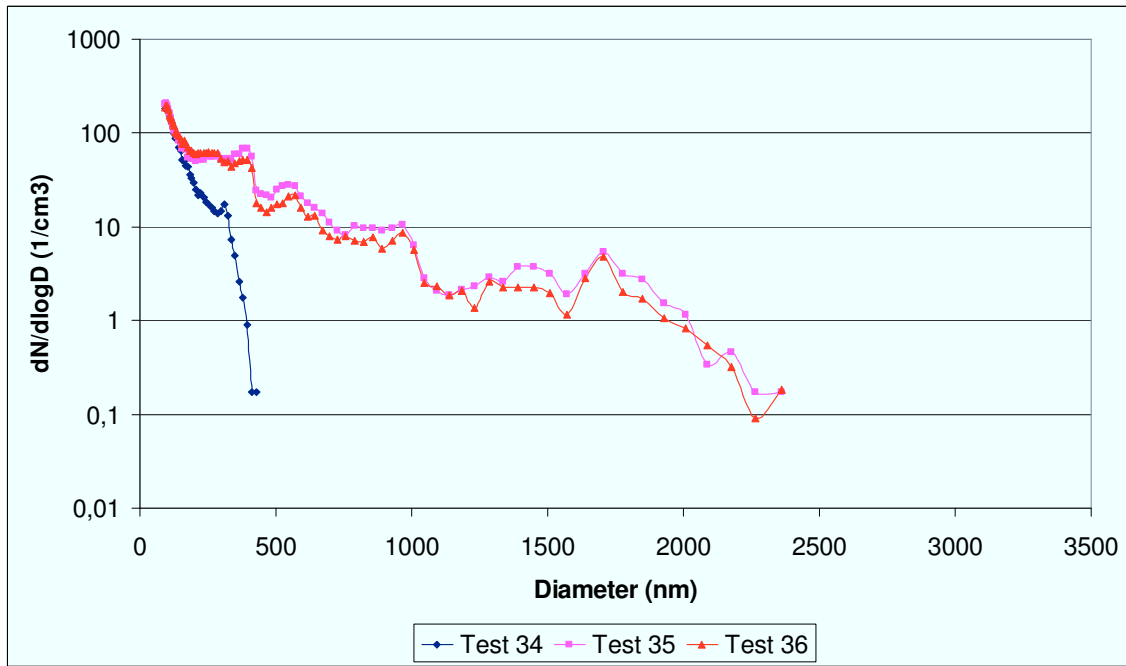


**Figure 4.14** – Size distribution vs diameter in Test 34 - 35 - 36, with  $\Phi=3.30$ . The test 34 is performed without liquid film in the growth tube.

As can be seen from comparison between blank tests - performed only with air - and the tests performed in presence of flame with two equivalent ratio,  $\Phi=2.38$  (Figures 4.3-8), and  $\Phi=3.30$  (Figures 4.9-14), there is not a remarkable difference between the size distribution. As expected, the concentration of droplet increases with the equivalent ratio but the increase is small. This effect can be addressed to two main reasons. The first is related to the experimental conditions, i.e. to the high dilution ratio that reduces the concentration of the particles produced by flame. The second is related to the effect of aggregation, between both the particles both the droplets, which occurs when in the gas increases the concentration of particles.

Therefore for the Figures 4.3-14 the same considerations done for Figure 4.2 can be applied.

### 3. Critical diameter

The two curves corresponding to the size distribution at two wall temperatures in Figures 4.3-14 and 4.2 have the same behaviour. Indeed these curves initially, i.e. at low values of diameter, decrease with the same trend of the size distribution measured in the absence of the liquid film in the growth tube. Then, at a determined value of diameter, these curves change slope, because the heterogeneous condensation is activated. In the chapter 2 we have seen that the heterogeneous condensation starts when the supersaturation in the growth tube is equal to the critical supersaturation. This condition determines the diameter,

which we can call *critical diameter*, corresponding to slope change of the abovementioned curves. The meaning of critical diameter is that the particles with lower size are not activated by heterogeneous condensation. The identification of the critical diameter can be also achieved graphically as in the following reported examples. In Figure 4.15 the supersaturation and critical supersaturation profiles versus residence time (graphs a and c) and critical supersaturation profile versus particle diameter (graphs b and d) of the Test 2 ( $T_w=313$  K) and 3 ( $T_w=323$  K) (Figure 4.3) are shown respectively. The curves are relative only to profile along centreline for clarity.

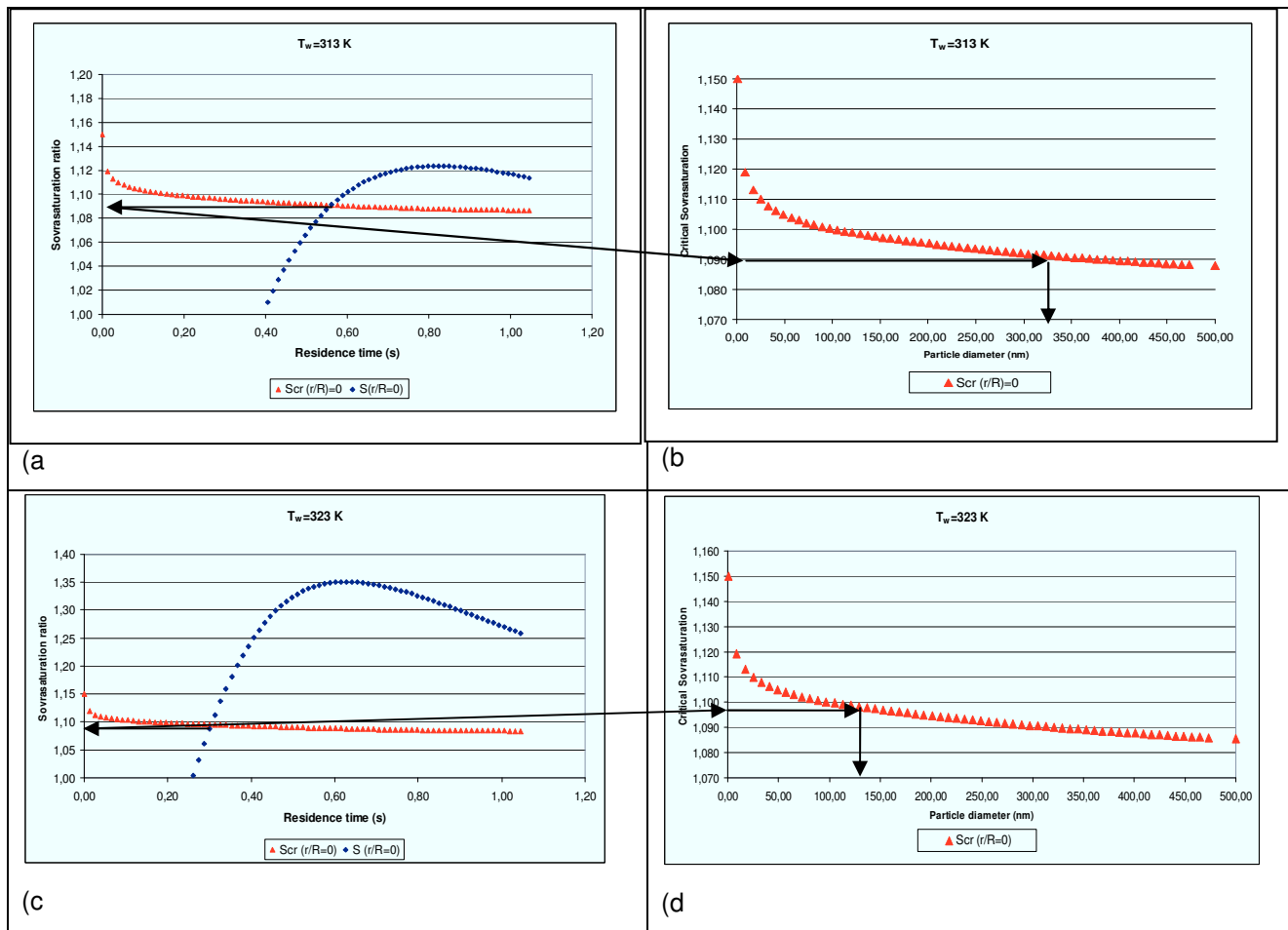


**Figure 4.15** - Supersaturation and critical supersaturation profiles along centreline ( $r/R=0$ ) versus residence time (graphs a and c) and critical supersaturation profile along centreline ( $r/R=0$ ) versus particle diameter (graphs b and d) of the Test 2 and 3 (Figure 4.3) and Test 20 and 21 (Figure 4.9).

The intersection between curves (graphs a and c) represents the abovementioned condition  $S = S_{cr}$ . Since critical supersaturation depends on the temperature and diameter (see Chapter 2), from curves b and d it is possible to individuate the diameter corresponding to the intersection point for each wall temperature. The arrows in Figure 4.15 show the procedure to individuate the theoretical critical diameter.

Taking into account also the radial positions ( $r/R=0.4$ ) and ( $r/R=0.8$ ), it is possible to individuate the diameter corresponding to the intersection point for each wall temperature and for each radial position; in this way it is possible to individuate a critical diameters range within which the heterogeneous condensation starts. The range diameters is limited by the lowest and the higher diameter individuated with the previously described procedure, for each curves of supersaturation and critical supersaturation relative to three radial position ( $r/R=0$ ,  $r/R=0.4$ ,  $r/R=0.8$ ). In the following, the figures with supersaturation and critical supersaturation profile versus residence time and the critical supersaturation profile versus particle diameter, at three radial positions, of test presented in Figures 4.3-14, are shown.

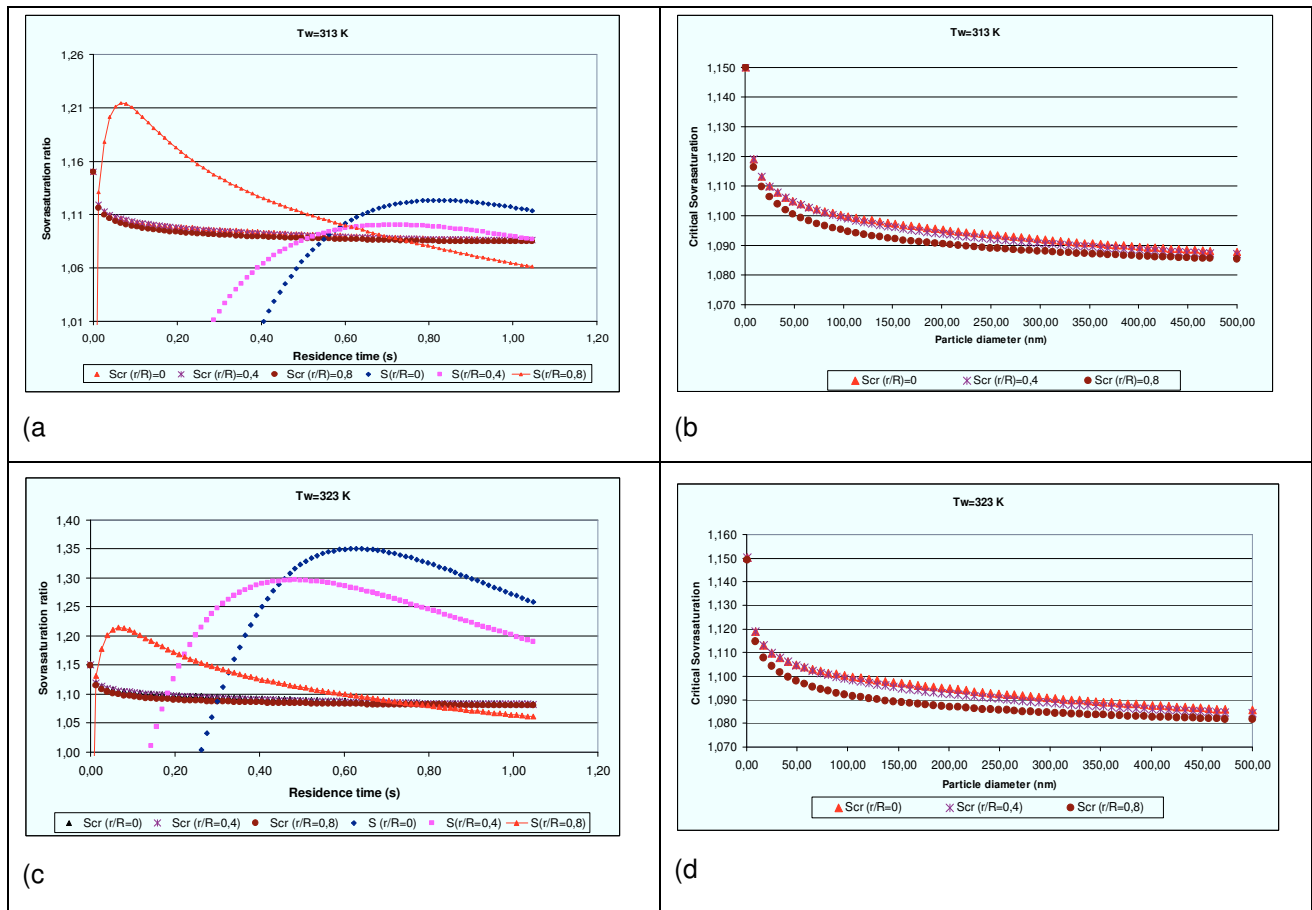


**Figure 4.16** - Supersaturation and critical supersaturation profiles versus residence time (graphs a and c) and critical supersaturation profile versus particle diameter (graphs b and d) for three different radial position ( $r/R=0$ ,  $r/R=0.4$ ,  $r/R=0.8$ ) of the Test 2 and 3 (Figure 4.3) and Test 20 and 21 (Figure 4.9).

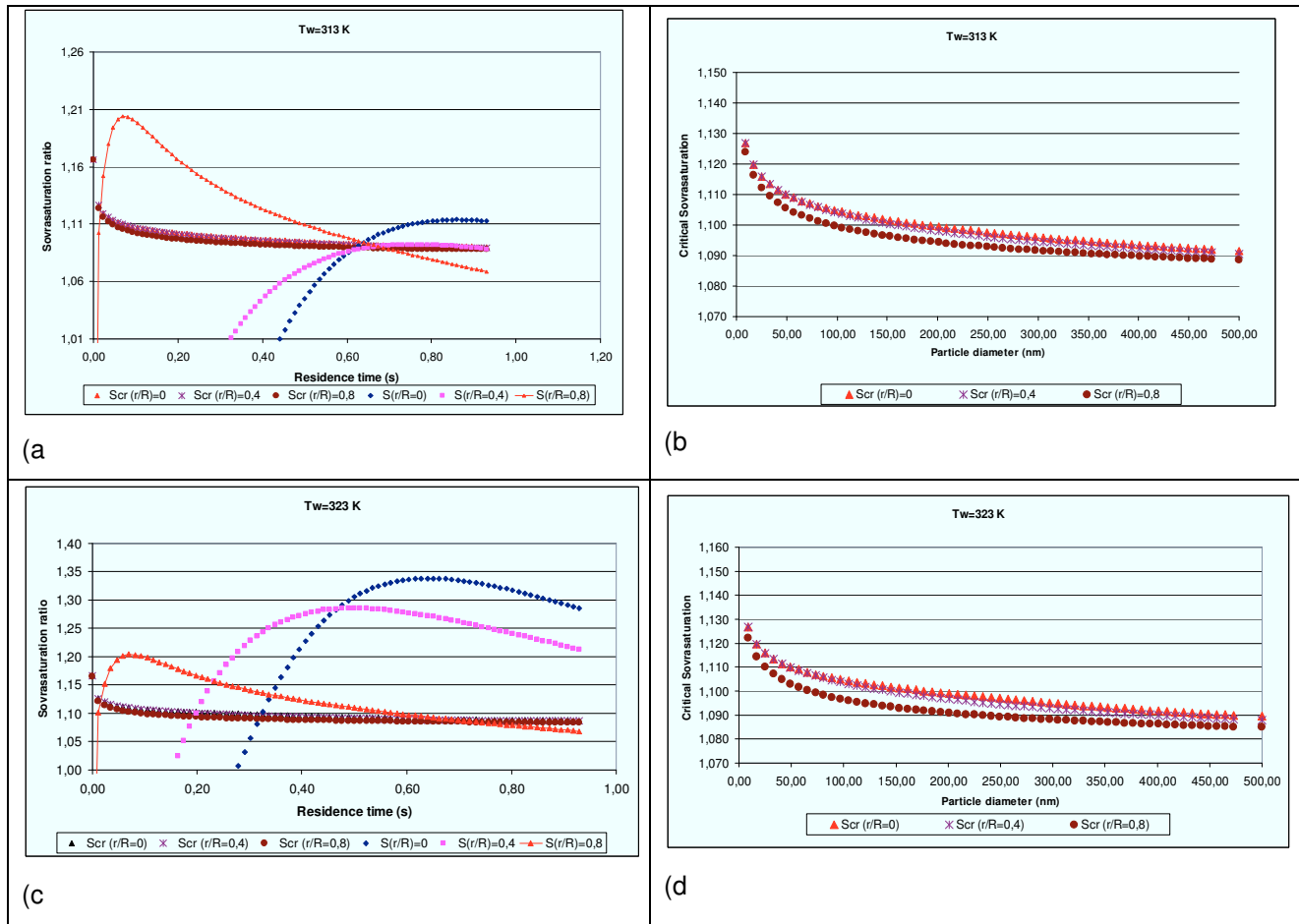


**Figure 4.17** - Supersaturation and critical supersaturation profiles versus residence time (graphs a and c) and critical supersaturation profile versus particle diameter (graphs b and d) for three different radial position ( $r/R=0$ ,  $r/R=0.4$ ,  $r/R=0.8$ ) of the Test 5 and 6 (Figure 4.4) and Test 23 and 24 (Figure 4.10).

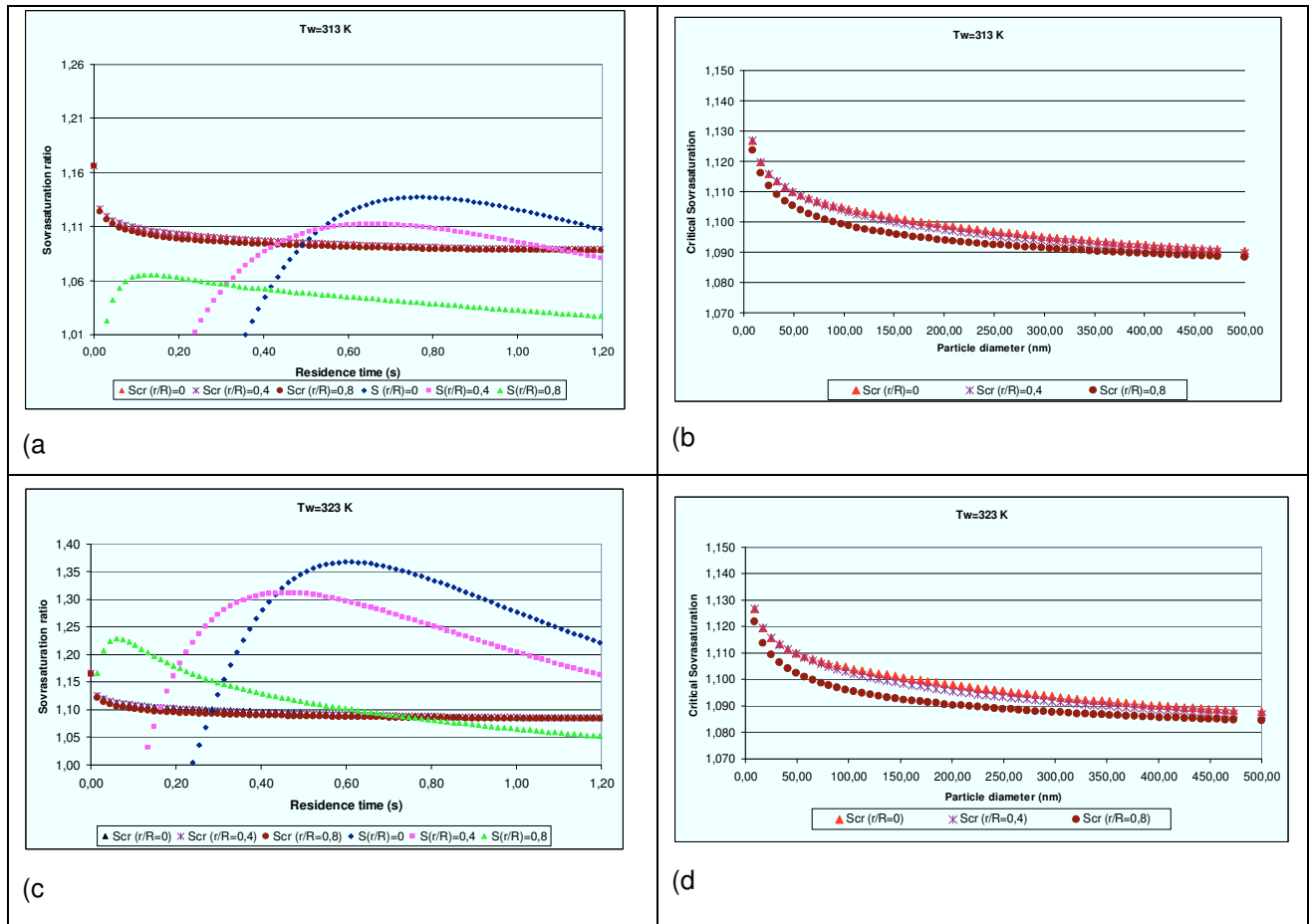


**Figure 4.18** - Supersaturation and critical supersaturation profiles versus residence time (graphs a and c) and critical supersaturation profile versus particle diameter (graphs b and d) for three different radial position ( $r/R=0$ ,  $r/R=0.4$ ,  $r/R=0.8$ ) of the Test 8 and 9 (Figure 4.5) and Test 26 and 27 (Figure 4.11).

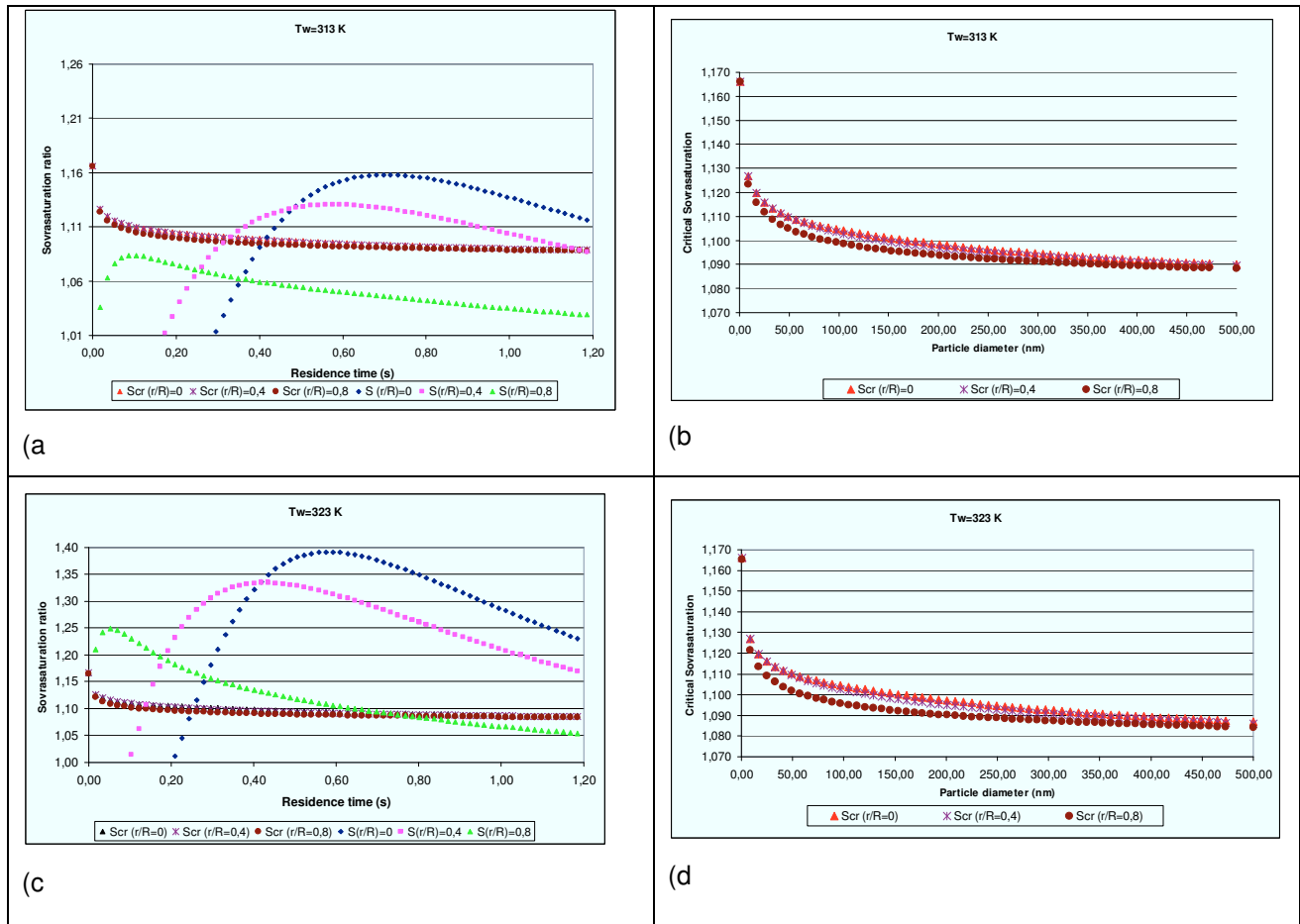


**Figure 4.19** - Supersaturation and critical supersaturation profiles versus residence time (graphs a and c) and critical supersaturation profile versus particle diameter (graphs b and d) for three different radial position ( $r/R=0$ ,  $r/R=0.4$ ,  $r/R=0.8$ ) of the Test 11 and 12 (Figure 4.6) and Test 29 and 30 (Figure 4.12).

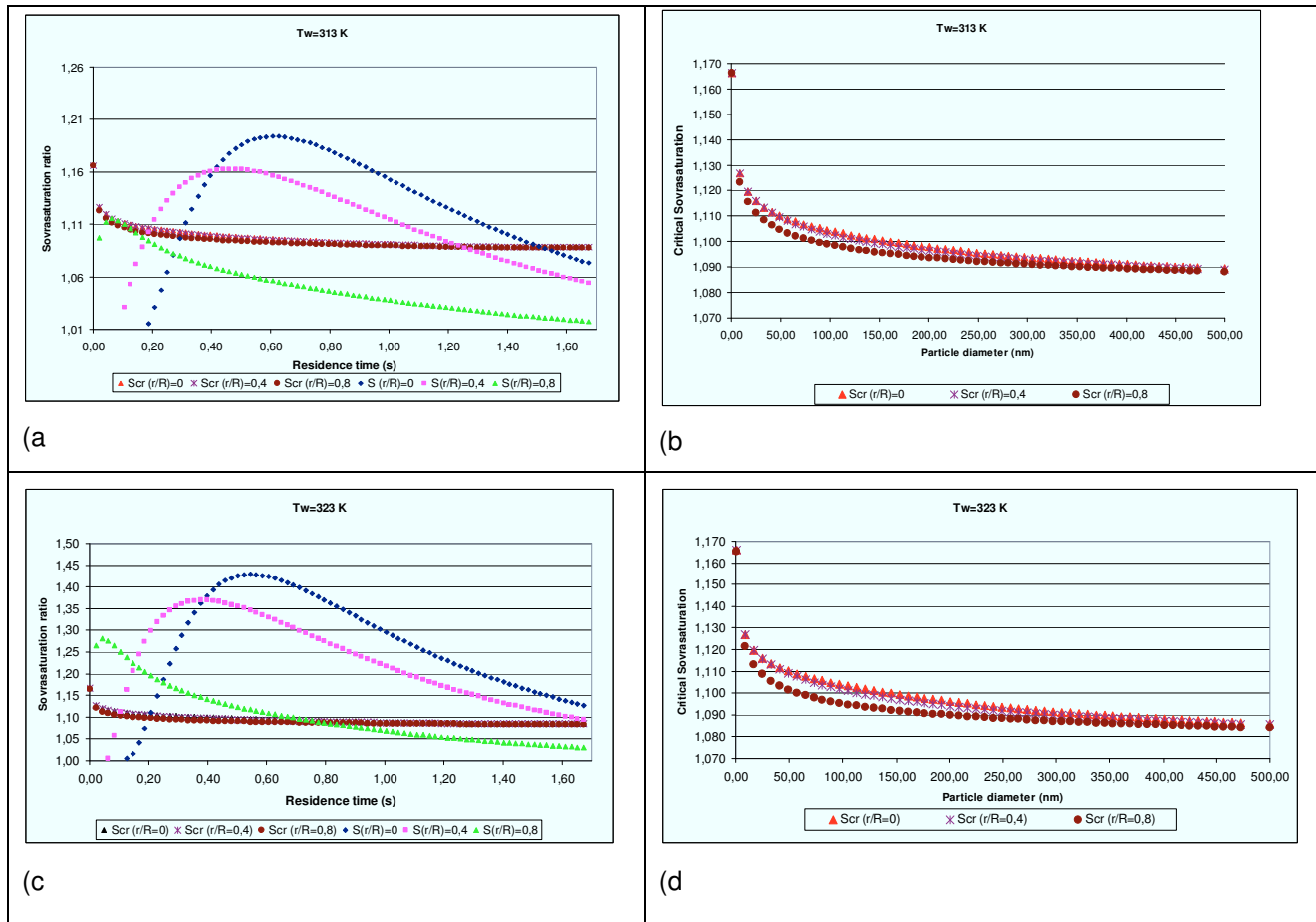


**Figure 4.20** - Supersaturation and critical supersaturation profiles versus residence time (graphs a and c) and critical supersaturation profile versus particle diameter (graphs b and d) for three different radial position ( $r/R=0$ ,  $r/R=0.4$ ,  $r/R=0.8$ ) of the Test 14 and 15 (Figure 4.7) and Test 32 and 33 (Figure 4.13).



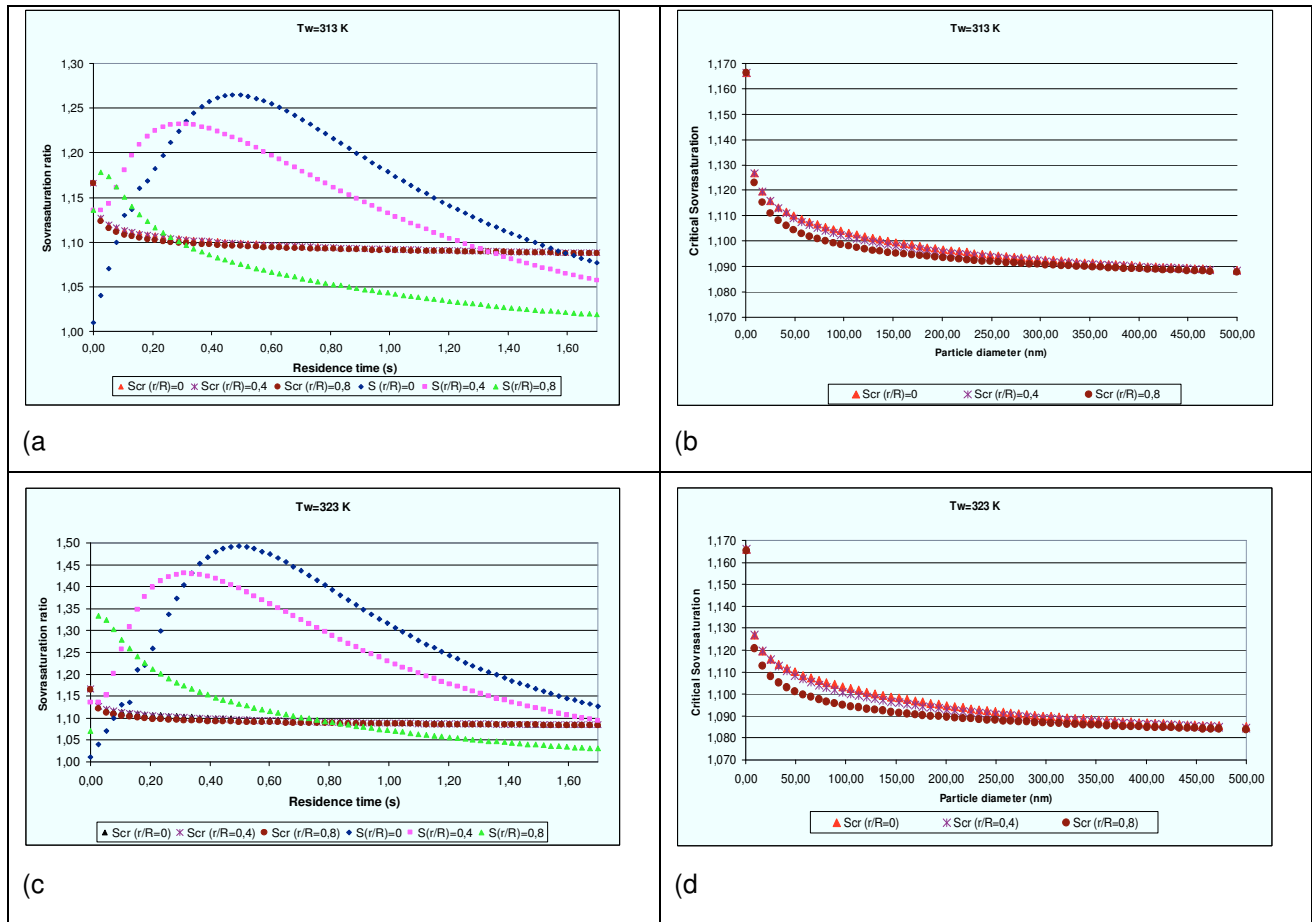


**Figure 4.21** - Supersaturation and critical supersaturation profiles versus residence time (graphs a and c) and critical supersaturation profile versus particle diameter (graphs b and d) for three different radial position ( $r/R=0$ ,  $r/R=0.4$ ,  $r/R=0.8$ ) of the Test 17 and 18 (Figure 4.8) and Test 35 and 36 (Figure 4.14).

The theoretical critical diameters range individuated in this way,  $(150 \div 300)\text{ nm}$ , fit with a good approximation to the range of diameters found experimentally,  $(100 \div 200)$ .

#### 4. Comparison between experimental data and modelling

In this section a comparison between the experimental data and the model (equations 2.99 and 2.108) described in Chapter 2 will be performed. For this purpose a mean diameter of measured droplets have to be defined. This value must be representative of the diameter of the droplet reached in the growth tube through heterogeneous condensation.

In the outlet of growth tube there is an aerosol, composed by droplet and particles that are not activated by heterogeneous condensation. The instrument LAS 3340, which is an optical device, does not distinguish between particles and droplets. Therefore, in order to be sure to consider only diameters of droplets and not those of particles, we have subtracted the diameters measured in the tests without liquid film from the distribution of

diameters present in the test with the liquid film. With this procedure we have adopted two hypotheses: a) negligible presence of large solid particles formed by aggregation; b) all the particles larger than critical diameter are activated by heterogeneous condensation. In the following figure an example, by Test 1-2-3, of procedure to define the range of droplet diameter.

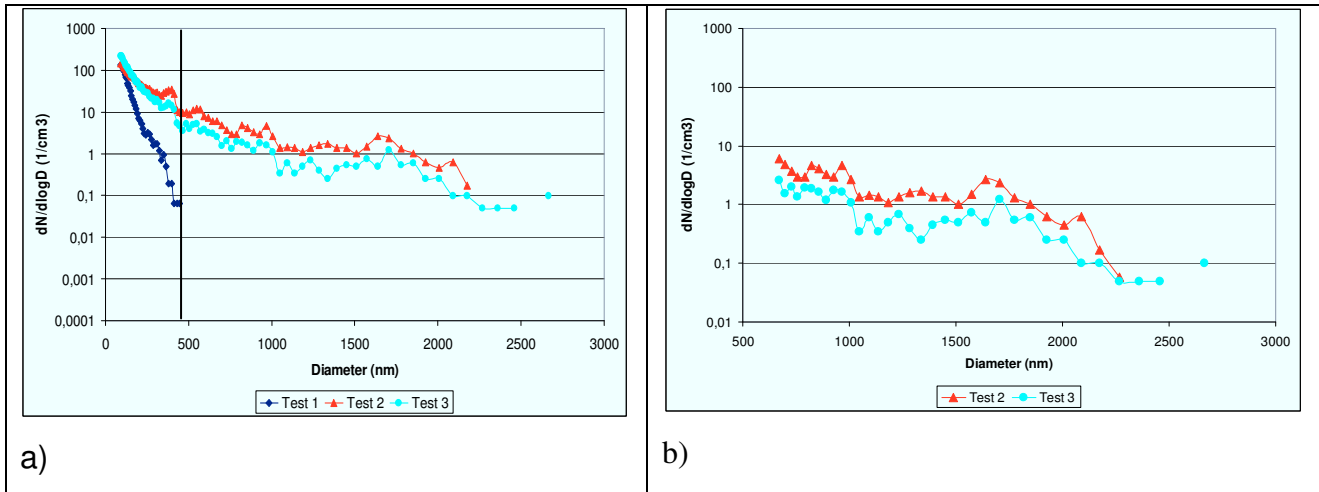


**Figure 4.22** – Procedure to define the size distribution of diameter of the droplet in outlet of growth tube

As can be seen from the size distribution of the test with and without liquid film (Figure 4.22a), we can obtain the size distribution of droplet (Figure 4.22b).

Then we proceed to define a mean diameter, through a weighted average of the diameters of the droplet, where the weight is the normalised concentration, as follows:

$$\bar{D} = \frac{\sum D_i * (dN / dLogD_i)}{\sum (dN / dLogD_i)} \quad (4.1)$$

In following table an example, by Test 2 and 3, of normalised concentration utilised as weight to define the abovementioned diameter through the (4.1).

$D_i$ (nm)	Test 3	Test 2
	$T_w = 323$ K $dN/d\log D_i$	$T_w = 313$ K $dN/d\log D_i$
671	2,57844233	6,103227
699	1,53703181	4,79093
728	1,98290858	3,706348
758	1,33892958	2,966356
789	1,93302629	2,964977
822	1,88437651	4,734651
856	1,63608349	4,106261
891	1,18978013	3,250407
928	1,78507788	2,965862
967	1,63579252	4,675986
1007	1,09074302	2,680488
1048	0,34705694	1,36884
1092	0,59506738	1,425945
1137	0,34703703	1,368805
1184	0,49586049	1,08362
1233	0,69407374	1,368673
1284	0,39663058	1,596831
1337	0,24792771	1,710872
1393	0,44621955	1,368973
1450	0,54532134	1,368859
1510	0,49580852	1,026687
1573	0,74359972	1,482464
1638	0,49582815	2,680671
1706	1,2394724	2,338099
1777	0,54534012	1,311742
1850	0,59494215	1,026459
1927	0,24789476	0,627365
2007	0,24787527	0,456351
2090	0,09915704	0,627374
2176	0,09917105	0,171079
2266	0,0495905	0
2360	0,049566	0
2458	0,04957135	0
2666	0,09916142	0

**Table 4.3** – Numerical size distribution for Test 2 and 3

In the following table the results, for each test, of this procedure.

Test	$\Phi$	Residence time (s)	Q (l/min)	$\bar{D}$ ( $\mu\text{m}$ )	
				$T_w = 313 \text{ K}$	$T_w = 323 \text{ K}$
B	2.38	0,94	4,5	0,948	0,941
A		1,06	4	1,055	1,050
C		1,21	3,5	0,941	0,803
D		1,41	3	0,712	0,782
E		1,7	2,5	1,272	1,244
F		2,12	2	1,061	1,207
H	3.30	0,94	4,5	0,538	0,567
G		1,06	4	0,811	0,811
I		1,21	3,5	0,746	0,809
J		1,41	3	0,758	0,656
K		1,7	2,5	1,157	1,116
L		2,12	2	1,120	1,115

**Table 4.4** – Mean droplet diameter for each test

In order to calculate the temperature and pressure profiles in the presence of solid particles, the calculation of the term  $\sum C_i I_i$ , will be now considered. This term is contained in equations 2.93 and 2.97. In the following table an example of calculation by Test 1. The fluxes of mass  $I_i$  are calculated through the 2.49. The particles concentration,  $C_i$ , for each diameter  $i$ , is measured by LAS 3340. Then for each particle diameter, for each temperature profile in the growth tube derived by the two wall temperature, and for each radial position ( $r/R=0$ ,  $r/R=0.4$  and  $r/R=0.8$ ), is calculated  $\sum C_i I_i$ . A mean between the radial position is performed in order to have one value for each particle diameter and wall temperature.

Particles diameter (nm)	Concentration ( $\text{n/m}^3$ )	$\sum C_i I_i$ ( $T_w=313 \text{ K}$ )	$\sum C_i I_i$ ( $T_w=323 \text{ K}$ )
92	2,68E+06	5,03E-04	2,21E-03
96	2,69E+06	5,07E-04	2,22E-03
100	2,59E+06	5,22E-04	2,15E-03
104	2,50E+06	4,79E-04	2,18E-03
108	2,21E+06	5,02E-04	2,29E-03
113	2,09E+06	5,09E-04	1,74E-03
117	1,84E+06	5,17E-04	1,77E-03
122	1,65E+06	3,27E-04	1,39E-03
127	1,55E+06	3,36E-04	1,43E-03
132	1,33E+06	3,65E-04	1,55E-03

138	1,25E+06	3,94E-04	1,67E-03
144	1,16E+06	2,34E-04	1,72E-03
149	1,03E+06	2,50E-04	8,75E-04
156	8,63E+05	2,70E-04	9,46E-04
162	8,11E+05	3,11E-04	1,09E-03
169	7,04E+05	3,08E-04	1,08E-03
176	6,39E+05	3,40E-04	1,19E-03
183	6,05E+05	1,27E-04	1,36E-03
191	4,97E+05	1,35E-04	4,34E-04
199	4,07E+05	1,43E-04	4,61E-04
207	3,90E+05	1,55E-04	5,00E-04
215	3,50E+05	1,72E-04	5,53E-04
224	3,07E+05	1,97E-04	6,34E-04
234	2,82E+05	2,34E-04	7,52E-04
243	2,60E+05	2,30E-04	7,39E-04
253	2,42E+05	1,89E-04	2,19E-04
264	2,11E+05	1,82E-04	2,11E-04
275	1,37E+05	3,03E-05	1,80E-04
286	1,31E+05	4,06E-05	1,21E-04
298	1,25E+05	3,57E-05	1,06E-04
310	1,24E+05	3,54E-05	1,05E-04
323	9,68E+04	3,94E-05	1,17E-04
337	6,90E+04	4,85E-05	6,51E-05
350	5,94E+04	3,07E-05	4,12E-05
365	3,93E+04	9,03E-06	5,10E-05
380	2,40E+04	1,47E-05	8,30E-05
396	1,25E+04	7,64E-06	4,32E-05
412	7,67E+03	1,41E-05	7,96E-05
429	2,88E+03	5,29E-06	2,99E-05
447	9,57E+02	2,27E-07	9,57E-07
466	9,57E+02	2,27E-07	9,57E-07
485	9,57E+02	2,27E-07	9,57E-07
505	1,92E+03	4,55E-07	1,92E-06
526	1,92E+03	4,55E-07	1,92E-06
548	2,87E+03	2,27E-07	9,58E-07
570	2,87E+03	2,27E-07	9,58E-07
594	1,92E+03	4,79E-07	2,06E-06
619	1,92E+03	4,79E-07	2,06E-06
644	1,92E+03	4,79E-07	2,06E-06
Sum		<b>8,75E-03</b>	<b>3,44E-02</b>

**Table 4.5** – Example of calculation of terms  $\sum C_i I_i$  by Test 1

Then it is possible to perform a comparison between the experimental data and equation (2.99). In the following figures a comparison between the experimental data,  $\bar{D}$ , and the model is presented for the two equivalent ratio 2,38 and 3,30 respectively.

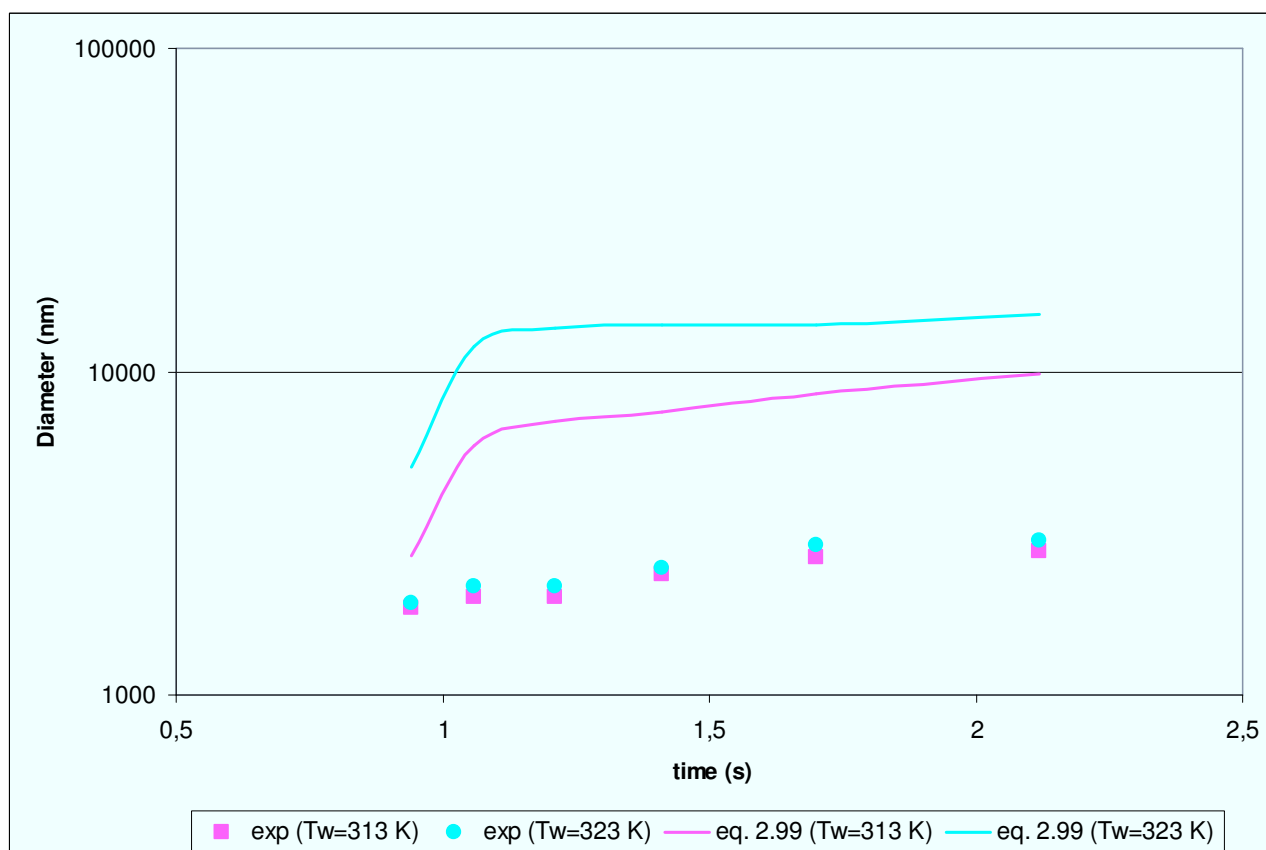


**Figure 4.23** – Comparison between experimental data,  $\bar{D}$ , and model by (2.99), for  $\Phi=2,38$ , vs residence time (s)

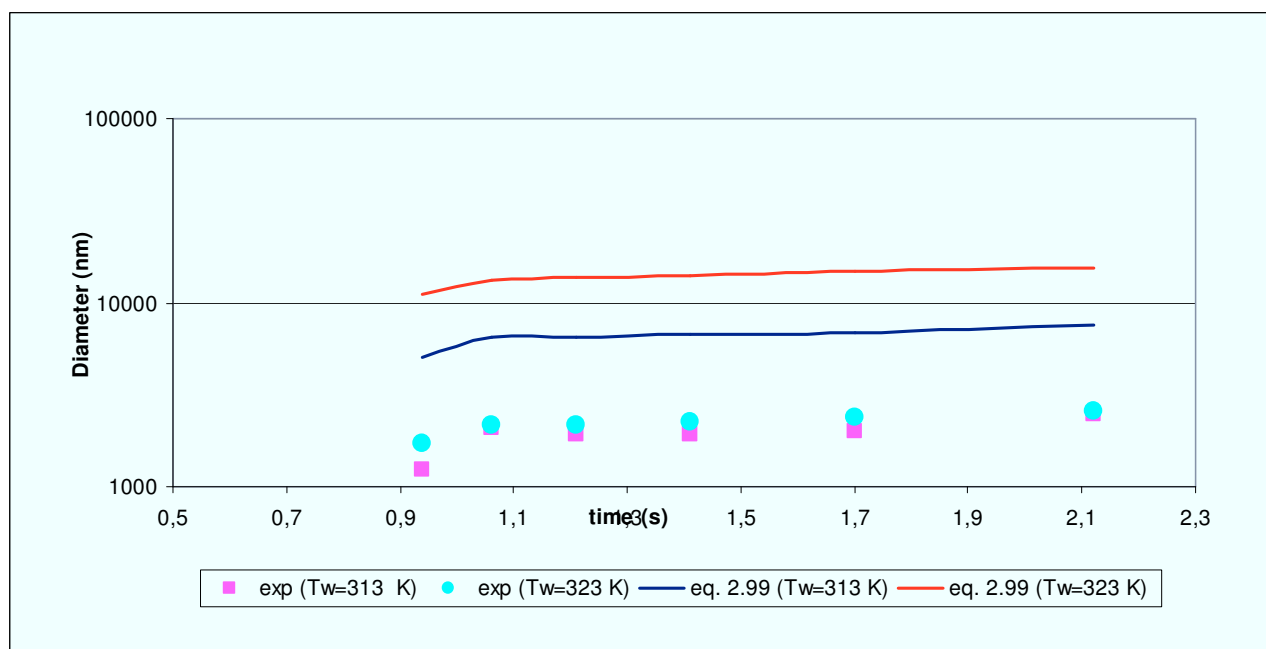


**Figure 4.24** - Comparison between experimental data,  $\bar{D}$ , and model by (2.99), for  $\Phi=3,30$ , vs residence time (s)

As can be seen from Figures 4.23 and 4.24, the experimental data reproduce the same behaviour of the model, that is, for an adiabatic system, increasing for low residence time

while became constant for long times. The light dependence of growth rate and of final droplet diameter on the temperature has been already reported, for the adiabatic case (Heidenreich *et al.*, 1995).

However, as can be seen from the above figures, there is a gap between experimental and model droplet diameter. In particular the model overestimates the final diameter.

The model is based on simplified hypothesis of smooth, spherical and homogeneous particle, then it is acceptable that it diverges from the experimental data, but in this case the gap appears quite large.

Then, in order to apply the equation (2.108) to our experimental data through the procedure defined in paragraph 2.6, we carry on to define the factors  $a$  and  $n$  of equation (2.107).

For each test performed, we have calculated the parameters  $M$  defined in (2.105). The results are presented in following table.

$\Phi$	Test	$T_w$	$\frac{P_b^{eff}}{T_b}$	$\frac{P_w}{T_w}$	$\frac{P_b}{T_b}$	$M = \frac{\frac{P_w}{T_w} - \frac{P_b^{eff}}{T_b}}{\frac{P_w}{T_w} - \frac{P_b}{T_b}}$
2,38	2	313	19,66	38,10	25,06	1,41
	3	323	17,38	23,51	16,60	1,51
	5	313	18,38	23,51	15,84	0,67
	6	323	20,87	38,10	23,83	1,21
	8	313	16,40	23,51	17,45	1,45
	9	323	18,46	38,10	26,44	1,68
	11	313	15,55	23,51	18,40	1,56
	12	323	17,40	38,10	27,99	2,05
	14	313	14,99	23,51	19,45	2,1
	15	323	16,63	38,10	29,72	2,56
	17	313	14,88	23,51	20,60	2,96
	18	323	16,29	38,10	31,62	3,37
3,3	20	313	17,38	23,51	16,60	0,89
	21	323	19,66	38,10	25,06	1,21
	23	313	18,38	23,51	15,84	0,67
	24	323	20,87	38,10	23,83	1,41
	26	313	16,40	23,51	17,45	1,17
	27	323	18,46	38,10	26,44	1,68
	29	313	12,43	23,51	18,40	2,17
	30	323	17,40	38,10	27,99	2,05
	32	313	13,96	23,51	19,45	2,35
	33	323	15,64	38,10	29,72	2,68
	35	313	14,88	23,51	20,60	2,96
	36	323	16,29	38,10	31,62	3,37

**Table 4.6** – Factor  $M$  calculated for each test

From equation (2.99) and from experimental data we can calculate the factor B defined by (2.106) as

$$B = \frac{\overline{D}}{D_{eq.2.99}} \quad (4.2)$$

From (2.107) we have that  $B = aM^n$ , that can be rewritten as:

$$\ln(B) = \ln(aM^n) = \ln a + n \ln(M) \quad (4.3)$$

that is the equation of a straight line in a graph in logarithmic scale. In the following table the factors B and M, and their natural logarithms, calculated for each test, are reported.

$\Phi$	M		B		Ln(B)		Ln(M)	
	$T_w = 313 \text{ K}$	$T_w = 323 \text{ K}$	$T_w = 313 \text{ K}$	$T_w = 323 \text{ K}$	$T_w = 313 \text{ K}$	$T_w = 323 \text{ K}$	$T_w = 313 \text{ K}$	$T_w = 323 \text{ K}$
2,38	0,6694	1,2072	0,3505	0,1857	-1,0483	-1,6836	-0,4014	0,1883
	1,4144	1,5100	0,1788	0,0807	-1,7213	-2,5167	0,3467	0,4121
	1,4500	1,6849	0,1337	0,0591	-2,0122	-2,8286	0,3716	0,5217
	1,5569	2,0484	0,0946	0,0577	-2,3580	-2,8521	0,4427	0,7171
	2,0977	2,5617	0,1491	0,0913	-1,9034	-2,3931	0,7408	0,9407
	2,9648	3,3654	0,1080	0,0840	-2,2257	-2,4773	1,0868	1,2135
3,3	0,6694	1,4144	0,0896	0,0431	-2,4119	-3,1447	-0,4014	0,3467
	0,8879	1,2072	0,1262	0,0607	-2,0698	-2,8016	-0,1189	0,1883
	1,1738	1,6849	0,1147	0,0593	-2,1657	-2,8260	0,1602	0,5217
	2,1677	2,0484	0,1153	0,0469	-2,1603	-3,0608	0,7737	0,7171
	2,3535	2,6797	0,1673	0,0754	-1,7878	-2,5844	0,8559	0,9857
	2,9648	3,3654	0,1468	0,0721	-1,9184	-2,6301	1,0868	1,2135

**Table 4.7** – Factors M and B and their natural logarithms calculated for each test

Each pair of value  $\ln(B)$  and  $\ln(M)$ , at same  $T_w$  and same  $\Phi$ , is a point in the following graphs in Figures 4.25 and 4.26. Then through a linear regression it is possible to obtain the parameters  $a$  and  $n$  from equation (4.3).



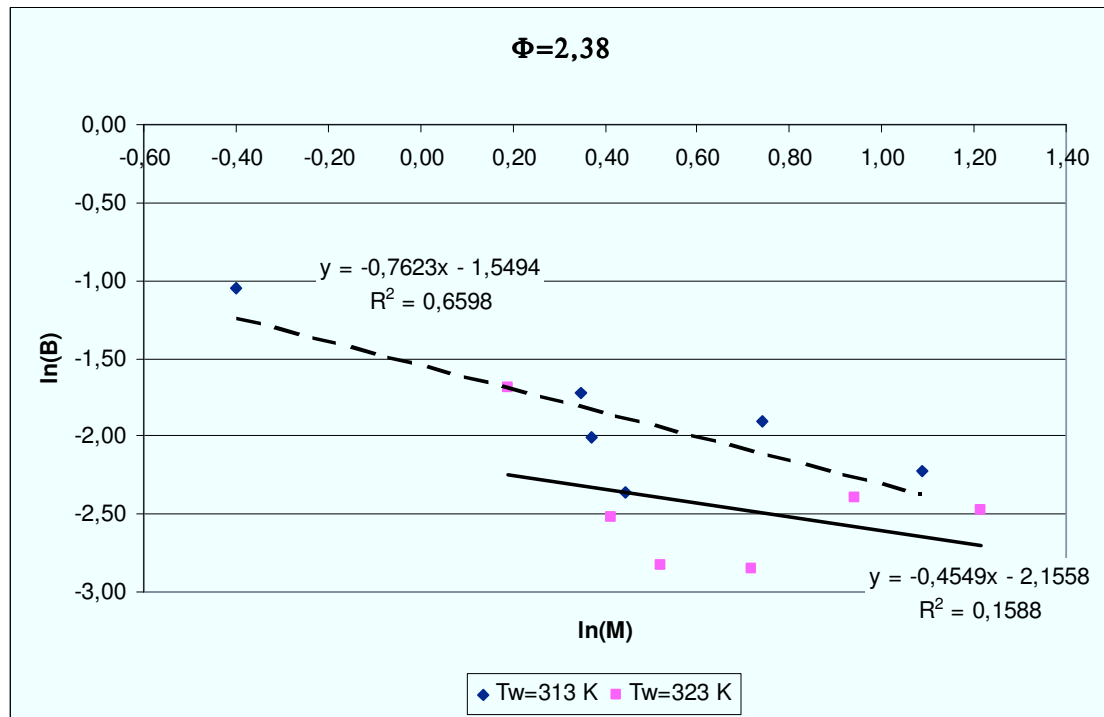


**Figure 4.25** –  $\ln(B)$  vs  $\ln(M)$  calculated for test with equivalent ratio  $\Phi=2,38$ . The continue line is the linear regression for the points corresponding to  $T_w= 323$  K. The dashed line is the linear regression for the points corresponding to  $T_w= 313$  K

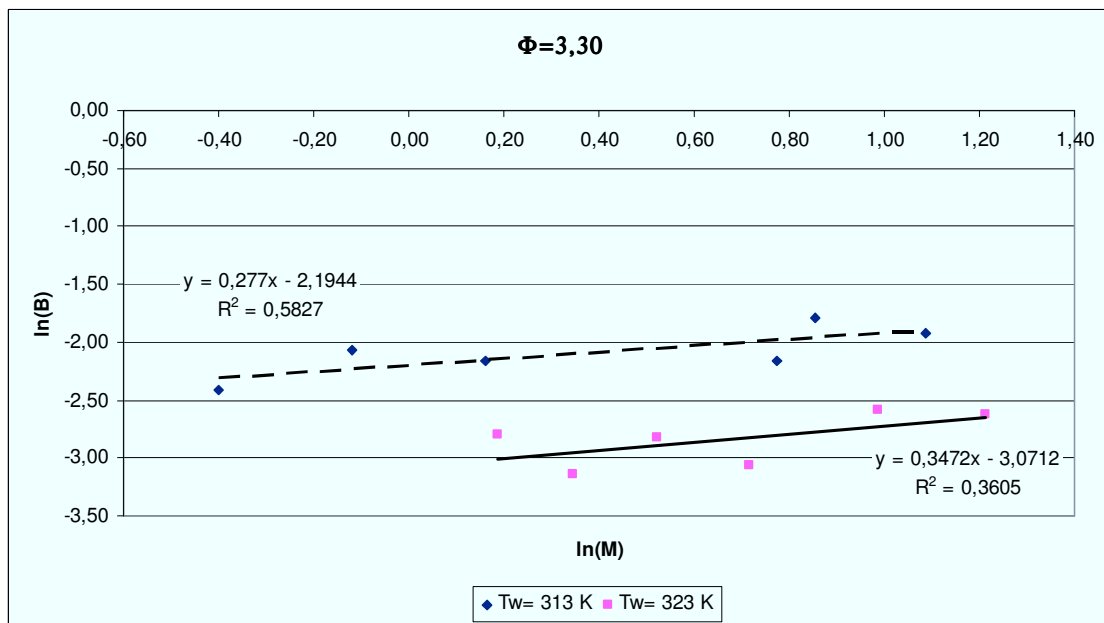


**Figure 4.26** –  $\ln(B)$  vs  $\ln(M)$  calculated for test with equivalent ratio  $\Phi=3,30$ . The continue line is the linear regression for the points corresponding to  $T_w= 323$  K. The dashed line is the linear regression for the points corresponding to  $T_w= 313$  K

As can be seen from Figure 4.25 and 4.26 the best linear regression fit is obtained for low wall temperature.

Then it is possible to have a pair of  $a$  and  $n$  for each wall temperature and for each equivalent ratio, as reported in the following table.

$\Phi$	$T_w$ (K)	$a$	$n$
2,38	313	0,212	-0,7623
	323	0,116	-0,4549
3,30	313	0,111	0,277
	323	0,046	0,3472

**Table 4.8** – Factors  $a$  and  $n$  calculated for each  $\Phi$  and  $T_w$

Through an arithmetic mean we have that

$$a = 0.121$$

$$n = -0.148$$

Now it is possible to draw the curve corresponding to equation (2.108) and make the comparison with the experimental data,  $\bar{D}$ , for each equivalent ratio.

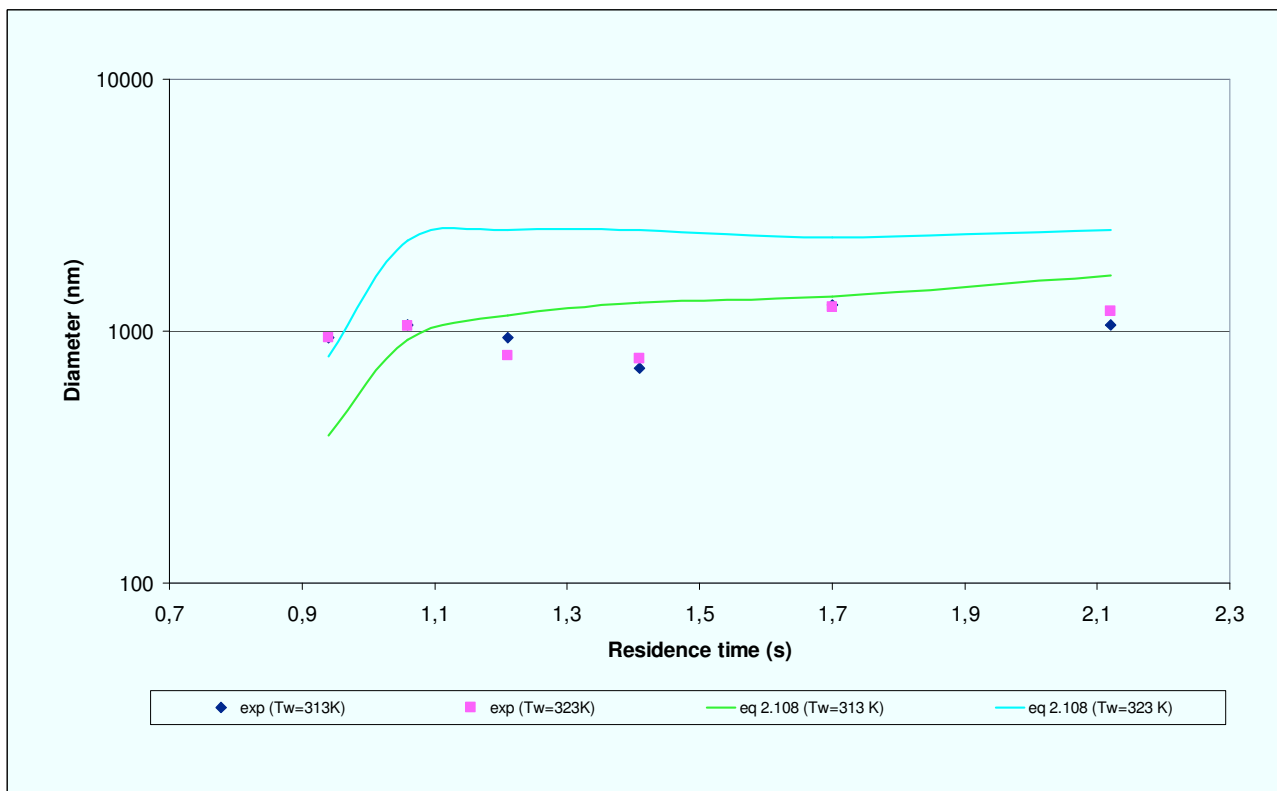


**Figure 4.27** – Comparison between experimental data,  $\bar{D}$ , and model by (2.108), for  $\Phi=2,38$ , vs residence time (s)

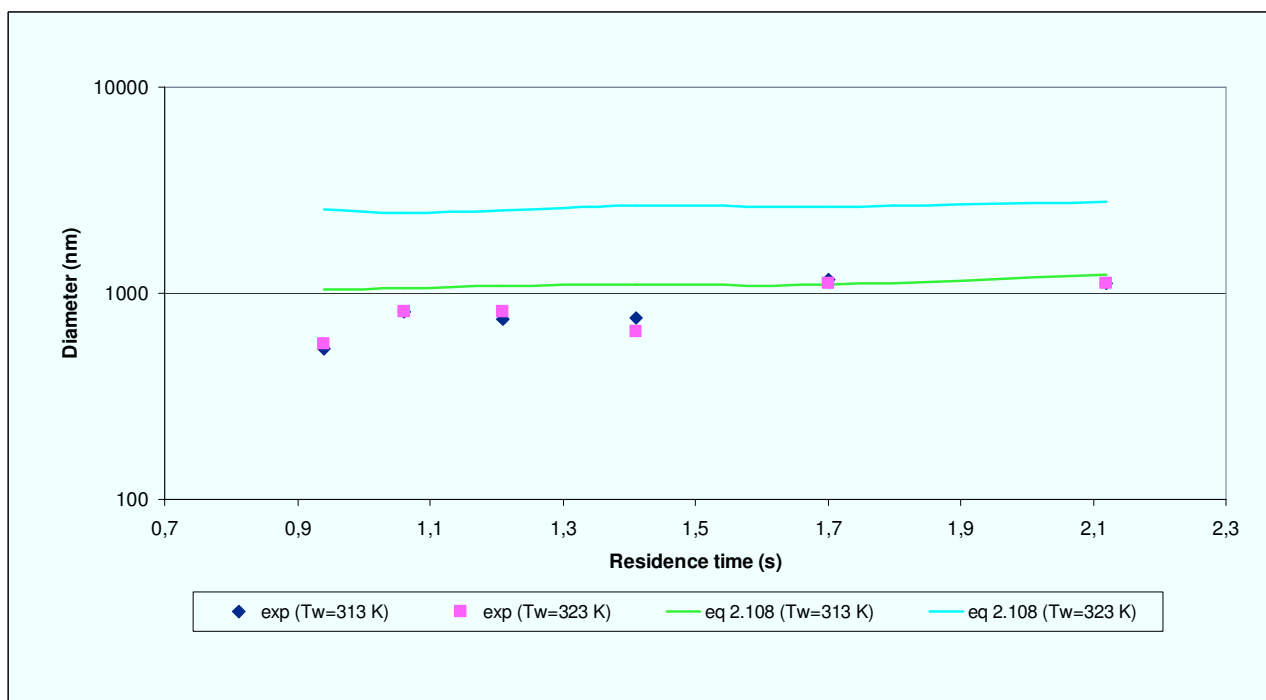


**Figure 4.28** - Comparison between experimental data,  $\bar{D}$ , and model by (2.108), for  $\Phi=3.30$ , vs residence time (s)

As can be seen from the Figures 4.27 and 4.28, the equation (2.108) provides a better fitting of experimental data with respect to equation (2.99).

## Conclusions

This Ph.D. thesis has faced the study of the heterogeneous condensation as a technique to pre-conditioning the sub-micrometric particles contained in a gas with the aim of increase their dimensions enough to allow the use of consolidate cleaning techniques. This problem is important especially for sub-micrometric particles in the Greenfield gap 0.1-2  $\mu\text{m}$ , for which the traditional methods are far less ineffective.

For this purpose instrumented lab scale equipment has been designed, constructed and tested. Experimental protocols and measurement techniques have been optimized. The core of the equipment is the growth tube, that consists in a glass tube where the particle laden gas flows comes into contact with a supersaturated water vapour environment, generated by a liquid film flowing on the tube internal walls.

The sizing of this reactor is based on the results of a theoretical model, aimed to obtain a sufficient residence time for the particle-laden gas, high enough to allow: 1) the complete diffusion of the vapour from the walls to the centre of the tube, 2) the nucleation and the growth of the liquid-solid aerosols.

Since the gas exiting the growth tube is saturated with water and contains liquid-solid aerosols, there were several problems to measure of the size and the concentration of the enlarged drops with the included particles, and to distinguish them from solid particles not covered by liquid. Several measurement systems were used: DMA (Model 3936), DLS (Model Hpps-Et Standard System) and LAS (Model 3340). Each of these devices is based on a different functioning principle. In particular the most reliable systems were considered the LAS 3340, an optical instrument that bases its measures on the refractive index of the material. This condition has posed some doubts on the real capacity of this system to discriminate between drops with a particle inclusion “solid core”, that not have an homogeneous refractive index. A simulation has allowed to evidence that, date the increase previewed by the models, the influence of the solid core on the measure considering the drop composed by pure water, is minimal.

A simplified theoretical model has been used to estimate temperature, pressure and supersaturation profiles along the growth tube at different radial positions. Water condensation on the sub-micrometric particles, liquid-solid droplet growth, temperature and water vapour profiles in the growth tube have been calculated and they have been used to interpret the experimental results. Although qualitatively consistent, theoretical

models overestimate the experimental data. This seems to be a consequence of a limited flux of water vapour from the liquid film that eventually limits the actual droplet growth. This mass flux limitation is not considered in the simplified theoretical model at present, but can be taken into account by introducing a semi-empirical relation to estimate the actual mass flux from the liquid. With this modification, the model is able to provide a reliable description of experimental data.

The experimental results and the model considerations shows that the heterogeneous condensation can be easily carried out with the simple growth tube has the advantage to be simple, therefore of easy realization and then not expensive. Therefore it should be worth of consideration for a large scale industrial application. In this sense, the next step of this research should be represented by the design and the construction of a pilot scale prototype.

## Appendix

### Definition of particle diameters

For a spherical particle of unit density, the size can be simply characterized by the geometric diameter ( $d_p$ ). However, atmospheric particles can have arbitrary shape and density. Therefore their diameters are described by an equivalent diameter, defined as the diameter of a sphere that would have the same physical behaviour as the particle in question (US EPA, 2004). The appropriate particle size definition depends primarily on the type of measurement made (John, 2001):

- *Aerodynamic diameter* ( $d_a$ ): The aerodynamic diameter is defined as that of a spherical particle of unit density having the same settling velocity as the particle considered. It is usually used to analyze the data from a cyclone, a cascade impactor, an Electrical Low Pressure Impactor (ELPI) and an Aerodynamics Particle Sizer (APS)
- *Diffusive diameter* ( $d_d$ ): The diffusive diameter is the diameter of a particle of unit density having the same rate of diffusion as the particle. This diameter would be used for a diffusion battery measurement
- *Stokes diameter* ( $d_{St}$ ) or *hydrodynamic diameter* ( $d_H$ ): The Stokes diameter describes particle size based on the aerodynamic drag force imparted when its velocity differs from that of the surrounding fluid. The Stokes diameter is the appropriate parameter for particle behaviour governed by diffusion, because the particle diffusion coefficient and Brownian diffusion velocity can be related through the Stokes-Einstein equation:

$$d_H = \frac{kT}{3\pi\mu D} \quad (1)$$

where:

$d_H$  = hydrodynamic diameter

$D$  = translational diffusion coefficient

$k$  = Boltzmann's constant

$T$  = absolute temperature

$\mu$  = viscosity

The Stokes diameter would be used in size distributions based on light scattering and mobility analysis. Thus particles of equal Stokes diameters that carry the same electrical charge will have the same electrical mobility. For spherical particles, the electrical mobility diameter would equal the Stokes diameter. The *mobility diameter* ( $d_m$ ) is diameter of a spherical particle that would have the same electrical mobility. To correlate the mobility diameter with the actual diameter (geometric diameter of known spherical particles), it is necessary to consider an effective diameter ( $d_o$ ) of the gas in which the aerosol is immersed for the measurement:

$$d_m = d_p + d_o \quad (2)$$

For air at standard conditions, experimentally measured a value of  $d_o \sim 0.53$  nm (Fernandez de la Mora *et al.*, 2003).

- *Optical diameter* ( $d_{OP}$ ) = The optical diameter is defined as the diameter of a calibration particle having the same response in an instrument detecting particles by their interaction with light, namely that scatters the same amount of light into the solid angle measured. The optical diameter would be used with an Optical Particle Counter (OPC).
- *Equivalent spherical diameter (ESD)* = The equivalent spherical diameter of an irregularly-shaped object is the diameter of a sphere of equivalent volume (Jennings *et al.*, 1988). This would be used with an Atomic Force Microscopy (AFM).
- $d_{6-3}$  = This mean particle diameter is given by the ratio between the sixth and third moments of the particles number distribution function.

### Definitions of particle size distribution functions

*Monodisperse* aerosols have a single mode of particles that are all contained within a narrow size range, and are usually generated in laboratory. Aerosols containing a wide range of particle sizes are said to be *polydisperse* (Hinds, 1999). The mathematical description of particle size distributions is characterized by very fine successive size intervals, each of them containing a counted number of particles. Because the dependent variable, or the ordinate of the plot, is the number of particles, such a distribution is called a *number distribution* (John, 2001). If  $N(dp)$  is the number of particles in the size interval

centered between  $dp$  and  $dp+ddp$ , where  $dp$  is the particle number, the number distribution is

$$dN = N(dp) ddp \quad (3)$$

Since the particle diameter typically ranges over several orders of magnitude, it is common to use  $d \ln dp$  (or  $d \lg dp$ ) for the size interval, and the number distribution becomes

$$dN = N(dp) d \ln dp \quad (4)$$

Similarly, frequently used size distributions are the *surface distribution*, the *volume distribution* and the *mass distribution*:

$$\begin{aligned} dS &= S(dp) d \ln dp \\ dV &= V(dp) d \ln dp \\ dM &= M(dp) d \ln dp \end{aligned} \quad (5)$$

The data for one of the above distributions might be obtained directly by an appropriate analyzer or indirectly by the measured number distribution. The total particle number concentration is expressed as:

$$N_T = \sum_i N(d_{p,i}) \quad (6)$$

Assuming the particle as spherical, the total volume fraction is expresses as:

$$FV_T = \sum_i \left[ \sum_i N(d_{p,i}) \left( \frac{\pi}{6} \right) (d_{p,i})^3 \right] \quad (7)$$

It is necessary to know the density,  $\rho$ , of the particle to obtain the total mass from the total volume fraction.

Other useful parameters that are calculated from the size distributions are:

- the *mean arithmetic diameter*,



$$\bar{d} = \frac{\sum_i N(d_{p,i}) d_{p,i}}{\sum_i N(d_{p,i})} \quad (8)$$

- the *median diameter* defined as the diameter for which one-half the total number of particles are smaller and one-half larger
- the *mode diameter* defined as the diameter associated to the peak of the lognormal distribution
- the *mean geometric diameter* ( $d_g$ ),

$$\log d_g = \frac{\sum_i N(d_{p,i}) d_{p,i}}{\sum_i N(d_{p,i})} \quad (9)$$

- the *geometric standard deviation* ( $\sigma_g$ ),

$$\log \sigma_g = \left[ \frac{\sum_i N(d_{p,i}) (\log d_g - \log d_i)^2}{\sum_i N(d_{p,i}) - 1} \right]^{1/2} \quad (10)$$

## Bibliography

- Adachi, M., Okuyama, K., Kousaka, Y., Electrical Neutralization of Charged Aerosol Particles by Bipolar Ions, *Journal of Chemical Engineering Japan* 16 (1983) 229-235.
- Aitken, J. On Improvements in the Apparatus for Counting the Dust Particles in the Atmosphere, *Proceedings of the Royal Society of Edinburgh* XVI:207–235 (1888–1889)
- Allen, M.D., Raabe, O.G., Slip Correction Measurements of Spherical Solid Aerosol Particles in an Improved Millikan Apparatus, *Aerosol Science and Technology* 4 (1985) 269-286.
- Alonso, M., Kousaka, Y., Nomura, T., Hashimoto, N., Hashimoto, T., Bipolar charging and neutralization of nanometer-sized aerosol particles, *Journal of Aerosol Science* 28 (1997) 1479-1490.
- Andre Nel, *et al.*, Toxic Potential of Materials at the Nanolevel, *Science* 311, 622 (2006)
- Andronache C., Diffusion and electric charge contributions to below-cloud wet removal of atmospheric ultra-fine aerosol particles. *Journal of Aerosol Science*, 35 (2004)1467-1482
- Barrett J. C., C. F. Clement, Growth rates for liquid drops *J. Aerosol Sci.*, 19 (2) (1988), 223-242.
- Barrett J. C., H. J. Fissan, Aerosol Growth By Condensation In A Well-Mixed Chamber. *J Aerosol Sci.*, 20 (3), (1989), 279-288,
- Barrett J. C. and Baldwin T. J., Aerosol nucleation and growth during laminar tube flow: maximum saturations and nucleation rates, *J. Aerosol Sci.* Vol. 31, No. 6, pp. 633-650, 2000
- Bird B.R., Warren E.S., Lightfoot E. N., *Transport Phenomena, John Wiley & Sons*, (2002) Second edition
- Biswas P., Chang-Yu Wu, Nanoparticles and the Environment. *Journal of the Air & Waste Management Association*, J. Air & Waste Manage. Assoc. 55 (2006) 708–746
- Biswas S., V. Verma, J.J. Schauer, C. Sioutas, Chemical speciation of PM emissions from heavy-duty diesel vehicles equipped with diesel particulate filter (DPF) and selective catalytic reduction (SCR) retrofits, *Atmos. Environ.* 43 (2009) 1917- 1925.
- Biswas, P.; Wu, C.Y. Control of Toxic Metal Emission From Combustors Using Sorbents: A Review; *J. Air & Waste Manage. Assoc.* 1998, 48, 113-127.

- Brin A. A. and Fisenko S. P., Growth and Motion of Heterogeneous Water Droplets in Laminar Flow Diffusion Chambers, *Colloid Journal*, 69 (6) (2007), 679–684
- Calvert, S. and Englund, H.M. Editors,. *Handbook of Air Pollution Technology* Wiley, New York, (1984) 236
- Carstens J. C., Williams A. and Zung J. T., Theory of droplet growth in clouds. II. Diffusional interaction between two growing droplets, *J. Atmos. Sci.*, 27 (1970) 798-803.
- Chang, M.C.O., Chow, J.C.; Watson, J.G.; Hopke, P.K.; Yi, S.M.; England, G.C. Measurement of Ultrafine Particle Size Distributions From Coal-, Oil-, and Gas-Fired Stationary Combustion Sources; *J. Air & Waste Manage. Assoc.* 2004, 54, 1494-1505.
- Christensen, K.A., Stenholm, M. and Livbjerg, H., The formation of submicron aerosol particles, HCL and SO<sub>2</sub> in straw-fired boilers. *Journal of Aerosol Science* 29 (1998) 421–444.
- D'Alessio, A., Barone, A.C., Cau, R., D'anna, A., Minutolo, P., Surface deposition and coagulation efficiency of combustion generated nanoparticles in the size range from 1 to 10 nm, *Proceedings of the Combustion Institute* 30 (2005) 2595-2603.
- D'Alessio, A., D'Anna, A., Gambi, G. and Minutolo, P., The spectroscopic characterisation of UV absorbing nanoparticles in fuel rich soot forming flames. *Journal of Aerosol Science* 29 (1998) 397–409.
- D'Anna, A., Combustion-formed nanoparticles, *Proceedings of the Combustion Institute* 32 (2009) 593–613
- D'Anna, A., Commодо, M., Sirignano, M., Minutolo, P., Pagliara, R., Particle Formation in Opposed-Flow Diffusion Flames of Ethylene: an Experimental and Numerical Study, *Proceedings of the Combustion Institute* 32 (2009) 793-801.
- D'Anna, A., Commодо, M., Violi, S., Allouis, C., Kent, J., Nano organic carbon and soot in turbulent non-premixed ethylene flames, *Proceedings of the Combustion Institute* 31 (2007) 621-629.
- Dahlin, R.S., Su, Ja.-An. and Peters, L.K.,. Aerosol formation in reacting gases: Theory and application to the anhydrous NH<sub>3</sub>–HCl system. *AIChE Journal*, 27 (1981) 404–418.
- De Filippo, A., Maricq, M.M., Diesel nucleation mode particles: Semivolatile or solid?, *Environmental Science Technology* 42 (2008) 7957-7962.
- Donaldson, K., Li, X.Y., Macnee, W., Ultrafine (Nanometre) particle mediated lung injury, *Journal of Aerosol Science* 29 (1998) 553-560.

- Echavarria C. A., Sarofim A. F., Lighty J. S., D'Anna A., Evolution of soot size distribution in premixed ethylene/air and ethylene/benzene/air flames: Experimental and modeling study, in press at Combustion and Flame (2010)
- Eckert E. R. G. and Drake R. M., , Analysis of Heat and Mass Transfer, (1972)McGraw-Hill
- Ehrlich, C., Noll, G. and Kalkoff, W-D. PM<sub>10</sub>, PM<sub>2.5</sub> and PM<sub>1.0</sub>-emissions from industrial plants-results from measurement programmes in Germany. s.l. : Atmospheric Environment 41, 6236–6254, 2007
- Fan Fengxian, Yang Linjun, Yan Jinpei, Yuan Zhulin, Numerical analysis of water vapour nucleation on PM<sub>2.5</sub> from municipal solid waste incineration, Chem. Eng. J. 146 (2009) 259–265
- Fernandez De La Mora, J.J., De Juan, L.L., Liedtke, K., Schmidt-Ott, A., *Mass and size determination of nanometer particles by means of mobility analysis and focused impaction*, Journal of Aerosol Science 34 (2003) 79-98.
- Fisenko S. P., Brin A. A., Heat and mass transfer and condensation interference in a laminar flow diffusion chamber, International Journal of Heat and Mass Transfer 49 (2006) 1004–1014
- Fisenko S. P., Wang Wei-Ning, Shimada Manabu, Okuyama Kikuo, Vapour condensation on nanoparticles in the mixer of a particle size magnifier, International Journal of Heat and Mass Transfer, 50 (2007) 2333–2338
- Flagan, R.C., *History of Electrical Aerosol Measurements*, Aerosol Science and Technology 28 (1998) 301-380.
- Flagan and Seinfeld. Fundamentals of air pollution engineering, (1988) Prentice Hall, USA
- Fletcher, Size effect in heterogeneous Nucleation, The journal of chemical physics, 29 (3) (1958), 572-576.
- Fuchs, N. A. Evaporation and Droplet Growth in Gaseous Media. Pergamon Press, (1959) London.
- Fuchs N. A. and Sutugin A. G., High-dispersed aerosols, in G. M. Hidy and J. R. Brock (ed.) *Topics in Current Aerosol Research*, Pergamon Press, London, (1971) 2, I.
- Graetz L., Ueber die Wärmeleitungsfähigkeit von Flüssigkeiten, Annalen der Physik und Chemie 18, 79 (1883).
- Gretschner Harald, Schaber Karlheinz, Aerosol formation by heterogeneous nucleation in wet scrubbing processes Chemical Engineering and Processing 38 (1999) 541–548

- Heidenreich S., Condensational Droplet Growth In The Continuum Regime--A Critical Review For The System Air-Water *J. Aerosol Sci.*, 25 (1) (1994), 49-59,
- Heidenreich S., Condensational droplet growth as a preconditioning technique for the separation of submicron particles from gases, *Chemical Engineering and Processing* 34 (1995) 235-244
- Heidenreich S., U. Vogt, H. Büttner, F. Ebert, A novel process to separate submicron particles from gases - a cascade of packed columns, *Chemical Engineering Science* 55 (2000) 2895-2905
- Heim, Mullins, Wild, Meyer, Kasper. Filtration efficiency of aerosol particles below 20 nanometers. *Aerosol Science. Technology*. 39 (2005) 782-789.
- Hering Susanne V. (1), Stolzenburg Mark R., A Method for Particle Size Amplification by Water Condensation in a Laminar, Thermally Diffusive Flow, *Aerosol Science and Technology*, 39 (2005) 428–436,
- Hering Susanne V. (2), Stolzenburg Mark R., Quant Frederick R., Oberreit Derek R. and Keady Patricia B., A Laminar-Flow, Water-Based Condensation Particle Counter (WCPC) *Aerosol Science and Technology*, 39 (2005) 659–672.
- Hildemann, L.M.; Markowski, G.R.; Jones, M.C.; Cass, G.R. Submicrometer Aerosol Mass Distributions of Emissions From Boilers, Fireplaces, Automobiles, Diesel Trucks, and Meat-Cooking Operations; *Aerosol. Sci. Technol.* 1991, 14, 138-152.
- Hinds, W.C., *Aerosol Technology. Properties, behavior, and measurement of airborne particles*, 2nd ed 1999, John Wiley & Sons, New York, NY
- Hogan, C.J.; Lee, M.H.; Biswas, P. Capture of Viral Particles in Soft X-Ray-Enhanced Corona Systems: Charge Distribution and Transport Characteristics; *Aero. Sci. Technol.* 2004, 38, 475-486.
- Jennings, B.R., Parslow, K., *Particle Size Measurement: The Equivalent Spherical Diameter*, Proceedings of the Royal Society of London, Series A 419 (1988) 137-149.
- Johannessen T., Christensen, J.A., Simonsen, O. and Livbjerg, H., The dynamics of aerosols in condensational scrubbers. *Chemical Engineering Science* 52, (1997) 2541–2556
- John, W., *Size distribution Characteristics of Aerosols*, in *Aerosol Measurement: Principles, Techniques, and Applications*, 2nd Ed. by Baron, P.A., Willeke, K., (2001) 99-116, John Wiley & Sons, New York, NY.
- Jung, C.H., Kim, Y.P, *Numerical estimation of the effects of condensation and coagulation on visibility using the moment method*, *Journal of Aerosol*

Science 37 (2006) 143-161.

Kashchiev D.. Analysis of experimental data for the nucleation rate of water droplets. The journal of chemical physics 125 (2006) 044505

Kittelson, D.B. Engines and Nanoparticles: A Review; J. Aero. Sci. 1998, 29, 575-588.

Köhler, H. Trans. Faraday Soc. 1936, 2, 1152.

Köhler, H. (1921). Zur kondensation des wasserdampfe in der atmosphäre, Geofys. Publ. 2:3–15.

Köhler, H. (1926). Zur Thermodynamik der Kondensation an hygroskopischen Kernen und Bemerkungen uK ber das Zusammenfließen der Tropfen. Meddelanden fran Statens Meteorologisk-Hydrograxska Anstalt, Bund 3, No. 8, 1-16.

Krames, J., Büttner, H., & Ebert, F.. Submicron particle generation in wet scrubbing systems. Abstracts of the annual meeting of American association for aerosol research (1992) 236.

Krastanov, L. Idojaras 1957, 61, 333

Kuang-Yu Liu, Ming-Yen Wey. Filtration of nano-particles by a gas-solid fluidized bed. Journal of Hazardous Materials, 147 (2007) 618-624.

Kulmala M., Condensational Growth and Evaporation in the Transition Regime An Analytical Expression Aerosol Scicncc and Technology 19:381-388 (1993)

Kulmala, M. How Particles Nucleate and Grow; Science 2003, 302, 1000-1001.

Kulmala, M.; Vehkamäki, H.; Petäjä, T.; Dal Maso, M.; Lauri, A.; Kerminen, V.M.; Birmili, W.; McMurry, P.H. Formation and Growth Rates of Ultrafine Atmospheric Particles: A Review of Observations; J. Aero. Sci. 2004, 35, 143-176.

Lancaster B. W. and W. Strauss, A study of steam injection into wet scrubbers, *Ind. Eng. Chem., Fundam.*, 10 (1971) 362- 369

Lee Doh-Won, Hopke Philip K., Don H. Rasmussen, Hwa-Chi Wang, and Rashid Mavliev, Comparison of Experimental and Theoretical Heterogeneous Nucleation on Ultrafine Carbon Particles *J. Phys. Chem. B*, 107 (2003), 13813-13822

<http://www.lungusa.org/site/pp.asp?c=dvLUK9O0E&b=39308>

Lloyd, S.M.; Lave, L.B.; Matthews, H.S. Life Cycle Benefits of Using Nanotechnology to Stabilize Platinum-Group Metal Particles in Automotive Catalysts; *Environ. Sci. Technol.* 2005, 39, 1384-1392.

- Matti Maricq M., On the electrical charge of motor vehicle exhaust particles, *J. Aerosol Sci.*, 37 (2006) 858-874.
- Mavliev, R.; Hopke, P. K.; Wang, H.-C.; Lee, D.-W. A Transition from Heterogeneous to Homogeneous Nucleation in the Turbulent Mixing CNC *Aerosol Sci. Technol.* (2001), 35, 586
- Maxwell J.C., Diffusion. In: W.D. Niven, Editor, *The Scientific Papers of James Clerk Maxwell* Vol. 2, Cambridge University Press (1890), 625.
- McDonald J. E. Homogeneous Nucleation of Vapour Condensation. I. Thermodynamic Aspects. *American Journal of Physics*, 30 (1962) 870-877.
- McMurry, P.H.; Woo, K.S.; Weber, R.; Chen, D.R.; Pui, D.Y.H. Size Distributions of 3–10 nm Atmospheric Particles: Implications for Nucleation Mechanisms; *Philos. Trans. Royal Soc. Lond. Series a-Math. Phys. Eng. Sci.* 2000, 358, 2625-2642.
- Menon S., J. Hansen, L. Nazarenko, Y. Luo, Climate Effects of Black Carbon Aerosols in China and India, *Science* 297 (2002) 2250 -2253.
- Minutolo P., A. D'Anna, A. D'Alessio, On detection of nanoparticles below the sooting threshold, *Combust. Flame*, 152 (1-2) (2008) 287-292.
- Nemmar, A., Hoylaerts, M.F., Hoet, P.H., Nemery, B., Possible mechanisms of the cardiovascular effects of inhaled particles: systemic translocation and prothrombotic effects, *Toxicological Letters* 149 (2004) 243-253.
- Nemmar, A., Hoet, P.H.M., Thomeer, M., Nemery, B., Vanquickenborne, B., Vanbillonen, H., Passage of inhaled particles into the blood circulation in humans, *Circulation* 105 (2002) 411-414.
- Nusselt W., *Z. Ver. Deut. Ingr.*, 54 (1910) 1154.
- Oberdorster, G., Sharp, Z., Atudorei, V., Elder, A., Gelein, R., Lunts, A., Extrapulmonary translocation of ultrafine carbon particles following whole-body inhalation exposure of rats, *Journal of Toxicology and Environmental Health A* 65 (2002) 1531-1543.
- Oberdorster, G., Pulmonary effects of inhaled ultrafine particles, I. of the alveolar macrophage in lung injury: study with ultrafine particles, *International Archives of Occupational and Environmental Health* 74 (2001) 1-8.
- Oberdorster, G., Ferin, J., Gelein, R., Soderholm, S.G., Finkelstein, J., Role of the alveolar macrophage in lung injury: study with ultrafine particles, *Environment and Health Perspectives* 97 (1992) 193-199.
- Okuyama K., Y. Kousaka, and T. Motouchi, Condensational Growth of Ultrafine Aerosol Particles in a New Particle Size Magnifier, *Aerosol Science*

*and Technology* (1984) 353-366

Onyango, M.S.; Kojima, Y.; Matsuda, H.; Ochieng, A. Adsorption Kinetics of Arsenic Removal From Groundwater by Iron-Modified Zeolite; *J. Chem. Eng. Japan* 2003, 36, 1516-1522.

Park S.H. and Lee K.W., Condensational growth of polydispersed aerosols for the entire particle size range *Aerosol Sci.* 3, (I), (2000), 813-814.

Peng, X.J.; Luan, Z.K.; Ding, J.; Di, Z.H.; Li, Y.H.; Tian, B.H. Ceria Nanoparticles Supported on Carbon Nanotubes for the Removal of Arsenate From Water; *Mater. Lett.* 2005, 59, 399-403.

Perry R. H., Green D. W., Perry's Chemical Engineering Handbook, (Sixth Edition), McGraw-Hill Ed. 1984

Peukert W., Wadenpohl C.. Industrial separation of fine particles with difficult dust properties. *Powder Technology*, 118 (2001)136-148.

Podzimek, J., and Carstens, J. C. (1985). The 100Year Evolution of Aitken Nuclei Counters: Current and Future Problems, *J. Rech. Atmos.* 19:257–274

Pope C.A. III, R.T. Burnett, M.J. Thun, E.E. Calle, D. Krewski, K. Ito, G.D. Thurston, Cancer, cardiopulmonary mortality, and long-term exposure to fine particulate air pollution, *J. Amer. Med. Assoc.* 287 (2002) 1132-1141.

Reischl, G.P., Makela, J.M., Karch, R., Necid, J., *Bipolar charging of ultrafine particles in the size range below 10 nm*, *Journal of Aerosol Science* 27 (1996) 931-949.

Schaber, K.,. Aerosol formation in absorption processes. *Chemical Engineering Science* 50, (1995) 1347–1360.

Schauer P. J., Removal of submicron particles from a moving gas stream, *Ind. Eng. Chem.*, 43 (1951) 1532-1538

Seinfeld and Pandis. Seinfeld, J.H., Pandis, S.N., 1998. *Atmospheric Chemistry and Physics*. Wiley, New York, (1998)1326.

Smorodin, V. Ye. In *Circulation of Atmosphere and Moisture Transfer oVer the Central and East Europe*. Abstracts of the International Symposium of Interdepartmental Commission at the USSR, Moscow, (1983) 12-13

Smorodin, V. Ye.; Bazzaev, T. V. *Trudy Tsentralnoy Aerologitcheskoy ObserVatorii* (Russian) (1986) 162-169

Smorodin V. Y., Hopke P. K., Condensation Activation and Nucleation on Heterogeneous Aerosol Nanoparticles, *J. Phys. Chem. B*, 108 (2004), 9147-9157



Thomson W. T. Lord Kelvin, *Phil. Mag.* 42, 448 (1871)

TSI Incorporated – 500 Cardigan Road, Shoreview, MN 55126 USA, Http:  
//www.tsi.com

US EPA, 2009, HTTP: //

[WWW.EPA.GOV/OAR/PARTICLEPOLLUTION/PUBLICATIONS.HTML](http://WWW.EPA.GOV/OAR/PARTICLEPOLLUTION/PUBLICATIONS.HTML)

US EPA, *Air Quality Criteria Document for Particulate Matter (October 2004)*  
Volume I & II, HTTP: //

[WWW.EPA.GOV/OAR/PARTICLEPOLLUTION/PUBLICATIONS.HTML](http://WWW.EPA.GOV/OAR/PARTICLEPOLLUTION/PUBLICATIONS.HTML)

US EPA, *The Particle Pollution Report Current Understanding of Air Quality  
and Emissions through 2003*, HTTP:

[//WWW.EPA.GOV/AIRTRENDS/AQTRND04/PMREPORT03/REPORT\\_2405.PDF](http://WWW.EPA.GOV/AIRTRENDS/AQTRND04/PMREPORT03/REPORT_2405.PDF)

Vincent, J.H.; Clement, C.F. Ultrafine Particles in Workplace Atmospheres;  
*Philos. Trans. Royal Soc. Lond. Series a-Math. Phys. Eng. Sci.* 2000, 358,  
2673-2682.

Wagner P. E., Aerosol growth by condensation, in W. H. Marlow (ed.), *Aerosol  
Microphysics II*, Springer, Berlin, (1982) 129.

Wang and Kasper, Filtration efficiency of nanometer-size aerosol particles.  
*Journal of Aerosol Science*, 22 (1991) 31-41.

Whitby, K.T., *The physical characterization of sulfur aerosols*, Atmospheric  
Environment 12 (1978) 135-159.

Wichmann, H.E., Spix, C., Tuch, T., Wolke, G., Peters, A., Heinrich, J., Kreyling,  
G., Heyder, J., *Daily mortality and fine and ultrafine particles in Erfurt,  
Germany. Part-I: Role of particle number and particle mass.*, Health Effects  
Institute Research Report, number 98 (2000).

Wiedensohler, A., *An approximation of the bipolar charge distribution for  
particles in the submicron size*, Journal of Aerosol Science 19 (1988) 387-  
389.

Wiedensohler, A., Lutkemeter, E., Feldpaush, M., Helsper, C., *Investigation of  
the Bipolar Charge Distribution at Various Gas Conditions*, Journal of  
Aerosol Science 17 (1986) 413-416.

Williams M. M. R., Growth rates of liquid drops for large saturation ratios J.  
*Aerosol Sci.*, 26, (3) (1995), 477-481.

Woodard, K. Stationary Source Control Techniques Document for Fine  
Particulate Matter. s.l.: EPA CONTRACT NO. 68-D-98-026, (1998).

Yan Jin-pei, Yang Lin-jun, Zhang Xia, Sun Lu-juan, Zhang Yu, Shen Xiang-lin.  
Separation of PM<sub>2.5</sub> from combustion based on vapour condensation and

scrubbing. Journal of fuel chemistry and technology, 36 (3), (2008) 267-272

Yang Linjun, Bao Jingjing, Yan Jinpei, Liu Jinhui, Song Shijuan, Fan Fengxian, Removal of fine particles in wet flue gas desulfurization system by heterogeneous condensation, Chemical Engineering Journal, 156 (2010) 25-32

Yoshida T., Kousaka Y. and Okuyama K., Growth of aerosol particles by condensation, Ind. Eng. Chem., Fundam., 15 (1976) 37-41

Young, T. "An Essay on the Cohesion of Fluids". Phil. Trans. R. Soc. Lond. 95 (1805) 65–87.

Zhang, W.; Wang, C. Nanoscale Metal Particles for Dechlorination of PCE and PCBs; Environ. Sci. Technol. 1997, 31, 2154-2156.

Zhang, W.X. Nanoscale Iron Particles for Environmental Remediation: an Overview; *J. Nanopart. Res.* 2003, 5, 323-332.